

Von der Fakultät für
Bauingenieurwesen und Geodäsie der
Gottfried Wilhelm Leibniz Universität
Hannover zur Erlangung des Grades
Doktor-Ingenieur genehmigte Dissertation



Multiscale Analysis of Textile Composites - Stiffness and Strength -

vorgelegt von:

Dipl.-Ing. Gerald Ernst

Tag der Promotion:

12. Dezember 2008

Referent:

Prof. Dr.-Ing. habil. Raimund Rolfes,
Leibniz Universität Hannover

Korreferent:

Prof. Dr.-Ing. habil. Volker Ulbricht,
Technische Universität Dresden

Gutachter:

Prof. Murray Scott,
Royal Melbourne Institute of Technology

Herausgeber:

Prof. Dr.-Ing. habil. R. Rolfes

Institut für Statik und Dynamik
Leibniz Universität Hannover


Appelstraße 9A
30167 Hannover

Tel: 0511 - 762 3867

Fax: 0511 - 762 2236

www.isd.uni-hannover.de

info@isd.uni-hannover.de



© Gerald Ernst,
Institut für Statik und Dynamik

Alle Rechte, insbesondere das der Übersetzung in fremde Sprachen, vorbehalten. Ohne Genehmigung des Autors ist es nicht gestattet, dieses Heft ganz oder teilweise auf photomechanischem, elektronischem oder sonstigem Wege zu vervielfältigen.

ISSN 1862-4650

Mehrskalenanalyse textiler Faserkunststoffverbunde - Steifigkeit und Festigkeit

Kurzfassung Die experimentelle Bestimmung von Steifigkeiten und Festigkeiten textiler Faserkunststoffverbunde ist teuer und zeitaufwendig. Darüber hinaus ist es wünschenswert, Parameter einer Lage innerhalb eines textilen Preforms zu bestimmen, weil damit eine sehr viel genauere und einfachere Analyse des Versagens vorgenommen werden kann, auch wenn dadurch Effekte der textilen Geometrie eventuell vernachlässigt werden. Sind nur Parameter für eine textile Lage, die mehrere Faserorientierungen enthält, bekannt, so ist es schwer, Aussagen über das Versagen und Schwachstellen des Laminates zu treffen. Experimentell ist es jedoch ausschließlich möglich, eine komplette textile Lage in eine Prüfmaschine einzuspannen.

Mit der vorgestellten Finite-Elemente-Mehrskalenanalyse ist es möglich, allein aus der Kenntnis des (nichtlinearen) Verhaltens von Epoxidharz und der Fasern, sowie der textilen Geometrie, Steifigkeiten und Festigkeiten von textilen Faserkunststoffverbunden zu bestimmen. Sowohl Parameter für eine einzelne Lage in einem textilen Preform, als auch für mehrere textile Lagen können berechnet werden, wobei der Schwerpunkt aus oben genannten Gründen auf der einzelnen Lage liegt. Nebenbei können mit der Mehrskalanalyse auch Steifigkeiten und Festigkeiten unidirektionaler Faserkunststoffverbunde ermittelt werden.

Ein besonderer Schwerpunkt liegt im Rahmen dieser Arbeit auf der Entwicklung und Verwendung von Materialmodellen und Versagenskriterien, die in der Lage sind, das nichtlineare und vom hydrostatischen Druck abhängige Verhalten der betrachteten Materialien realitätsnah zu beschreiben. Dabei kommen auch Regularisierungstechniken zum Einsatz, um eine Netzabhängigkeit der Lösung der Finite-Elemente Berechnung soweit wie möglich zu vermeiden. Die vorgenommenen Berechnungen und das vorgestellte Invarianten-basierte quadratische Versagenskriterium (IQC) werden anhand zahlreicher experimenteller Versuchsergebnisse validiert.

Schlagwörter: Mehrskalanalyse, textiler Faserkunststoffverbund, Materialmodelle

Multiscale Analysis of Textile Composites - Stiffness and Strength

Abstract The experimental determination of stiffness and strength of textile composites is expensive and time-consuming. Furthermore, it is desirable to determine the material behaviour of a single ply within a textile preform, because this enables a more exact and simple analysis of failure, even though effects of the textile geometry will be neglected. If only the behaviour of a whole textile layer is known, it is cumbersome to make predictions for failure and to conclude on weaknesses of the laminate. However, experimental tests allow for testing of a whole textile layer only, because it cannot be decomposed.

The presented finite element multiscale analysis is able to predict material behaviour of textile composites, solely from the (nonlinear) material behaviour of epoxy resin and glass fibres, as well as the textile fibre architecture. It is possible to make predictions for a single layer within a textile preform or for multiple textile layers at once, however the main emphasis in this work is on the single layer due to reasons stated above. Along the way stiffness and strength of UD-composites can be predicted as well.

The special emphasis of this work is the development and use of material models and failure criteria, that are able to describe the nonlinear and pressure-dependent behaviour of the materials occurring in the multiscale analysis. In order to avoid mesh-dependent solutions in the finite-element simulations, regularization techniques are applied. The simulations and the presented invariant-based quadratic criterion are validated on numerous experimental test results.

Keywords: Multiscale analysis, textile composites, material models

Vorwort

Die vorliegende Arbeit entstand während meiner Tätigkeit als wissenschaftlicher Mitarbeiter am Institut für Statik und Dynamik (ISD) der Leibniz Universität Hannover.

Meinem Doktorvater, Herrn Prof. Dr.-Ing. habil. R. Rolfes, Leiter des ISD, danke ich herzlich für seine engagierte Betreuung und insbesondere die vielen kritischen Fragen, die letztlich zum Erfolg dieser Arbeit beigetragen haben, sowie für die Übernahme des Hauptreferats.

Herrn Prof. Dr.-Ing. habil. V. Ulbricht vom Institut für Festkörpermechanik (IFKM) der TU Dresden danke ich für die freundliche Übernahme des Korreferates und die wertvollen Anregungen.

I would like to thank Prof. Murray Scott, CEO of the CRC-ACS, very much for reporting on this thesis and for inviting me to the CRC-ACS. He and his coworkers have given me a very warm welcome in Melbourne and have contributed to this thesis with many helpful discussions and hints.

Der Deutschen Forschungsgesellschaft möchte ich für die Förderung im Rahmen des Schwerpunktprogramms (SPP) 1123 danken, sowie den dort beteiligten Kollegen für die sehr gute Zusammenarbeit. Ein besonders großer Dank gebührt dabei Georg Haasemann vom IFKM sowie Daniel Hartung und Lars Aschenbrenner vom Deutschen Zentrum für Luft- und Raumfahrt in Braunschweig für die zahlreichen fachlichen Diskussionen und die Versuchsergebnisse, sie mir zur Verfügung gestellt haben. Bei Stephan Adden vom Institut für Flugzeugbau und Leichtbau der TU Braunschweig und Bodo Fiedler vom Institut für Kunststoffe und Verbundwerkstoffe der TU Hamburg-Harburg möchte ich mich ebenfalls für die von Ihnen zur Verfügung gestellten Versuchsdaten bedanken. Herrn Professor Ralf Cuntze danke ich für die interessanten Diskussionen und seine wertvollen Hinweise. Herrn Professor Hufenbach und seinen Mitarbeitern möchte ich für die gelungene Organisation und Leitung des SPP 1123 danken.

Dem Deutschen Akademischen Auslandsdienst danke ich sehr herzlich für das 3-monatige Auslandsstipendium für meinen Aufenthalt am Cooperative Research Center for Advanced Composite Structures (CRC-ACS) in Melbourne.

Besonders herzlich danke ich meinem Kollegen Matthias Vogler für die hervorragende und äußerst fruchtbare Zusammenarbeit. Einen ebenso herzlichen Dank möchte ich meinem Abteilungsleiter Christian Hühne für seine wertvollen Anregungen aussprechen und dafür, dass er mir oft den Rücken freigehalten hat. Für die wertvolle Hilfe und den großen Einsatz von „meinen“ Studenten Stefan Krieger, Sebastian Rileit, Alina Dukiewicz, Sina Berg und Bernd Böttcher möchte ich mich ebenfalls sehr herzlich bedanken. Herrn Prof. Dr.-Ing. habil. Dr.-Ing. E.h. H. Rothert möchte ich danken, dass er mir vor fünf Jahren die Chance eröffnet hat, am Institut für Statik mit der Promotion zu beginnen. Außerdem möchte ich allen anderen Kollegen, insbesondere Nina, Anne und Thomas, sowie Diedrich, Kai-Uwe, Lutz und Birger für die gute Zusammenarbeit und die angenehme Arbeitsatmosphäre danken.

Ein sehr großer und herzlicher Dank für die Unterstützung und Ermutigung gebührt meiner Familie und meinen Freunden, insbesondere meinen Eltern und meiner Freundin Olga, auch für das Verständnis dafür, dass diese Arbeit eine Menge Zeit in Anspruch genommen hat.

Hannover, im Dezember 2008

Gerald Ernst

Alles in der Welt endet durch Zufall und Ermüdung.

Heinrich Heine

Contents

1	Introduction	1
1.1	Rationale and Motivation	1
1.2	Literature Review	2
1.2.1	Mechanical Properties of Unidirectional Composites	2
1.2.2	Mechanical Properties of Textile Composites	3
1.3	Objective and Outline	10
2	Experimental Behaviour	12
2.1	Epoxy Resin	12
2.2	Glass Fibres	14
2.3	UD-Composites, Fibre Bundles	14
2.3.1	Material Characteristics	15
2.3.2	Failure Characteristic	16
2.4	Textile Composites	18
2.4.1	Types of Textile Composites	19
2.4.2	Material Characteristics of Textile Composites	22
3	Elastic-Plastic Material Models	25
3.1	Isotropic Material Model	25
3.1.1	Yield Surface	26
3.1.2	Flow Rule	27
3.1.3	Hardening Formulation	27
3.1.4	Numerical Treatment	29
3.2	Transversely Isotropic Elastic-Plastic Material Model for Fibre Bundles	30
3.2.1	Elastic Stress-Strain Relations	31
3.2.2	Transversely Isotropic Yield Surface	32
3.2.3	Hardening Formulation	35
3.3	Parameter Identification	37
4	Failure Criteria and Softening Formulations	40
4.1	Failure and Softening for Epoxy Resin	40
4.1.1	Failure Criterion	40
4.1.2	Damage Evolution and Stiffness Degradation	41
4.1.3	Fracture Energy Regularization	43
4.1.4	Tension Rod Regularization	49
4.1.5	Voxel Discretization	49

4.2	Failure and Softening Formulations for UD-Composites	53
4.2.1	Failure Criteria and Softening Formulations from Literature	53
4.2.2	New Invariant-based Quadratic Failure Criterion (IQC) and Softening Formulation	64
4.2.3	Comparison of Failure Criteria	67
4.3	Failure Criterion for Textile Composites	87
4.3.1	Failure Criterion of Juhasz	87
4.3.2	Off-Axis Tests for Criterion of Juhasz	89
4.3.3	Discussion of Juhasz-Criterion	90
5	Multiscale Analysis	93
5.1	Basic Concept of Multiscale Analysis	93
5.1.1	Need for Different Length Scales	93
5.1.2	Information-passing and Coupled Multiscale Analysis	94
5.2	Homogenization	95
5.2.1	Representative Volume Element and Unit Cell	96
5.2.2	Boundary Conditions	98
5.2.3	Determination of Homogenized Material Properties	103
5.3	Multiscale Algorithm for Stiffness and Strength of Textile Composites	104
5.3.1	Micromechanical Unit Cell	106
5.3.2	Mesomechanical Unit Cell	106
5.3.3	Macroscale Computations	106
6	Micromechanical Unit Cell Examples	107
6.1	Analytical Rules of Mixture for Stiffness and Strength of UD-composites	107
6.1.1	Transverse Young's Modulus E_{\perp}	108
6.1.2	In-Plane Shear Modulus $G_{\parallel\perp}$	108
6.2	Periodic Unit Cells	109
6.2.1	Comparison with Test Results from WWFE	112
6.2.2	Different Stiffness of Arrangements	116
6.3	Unit Cells with Random Fibre Arrangement	117
6.3.1	Linear-elastic Stiffness Prediction	118
6.3.2	Inelastic Computations	125
6.4	Summary	129
7	Mesomechanical Unit Cell Examples	131
7.1	Material Parameters of Fibre Bundles	131
7.2	Non-Crimp Fabrics	132
7.3	Biaxial Weft-Knit Fabrics	141
8	Macroscopic Examples	144
8.1	Coupon Test	144
8.2	3-Point-Bending Test	147
8.3	Summary	153

9	Summary and Conclusion	154
9.1	Summary	154
9.1.1	Material Model	154
9.1.2	Failure Criteria and Softening Formulations	155
9.1.3	Micromechanical Unit Cells	155
9.1.4	Mesomechanical Unit Cells	155
9.1.5	Macroscale Computations	156
9.2	Outlook	156
	References	158

List of Figures

1.1	Different preforms used in textile composites	2
1.2	Mosaic model of a repeating unit for an 8 harness satin.	5
1.3	Bridging model of a repeating unit for an 8 harness satin.	5
1.4	Finite element meshes of textile composites	6
1.5	Binary Model: Tow and matrix elements in a layer-to-layer angle interlock woven composite	7
2.1	Nonlinear material behaviour of Epoxy Resin RIM 135	13
2.2	Viscous material behaviour of Epoxy Resin	13
2.3	Nonlinear material behaviour of UD-layer	15
2.4	Shear stress-strain curve for cyclic $(+45/-45)_{2s}$ tensile test.	16
2.5	Fibre and inter-fibre failure modes	17
2.6	Stress distribution in laminate at first crack and at characteristic damage state	18
2.7	Multiaxial non-crimp fabric	20
2.8	Liquid resin infusion processes for textile preforms	21
2.9	Computer tomography of biaxial weft-knitted fabric before and after bending test	23
2.10	Stress-strain curves of biaxial weft-knitted fabric under different load directions	23
2.11	Strain rate dependent crack densities in biaxial weft-knitted fabric, increasing strain rate from left to right	24
2.12	Fibre waviness and resin pockets on micromechanical level (undulations) of a stitched NCF	24
3.1	Representation of plastic potential, yield surface and failure surface in σ_{vm} - p -invariant-plane	28
3.2	Preparation of experimentally obtained hardening curves for input as tabulated data: Total strains have to be converted into plastic strains by eq. 3.7	29
3.3	Radial return algorithm	30
3.4	Yield and failure surface of the transversely isotropic material model in $\sqrt{I_1}$ - I_3 -invariant-plane	36
3.5	Stress-strain curves of epoxy matrix RIM 135 from tests and curves used in computation	38
3.6	Widening of transversely isotropic yield surface with increasing equivalent plastic strain	38

4.1	Damage formulation	42
4.2	Evolution of damage for linear and exponential softening	42
4.3	Mesh-dependency and regularization of softening	44
4.4	Determination of strain energy release rate/fracture energy G_f	46
4.5	Stress-strain curves of micromechanical unit cell under tension and compression. Influence of softening on unit cell.	46
4.6	Influence of softening curvature on damage evolution in micromechanical unit cell under compression.	47
4.7	Influence of softening curvature on damage evolution in micromechanical unit cell under tension.	48
4.8	Load-displacement curve of tension rod for different mesh refinement	49
4.9	Damage evolution in conventional mesh dependent on mesh	50
4.10	Damage evolution under compression	51
4.11	Discretization of square unit cell	52
4.12	Influence of discretization and volume fraction on predicted stiffness	52
4.13	Survey of Post-Failure Theories	54
4.14	Definition of fracture plane angle θ	56
4.15	Master fracture body and its sections	58
4.16	Progressive weakening of IFF resistances due to σ_1	60
4.17	Puck's softening function $\eta = f(f_E)$	61
4.18	Load-displacement curves of tension rod	62
4.19	Yield and failure surface of the transversely isotropic material model in $\sqrt{I_1}$ - I_3 -invariant-plane	65
4.20	Failure surface of IQC in stress space	66
4.21	Implemented laminates from the WWFE	68
4.22	Finite element discretization of WWFE tests	70
4.23	Load case 1	72
4.24	Load case 2	73
4.25	Load case 3	74
4.26	Load case 4	75
4.27	Load case 5	76
4.28	Load case 6	77
4.29	Load case 7	78
4.30	Load case 8	79
4.31	Load case 9	80
4.32	Load case 10	81
4.33	Load case 11	82
4.34	Load case 12	83
4.35	Load case 13	84
4.36	Load case 14	85
4.37	Definition of action-plane angle θ	88
4.38	Off-axis-tests	90
4.39	Normalized strength dependent on off-axis angle α (source: DLR/FA)	91
4.40	Action-plane strengths after Juhasz for transversely isotropic material	92

5.1	Homogenization of heterogeneous structure via Representative Volume Element (RVE)	95
5.2	Crack under transverse compression in different unit cells	97
5.3	Randomized unit cell	98
5.4	Averaging of stresses and strains of the RVE	98
5.5	Displacement boundary conditions on randomized unit cell	99
5.6	General Periodic boundary conditions	100
5.7	Symmetric Periodic boundary conditions	101
5.8	Multiscale algorithm	105
6.1	Micromechanical unit cell	109
6.2	Discretization of one quarter of micromechanical unit cell	110
6.3	Virtual tests for homogenization	110
6.4	Stress-strain curves of micromechanical unit cell computations with different element number	111
6.5	Stress-strain curves of micromechanical unit cell computations compared with test results from WWFE	114
6.6	Damage evolution in micromechanical unit cell	115
6.7	Stress triaxiality $\frac{p}{\sigma_{vM}}$ in micromechanical unit cell under transverse compression	116
6.8	Stress Invariants in micromechanical unit cell	117
6.9	Strain distribution in square and hexagonal arrangement of unit cell	117
6.10	Stiffness of square and hexagonal unit cells after variation of aspect ratio	118
6.11	Different distributions of 4 fibres	118
6.12	Deformations and von-Mises stresses of randomized unit cells under tension	119
6.13	Evolution of mean Young's Modulus E_{22} and E_{33} over number of tests and increased fibre number	119
6.14	Evolution of mean Shear Modulus G_{23} over number of tests and increased fibre number; Values of virtual shear test are compared with calculated values Young's modulus and Poisson's ratio, denoted by "c"	120
6.15	Evolution of mean Shear Modulus G_{12} over number of tests and increased fibre number	120
6.16	Evolution of mean Poisson's ratio ν_{23} over number of tests and increased fibre number	121
6.17	Young's Modulus E_{22} over E_{33}	122
6.18	Histograms of Young's Modulus E_{22} for different fibre number	123
6.19	Histograms of shear modulus G_{12} for different fibre number	123
6.20	Histograms of Poisson's ratio ν_{23} for different fibre number	124
6.21	Mean elastic parameters for different fibre number	124
6.22	Stress-strain curves of randomized unit cells with 4 fibres	125
6.23	Averaged stress-strain curves of randomized unit cells under compression, sensitivity analysis	126
6.24	Failure of randomized cells	127
6.25	Histograms of Strength R_c for different fibre number	127
6.26	Transverse Young's modulus E_{\perp} from test result, unit cell computations (25 fibres) and analytical rules of mixture	129

6.27	In-plane shear modulus $G_{\parallel\perp}$ from test result, unit cell computations (25 fibres) and analytical rules of mixture	130
7.1	Stress-strain curves of square micromechanical unit cell computations for use in mesomechanical unit cells $v_f = 0.5$	132
7.2	mesomechanical non-crimp fabric unit cell	132
7.3	Geometry of mesomechanical unit cell for non-crimp fabric	135
7.4	Fibre orientation in mesomechanical NCF unit cell	135
7.5	Different discretization of epoxy resin pocket with voxel mesh	136
7.6	Load cases of mesomechanical unit cell for non-crimp fabric	137
7.7	Stress-strain curves of mesomechanical NCF unit cell computations	139
7.8	Damage evolution in mesomechanical NCF unit cell	140
7.9	Shear load cases of mesomechanical unit cell for weft-knitted fabric	141
7.10	Geometry of mesomechanical unit cell for two weft-knitted fabrics	142
7.11	Stress-strain curves of weft-knitted fabrics unit cell	143
8.1	Discretization of coupon test	145
8.2	Tensile test in 0° direction: stress-strain curve experimental results vs Simulation	145
8.3	Young's Modulus from tensile test in 0° direction	146
8.4	3-point-bending test	147
8.5	Finite-element mesh 3-point-bending test	147
8.6	3-point-bending test: load-displacement curve experimental results vs Simulation	148
8.7	3-point-bending test: Stiffness-displacement curve	149
8.8	3-point-bending test: finite-element mesh, fibre direction stress	150
8.9	3-point-bending test: damage in bottom 90° -layer, characteristic damage state	151
8.10	3-point-bending test: finite-element mesh, FF damage variable at failure	152

List of Tables

1.1	Elasticity and strength properties of UD- and textile lamina	4
3.1	elasticity constants for transversely isotropic elasticity	39
4.1	Characteristic internal length L_i of different materials	43
4.2	Slope parameters for criterion of Puck	58
4.3	Softening parameter for PUCK's criterion	61
4.4	Input parameters of failure criteria (for GFRP)	67
4.5	Material properties of UD laminae used for the implementation	69
4.6	WWFE load cases: overview	71
4.7	Strengths and strength parameters of Juhasz's criterium	89
6.1	Material properties of fibre and matrix	112
6.2	Mechanical properties of E-Glass/MY750/HY917/DY063-epoxy lamina . .	113
6.3	Values of stress triaxiality	115
7.1	Mechanical properties of E-Glass/RIM 135 fibre bundles	133
7.2	Mechanical properties of non-crimp fabric layer made of E-Glass/RIM 135	138

Nomenclature

Abbreviations

CFRP	Carbon fibre reinforced plastics
CLT	Classical Laminate Theory
DBC	Displacement boundary conditions
E-Glass	Glass fibre variety
FF	Fibre failure
FEM	Finite element-method
FRP	Fibre reinforced plastics
GFRP	Glass fibre reinforced plastics
IFF	Inter-fibre failure
NCF	Non-crimp fabric
PBC	Periodic boundary conditions
RUC	Randomized unit cell
RTM	Resin Transfer Moulding
RVE	Representative volume element
UC	Unit cell
UD	Unidirectional
WKF	Weft-knitted fabric
WWFE	World-Wide Failure Exercise by Hinton, Kaddour, and Soden (2004)

Glossary

Layer	Physically existent layer of fibres with equal direction
Lamina	Constituent of laminate in simulation with homogeneous mechanical properties, usually represents one layer, but multiple layers can be represented by one lamina, or multiple laminae can be used to represent one layer
Laminate	Stacked FRP, physically consisting of several stacked layers, usually with different fibre directions, discretized in the simulation with stacked laminae, usually with one for each layer, but a single anisotropic lamina is possible as well

Textile layer	Infiltrated textile fabric, comprises of multiple layers that are held together by a textile reinforcement
Mechanical properties	All material parameters that characterize mechanical behaviour of material, here: elastic constants, hardening parameters, strengths, strain energy release rate
Elastic constants	Material parameters that characterize linear elastic material, i.e. E and ν isotropic case
Strength	Maximum stress that material can bear (dependent on load case)
Damage	General loss of stiffness, e.g. in form of crack
Degradation	Loss of stiffness, positive tangent modulus, e.g. plastic hardening
Failure	Start of softening; It must be discriminated between local and global failure, local failure in one lamina does not necessarily lead to global failure of a laminate
Softening	Loss of stiffness, negative tangent modulus

Symbols, Characters, Coding

Symbols

\parallel	In (parallel to) fibre direction
\perp	Transverse direction
$\perp\perp$	Transverse shear direction
$\perp\parallel$	In-plane shear direction
$\langle \rangle$	Mean value of field

Latin Characters

\mathbf{A}	Structural tensor
$[A], [B], [D]$	in-plane (stretching), bending-stretching coupling and bending-stiffness sub-matrix
\mathbb{C}_e	Elasticity tensor
E	Young's Modulus
F	Force
f_E	Stress exposure factor
G	Shear Modulus
G_f	Strain energy release rate
I	Invariant
L	Characteristic length of upper scale
L_e	Characteristic element length
L_i	Characteristic internal length
R	Strength

a	Parameter of isotropic yield surface; dimension of RVE
\mathbf{a}	Preferred direction in transverse isotropy
b	Parameter of isotropic failure surface
c	Softening parameter of Puck
d	Damage variable
f	Yield condition
g	Plastic potential
l	Characteristic length of lower scale
\mathbf{m}	Direction of plastic flow
n	Number of layers, current time step
p	Hydrostatic pressure; slope parameters of Puck, SPC and Juhasz
r	Failure condition
t	Time
v_f	Fibre volume fraction

Greek Characters

θ_{fp}	Fracture plane angle
θ	Action plane angle
Ψ	Ratio of action plane shear stresses
α	Parameter of transversely isotropic yield surface, flow parameter, Off-Axis angle
β	Parameter of transversely isotropic failure surface
δ	Displacement from between reference and actual configuration
$\Delta\lambda$	Plastic multiplier
η	Softening parameter of Puck
γ	Shear strain
ε	Strain
$\bar{\varepsilon}^{pl}$	Equivalent plastic strain
$\boldsymbol{\varepsilon}$	Strain tensor
ρ	Density
σ	Stress
σ_{vm}	Von-Mises stress
$\boldsymbol{\sigma}$	Stress tensor
$\boldsymbol{\sigma}^{pind}$	Plasticity inducing stress tensor
$\boldsymbol{\sigma}^{reac}$	Reaction stress tensor
φ	Fibre volume fraction
ν	Poisson's Ratio
ν_p	Plastic Poisson's Ratio
ξ	Softening parameter of Puck

SV-Coding (Examples)

$[0/90]_s$	Definition of a symmetric laminate
$(20\% 0^\circ/70\% \pm 45^\circ/10\% 90^\circ)$	Definition of a laminate with specification of fibre fractions
$(0^\circ, +45^\circ, -45^\circ, 90^\circ)$	Group of laminates
$[90_2^G/0_3^C/\pm 45_2^G/0^C]_{2s}$	Definition of a laminate with specification of fibre material
$[0/0/\pm 45 \text{ Weave}/0/0]$	Definition of a laminate with specification of textile geometry

Superscripts and subscripts

Superscripts

c	Compression
t	Tension
s	Shear
pl	plastic

Subscripts

c	Compression
exp	exponential (softening)
f	Fibre
$fail$	At failure
lin	linear (softening)
m	Matrix
s	Shear
t	Tension
ult	ultimate, complete failure
Y	yield

Coordinate systems

x, y, z	Laminate, Component
x_1, x_2, x_3	Lamina
x_I, x_{II}	Principal axes
\parallel, \perp	UD-layer, transversely-isotropic material symmetry
n, t, l	Action plane
u, v, w	Displacements

Basic values and dimensions

Force	N
Length	mm, m
Area	mm ² , m ²
Stress	N/mm ² = MPa
Modulus	GPa = 10 ³ MPa = 10 ³ N/mm ²
Density	t/m ³ = g/cm ³

1 Introduction

1.1 Rationale and Motivation

Fibre reinforced plastics are becoming more and more popular these days. The reason for their success is the wide variety of properties FRP offer in combination with low weight. Versatility and low weight are leading to efficiency, which is a great demand of the future. More than any other material, FRP can be designed to fulfill a special purpose, while always remaining especially light. Actually, their adaptability comes from the fact that they are more of a structure than a material. Therefore, they require much more attention in the design and manufacturing process, which makes them overall rather more expensive than other materials. Naturally, they were used in expensive high performance structures like spacecrafts, military aircrafts, racing cars, boats etc. in the beginning, where the demand for low weight exceeds the demand for low cost by far. Nowadays, the cost for FRP has been reduced mostly due to the experience that has been made, cheaper production methods, but also due to more competition. Hence, FRP have become indispensable for many applications.

Textile composites are characterized by the manufacturing process which involves machines usually used for production of textiles. With these machines, the "dry" rovings are laid and connected, e.g. knitted, woven, braided, etc., in a preform. The lay-up of these dry preforms is easier than with less flexible pre-impregnated layers and allows for more draping and easier connection of the layers via pinning, stitching etc.. The resin infiltration of the fibres after the lay-up is followed immediately by the consolidation. During the infiltration process the fibres are held in place by the textile structure of the preform. Because the consolidation process, beginning with the infiltration, does not have to be stopped textile composites are cheaper than prepreg material, which generate storage cost.

Compared to prepreg-composites, the structure of textile composites is much more heterogeneous. In textile composites, the fibres are only equally dispersed throughout the fibre bundles, but not over the whole layer. Between the fibre bundles, epoxy resin pockets can be found and, depending on the textile preform, stitch- or knitting yarns. In addition, fibre undulations are characteristic for textile composites. Therefore, the overall mechanical performance of prepreps is better, but textile composites often have advantages in through-thickness strength, delamination sensitivity and crashworthiness.

Usually, mechanical material parameters of FRP are determined with expensive experimental tests. For unidirectional FRP, it is assumed that each layer is transversely isotropic but textile composites exhibit orthotropic behaviour due to their through-thickness reinforcement. Thus, nine instead of five elastic properties as well as strengths have to be

determined. However, not only the number increases, it is also much more difficult to determine through-thickness properties. Therefore, it is a big challenge to determine the material properties of textile properties.

Examples of textile preforms are shown in fig. 1.1.

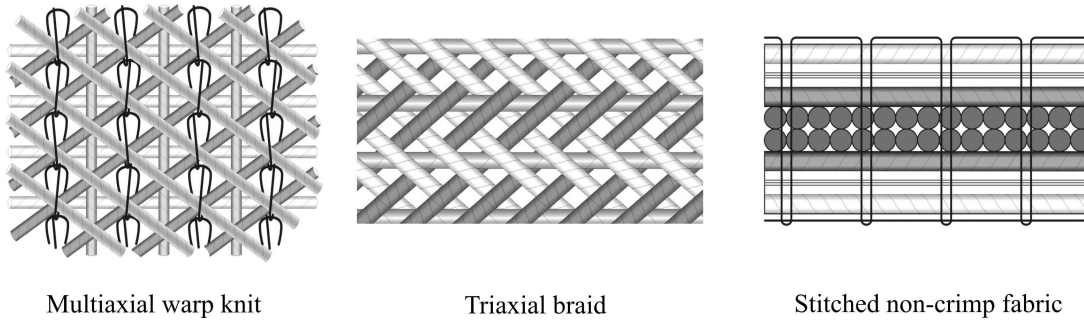


Figure 1.1: Different preforms used in textile composites

1.2 Literature Review

In this section, a literature review is given on the determination of mechanical properties of fibre reinforced plastics and the description of its material behaviour with material models. The term mechanical properties includes elastic constants as well as hardening, damage, viscosity and strength parameters.

1.2.1 Mechanical Properties of Unidirectional Composites

Due to the widespread use of UD-composites several models for the stiffness determination of unidirectional composites exist as an alternative to tests. Usually analytical rules of mixture (e.g. Halpin-Tsai) are applied. Actually, these rules of mixture have often been used to determine the fibre properties via reverse engineering. Nonlinear material properties are not covered by these rules of mixture and their applicability to strength prediction is judged not to be reliable. Therefore, experimental methods are first choice for the determination of nonlinear behaviour and strength. However, several analytical and numerical approaches exist as well.

Material models Numerous approaches to describe the nonlinear material behaviour of UD-Composites have been developed. In the World-Wide-Failure-Exercise (WWFE) by Hinton et al. (2004) a number of these has been published. For example, Cuntze and Freund (2004) model the nonlinear behaviour under shear with an exponential Ramberg/Osgood approach. In this phenomenological approach, nonlinearity is modelled with plasticity. Schuecker and Pettermann (2007) additionally take into account that Mechanical Properties of damage and plasticity occur in combination.

A more detailed approach to damage in UD-composites was developed by Ladeveze and Lubineau (2002). It takes multiple forms of damage into account, namely fibre breakage, matrix microcracking, deterioration of fibre-matrix bonds and delamination. Ladeveze and LeDantec (1992) also take inelastic effects into account.

Micromechanical unit cells Often the random fibre distribution has been reduced to periodical arrangements as hexagonal or square unit cells to allow for a closed analytical solution. Stiffness and strength predictions for the fibre direction are easily done with reasonable results, but in transverse direction the assumption of periodicity does not account for the randomness of the fibres in reality. Moreover, the square arrangement is questionable as it yields orthotropic properties instead of transversely isotropic. Consequently, numerical approaches for elastic constants with a random fibre arrangement in RVEs have been undertaken by Gusev, Hine, and Ward (2000). Blacketter, Upadhyaya, and King (1993) used a micromechanical unit cell to predict strengths of tows in a plain weave fabric.

1.2.2 Mechanical Properties of Textile Composites

In contrast to UD-composites, the layers of a textile composite are not only connected through the matrix, but also through fibres or yarn. In the manufacturing process, this through-thickness reinforcement is needed to hold the load-carrying fibres in place. Therefore, in theory the assumption of transverse isotropy does no longer hold for textile composites. Nonetheless, textile composites are mostly used in thin-walled structures and therefore only the in-plane properties are of interest and transverse isotropy is a valid assumption. Non-crimp fabrics, for instance, are often treated as UD-composites, only a knock-down factor to account for higher undulations compared to prepreg-composites is applied, see B. N. Cox and Flanagan (1997). On the other hand, textile composites are also used because of their higher delamination strength and damage tolerance resulting from the through-thickness reinforcements. Furthermore, the connection of FRP-structures is becoming more and more a crucial for their successful application. At the connections three-dimensional stress states have to be modelled locally and textile composites thus require more sophisticated modelling techniques than UD-composites.

A textile layer with multiple fibre directions behaves generally anisotropic, but a single layer inside a textile fabric with in-plane- and through-thickness reinforcement can often be assumed to be an orthotropic material. In the case of a planar (2D) state of stress as found in thin-walled structures, the number of required mechanical properties of UD- and textile layer is equal, but in a spatial (3D) stress state four more stiffness and strength parameters each have to be determined for the textile layer, see Table 1.1. Not only the number of parameters increases but also the complexity of determination. It is hardly possible to determine through-thickness parameters experimentally. B. N. Cox and Flanagan (1997) have proposed a number of analytical methods to describe the three-dimensional reinforcement structure and fibre undulations, but most of these are adapted to specific cases rather than being generally valid. A numerical approach promises a more general

description of textile composites and seems quite possible with the ever rising computational power. Whilst for stiffness prediction only the geometry has to be modelled well, for strength prediction the nonlinear material behaviour has also to be taken into account.

Table 1.1: Elasticity and strength properties of UD- and textile lamina

lamina	elastic constants		strength parameters	
	2D	3D additional	2D	3D additional
UD-layer (transversely-isotropic)	$E_{\parallel}, E_{\perp}, \nu_{\perp\parallel}, G_{\perp\parallel}$	$\nu_{\perp\perp}$	$R_{\parallel}^{t,c}, R_{\perp}^{t,c}, R_{\perp\parallel}, R_{\perp\perp}$	-
textile layer (orthotropic)	$E_1, E_2, \nu_{12}, G_{12}$	$E_3, \nu_{13}, \nu_{23}, G_{13}, G_{23}$	$R_1^{t,c}, R_2^{t,c}, R_{12}$	$R_3^{t,c}, R_{13}, R_{23}$

Yet another challenge arises in the prediction of mechanical properties of textile composites. For UD-composites it is easily possible to determine properties of a single layer experimentally, that is treated to be transversely isotropic in the following. This is not possible for textile composites, the smallest producible unit already consists of at least two layers with different fibre directions that behaves like a laminate. Thus, coupling effects, e.g. between bending and elongation, are already present in a textile layer. A textile layer also exhibits different bending stiffness depending on the direction although the normal stiffness is the same. This behaviour cannot be represented by a standard CAUCHY continuum, but requires higher order continua like the COSSERAT continuum as proposed by Haasemann and Ulbricht (2006). However, other theoretically more simple work-arounds have been proposed. One possibility is to neglect this phenomenon, that admittedly vanishes the more layers are used. Another possibility is to split up the textile layer in layers of common fibre direction, that are then assumed to be unidirectional and can thus be treated like lamina of UD-composites. The mechanical properties of these pseudo-unidirectional (quasi-laminar) layers are sometimes weakened by a knock-down factor for the increased fibre undulations. Good introductions are given by B. N. Cox and Flanagan (1997) and Crookston (2005).

1.2.2.1 Analytical Methods for Elastic Constants

The Mosaic Model presented by Ishikawa and Chou (1982) is one of the first analytical approaches for woven composites. It is based on laminate theory and ignores the continuity of the fibres to represent the geometry of satin weaves in a mosaic fashion, see Figure 1.2. By adding an approach for fibre undulation, this model was extended to the Bridging Model that also includes mosaic regions for the crimped parts in the satin weave, see Figure 1.3.

The Bridging Model takes into account that regions with undulating fibres, such as C in Figure 1.3, carry a lower load than regions with straight fibres, such as A, B, D and E. For

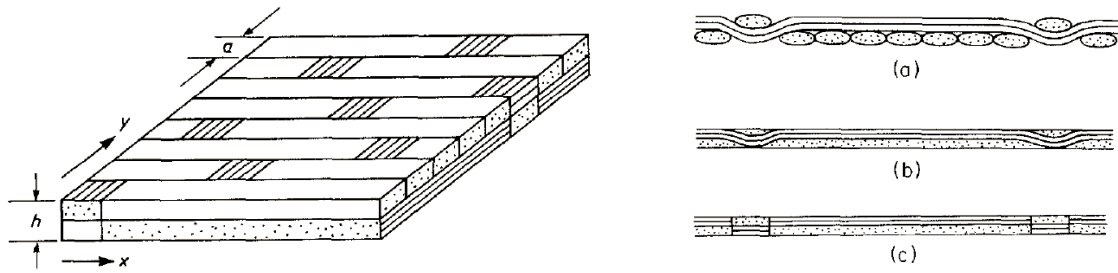


Figure 1.2: Mosaic model of a repeating unit for an 8 harness satin by Ishikawa and Chou (1982).

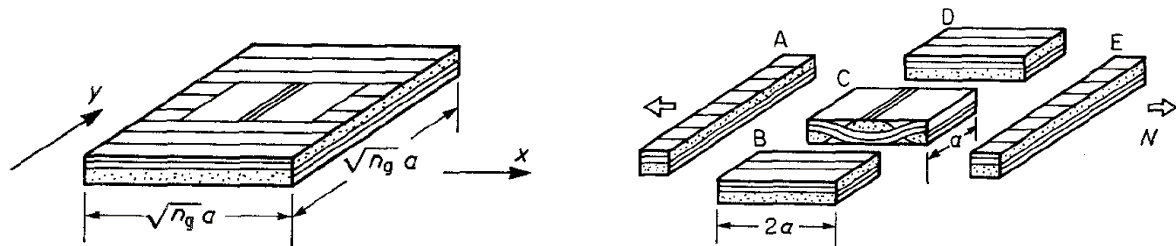


Figure 1.3: Bridging model of a repeating unit for an 8 harness satin by Ishikawa and Chou (1982).

a given load N this is ensured by firstly averaging regions B, C and D as parallel springs and secondly averaging regions A, BCD and E as series springs.

Stiffness knock-down factors for non-crimp fabrics are presented by Edgren and Asp (2005). Their work is based on Timoshenko beam theory, modelling the wavy tows as curved beams. Strength is not incorporated into the model.

1.2.2.2 Numerical Methods for Mechanical Properties

Analytical methods are mostly adapted to one specific textile geometry and incorporate many assumptions and simplifications. Thus, it is natural to look for a more general approach, as it is the finite element method. With a FE-model it is possible to describe the complex textile architecture in a more general and less simplified representative volume element (RVE). Over the years a reasonable progress in describing the fabrics has taken place, as Figure 1.4 illustrates. This progress mainly is a benefit of the ever-increasing computational power.

One of the first numerical approaches by Blacketter, Walrath, and Hansen (1993) already features a 3D-unit cell of a plain weave fabric, although the geometry is simplified. The unit cell consists of two constituents, epoxy resin and tows, which are assumed to have a fibre volume fraction of 70%, to give an overall fibre volume fraction of 60%. For the tows a material model with an anisotropic invariant-based flow rule and a constant damage formulation is presented.

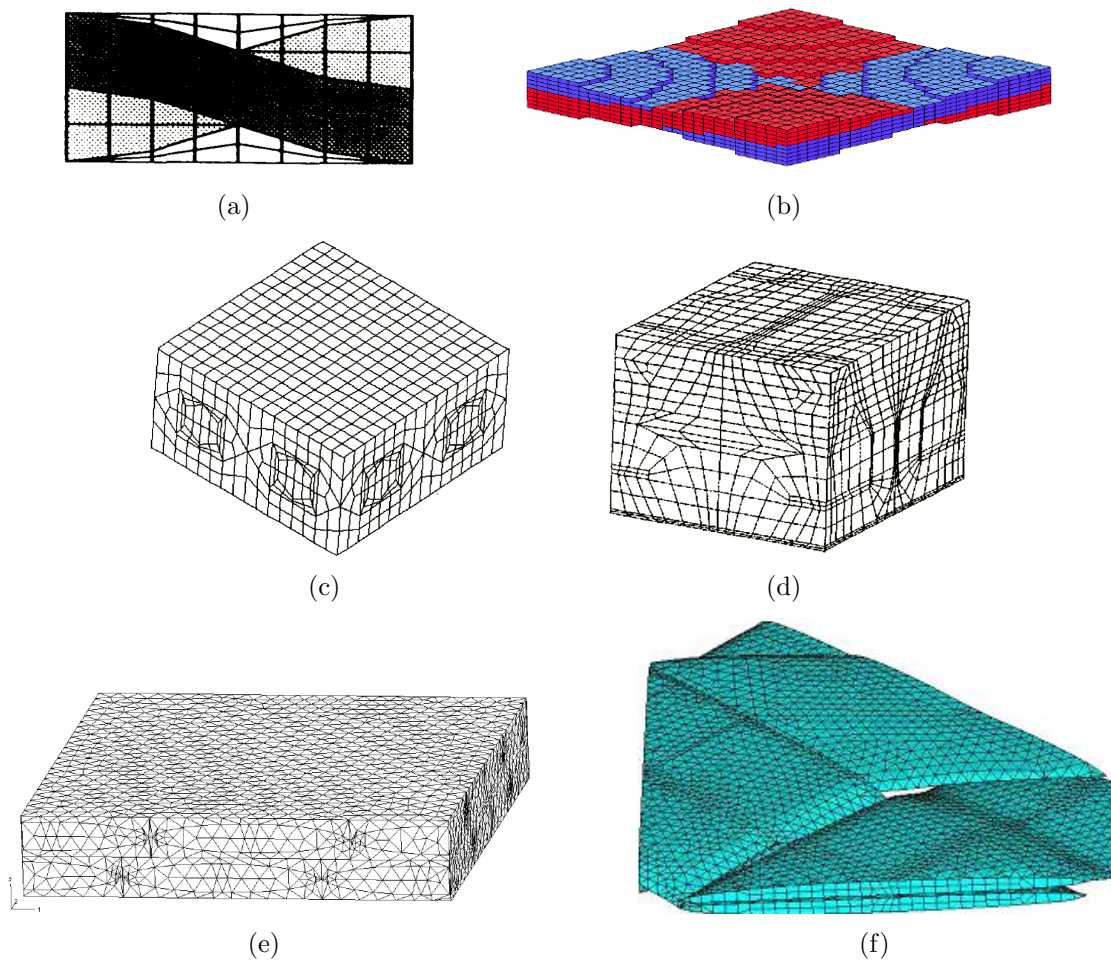


Figure 1.4: Finite element meshes of textile composites: (a) 2D-mesh of plain weave fabric by Woo and Whitcomb (1994), (b) Voxel mesh of plain weave by Gunnion (2004), (c) Mesh of plain weave fabric by Takano et al. (1999), (d) Mesh of weft-knitted fabric by Takano et al. (1999), (e) Tetrahedron-mesh of plain weave by Crookston (2005), (f) Tetrahedron-mesh of plain weave by Lomov et al. (2007).

The damage initiation is predicted by a modified maximum stress criterion that is based on stresses with respect to material coordinate directions instead of principal stresses. Six failure modes are defined to allow for differentiated failure, e.g. that a pure matrix crack parallel to the fibres does not reduce the strength in fibre direction significantly. When failure is detected, the stiffnesses of the material are reduced instantaneously to a very small value in the gauss point where failure has occurred. Thus, a progressive failure is modelled in the ongoing computation. This constant damage allows to model a progressive failure with little computational effort, however, the results are conservative and mesh dependent, because the energy dissipation of the crack tends to zero, when the mesh is refined. The material properties of the tows were determined with a micromechanical unit cell, that will be discussed in chapter 1.2.1. This approach is an information-passing

multiscale analysis, where several scales are computed independently.

Usually, only normal forces are taken into account in a unit cell, which is, however, not valid for very thin laminates consisting of a single fabric, for example. In such a case also bending of the unit cell has to be considered, as presented in a coupled multiscale analysis by Woo and Whitcomb (1994). Here, a macro solution of a short cantilever is retrieved by simultaneously solving unit cell computations on the mesoscale. Naturally, the mesh of the mesoscale unit cell cannot have to be rather coarse, see Figure 1.4, because its solution time is crucial for the overall performance of the computation as it has to be solved multiple times in one macroscale solution step. Thus, Woo and Whitcomb (1994) presented an algorithm for a 2D problem and enhanced it to 3D later, see Woo and Whitcomb (1996). For failure initiation maximum stress and Tsai/Hill failure criteria are used, but neither material nonlinearities nor progressive failure are taken into account.

B. Cox, Carter, and Fleck (1994) proposed a Binary Model that describes the fibre architecture with truss-elements. The axial properties of the fibres or tows are represented by truss elements, whereas solid elements represent an "effective medium" that accounts for all other mechanical properties. Due to the use of truss elements it is very efficient and capable of describing the textile architecture by simplest means.

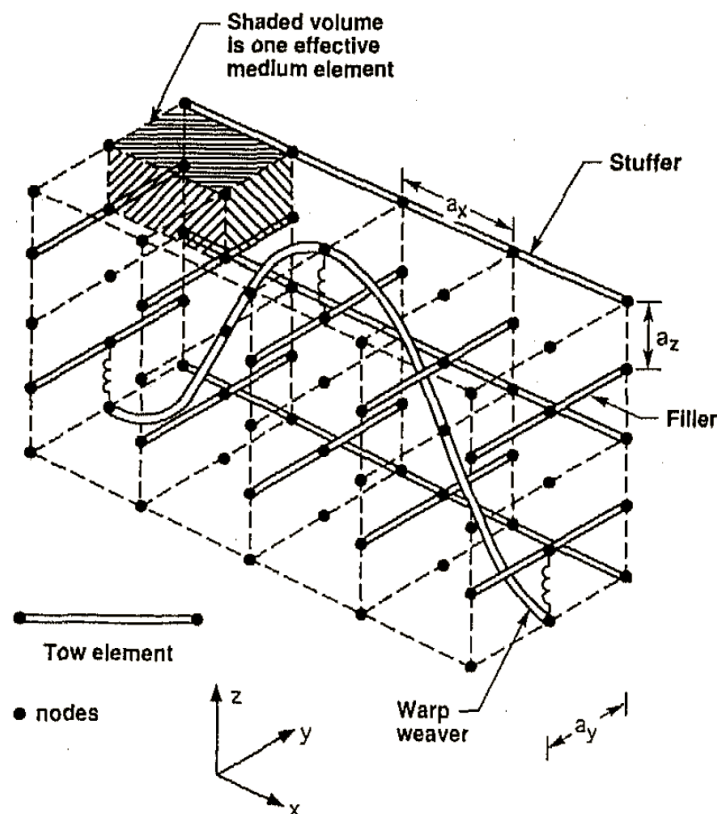


Figure 1.5: Binary Model: Tow and matrix elements in a layer-to-layer angle interlock woven composite (B. Cox et al., 1994).

It is very well suited to carry out statistical variations of mechanical properties due to

its numerical effectiveness. Even cyclic loading can be simulated to account for fatigue failure. The separation of the axial fibre properties from other mechanical properties is done because they are dominating the mechanical behaviour of the whole material, being two orders of magnitude greater than the other properties. The effective medium is explicitly designed to represent transverse and shear behaviour as well as to incorporate statistically distributed flaws in an averaged sense. It is possible to describe material nonlinearities as well as progressive damage with the effective medium, if enough test data are available for calibration. However, it is impossible to account for microstresses around the tows and not very well suited for the application in a bottom-up approach, because the properties of the effective medium have to be calibrated against the macroscale. With today's increased computational power, a higher resolution on the mesoscale is usually favored.

The binary model was taken up by Haasemann and Ulbricht (2006) because its numerical effectiveness combines very well with a coupled multiscale analysis, where many computations have to be carried out on the microscale. They are performing a homogenization of elastic constants for a Cosserat continuum, that is able to describe a textile layer completely.

There are also numerous approaches, which model the structure by volume elements and thus allow for consideration of different Poisson's ratios of fibre and matrix. Lomov et al. (2002) conduct detailed studies on the geometry of textile preforms and developed a program to model various textile architectures and calculate stiffness of textile composites using the method of inclusions.

Karkkainen and Sankar (2006) compute the strengths of woven composites with the "Direct Micromechanics Method". They use a unit cell to compute the microstresses in the constituents, which are then evaluated by using either Tsai/Wu or maximum stress failure criterion. As a very conservative approach failure of the first element is taken to be the failure of the unit cell, i.e. the whole textile lamina. Karkkainen and Sankar (2006) show that a change in the definition of failure, from first element to 1% of elements increases the strength up to 30 %. Furthermore, material nonlinearities are not included into this model. Bending of the unit cell is considered to enable the simulation of thin laminates also.

Modelling the complex structure of textile composites in a unit cell is not an easy task. The discretization of the structure requires a mathematical description and usually an automated meshing algorithm. For a conventional mesh that describes the boundaries between the constituents of textile composites as exactly as possible, this procedure leads inevitably to heavily deformed element shapes, especially for hexahedra. Bad shaped elements have a considerable influence on the quality of the solution, namely its convergence and local stresses. In a study by Thom (1999) different conventional meshes of a woven fabric are compared. The meshes differ by number of elements as well as mesh geometry. Thom concludes that the effective Young's modulus of the unit cell is only slightly influenced, but a convergence can hardly be seen. However, even though Thom uses higher order 20-node-hexahedron and 15-node-pentahedron elements, the through-thickness stress is significantly reduced by around 70% in finer meshes.

An approach to avoid bad element shapes and to simplify mesh generation is the approximate Voxel meshing. The name comes from "Volume Pixel" and means that the mesh consists of elements having all the same size with an aspect ratio of one. Thus, the shapes of the constituents of a textile composite can only be approximated. Kim and Swan (2003) present a refined voxel method to reduce the relatively high number of elements to give a good approximation of the geometry. A "selective refinement" along the boundary between the constituents alone results in elements with very different sizes adjacent to each other, leading to highly inaccurate numerical results. Therefore, they propose a "constrained selective refinement" that constraints the size difference of adjacent elements and, even better an "adaptive refinement" based on error estimators.

Gunnion (2004) uses the Voxel approach as well to model micromechanical and mesomechanical unit cells of plain weave and stitched fabrics, but without mesh refinement as described above. Instead, he does vary the aspect ratio of the elements in the plain weave fabric unit cell in the third direction.

The reason for this is at hand when looking at the geometry. Over the thickness of the cell, which is much smaller than the other dimensions, two tows and the matrix phase must be discretized. A study over aspect ratio of the elements and the number of elements in thickness direction yields the conclusion that this thickness-refinement yields very good results, where a coarse mesh refinement differs only by 4 % from the reference solution. The work is focused on elastic constants of textile composites. Thus neither material nonlinearities nor failure are included in the model.

Takano et al. (1999) present a hierarchical model for textile composites that utilizes a periodic unit cell of woven or weft-knitted fabrics. With a mesh superposition technique it allows for the discretization of critical regions in a finer, local mesh. The material formulation does not include material nonlinearities but an anisotropic damage formulation. For damage initiation in the tows the Hoffman criterion, see Hoffman (1967) for UD-composites is applied. A constant damage is applied similarly to the work of Blacketter, Walrath, and Hansen (1993) that exhibits the same conceptual weaknesses, namely conservative results and mesh dependency.

Mattsson and Varna (2007) state that the exact geometry of fibre bundles is of little significance for stiffness prediction.

1.2.2.3 Failure Criteria for Textile Composites

As mentioned before, textile lamina are orthotropic or general anisotropic, therefore well-known failure criteria for UD-lamina fall short in predicting failure of textile composites. Only textile composites with minimal fibre undulations and low 3D-reinforcement density can be described by failure criteria developed for UD-composites, such as the Tsai-Wu or Puck criteria, see Hinton et al. (2004). For other textile composites it is necessary to use appropriate failure criteria, that are mostly still to be developed. Juhasz, Rolfes, and Rohwer (2001) developed a failure criterion for orthogonal 3D fibre reinforced plastics e.g. non-crimp fabrics. It is based on the criterion of Puck mentioned above and described in Section 2.

Another proposal for a failure criterion was made by Cuntze (2007), that is based on his Failure Mode Concept.

Smith and Swanson (1996) find that a maximum strain criterion works well for the in-plane strengths of a 2D-braided fabric, but do not deliver any strengths for the third direction. Tan, Tong, and Steven (2000) present a maximum stress criterion for a 3D orthogonal woven CFRP composite, that gives good results in fibre direction, but has weaknesses in predicting transverse strengths. Karkkainen, Sankar, and Tzeng (2007) present a direct micromechanics approach towards Quadratic Stress Gradient Failure Criteria

1.3 Objective and Outline

The determination of material properties of textile composites is very time-consuming and expensive. Especially through-thickness parameters are nearly impossible to determine, but needed for solving impact, delamination and load introduction problems. Therefore, a virtual testing algorithm to determine elastic and strength properties of textile composites is presented in this work, which shall complement and replace these expensive experimental tests. So far, several models for this purpose were presented in literature, but in these models the nonlinear behaviour of composite material was neglected. Some models included the prediction of failure, but mostly with either mesh-dependent softening algorithms or even without progressive failure, which is very conservative. However, for an accurate prediction of the textile composites' characteristic material behaviour with a multiscale simulation it is necessary to include nonlinearities and to eliminate the mesh dependency of the algorithm as far as possible. This is the main focus of this work. To provide a most general approach, the algorithm is able to predict the material behaviour with the sole knowledge of the textile architecture and the properties of fibre and matrix. The algorithm includes a multiscale simulation on three scales with unit cells on micro- and mesoscale.

The multiscale algorithm is utilized to describe the inherent structure of textile composites. On the mesoscale, between 1 mm and 1 cm, the textile architecture is discretized in an unit cell, but it is neither possible nor necessary to discretize single fibres. Fibre bundles, consisting of fibre and matrix, are treated as continua, for which material parameters are generated on the microscale, typically around 10 μm . In the micromechanical unit cell the interaction of a single fibre and the matrix around is discretized. The discretization of the unit cells is done with voxel-elements, that allow for a simple discretization of complex geometries. Furthermore, together with the applied fracture energy regularization, they alleviate the inevitable mesh dependency that occurs when material softening is computed. With the presented algorithm it is possible to determine strength parameters for failure criteria not only for the whole preform, but also for single layers within the preform. Therefore, it is possible to apply layer-based criteria that allow for a more detailed analysis of textile composites.

The material behaviour of epoxy resin and fibre bundles has to be described in unit cells presented in this work. Both are elastic-plastic materials that exhibit pressure-dependent material behaviour, i.e. they behave differently under tension, shear and compression. For

both new material models are presented that allow for the realistic simulation of these material characteristics and offer very powerful but simple input possibilities. Tabulated hardening curves under tension, compression and shear are used to model the nonlinear behaviour. They are obtained from load-displacement curves, and allow for a very convenient parameter identification. In addition, they have the big advantage that they are physically meaningful and can thus be controlled easily by comparison of virtual and experimental test.

Foundation of material modelling is a study of the experimentally observed material behaviour, which is presented in chapter 2 for epoxy resin, glass fibres, UD-composites and textile composites. Most important, it is judged which material behaviour is relevant for determination of strengths. In this work the three different phases of material behaviour are discriminated. Firstly the elastic phase with linear material behaviour, secondly the degradation phase with nonlinear material behaviour and a positive tangent modulus and thirdly the softening phase that exhibits a negative tangent modulus. Failure is indicated by transition from positive to negative tangent modulus and thus, located between degradation and softening. Hence accumulating microcracks in the degradation phase are not considered as failure.

Based on this study material models are presented in chapter 3 for a realistic description of the nonlinear material behaviour of epoxy resin and UD-composites up to failure. In chapter 4 failure criteria used to identify the failure of epoxy resin, UD- or textile composites, and softening formulations to describe the progressive failure of each material are presented. A validation of the Invariant-based Quadratic Criterion (IQC) and a softening formulation presented in chapter 4 as well, highlights the importance of a proper softening formulation.

The basis of multiscale simulations and homogenization are presented in chapter 5, together with an overview on the multiscale algorithm used for determination of stiffness and strength of textile composites.

The first step of the multiscale algorithm, virtual tests of micromechanical unit cells, are presented in chapter 6. Here, different representative volume elements are compared and parameters for fibre bundles or UD-layers are generated.

Fibre bundles are used in the mesomechanical unit cells in chapter 7 to discretize the textile architecture of two different textile reinforcements, non-crimp fabric and weft-knitted fabric. The outcome of the virtual tests carried out with the mesomechanical unit cells are homogenized material properties of non-crimp fabrics and weft-knitted fabrics for use in macroscale computations presented in chapter 8. The validation of the material models and the multiscale algorithm is accomplished by simulation of two experimental tests.

A conclusion of the presented work and an outlook on promising, continuative research areas are given in chapter 9.

2 Experimental Behaviour of Textile Composites and its Constituents

In this chapter the experimentally observed behaviour of textile composites is described. To understand the behaviour of textile composites it is important to understand the behaviour of its components, fibre and matrix, here glass fibres and epoxy resin. The behaviour of UD-composites is described here as well, because they occur as fibre bundles in textile composites at mesoscale.

2.1 Epoxy Resin

Epoxy resins, i.e. thermosetting epoxide polymers, are widely used in composites manufacturing. They offer a great variety of properties, including high stiffness and strength as well as high viscosity. Of course, they do not possess all of these desirable properties together, but they can be adapted to a special purpose. The curing of these polymers is induced by a "hardener" and the curing time can be influenced as well. A thorough mixing procedure is required to ensure an even curing throughout the whole matrix. The viscosity of epoxies can be influenced as well, which makes them very attractive for textile composites, that require a high viscosity of the matrix in the manufacturing process.

The mechanical properties of epoxies are influenced by the polymerization process, i.e. ratio of polymer and hardener, their mixing quality and the temperature at which the whole process takes place. Usually, epoxy resins are tempered at elevated temperatures in an oven to speed up the polymerization process. Because of different temperature coefficients of fibres and matrix, composites made of epoxy resin mostly incorporate residual thermal stresses at room temperature.

The mechanical behaviour of epoxy resins is as complex as the atomic structure of the polymer chains. Due to viscosity, plasticity, accumulating damage and pressure dependency the stress strain curves are nonlinear, see Figure 2.1. Furthermore, they are influenced chemically, by shrinkage as well as healing and physically by moisture as well as temperature.

Viscosity of epoxy resin is described by e.g. Gilat et al. (2005). They report that high strain rates increase stiffness and strength of three commercially available epoxy resins under tension and shear, see Figure 2.2(a). In Figure 2.2(b) the stress relaxation of an epoxy under shear can be seen. At low strain rates the effect of viscosity is mostly negligible. For simplicity, viscosity of epoxy resins is neglected in this work.

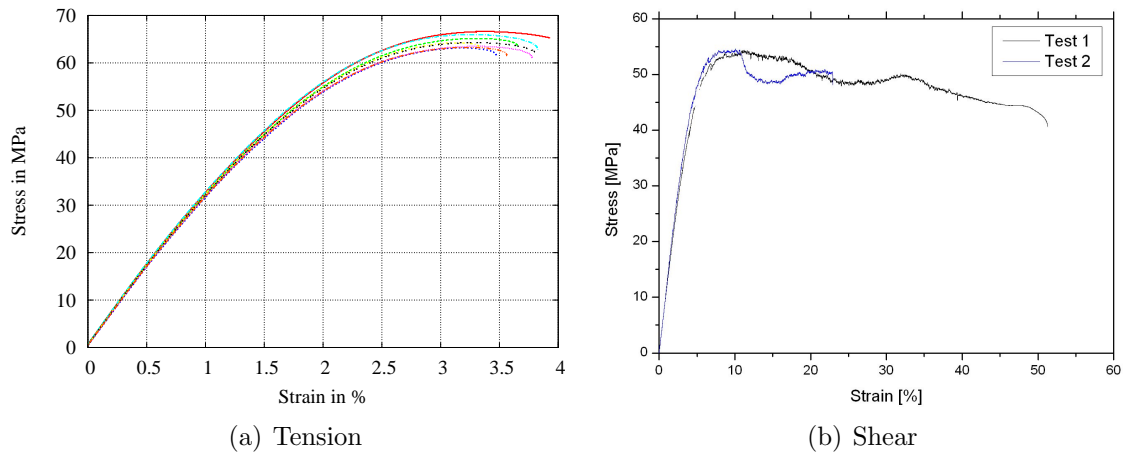


Figure 2.1: Nonlinear material behaviour of Epoxy Resin RIM 135 (Courtesy of Adden, Fiedler)

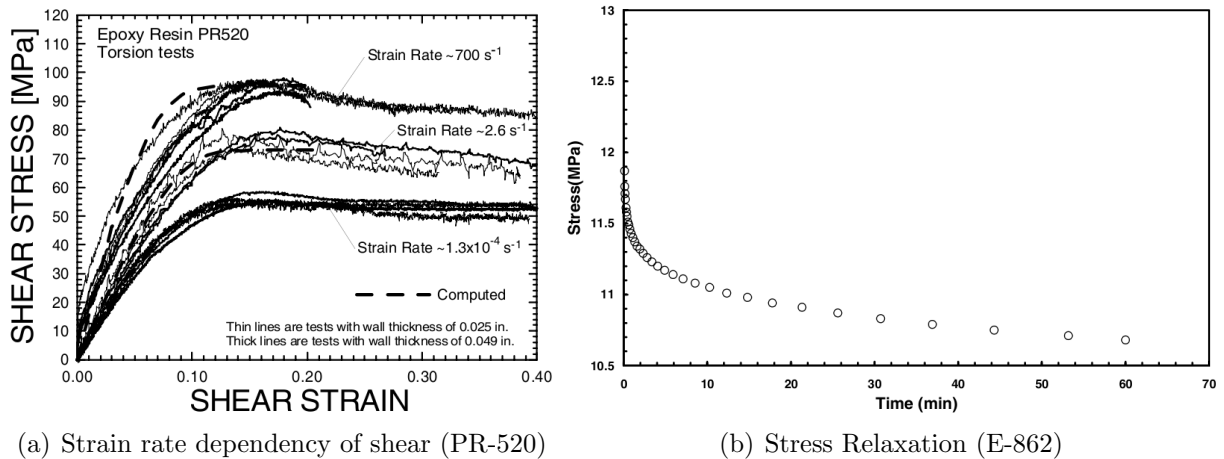


Figure 2.2: Viscous material behaviour of Epoxy Resin, source: Gilat et al. (2005)

To experimentally quantify viscosity, plasticity and damage in epoxy resins is extremely difficult. Multiple tests are needed to discriminate these phenomena. Plasticity and damage can only be separated through cyclic tests, with very slow strain rates to avoid viscous effects. Tests with different strain rates are required to identify viscosity. Furthermore, the nonlinear stress-strain behaviour is highly affected by hydrostatic pressure, i.e. the epoxy resin behaves differently under tension, shear and compression. For example, under biaxial tension so-called crazing, i.e. microcracks, occurs, but not under other load cases. Therefore, the described tests have to be done for each of these load cases, to allow for a complete description of the material behaviour. Such a complete test setup is seldomly available.

Bowden and Jukes (1972) describe the plastic flow of epoxy resins amongst other polymers. They propose a modified von Mises yield criterion that is linearly dependent on the hydrostatic pressure, but do not verify this for epoxy resin.

Fiedler, Hojo, Ochiai, Schulte, and Ando (2001) describe the pressure dependency of

epoxy resin, i.e. the different material behaviour under tension, shear and compression and propose a quadratic failure criterion. Under tension, Figure 2.1(a) the nonlinearity of the stress-strain curve is relatively small compared to shear, Figure 2.1(b). Moreover, the strengths are very different under compression, tension and shear, see table 6.1. The higher the hydrostatic compression, the higher the strength.

Under very high hydrostatic compression on the one hand the 2. Glass transition temperature shifts and the stiffness is reduced whilst on the other hand a stiffness increase can be observed, probably due to closing micropores and -cracks. These effects have been mostly neglected, but shall be worked on in the second part of the WWFE by Kaddour and Hinton (2005).

Moisture absorption reduces the stiffness of epoxy resins, but thus leads to an increased failure strain, which is also desirable in composites. Therefore, a medium moisture content is aimed for. Polymers are affected by the so-called glass transition through temperature. Below the glass transition temperature they are in a stiff, brittle state and above in a soft amorphous state. The glass transition temperature of epoxy resin ranges from 50 °C to 300 °C and depends on the curing temperature. High performance epoxy resin have a high glass transition temperature. Chemically, epoxy resins are very stable and not affected by corrosion. They are affected by other aggressive media, but this depends very much on the special configuration of each epoxy resin system and thus is not discussed here. Epoxy resins exhibit chemical shrinkage of only 2-5 %, which is low compared to other matrix system. Therefore, they are best suited for high precision structures.

2.2 Glass Fibres

Glass Fibres are anorganic fibres consisting of silica and oxygen. They possess isotropic material properties, and compared to other fibres, low stiffness, high strengths and high failure strains. The stress-strain curve of glass fibres is nearly linear elastic up to brittle failure. In brittle material the number of flaws is crucial for the strength, because the stress concentrations around the flaws lead to an early failure of the whole material. Thus the small diameter of the fibres implies less flaws than in bulk material, thus the strength of glass fibres is much higher than of bulk glass.

2.3 UD-Composites, Fibre Bundles

The term UD-composites usually means a laminated composite, consisting of several layers of fibres. Each UD-layer consists of parallel fibres that are aligned optimally. It is assumed to have transversely isotropic properties, with the plane of isotropy being normal to the fibre direction. They are manufactured either out of pre-impregnated layers (prepregs) or filament wound with a winding machine.

In textile composites at mesoscale fibre bundles, consisting of one or more impregnated rovings, can be regarded as regions with unidirectional fibre alignment as well. Depending

on the textile architecture the shape of these fibre bundles is seldom constant along its axis, and neither is the fibre volume fraction. Therefore, the fibre waviness in a fibre bundle of a textile composite is higher than in other UD-composites, but they can be treated as transversely isotropic UD-Composites.

Due to their optimal fibre alignment UD-composites provide the highest potential for optimized lightweight constructions with fibre reinforced plastics.

2.3.1 Material Characteristics

UD-Composites inherit the characteristics of their constituents and further some that are caused by the combination of fibre and matrix. The most important characteristic of UD-composites is their direction dependent behaviour. In fibre direction the characteristics of the fibre are dominating and the matrix characteristics can be neglected, whereas in transverse direction the characteristics of the matrix, as described above, are occurring. As described above they therefore exhibit viscosity, plasticity, damage, chemical shrinkage, moisture sensitivity, etc. But damage and plasticity of an UD-composite are not caused by the nonlinear epoxy resin behaviour alone, they are as well originated by microdamage in the composite.

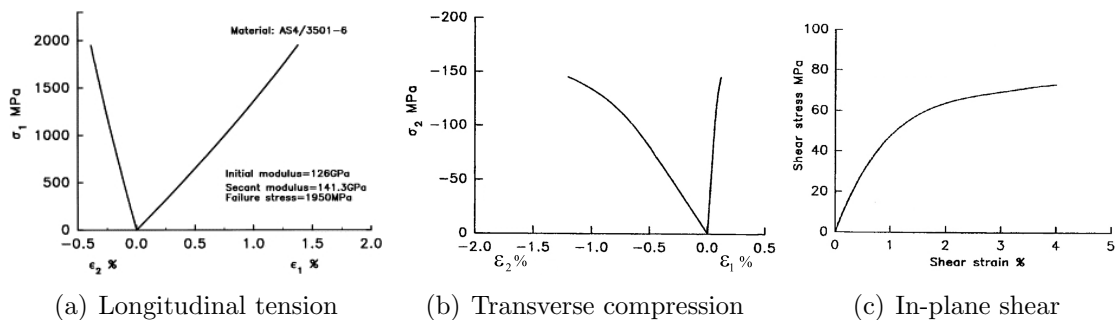


Figure 2.3: Nonlinear material behaviour of UD-layer Hinton et al. (2004)

Nonlinear material behaviour of an UD-layer under transverse compression and in-plane shear is shown in Figure 2.3. The nonlinearity is much more pronounced under shear than under transverse compression, but it is still not negligible.

Paepegem, Baere, and Degrieck (2006) used an ASTM D3518/D3518M-94(2001) standard test method for in-plane shear response of polymer matrix composite materials by tensile test of a $\pm 45^\circ$ laminate to quantify permanent strains and damage as shown in Figure 2.4 with a cyclic test. Viscosity is demonstrated by the hysteresis loops of the unloading-loading paths. Therefore it is not clear whether the remaining strain can be attributed to viscosity or plasticity, i.e. if it is permanent at all. Also the secant moduli indicated by the dotted lines are debatable, because it is clear that they are influenced by remaining viscous strains.

In fibre direction the stress strain curve is almost linear, see Figure 2.3(a), but still initial and secant Young's modulus differ by nearly 10%. Different standards exist to determine

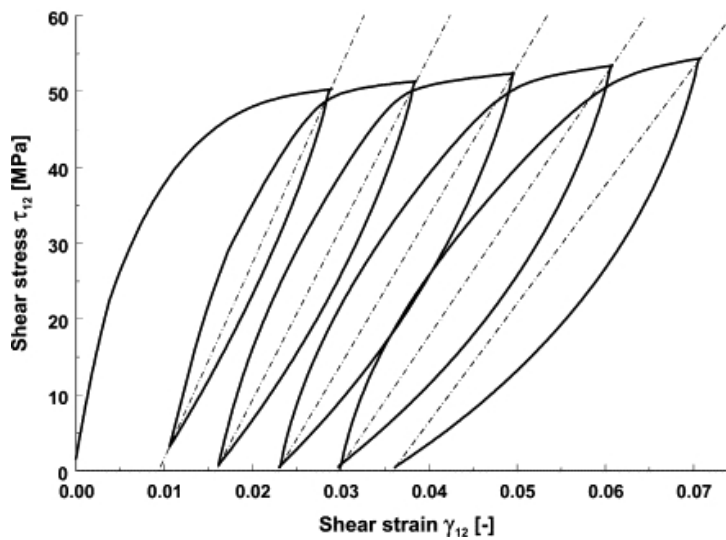


Figure 2.4: Shear stress-strain curve for cyclic $[+45^\circ/-45^\circ]_{2s}$ tensile test. Paepegem et al. (2006)

Young's Moduli under tension EN-2561 (1995) and compression EN-2850 (1995). Both are determined as secant moduli between 10% and 50% of the failure strength. The compressive secant modulus is the lowest, followed by the initial modulus and the tensile modulus is the highest. However, it is not uncommon to neglect these differences.

Due to different thermal expansion of resin and fibre, residual thermal stresses arise on the microscopic level after curing. It is assumed that these stresses are partly decreased by moisture absorption of the composite under environmental conditions but they are potentially able to imply microstructural cracks.

The adhesion of fibre and matrix is of great importance as well, because the fibres are bearing the main loads, but the loads have to be transferred into and between the fibres through the matrix. Fibre coating therefore is a major topic in composites and only the advances made in the past allow for an application of FRP at all.

Alternating lamina orientations cause inhomogeneous stress distributions and stress peaks at the free edges already under unidirectional loads. This effect is commonly known as the free-edge effect and significantly restricts the validity of tensile material tests on coupon level. Generally, for industrial components a quasi-isotropic stacking sequence is used to minimize stress peaks between different lamina directions.

2.3.2 Failure Characteristic

The failure characteristic of composites is complex and based on different anisotropic effects. As for epoxy resin, failure of an UD-layer is pressure-dependent, i.e. tensile, shear and compressive strengths are different. A single UD-layer fails in a brittle manner, it can be separated into fibre failure (FF) and inter-fibre failure (IFF). In fibre direction compressive strength is lower than tensile strength, because the predominant failure mode

under compression is microbuckling that occurs before fibre rupture. Compressive FF is therefore heavily dependent on fibre undulations that stimulate buckling and the matrix that inhibits buckling. Tensile FF is predominantly dependent on the strength of the fibres itself, only a bad fibre-matrix interface may lead to fibre pull-out. The most important influences on strength in transverse direction are the strengths of matrix and of fibre-matrix interface. The latter has a detrimental influence only on the tensile strength. Therefore, in transverse direction the compressive strength is significantly higher than the tensile strength. Compared to the epoxy resin they are made of, UD-layers or fibre bundles have a lower tensile strength, but a higher compressive strength in transverse direction.

The transversely-isotropic material symmetry of UD-composites is used to determine fracture modes, for example Puck (1996) defines different modes for inter-fibre failure, see Figure 2.5. Besides the fracture mode Puck also determines the fracture angle and thus is able to distinguish between critical and uncritical IFF. When the fracture angle is different from 0° and transverse compression acts in the lamina, a wedge shaped failure can lead to a delamination and buckling failure of the whole laminate. Other IFFs are rather uncritical. This classification allows for an evaluation of the criticality of the failure, which is crucial for the design engineer in order to be able to avoid overly conservative results.

Another failure mode of laminates is delamination, where the layers are separated from each other. Delamination can occur due to impact, manufacturing defects, IFF and the free-edge effect. It is a very critical failure, because it occurs inside the laminate and is very hard to detect from outside. At free edges of the laminate and at IFF cracks shear stresses develop between the layers, which lead to delaminations subsequently.

The failure of a laminate is more complicated, because it is a redundant system. According to the classical laminate theory it is commonly assumed that a first failure in a single lamina simply reduces the overall stiffness, whereas the laminate is able to withstand further monotonic load increase until the last lamina fails. This simple approach is com-

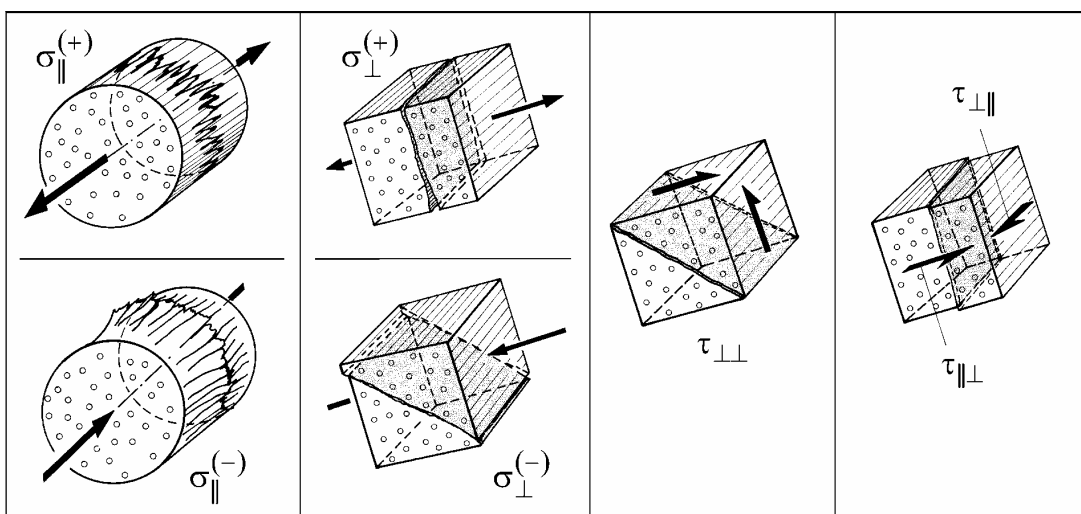


Figure 2.5: Fibre and inter-fibre failure modes (Puck (1996))

only known as the first-ply failure (FPF) and last-ply failure (LPF). IFF is usually the first failure to occur in a laminate, and in the majority of cases this failure is non-critical. In a laminate it is assumed that an IFF crack always runs through the whole thickness of the layer, but does not continue in the adjacent layers. Therefore, the load is transferred around the crack through the adjacent layers and the cracked layer can still carry loads in its uncracked regions. A layer inside a laminate never fails completely in IFF because of the adjacent layers. Only a characteristic damage state is reached where the layer is saturated with cracks, but the layer still has a small percentage of its original stiffness. Figure 2.6 illustrates this effect in a $0^\circ/90^\circ/0^\circ$ -laminate under σ_x -load. Typically, an IFF in the 90° -layer occurs first in such a load case. At the macroscale stresses and strengths are assumed to be homogeneous in a lamina, but in reality they are not, of course. Due to the stochastic fibre-distribution stresses and strengths are inhomogeneous at the microscale. Therefore, only one crack occurs first at the weakest spot. The crack then spreads throughout the whole layer, but stops at the layer boundaries. The stresses from the 90° -layer are transferred into the adjacent 0° -layers over inter-laminar shear stresses and back into the 90° -layer on the other side of the crack. Therefore, the first crack is not very critical, because the additional stresses in the adjacent layers can be carried by the fibres easily and the 90° -layer is weakened only locally around the crack.

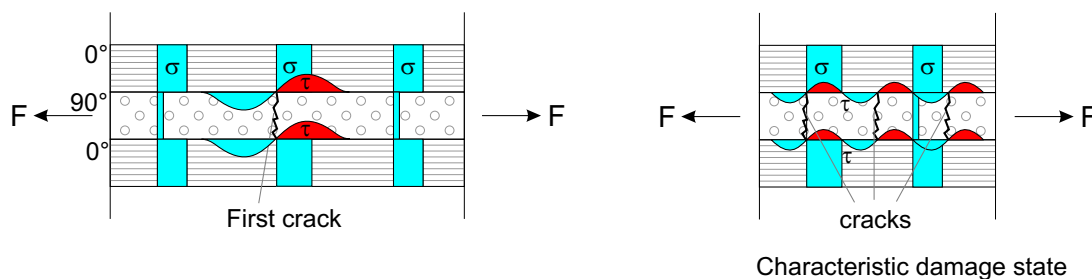


Figure 2.6: Stress distribution in laminate at first crack and at characteristic damage state

In contrast to IFF a FF weakens the laminate so drastically that it is the LPF, because the load of the broken fibres can't be redistributed in the laminate. Of course, thick laminates made of many layers may be able to redistribute loads, but the majority of lightweight composite structures do rather consist of as few layers as possible.

2.4 Textile Composites

Textile composites have mainly been developed to enable an industrialization of composites manufacturing, i.e. to cut down price and production time. The mechanical properties have, therefore, been compromised, mostly due to the increased fibre misalignment, see Bibo, Hogg, Backhouse, and Mills (1998); Godbehere, Mills, and Irving (1994); Truong, Vettori, Lomov, and Verpoest (2005); G.-C. Tsai and Chen (2005); Wang (2002). However, textile composites have advantages over UD-composites in through-thickness strengths, delamination resistance and crashworthiness, see Dransfield, Baillie, and Mai (1994); Jain, Dransfield, and Mai (1998); Mouritz, Leong, and Herszberg (1997).

2.4.1 Types of Textile Composites

Various types of textile composites are in common use with different textile architectures. For high performance structures, fibre architectures, which are capable of utilizing the full fibre potential are favored. Therefore, textile architectures without continuous fibre directions, like knitted fabric reinforcements or randomly oriented milled fibre composites, are only useful for applications without high demands on mechanical performance. Continuous aligned fibre textile preforms for lightweight structures can generally be categorized in five main groups, with increasing fibre misalignments:

- Filament winding composites,
- Non Crimp Fabrics,
- Woven Fabrics,
- Braided Fabrics.
- Knitted Fabrics.

The winding process is different from the other textile manufacturing processes, as it is not restricted to the use of continuous dry fibre rovings. It is used for fabricating composites out of continuous fibres that are wound around a rotating, removable mandrel. Thus, it is also a combination of layer production and lay-up in one process, although it can also be used for lay-up alone. If it is used for lay-up only, it is clear that a multitude of basic materials can be used, from pre-impregnated UD-layers to dry textile layers, e.g. woven fabrics, or pre-impregnated textile layers. If fibre rovings are used, the filament winding technology provides most accurate fibre orientations and thus, can be regarded as an UD-composite from a mechanical point of view. A certain stitching yarn or interwoven configuration is not required. Therefore, the mechanical properties are similar to UD-composites, while the geometry is restricted according to the producibility of the winding technology.

Non-crimp fabric (NCF) reinforcements are manufactured by placing tows at the required orientations in discrete layers and stitching them together using a lightweight textured polyester thread. In the optimal case the stitching thread dissolves in the resin system during the curing process and the reinforcement fibres remain in a straight-lined orientation. These reinforcements are generally considered to offer mechanical properties superior to those available from woven reinforcements since the tows remain straight. Nevertheless, it is assumed that the material properties of NCF materials are significantly lower due to the fibre waviness compared to UD-composites. Concerning textile composites, the NCF material probably provides the highest potential for the construction of lightweight structures. Therefore, it is an interesting prospect to analyze the NCF material by an enhanced experimental evaluation and numerical models on micromechanical level.

For woven textiles, various weave styles exist that exhibit different grades of fibre crimp. A plain weave, for example, consists of two layers of tows in which every tow of the first layer

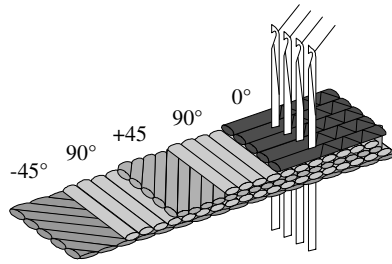


Figure 2.7: Multiaxial non-crimp fabric

is interwoven with each tow of the other layer. In an 8-harness satin weave, only each 8th tow is interwoven and the two layers are therefore less connected. The drapability of woven textiles is generally relatively good and increases with less connections between the layers. For the in-plane mechanical properties, the same applies, because each weave between the layers implies additional fibre crimp. These small periodical fibre misalignments are commonly described as fibre undulations.

Braided composites are basically a combination of filament winding and woven textiles, as they are made of tows woven around a certain geometry. A triaxial braid provides a third tow parallel to the component axis. The geometry inside the braid can be removable, or persist inside during the infiltration process. Braided composites are commonly used for long, tubular components like stiffeners, bars and tubes.

Knitted fabrics resemble common textiles most. The tows are heavily undulated and interlocked. Therefore, they provide an excellent drapability of the dry fabric, but very poor mechanical performance.

However, several combinations of these techniques exist. The biaxial weft-knit fabric presented in chapter 7 for instance consists of non-crimped main reinforcements that are held together by a weft-knitted yarn. Therefore, it combines the advantages of high drapability and good mechanical performance.

Generally textile fabrics and woven composites are manufactured by a process, wherein a warp thread is woven with a weft thread. Obviously this process leads to small periodical fibre misalignments on a micromechanical level due to interlacing of crossing tows. These misalignments decrease the in-plane material properties. The basic idea of non-crimp fabric materials is to align the fibres in a precise continuous orientation with as few undulations as possible.

Manufacturing of Textile Composites

An important aspect to understand the material behaviour, is their manufacturing. The fibre architecture and lay-up of the preforms is done in a “dry” state, i.e. without the resin. This saves cost significantly compared to prepreg production, because storage cost is reduced and handling is simplified. Furthermore, the drapability of the dry preforms is higher by far, although also dependent on the preform itself, and more complex components can be formed. After lay-up, the dry laminate is impregnated with a liquid resin

system by infusion, called liquid resin infusion method (LRI). This impregnation process is responsible for numerous fibre undulations due to the viscosity of the matrix.

The liquid resin infusion processes can be classified according to the resin impregnation technique and tooling. The traditional method is known as hand lay-up, in which a dry fibre reinforcement preform is cut to the desired shape and placed in a simple one sided mould. Resin systems are applied in liquid form to the preform by hand. The lamina is compacted by a roller and cured under ambient temperature or in an oven. This process enables a very low cost tooling but is restricted to a relatively low fibre volume fraction and material quality according to unprecise fibre orientations, undulations and void entrapments. Hence, this process is comparatively unimportant for the production of high performance structures.

The vacuum assisted infusion technology provides a closed mould and higher fibre volume fractions compared to the hand lay-up. The production procedure is slightly reminiscent to the prepreg process, in which the preform is assembled in a single sided mould and sealed under a vacuum bag. The resin is injected in the system at atmospheric pressure through an inlet and flows through the preform to the vent. Because of the low tooling cost and the environmental producibility this process is established for the production of large components and structures such as boat hulls and future airplane fuselage. Additionally the process is promoted by the ability to make high quality parts with low void content and high fibre volume fraction.

The resin transfer moulding (RTM) process provides relatively good material quality but requires expensive tools. Thus, RTM is especially suited for production of high volume applications. In the RTM process a dry textile preform is placed between a pair of rigid moulds, which are usually from metal. The liquid resin is injected under pressure and flows through the cavity of the mould towards a vent, which is maintained at atmospheric or lower pressure. The parts produced by this process have excellent dimensional accuracy, surface finish and a high potential for good mechanical properties and reproducible quality. Although only smaller parts are producible than with the vacuum bag assisted injection, the RTM process is used extensively for commercial production, especially in the automotive industry.

There are additional processes for the infusion of textile composites with more or less modifications on the above described technologies. An advanced interesting possibility

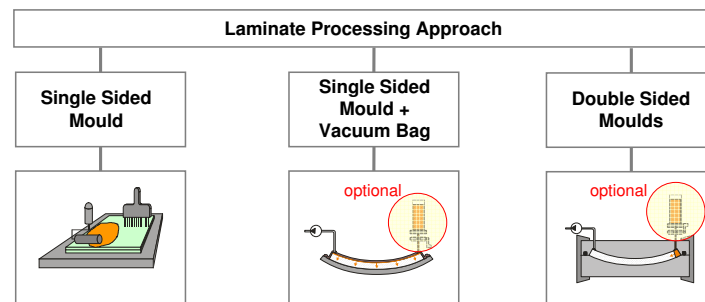


Figure 2.8: Liquid resin infusion processes for textile preforms Kleineberg et al. (2002)

provide the autoclave assisted injection, for example the single line injection (SLI) process, which was developed at the DLR Herrmann, Pabsch, and Kleineberg (2001). The SLI process is a vacuum assisted infusion process in combination with an autoclave to assure a precise fibre volume fraction and minimal fibre undulations provided by a low-cost tooling using a single sided mould.

Generally textile composites provide the possibility to integrate different components in one structure. This enables the possibility to reduce manufacturing cost, material amount, and weight of a structure. Therefore, textile structures provide an interesting prospect for lightweight and economical structures. A detailed evaluation of the NCF material is an essential step towards a qualified application of high performance lightweight structures. Thereby, the analysis on a micromechanical level seems to be a promising method, particularly for the stiffness and strength prediction of three dimensional reinforced NCF materials.

2.4.2 Material Characteristics of Textile Composites

The material behaviour of textile reinforced composites is generally the same as for UD-Composites. Basically two main differences in experimental behaviour are important:

1. Due to the textile architecture and the manufacturing process textile composites exhibit **increased fibre waviness**.
2. The smallest unit available for experimental testing is a **textile layer**.

Fibre waviness, misalignment, crimp or undulation compromises the mechanical behaviour of textile composites, because the bending stiffness of the fibres is negligible compared to the longitudinal stiffness. Fibre waviness occurs systematically due to the textile architecture, for example in woven fabrics, and stochastically due to the manufacturing inaccuracies. Systematical fibre waviness does not occur in UD-composites and is relatively critical, because it is uniformly distributed over a certain area and thus stimulates fibre kinking under compression. The flow of the viscous resin through the fabric during infiltration process causes stochastic fibre waviness, that is also unfavorable under compression. It occurs in UD-composites as well, but to a lesser extent.

Under tension, undulated fibres have to straighten before they can carry the full load. Therefore, the stiffness increases in the first load cycle, but this effect is rather unimportant, the accompanying microdamage in the matrix is probably more significant. Ulbricht and Haasemann (2007) report a significant change in the textile architecture of a biaxial weft-knitted fabric during a bending test, see Figure 2.9. It is clear that the tension in the knitting yarn in the manufacturing process thus has an important influence, not only on the drapability, but also on the mechanical performance.

The fact that the smallest unit available for testing is a textile layer does not influence the mechanical behaviour of a textile composite itself, but makes understanding the behaviour much more complicated. A textile layer is more of a laminate than a layer.

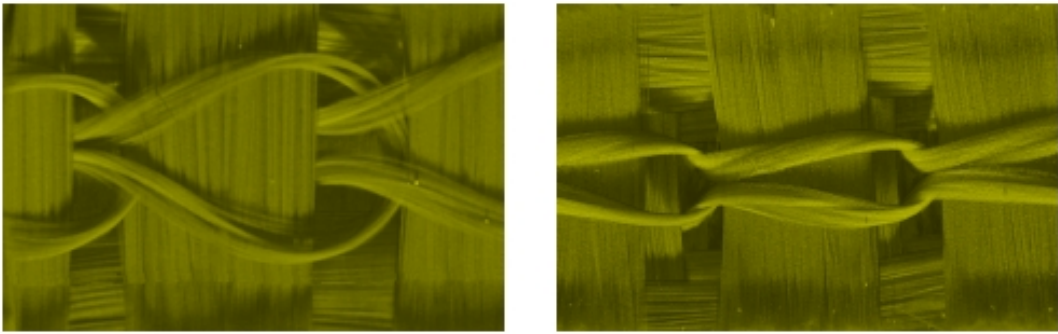


Figure 2.9: Computer tomography of biaxial weft-knitted fabric before and after bending test, Ulbricht and Haasemann (2007)

Its material symmetry is orthotropic, thus, unless only in-plane properties are required, nine instead of five material stiffnesses and strengths have to be determined. Through-thickness properties are nearly impossible to determine, because the thickness of a textile layer is too small for experimental testing devices. To produce a thicker textile layer is neither possible. Therefore, textile layers are often treated as laminates of UD-layers with decreased properties according to knock-down factors.

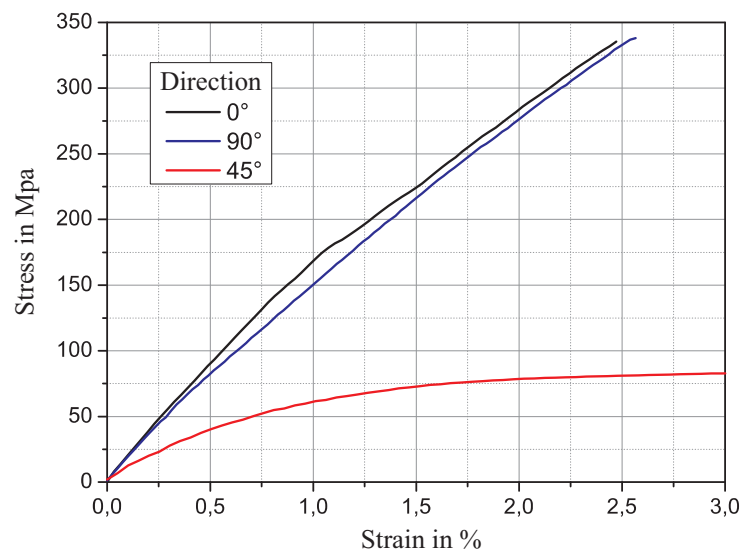


Figure 2.10: Stress-strain curves of biaxial weft-knitted fabric under different load directions, Ulbricht and Haasemann (2007)

Unfortunately, the detection of failure and the assignment of failure in a textile layer is not an easy task, because only FF is clearly visible in a load-displacement curve. In Figure 2.10 FF is depicted by the end of the curve, but from experience made with UD-composites it is most likely that IFF occurs earlier and thus yields a nonlinear stress-strain-curve. In a UD-layer IFF is determined by total failure under load in transverse direction. This is not possible for textile composites, because of multiple fibre directions. Therefore, IFF is detected either optically, see Figure 2.11 or acoustically, Hamstad (1986), but both methods have significant weaknesses. An optical determination of a crack density is not

continuous in time and does not deliver a strain at which failure occurs, whereas an acoustical detection does not deliver any information on the place of failure.



Figure 2.11: Strain rate dependent crack densities in biaxial weft-knitted fabric, increasing strain rate from left to right, Hufenbach (2007)

A further difference of textile composites from UD-Composites are the epoxy resin pockets that result from the textile architecture. Textile composites are manufactured with relatively large fibre tows which are interwoven or stitched in geometrically complex patterns, they contain significant volumes of resin pockets, which are recognizable in Fig. 2.12 as black areas. For the macroscale mechanical behaviour they are less significant, their existence is only a visualization of the inhomogeneous fibre distribution, but due to the plasticity of the epoxy resin, cracks seldom originate in the pockets. Edgren, Mattson, Asp, and Varna (2004) describe that failure of NCFs begins with transverse cracks inside fibre bundles. Resin pockets cause significant thermal residual stresses, that can be an issue for the adjacent fibre bundles. Another technical difference between textile composites and UD-composites is that infusible resin systems have particularly brittle mechanical failure behaviour. The infusible resin is optimized for a certain viscosity and provide usually lower allowable strains compared with the resin system used for UD-composites.

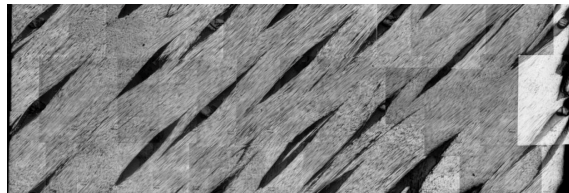


Figure 2.12: Fibre waviness and resin pockets on micromechanical level (undulations) of a stitched NCF Sickinger and Herrmann (2001)

3 Elastic-Plastic Material Models

In this chapter, two material models are presented: one for epoxy resin and one for fibre bundles, see also Vogler, Ernst, Hühne, and Rolfes (2007). Both models share one main concept, they use invariant-based, quadratic yield criteria to model pressure-dependent hardening. The required material parameters are hardening curves that can be taken directly from experimental stress-strain curves.

It should be stressed here that the identification and the number of material parameters are crucial for the usability of a material model. The more material parameters have to be determined, the more expensive tests have to be done. On the other side, a model with a small number of parameters is limited in its possibilities to describe nonlinearities, because it requires very restrictive assumptions. However, a high number of material parameters does not guarantee a realistic description of the material behaviour. Only the assumptions made in a material model do matter for the quality of its results. If, however, the physical meaning of the material parameters is too abstract or even unclear, the user of the material model may not be able to verify the validity of his input and is thus unable to judge upon the quality of his computations. In this sense, hardening curves are very good material parameters, because they have an obvious physical meaning that can be judged easily.

For epoxy resin, an isotropic elastic-plastic material model is presented in sec. 3.1. Characterizing the transversely isotropic behaviour of the fibre bundles, a transversely isotropic elastic-plastic material model is developed in sec. 3.2. As described in Chapter 2, both materials exhibit viscous material behaviour, but this is neglected here. The presented material models are used for quasistatic loads. Failure of the materials is described in the following Chapter 4.

3.1 Isotropic Elastic-Plastic Material Model for Epoxy Resin

Epoxy resin is an isotropic material that exhibits a nonlinear and pressure-dependent behaviour, see Section 2.1. A phenomenological material model was chosen here, that models the complete nonlinearity of the material via plasticity. It is assumed that up to the failure stress, only plastic hardening takes place, afterwards damage is applied to model softening, see Section 4.1. Therefore, the material model is only useful for monotonically increasing loads at low strain rates. Considering that the unit cell computations at micro- and mesoscale, where this material model shall be applied, are subjected to such loads, it becomes clear that it fulfills its purpose.

Apart from the nonlinear stress-strain curves, epoxy resin exhibits a pressure dependency as well, i.e. the hydrostatic pressure has an influence on the nonlinear material behaviour. Hydrostatic pressure does not affect epoxy resin in the linear regime, but the end of the linear regime, i.e. plastic hardening starts at lower stresses under tension. Therefore, a pressure-dependent yield surface is chosen. Furthermore, the occurring plastic strains are also pressure dependent, they are very small under tension, very high under shear and compression. Therefore, the ongoing hardening process, i.e. the parameters of the yield surface, is described by two hardening curves, one under tension and one under shear.

3.1.1 Yield Surface

To account for different yielding behaviour under uniaxial tension, uniaxial compression and simple shear (see fig. 3.5), a quadratic yield surface is chosen Haufe, Bois, Kolling, and Feucht (2005). In terms of the first two stress invariants hydrostatic pressure p and VON MISES stress σ_{vm} , the yield locus can be written as

$$f = \sigma_{vm}^2 - a_0 - a_1 p, \quad (3.1)$$

whereby

$$p = \frac{1}{3}\sigma_{ii} \quad \text{and} \quad \sigma_{vm} = \sqrt{\frac{3}{2}s_{ij}s_{ij}}. \quad (3.2)$$

The term s_{ij} is the stress deviator tensor. Notations $p = I_1$ and $\sigma_{vm} = J_2$ are chosen here to distinguish the isotropic invariants from the transversely isotropic invariants in the following Section 3.2. Hydrostatic pressure p is positive for hydrostatic tension and negative for hydrostatic compression, VON MISES stress σ_{vm} is always positive. The remaining parameters a_0 and a_1 are determined from hardening curves.

Experimental results for epoxy resin RIM135 are available from an uniaxial tensile test by ADDEN and a simple shear test by FIEDLER, see Figure 2.1. How the hardening curves

$$\begin{aligned} \sigma_t &= \sigma_t(\bar{\varepsilon}^{pl}) = \text{tensile hardening curve,} \\ \sigma_s &= \sigma_s(\bar{\varepsilon}^{pl}) = \text{shear hardening curve} \end{aligned} \quad (3.3)$$

are extracted from these stress-strain curves is described in Section 3.3. During the computation, the parameters a_0 and a_1 are calculated from these hardening curves by the plasticity algorithm and thus, the experimentally obtained test data are reproduced exactly in numerical simulations, see sec. 3.1.3. The remaining parameters a_0 and a_1 are given by

$$\begin{aligned} a_0 &= 3\sigma_s^2, \\ a_1 &= 3\frac{\sigma_t^2 - 3\sigma_s^2}{\sigma_t}. \end{aligned} \quad (3.4)$$

The yield stresses σ_s and σ_t are determined from the hardening curves eq. 3.3 in every time step, depending on the accumulated plastic strain $\bar{\varepsilon}^{pl}$. Hence, the experimentally measured yield stresses for uniaxial tension and pure shear are recovered exactly in the material model. Although only two hardening curves are considered, other stress states are properly regarded in the yield locus eq. 3.1. It should be noted that this yield surface does not allow plastic flow under pure hydrostatic compression.

3.1.2 Flow Rule

Generally, the flow rule that determines the direction of flow, is either formulated as associated or non-associated flow. Associated flow leads to plastic strain rate in terms of the normal vector to the yield surface. However, assuming an associated flow rule, the plastic Poisson's ratio, defined as the ratio of transverse to longitudinal plastic strain rate, is not reflected in a correct way under hydrostatic compression. In some cases even physically nonsensical values follow for the plastic Poisson's ratio. Further, there is no possibility to control the volumetric plastic straining. The assumption of a VON MISES plastic potential implies plastic flow under constant volume, i.e. $\nu_p = 0.5$, which is not a correct assumption for epoxy resin. Experiments show that the plastic Poisson's ratio depends on hydrostatic pressure and in particular that there is a different lateral behaviour in tension and in compression, see Fiedler et al. (2001). Assuming an associated flow rule, the volumetric plastic straining under pressure is overestimated. Under hydrostatic compression, the associated flow rule yields an increase in volume, which in turn leads to unrealistic results. To account for a realistic assumption for ν_p and to control the lateral plastic straining in dependence on hydrostatic pressure, the plastic potential is assumed as (see Haufe et al. (2005)):

$$g = \sqrt{\sigma_{vm}^2 + \alpha p^2} \quad . \quad (3.5)$$

The amount of dilatancy or compression, i.e. the increase or decrease in material volume due to yielding, can be controlled with the flow parameter α . It correlates to the plastic Poisson's ratio ν_p under uniaxial loading:

$$\nu_p = \frac{9 - 2\alpha}{18 + 2\alpha} \Rightarrow \alpha = \frac{9}{2} \frac{1 - 2\nu_p}{1 + \nu_p} \quad (3.6)$$

Plausible flow behaviour is given for $0 \leq \nu_p \leq 0.5$, which is equal to $0 \leq \alpha \leq \frac{9}{2}$. If the flow parameter α is set to zero, there is no change in material volume when yielding occurs and the VON MISES plastic potential is recovered. The plastic potential is illustrated in Figure 3.1. However, with this plastic potential and the quadratic yield surface the differences between associated and non-associated flow are very small under tension and shear.

3.1.3 Hardening Formulation

To describe the hardening behaviour under plastic flow, a nonlinear isotropic hardening model is used. Hardening curve is input via tabulated data. That is, the hardening

data obtained from uniaxial tension and simple shear test can directly be input in terms of load curves giving the yield stress as a function of the corresponding plastic strain. Consequently, the hardening is dependent on the state of stress and not only on the accumulated plastic strain. Figure 3.1 illustrates how hardening is dependent on the input curves, displayed on the right side. It shows the yield surfaces f^n and f^{n+1} of the time steps t_n and t_{n+1} in σ_{vm} - p -invariant-plane. From the equivalent plastic strain $\bar{\varepsilon}^{pl}$ of each time step, shear stress and uniaxial tension stress are taken out of the hardening curves. The yield surface is then defined by the shear stress and the uniaxial tension stress from the hardening curves.

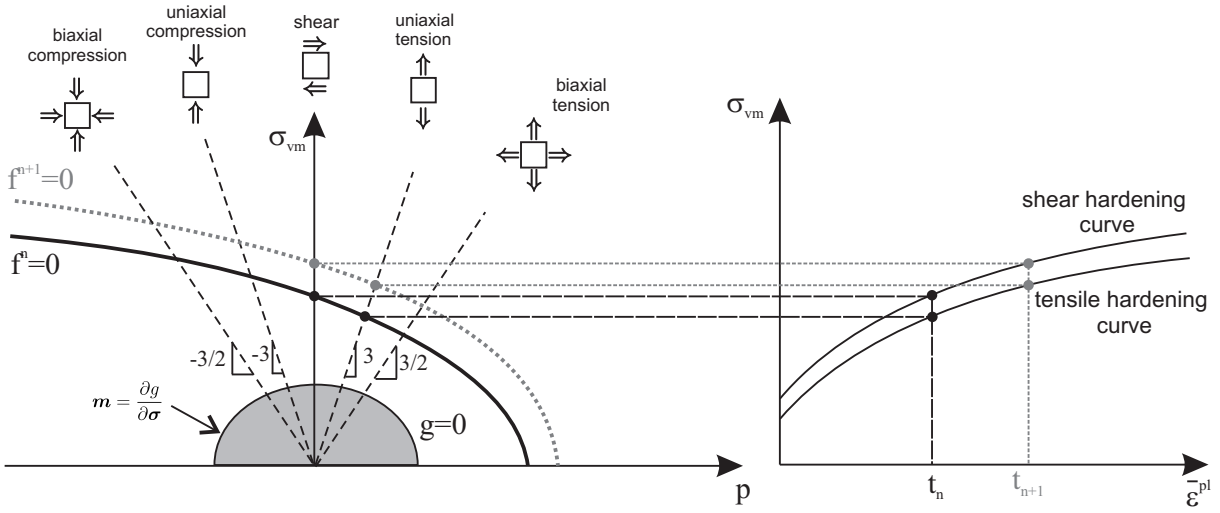


Figure 3.1: Representation of plastic potential, yield surface and failure surface in σ_{vm} - p -invariant-plane

As the measurement results from material testing are commonly provided as true stresses over true total strains, the hardening curves must be prepared by subtracting the elastic part of the strains from the total strains:

$$\begin{aligned}\varepsilon_t^{pl} &= \varepsilon_t - \frac{\sigma_t}{E}, \\ \varepsilon_s^{pl} &= \varepsilon_s - \frac{\sigma_s}{2G}.\end{aligned}\quad (3.7)$$

During the computation, only one equivalent plastic strain $\bar{\varepsilon}^{pl}$ is used that is given by:

$$\bar{\varepsilon}^{pl} = \varepsilon_t^{pl} = \frac{2}{\sqrt{3}} |\varepsilon_s^{pl}|. \quad (3.8)$$

If the test results are given in engineering stresses and strains, a conversion into true stresses and true strains has to be done. The concept of tabulated input of hardening data allows for a straight forward treatment in computation. The test results that are reflected in the load curves, are used exactly by the material model without fitting to any

analytical expression. There is no need for parameter fitting. Yet, in reality things are not always perfectly clear and neither is the determination of the starting point of plasticity in an experimental stress-strain curve. Therefore, a parameter identification procedure, described in Section 3.3 has to be carried out. The load curves expected as input are briefly described in fig. 3.2

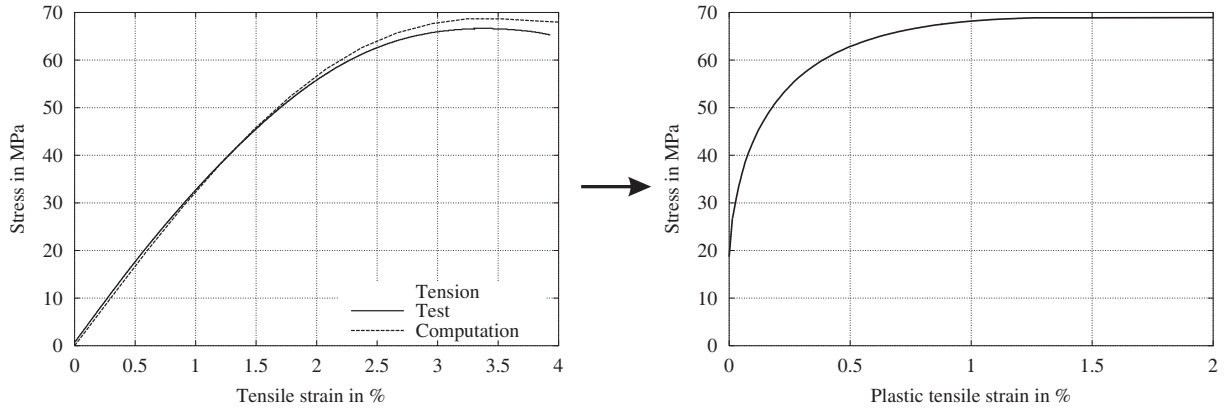


Figure 3.2: Preparation of experimentally obtained hardening curves for input as tabulated data: Total strains have to be converted into plastic strains by eq. 3.7

3.1.4 Numerical Treatment

The present model has been implemented as a user-defined material into ABAQUS implicit (user interface UMAT) and ABAQUS explicit (user interface VUMAT). Starting from the additive decomposition of the strain increment at time t_{n+1}

$$\Delta\varepsilon_{n+1} = \varepsilon_{n+1} - \varepsilon_n, \quad (3.9)$$

the trial stress, assuming elastic behaviour, is computed as

$$\boldsymbol{\sigma}_{n+1}^{\text{trial}} = \boldsymbol{\sigma}_n + \mathbb{C} : \Delta\varepsilon_{n+1}. \quad (3.10)$$

Checking the yield surface

$$f = f(\boldsymbol{\sigma}_{n+1}^{\text{trial}}, \bar{\boldsymbol{\varepsilon}}^{\text{pl}}) \quad (3.11)$$

indicates elastic either ($f \leq 0$) or plastic ($f > 0$) loading. In the case of plastic loading, a classical elastic-predictor plastic-corrector scheme is applied for stress integration, see Simo and Hughes (1998) or Hughes (2003). The increment of the equivalent plastic strain can be written as

$$\Delta \bar{\boldsymbol{\varepsilon}}_{n+1}^{\text{pl}} = \Delta \lambda_{n+1} \|\mathbf{m}_{n+1}\|. \quad (3.12)$$

where $\Delta \lambda$ is the sought plastic multiplier. The direction \mathbf{m} of the plastic flow in the case of a non-associated flow rule is given by the derivative of the plastic potential g with respect to the stresses :

$$\mathbf{m}_{n+1} = \partial g(\boldsymbol{\sigma}_{n+1}) / \partial \boldsymbol{\sigma}_{n+1}. \quad (3.13)$$

Hence, the stresses can be calculated through

$$\boldsymbol{\sigma}_{n+1} = \boldsymbol{\sigma}_{n+1}^{\text{trial}} - \Delta \lambda_{n+1} \mathbb{C} : \mathbf{m}_{n+1} \quad (3.14)$$

and the internal variable is updated by

$$\bar{\boldsymbol{\varepsilon}}_{n+1}^{\text{pl}} = \bar{\boldsymbol{\varepsilon}}_n^{\text{pl}} + \Delta \lambda_{n+1} \|\mathbf{m}_{n+1}\|. \quad (3.15)$$

Inserting in the active yield surface eq.3.11 formally leads to a nonlinear equation in $\Delta \lambda_{n+1}$ which is solved explicitly by the Newton-Raphson method. Fig. 3.3 shows an illustration of the applied elastic predictor-plastic corrector integration algorithm. From the stress state of the current time $\boldsymbol{\sigma}_n$, an elastic prediction $\boldsymbol{\sigma}_{n+1}^{\text{trial}}$ is done firstly. Subsequently, with the Newton-Raphson method the searched stress state $\boldsymbol{\sigma}_{n+1}$ is iteratively searched via radial return algorithm.

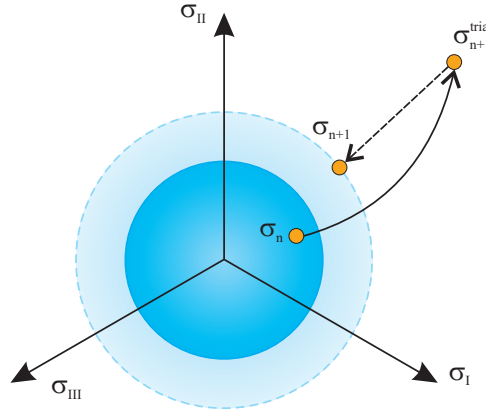


Figure 3.3: Radial return algorithm

3.2 Transversely Isotropic Elastic-Plastic Material Model for Fibre Bundles

A fibre bundle, or UD-composite, is a transversely isotropic material that exhibits nonlinear and pressure dependent behaviour, as described in Section 2.3. Nonlinear behaviour in

longitudinal, i.e. fibre, direction is neglected, because of its small magnitude. In transverse direction, the nonlinearity stems from viscosity, plasticity and damage, but the determination of the fractions is very difficult, as it is for epoxy resin. Since the presented material model is used for monotonically increasing, quasistatic loads, the nonlinear behaviour is modelled as purely plastic. Pressure-dependent hardening can be observed in transverse direction as well. Therefore, a material model equivalent to the isotropic material described above is presented here. Due to the transversely isotropic material symmetry, other invariants are required. An additive decomposition of the infinitesimal strain tensor into an elastic and a plastic part is assumed. For both the elastic and the plastic part of the transversely isotropic material model, the representation of the constitutive equations is carried out in the format of isotropic tensor functions by means of structural tensors. A further description of invariant theory is given by Boehler (1987).

3.2.1 Elastic Stress-Strain Relations

Transversely isotropic materials are characterized through a preferred direction \mathbf{a} . Thus, the material response is invariant with respect to arbitrary rotations around this preferred direction \mathbf{a} , to reflections at fibre parallel planes and with respect to the reflection at that plane, whose normal is \mathbf{a} . These are the group of symmetry transformations for transverse isotropy. Fibre bundles, as in the rovings, are a typical representative of transversely isotropic material models. The structural tensor \mathbf{A} of transverse isotropy, which represents the materials intrinsic characteristic, is defined as the dyadic product of the preferred direction \mathbf{a}

$$\mathbf{A} = \mathbf{a} \otimes \mathbf{a} \quad (3.16)$$

As only small elastic deformations are considered, the assumption of HOOKE's linear elasticity law $\boldsymbol{\sigma} = \hat{\boldsymbol{\sigma}}(\boldsymbol{\varepsilon})$ is justified. Postulating hyperelasticity, the first derivative of the free energy function $\hat{\Psi}$ with respect to the strains $\boldsymbol{\varepsilon}$ delivers the stresses $\boldsymbol{\sigma}$ and the second derivation with respect to the strains $\boldsymbol{\varepsilon}$ gives the elasticity tensor \mathbb{C}_e . In case of transverse isotropy, the free energy function is formulated in isotropic invariants of the strain tensor $\boldsymbol{\varepsilon}$ and the structural tensor \mathbf{A} . To derive a representation of $\hat{\Psi}$ and the infinitesimal stress tensor $\boldsymbol{\sigma}$ as isotropic tensor-functions, the functional basis of the two symmetric second order tensorial arguments $\boldsymbol{\varepsilon}$ and \mathbf{A} is needed. Assuming the stresses to be a linear function of the strains and providing a stress free undistorted initial configuration, i.e. $\boldsymbol{\sigma}(\boldsymbol{\varepsilon} = 0) = 0$, terms are neglected, which are linear or cubic in the strains. This enforces the elasticity tensor \mathbb{C}_e to be constant and yields a formulation of the free energy function with five elasticity constants λ , α , μ_L , μ_T and β describing the transversely isotropic material behaviour:

$$\begin{aligned} \hat{\Psi}(\boldsymbol{\varepsilon}, \mathbf{A}) := & \frac{1}{2} \lambda (\text{tr } \boldsymbol{\varepsilon})^2 + \mu_T \text{tr } (\boldsymbol{\varepsilon})^2 + \alpha (\mathbf{a} \boldsymbol{\varepsilon} \mathbf{a}) \text{tr } \boldsymbol{\varepsilon} + \\ & 2(\mu_L - \mu_T) (\mathbf{a} \boldsymbol{\varepsilon}^2 \mathbf{a}) + \frac{1}{2} \beta (\mathbf{a} \boldsymbol{\varepsilon} \mathbf{a})^2 \end{aligned} \quad (3.17)$$

For the stresses we obtain

$$\begin{aligned} \boldsymbol{\sigma} = & \lambda(\operatorname{tr} \boldsymbol{\varepsilon})\mathbf{1} + 2\mu_T \boldsymbol{\varepsilon} + \alpha(\mathbf{a}\boldsymbol{\varepsilon}\mathbf{a} + \operatorname{tr} \boldsymbol{\varepsilon} \mathbf{A}) \\ & + 2(\mu_L - \mu_T)(\mathbf{A}\boldsymbol{\varepsilon} + \boldsymbol{\varepsilon}\mathbf{A}) + \beta\mathbf{a}\boldsymbol{\varepsilon}\mathbf{a} \end{aligned} \quad (3.18)$$

and the elasticity tensor is

$$\begin{aligned} \mathbb{C}_e = & \lambda\mathbf{1} \otimes \mathbf{1} + 2\mu_T \mathbb{I} + \alpha(\mathbf{A} \otimes \mathbf{1} + \mathbf{1} \otimes \mathbf{A}) \\ & + 2(\mu_L - \mu_T)\mathbb{I}_{\mathbf{A}} + \beta\mathbf{A} \otimes \mathbf{A} \quad . \end{aligned} \quad (3.19)$$

Hereby, the 4th order tensor $\mathbb{I}_{\mathbf{A}}$ in index notation reads $A_{im}\mathbb{I}_{jmkl} + A_{jm}\mathbb{I}_{mikl}$. In matrix notation the 4th order elasticity tensor of transversely isotropic material for a preferred X_1 -direction in a Cartesian coordinate system, i.e. $\mathbf{a} = [1, 0, 0]^T$, reads:

$$\mathbb{C}_e = \begin{bmatrix} \lambda + 2\alpha + \beta + 4\mu_L - 2\mu_T & \lambda + \alpha & \lambda + \alpha & 0 & 0 & 0 \\ & \lambda + \alpha & \lambda + 2\mu_T & \lambda & 0 & 0 & 0 \\ & \lambda + \alpha & \lambda & \lambda + 2\mu_T & 0 & 0 & 0 \\ & 0 & 0 & 0 & \mu_L & 0 & 0 \\ & 0 & 0 & 0 & 0 & \mu_L & 0 \\ & 0 & 0 & 0 & 0 & 0 & \mu_T \end{bmatrix} \quad (3.20)$$

The transformation from engineering constants to those of the invariant representation and vice versa are listed in Table 3.1.

3.2.2 Transversely Isotropic Yield Surface

A transversely isotropic yield surface as an extension of a yield function following Rogers (1987) and its numerical treatment in Schröder (1995) is proposed in this work. This model is based on two assumptions, firstly on the assumption of plastic incompressibility and secondly on the assumption that projections of stress onto the preferred direction \mathbf{a} do not induce plastic yielding. This condition is taken into account by a decomposition of the stress tensor into an extra stress tensor $\boldsymbol{\sigma}^{\text{pind}}$, inducing plastic yielding, and a remaining reaction stress tensor $\boldsymbol{\sigma}^{\text{reac}}$:

$$\boldsymbol{\sigma} = \boldsymbol{\sigma}^{\text{pind}} + \boldsymbol{\sigma}^{\text{reac}} \quad (3.21)$$

The assumption of plastic incompressibility is fulfilled with the postulation

$$\operatorname{tr} \boldsymbol{\sigma}^{\text{pind}} = 0 \quad . \quad (3.22)$$

Presuming inextensibility of the preferred direction \mathbf{a} , in which plasticity is assumed not to occur, leads to an additional constraint. The projection of the stress tensor onto the fibre direction \mathbf{a} must vanish:

$$\mathbf{a}\boldsymbol{\sigma}^{\text{pind}}\mathbf{a} = \underbrace{\mathbf{a} \otimes \mathbf{a}}_{:= \mathbf{A}} : \boldsymbol{\sigma}^{\text{pind}} = 0 \quad . \quad (3.23)$$

\mathbf{A} is the structural tensor belonging to the fibre direction \mathbf{a} . For the reaction stresses $\boldsymbol{\sigma}^{\text{reac}}$ an ansatz of the form

$$\boldsymbol{\sigma}^{\text{reac}} = p\mathbf{1} + T_a \mathbf{A} \quad (3.24)$$

is used. From eq.3.22 and eq.3.23 follow the stress components $\boldsymbol{\sigma}^{\text{reac}}$ and $\boldsymbol{\sigma}^{\text{pind}}$:

$$\left. \begin{aligned} \boldsymbol{\sigma}^{\text{reac}} &= \left. \begin{aligned} &\frac{1}{2}(\underbrace{\text{tr } \boldsymbol{\sigma} - \mathbf{a}\boldsymbol{\sigma}\mathbf{a}}_p) \mathbf{1} - \frac{1}{2}(\underbrace{\text{tr } \boldsymbol{\sigma} - 3\mathbf{a}\boldsymbol{\sigma}\mathbf{a}}_{T_a}) \mathbf{A} \\ \boldsymbol{\sigma}^{\text{pind}} &= \boldsymbol{\sigma} - \frac{1}{2}(\text{tr } \boldsymbol{\sigma} - \mathbf{a}\boldsymbol{\sigma}\mathbf{a})\mathbf{1} + \frac{1}{2}(\text{tr } \boldsymbol{\sigma} - 3\mathbf{a}\boldsymbol{\sigma}\mathbf{a})\mathbf{A}. \end{aligned} \right\} \quad (3.25) \end{aligned}$$

As it can be seen in the following equation, T_a can be interpreted as a fibre overstress, exceeding the hydrostatical part of the stress tensor. The total stress of the fibre is

$$\mathbf{a}\boldsymbol{\sigma}\mathbf{a} = \mathbf{a}\boldsymbol{\sigma}^{\text{reac}}\mathbf{a} = p + T_a \quad (3.26)$$

To account for a possible influence of plastification in fibre direction, the projection of the deviatoric part of the reaction stress tensor $\boldsymbol{\sigma}^{\text{reac}}$ onto \mathbf{a} can be regarded:

$$\mathbf{a}(\text{dev } \boldsymbol{\sigma}^{\text{reac}})\mathbf{a} = \mathbf{a} T_a (\text{dev } \mathbf{A})\mathbf{a} = T_a \mathbf{a}(\mathbf{A} - \frac{1}{3}\mathbf{1})\mathbf{a} = \frac{2}{3}T_a \quad (3.27)$$

The construction of the anisotropic yield condition follows the same considerations as the derivation of the hyper-elastic potential $\hat{\Psi}$. The yield function has to be invariant with respect to transformations belonging to the group of symmetry transformations for transverse isotropy. The yield condition can be composed of the basic invariants of the related stresses and the structural tensor. As a first approach, we refer to the invariant sets used by Schröder (1995), who refers to the work of Spencer (1987) and Rogers (1987).

$$\left. \begin{aligned} I_1 &:= \frac{1}{2} \text{tr} (\boldsymbol{\sigma}^{\text{pind}})^2 - \mathbf{a} (\boldsymbol{\sigma}^{\text{pind}})^2 \mathbf{a} \\ I_2 &:= \mathbf{a} (\boldsymbol{\sigma}^{\text{pind}})^2 \mathbf{a} \end{aligned} \right\} \quad (3.28)$$

It can be observed that under in-plane shear stress considerable plastic yielding occurs in UD-material, see Figure 2.3. Under uniaxial tension and uniaxial compression perpendicular to the fibre direction, the material nonlinearities are rather small. To account for this pressure dependency in the yield surface, a third invariant I_3 is introduced in such a way, that the projection of the stresses in fibre direction is not affected:

$$I_3 := \text{tr } \boldsymbol{\sigma} - \mathbf{a}\boldsymbol{\sigma}\mathbf{a} \quad (3.29)$$

The yield function as a function of the introduced invariants is formulated as:

$$f = \alpha_1 I_1 + \alpha_2 I_2 + \alpha_3 I_3 + \alpha_{32} I_3^2 - 1 \quad (3.30)$$

with the flow parameters α_1 , α_2 , α_3 and α_{32} . This formulation of the yield surface makes it possible to account for pressure dependency of UD-material. The derivations of the yield surface are:

$$\left. \begin{aligned} \partial_{\boldsymbol{\sigma}} f &= \partial_{\boldsymbol{\sigma}} f = \partial_{I_i} f \partial_{\boldsymbol{\sigma}} I_i f = \\ &\alpha_1 \boldsymbol{\sigma}^{\text{pind}} + (\alpha_2 - \alpha_1) (\mathbf{A} \boldsymbol{\sigma}^{\text{pind}} + \boldsymbol{\sigma}^{\text{pind}} \mathbf{A}) + \alpha_3 (\mathbf{1} - \mathbf{A}) =: \mathbf{B} \\ \partial_{\boldsymbol{\sigma}\boldsymbol{\sigma}}^2 f &= \alpha_1 \mathbb{P}^{\text{pind}} + (\alpha_2 - \alpha_1) \mathbb{P}_{\mathbf{A}}^{\text{pind}} + 2\alpha_{32} (\mathbf{1} - \mathbf{A}) \otimes (\mathbf{1} - \mathbf{A}) \\ &\quad + \alpha_3 (\mathbf{1} - \mathbf{A}) =: \mathbb{A} \end{aligned} \right\} \quad (3.31)$$

with the projection tensor

$$\mathbb{P}^{\text{pind}} = \mathbb{I} - \frac{1}{2} (\mathbf{1} \otimes \mathbf{1}) + \frac{1}{2} (\mathbf{A} \otimes \mathbf{1} + \mathbf{1} \otimes \mathbf{A}) - \frac{3}{2} (\mathbf{A} \otimes \mathbf{A}) \quad (3.32)$$

and $(\mathbb{P}_{\mathbf{A}}^{\text{pind}})_{ijkl} := A_{im} \mathbb{P}_{mjkl}^{\text{pind}} + A_{mj} \mathbb{P}_{imkl}^{\text{pind}}$.

\mathbf{A}^{dev} is the deviator of the structural tensor \mathbf{A} , \mathbb{A} is the constant bending tensor and \mathbf{B} is the first derivative of the quadratic yield locus. Thus, the yield function eq.3.30 reads in the more general form:

$$f = \frac{1}{2} \boldsymbol{\sigma} : \mathbb{A} : \boldsymbol{\sigma} + \mathbf{B} : \boldsymbol{\sigma} - 1 \quad (3.33)$$

an associated flow rule is used for the transversely isotropic yield surface, because its theory is less difficult and it is numerically more stable. The associated flow direction is given by the partial derivative of the yield surface with respect to the plasticity inducing stresses

$$\mathbf{m}_{n+1} = \partial f^{n+1} / \partial \boldsymbol{\sigma}_{n+1}^{\text{pind}}. \quad (3.34)$$

It is possible that volume increases under hydrostatic compression, which is not physically reasonable. However, compared to the isotropic flow rule, this effect is smaller in the transversely isotropic flow rule. The isotropic yield function increases monotonically with increasing hydrostatic compression, because yielding is permitted under hydrostatic compression, thus volume would increase under all stress states if associated flow is applied. However, the transversely isotropic yield surface does not contain hydrostatic stress states, because the fibre-parallel stresses are not contained in the invariants and thus does not increase monotonically with increasing invariant I_3 , that stands for hydrostatic compression. The illustration of the transversely isotropic yield function in Figure 3.4 shows that the volume change is incorrect only under mixed shear and hydrostatic compression, where the yield function has a negative gradient. Therefore, the volume increase is delimited to a small sector in the transversely isotropic flow rule, where volume change is small anyway. Thus, this error is neglected here.

3.2.3 Hardening Formulation

To determine the four material parameters α_1 , α_2 , α_3 and α_{32} of the yield function, four stress-strain curves are needed, which can either be provided by experiments or by micromechanical computations. From the stress-strain curves hardening curves are generated by subtracting the elastic strains in the manner of eq. 3.3.

This process requires a parameter identification described in section 3.3. The material tests and their representation in stress space are:

- simple shear in the plane perpendicular to the fibre (transverse shear)

$$\boldsymbol{\sigma} = \text{dev } \boldsymbol{\sigma} = \boldsymbol{\sigma}^{\text{pind}} = \begin{bmatrix} 0 & \sigma_{Y,\perp\perp} & 0 \\ \sigma_{Y,\perp\perp} & 0 & 0 \\ 0 & 0 & 0 \end{bmatrix}, \quad \mathbf{a} = \begin{bmatrix} 0 \\ 0 \\ 1 \end{bmatrix}$$

$$I_1 = \sigma_{Y,\perp\perp}^2, \quad I_2 = 0, \quad I_3 = 0$$

$$\rightsquigarrow f = \alpha_1 \sigma_{Y,\perp\perp}^2 - 1 = 0$$

$\alpha_1 = 1/\sigma_{Y,\perp\perp}^2$

(3.35)

- simple shear in the fibre plane (in plane shear)

$$\boldsymbol{\sigma} = \text{dev } \boldsymbol{\sigma} = \boldsymbol{\sigma}^{\text{pind}} = \begin{bmatrix} 0 & \sigma_{Y,\perp\parallel} & 0 \\ \sigma_{Y,\perp\parallel} & 0 & 0 \\ 0 & 0 & 0 \end{bmatrix}, \quad \mathbf{a} = \begin{bmatrix} 1 \\ 0 \\ 0 \end{bmatrix}$$

$$I_1 = 0, \quad I_2 = \sigma_{Y,\perp\parallel}^2, \quad I_3 = 0$$

$$\rightsquigarrow f = \alpha_2 \sigma_{Y,\perp\parallel}^2 - 1 = 0$$

$\alpha_2 := 1/\sigma_{Y,\perp\parallel}^2$

(3.36)

- uniaxial tension and uniaxial compression perpendicular to the fibre

$$\boldsymbol{\sigma} = \begin{bmatrix} 0 & 0 & 0 \\ 0 & 0 & 0 \\ 0 & 0 & \sigma_{Y,\perp} \end{bmatrix}, \quad \mathbf{a} = \begin{bmatrix} 1 \\ 0 \\ 0 \end{bmatrix}$$

$$I_1 = \frac{\sigma_{Y,\perp}^2}{4}, \quad I_2 = 0, \quad I_3 = \sigma_{Y,\perp}$$

$$\rightsquigarrow f = \alpha_1 \frac{\sigma_{Y,\perp}^2}{4} + \alpha_3 \sigma_{Y,\perp} + \alpha_{23} (\sigma_{Y,\perp})^2 - 1 = 0$$

The parameter α_1 is known from the first material test (transverse shear), therefore two parameters α_3 and α_{32} remain to be determined. Inserting the yield stresses from uniaxial tension $\sigma_{Y,\perp}^t$ and uniaxial compression $\sigma_{Y,\perp}^c$ for $\sigma_{Y,\perp}$ in the yield function

leads to an equation system with two equations and two unknowns from which the parameters α_3 and α_{32} can be obtained :

$$\alpha_{32} := \frac{\frac{1}{\sigma_{Y,\perp}^t} - \frac{1}{\sigma_{Y,\perp}^c} - \frac{\alpha_1}{4}(\sigma_{Y,\perp}^t - \sigma_{Y,\perp}^c)}{\sigma_{Y,\perp}^t - \sigma_{Y,\perp}^c} \quad (3.37)$$

$$\alpha_3 := \frac{1}{\sigma_{Y,\perp}^t} - \frac{\alpha_1}{4}\sigma_{Y,\perp}^t - \alpha_{32}\sigma_{Y,\perp}^t \quad (3.38)$$

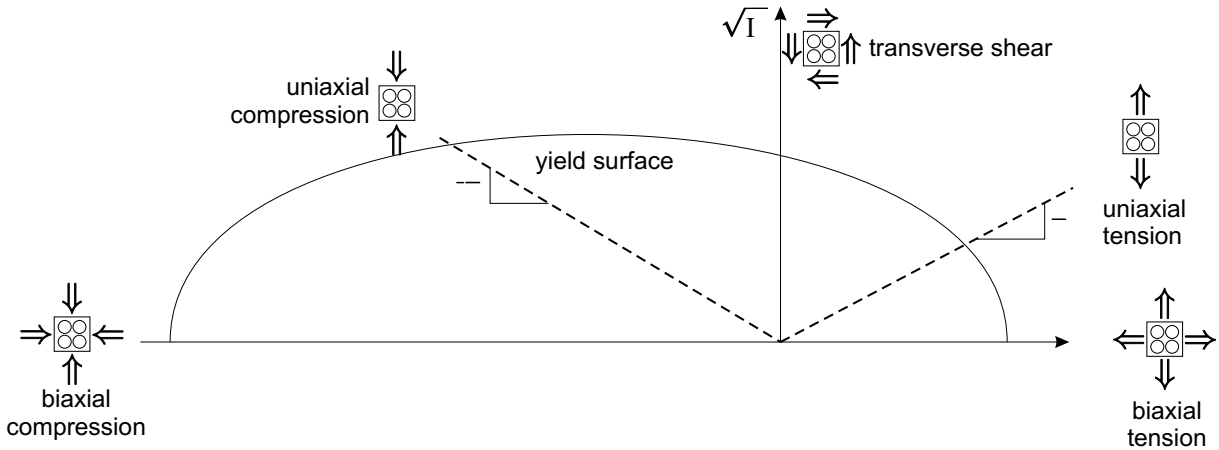


Figure 3.4: Yield and failure surface of the transversely isotropic material model in $\sqrt{I_1}$ - I_3 -invariant-plane

In analogy to the σ_{vm} - p -invariant-plane for the isotropic yield locus, the transversely isotropic yield locus can be illustrated in an invariant plane of the first and third invariant I_1 and I_3 . For convenience and for a better comparability with the invariant plane for the isotropic model, the abscissa is the third invariant I_3 and the ordinate is the square root of the first invariant I_1 , see fig. 3.4. To clarify this representation, the stress states for uniaxial, biaxial and pure shear loadings are indicated in fig. 3.4. Triaxial stress states are not represented in this invariant plane, because stresses in fibre direction are assumed to not induce yielding and so the projections of the stress tensor onto the preferred direction are not reflected in the invariants I_1 and I_3 . As illustrated in fig. 3.4, the ordinate corresponds to a pure transversal shear stress state, the abscissa represents biaxial stress states and the two dotted lines with a slope of 0.5 and -0.5 mark uniaxial tension and compression loading states. The stress states and their representation in the I_3 - $\sqrt{I_1}$ -plane are:

- transverse shear loading:

$$I_1 = \sigma_{Y,\perp\perp}^2, \quad I_3 = 0$$

- uniaxial loading:

$$I_1 = \frac{(\sigma_{Y,\perp})^2}{4}, \quad I_3 = \sigma_{Y,\perp}$$

- biaxial loading:

$$I_1 = 0, \quad I_3 = 2\sigma_{Y,biax}$$

3.3 Parameter Identification

The numerical stability of the presented plasticity algorithms is highly dependent on the quality of the hardening curves provided. It must be assured that the yield surface widens monotonically, because the algorithm does not converge for decreasing plastic stress with increasing plastic strains. Besides, this effect is not physically plausible. Experimental stress-strain curves do not always meet this criterion, oscillations are often incorporated. Thus, firstly these curves have to be smoothed out for the algorithm. Secondly, the so-called linear elastic region in the beginning is mostly rather non-linear, therefore it is not exactly clear where hardening begins. The choice of the starting point for hardening in each used stress-strain curve is influencing the yield surface. Each starting points has to be chosen in correspondence with the other ones to ensure that the yield surface is widening monotonically for each stress state.

For the isotropic yield surface, the following conditions must be fulfilled for each equivalent plastic strain:

$$\left. \begin{array}{l} a_0 > 0 \\ a_1 < 0 \\ \Delta a_0 > 0 \\ -\frac{\Delta a_0}{\Delta a_1} \geq -\frac{a_0}{a_1} \end{array} \right\} \quad (3.39)$$

The result of the parameter identification procedure can be seen in Figure 3.5. It shows the stress-strain curves under uniaxial tension and simple shear of epoxy resin RIM 135 from tests compared to the outcome of the parameter identification.

Figure 3.6 shows a cut through the transversely isotropic yield surface for $I_2 = 0$ and its evolution with increasing equivalent plastic strain. This cut equals the isotropic σ_{vm} - p -plane as far as possible, with $\sqrt{I_1}$ being representative for deviatoric stresses and I_3 for hydrostatic stresses. Different stress states, from biaxial tension to biaxial compression, are marked with different colors. It can be seen that the yield surface widens monotonically, as desired, and that the hardening modulus is higher under compression than under tension and shear.

It should be avoided to use ideally plastic behaviour, because it leads to localization of plasticity in one element. If plastic strains are then considered as a measure for damage initiation, which is a very common assumption, a mesh dependency of failure occurs that does not converge for refined meshes. Compared to global strain of the whole model local plastic strains in smaller elements are much higher and thus damage is initiated much earlier. This localization and the following mesh dependency do not occur if a hardening modulus is present, see also Figure 4.6. Besides, in (geometrically non-linear) three-dimensional simulations ideally plastic behaviour can lead to material failure. Imagine a

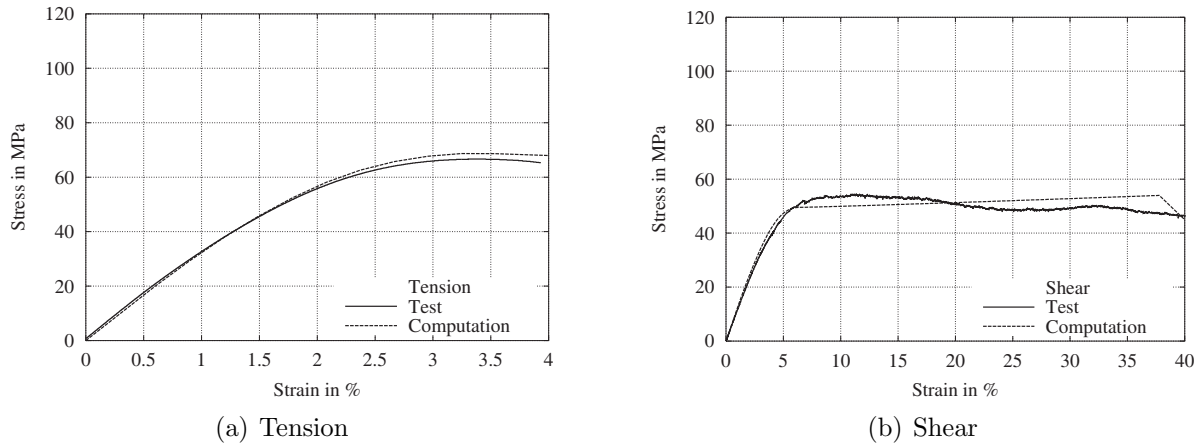


Figure 3.5: Stress-strain curves of epoxy matrix RIM 135 from tests and curves used in computation

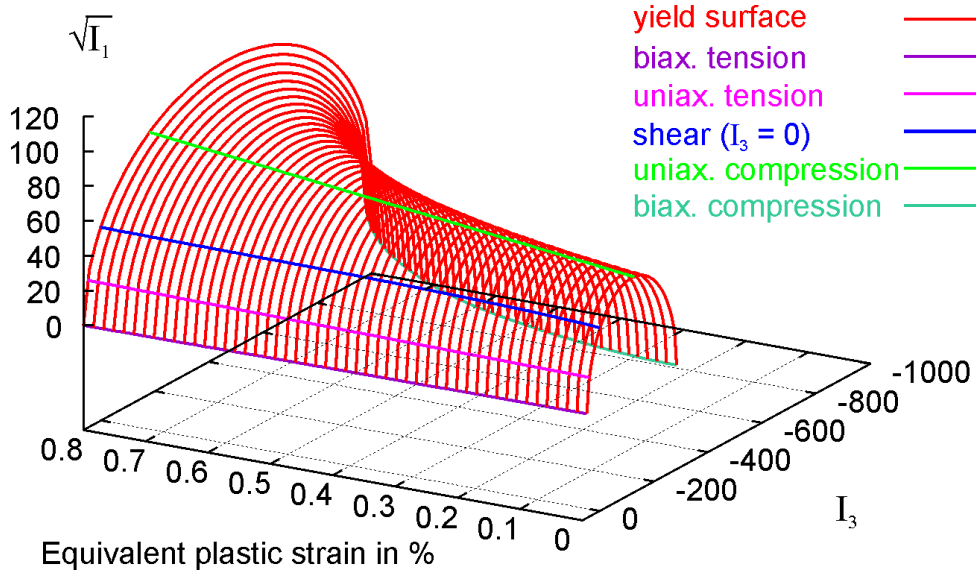


Figure 3.6: Widening of transversely isotropic yield surface with increasing equivalent plastic strain

tension rod discretized with one volume element. While the material yields, the element lengthens in tensile direction, but due to Poisson's effect its area decreases. Therefore, the applied tensile force goes to zero, because it is the product of the constant yield stress multiplied with the vanishing cross section. Thus, to avoid these effects, plastic hardening should always be present.

Table 3.1: elasticity constants for transversely isotropic elasticity

- symmetry of the elasticity tensor:

$$\frac{\nu_{12}}{E_{22}} = \frac{\nu_{21}}{E_{11}}; \quad \frac{\nu_{13}}{E_{33}} = \frac{\nu_{31}}{E_{11}}; \quad \frac{\nu_{23}}{E_{33}} = \frac{\nu_{32}}{E_{22}}$$
- constants of invariant formulation:

$$\lambda = E_{22}(\nu_{23} + \nu_{31}\nu_{13})/D$$

$$\alpha = E_{22}[\nu_{31}(1 + \nu_{32} - \nu_{13}) - \nu_{32}]/D$$

$$\beta = E_{11}(1 - \nu_{32}\nu_{23})/D + E_{22}[1 - \nu_{21}[\nu_{12} + 2(1 + \nu_{23})]]/D - 4\mu_{12}$$

$$\mu_l = \mu_{12}$$

$$\mu_t = \mu_{23}$$

$$D = 1 - \nu_{32}^2 - 2\nu_{13}\nu_{31} - 2\nu_{32}\nu_{31}\nu_{13}$$
- engineering constants:

$$E_{22} = E_{33}, \quad \nu_{23} = \nu_{32}, \quad \nu_{12} = \nu_{13}, \quad \nu_{21} = \nu_{31}, \quad \mu_{12} = \mu_{13}$$

$$E_{11} = -(\lambda\mu_t - 4\lambda\mu_l - \lambda\beta - 4\alpha\mu_t + 2\mu_t^2 - \beta\mu_t - 4\mu_l\mu_t + \alpha^2)/(\lambda + \mu_t)$$

$$E_{22} = -4\mu_t(\lambda\mu_t - 4\mu_l\lambda - \beta\lambda + 2\mu_t^2 - \beta\mu_t - 2\alpha\mu_t - 4\mu_t\mu_l + \alpha^2)/D_t$$

$$\nu_{12} = 2\mu_t(\lambda + \alpha)/D_t$$

$$\nu_{21} = (\lambda + \alpha)/(2\lambda + 2\mu_t)$$

$$\nu_{23} = -(\alpha^2 + 2\lambda\mu_t - \beta\lambda - 4\mu_l\lambda)/D_t$$

$$\mu_{12} = \mu_l$$

$$\mu_{23} = \mu_t$$

$$D_t = 4\mu_l\lambda + \beta\lambda - 4\mu_t^2 + 4\mu_t\alpha + 2\beta\mu_t + 8\mu_l\mu_t - \alpha^2$$

4 Failure Criteria and Softening Formulations

In this chapter failure criteria and softening formulations for epoxy resin, UD- and textile composites are presented. A failure criterion, consisting of one or more failure conditions, determines damage initiation, i.e. the moment when failure of a material starts. The softening formulation describes the following failure of the material with softening.

Material softening leads to numerical instabilities that have to be accounted for. Wherever a crack occurs, it localizes in a certain region, in reality as well as in simulation. In reality each material has its characteristic crack width, that does mainly depend on the homogeneity of the material, but in a simulation a crack localizes in only one element, if no precautions are taken. Thus, a mesh-dependency occurs, i.e. the simulation does not converge with a refined mesh. To avoid this, fracture energy regularization according to Hillerborg, Modeer, and Petersson (1976) is used in the softening formulations presented in this work.

4.1 Isotropic Failure Criterion and Softening Formulation for Epoxy Resin

Failure of epoxy resin exhibits one main trait, pressure dependency. Strength under compression is usually much higher than under tension. Therefore, a failure criterion based on the invariants hydrostatic pressure p and VON MISES stress σ_{vm} is presented here, analogous to the material model described in section 3.1. Fractography has shown that epoxy resin has two failure modes, ductile shear failure and brittle tensile failure. The quantification of these modes is rather difficult and not always clear, sometimes a mixture of both might occur. Therefore, the presented criterion consists of two phenomenologically derived failure conditions. To describe the softening and failure behaviour of epoxy resin, an isotropic damage model is implemented in the material model. The material stiffness degradation is controlled by a scalar damage parameter d .

4.1.1 Failure Criterion

Fiedler et al. (2001) propose a quadratic failure surface, that is defined over uniaxial tensile and compressive strength. The parabolic failure surface opens in direction of hydrostatic compression, i.e. no failure occurs under hydrostatic compression. To regard

the material strength under pure shear as well, the failure surface is split into two parts in this work, as illustrated in fig. 4.1 and fig. 3.1. Therefore, all input strengths can be used directly and a least-square fit of three input strengths on two parabolic parameters is avoided. In the region of hydrostatic tension, where brittle tensile failure is assumed the failure surface has a formulation in analogy to the yield surface:

$$r = \sigma_{vm}^2 - b_0 - b_1 p \text{ for } p > 0. \quad (4.1)$$

The failure criterion is fulfilled for $r = 0$ and stiffness degradation starts until the material finally fails. The parameters b_0 and b_1 are obtained in the same manner as the parameters a_0 and a_1 for the yield function eq. 3.4). Therefore, the material strengths of uniaxial tension R^t and of shear R^s have to be inserted instead of the yield stresses in 3.4. In the region of hydrostatic compression, where ductile shear failure takes place, a linear failure surface, connecting the uniaxial compressive strengths R^c and the shear strength R^s in the σ_{vm} - p -invariant-plane, is assumed (see fig. 3.1):

$$r = \sigma_{vm} - b_2 - b_3 p \text{ for } p < 0. \quad (4.2)$$

The parameters b_0, b_1, b_2 and b_3 are obtained from

$$b_0 = (R^s)^2 \quad (4.3)$$

$$b_1 = 3 \frac{(R^s)^2 - (R^c)^2}{R^c} \quad (4.4)$$

$$b_2 = R^s \quad (4.5)$$

$$b_3 = 3 \frac{R^s - R^c}{R^c}. \quad (4.6)$$

4.1.2 Damage Evolution and Stiffness Degradation

The damage evolution law describes the rate of degradation of the material stiffness once the corresponding initiation criterion has been reached. A scalar damage variable d is introduced to control the stiffness degradation Lemaitre and Chaboche (1988). At any given time during the analysis, the stress tensor in the material is given by the scalar damage equation

$$\boldsymbol{\sigma} = (1 - d)\boldsymbol{\sigma}_{eff}, \quad (4.7)$$

where d is the overall damage variable and $\boldsymbol{\sigma}_{eff}$ is the effective, i.e. undamaged, stress tensor computed in the current increment. If the failure surface is achieved at any stress state, the yield surface is forced to remain constant by setting the hardening modula to zero and stiffness degradation, controlled by the scalar damage variable d , starts until the material has lost its load-carrying capacity ($d = 1$), see fig. 4.1. In numerical analysis, then the concerning elements are removed from the mesh.

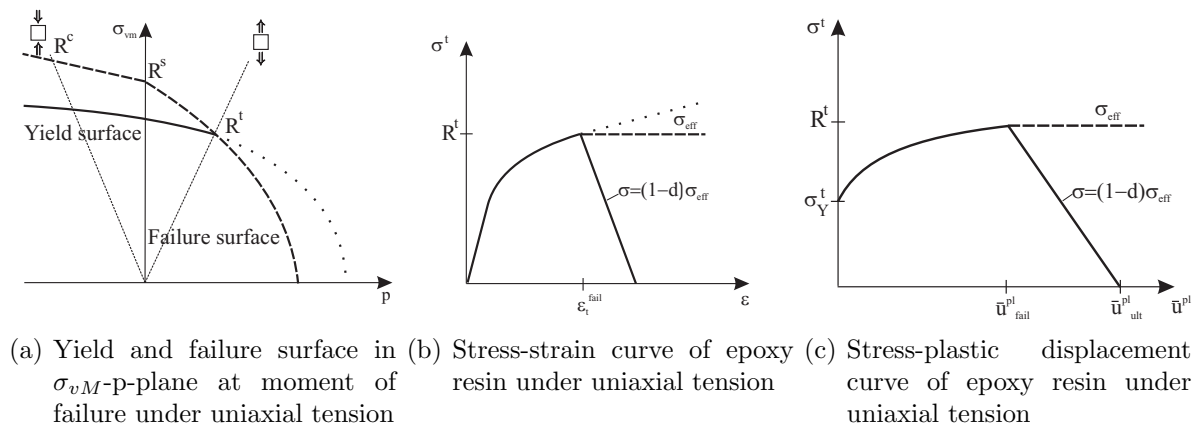


Figure 4.1: Damage formulation

The exact function of d is dependent on material as well as the scale of application. Usually a macromechanical damage evolution that incorporates the in-situ effect is required for the simulation of composite materials. Due to the in-situ effect embedded lamina do not reach a final damage of one, or complete damage respectively, see e.g. Kumar and Talreja (2003) or Puck (1996). However, in this work the evolution of mesomechanical cracks shall be described, which are not investigated experimentally due to its small size. Therefore, a common assumptions a exponential or linear functions, see Figure 4.2 are used here. A fracture energy is used to determine its quantitative gradient in this work.

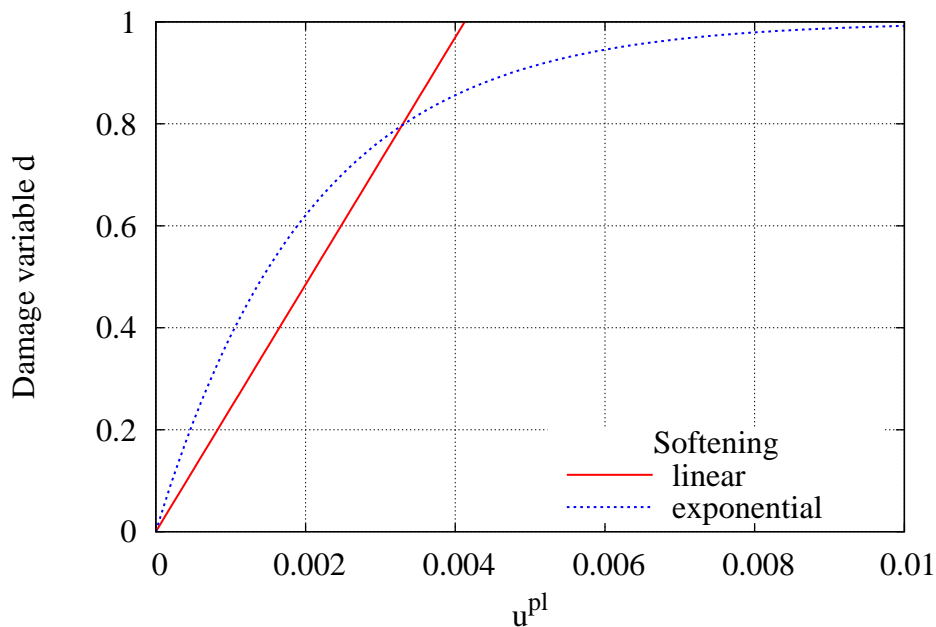


Figure 4.2: Evolution of damage for linear and exponential softening

4.1.3 Fracture Energy Regularization

Softening material behaviour, which results macroscopically in a loss of material stiffness with adjacent failure, is preceded by the initiation and accumulation of microscopical defects such as cracks, micro-pores, shear-bands or crazes, see Lemaitre and Chaboche (1988). The initiation and accumulation of such defects are a matter of local defects and are restricted to a local zone, whose size depends on the material. Lemaitre and Desmorat (2005) give the width of the localizing zone, in which shear-bands or crazes develop, as a material constant, see Table 4.1.

Table 4.1: Characteristic internal length L_i of different materials

material	crack width
Light alloys	0.2 to 0.5 mm
Steel	0.2 to 0.5 mm
Ceramics	0.1 to 1 mm
FRP	0.5 to 1 mm
Concrete	10 to 100 mm

When material softening occurs, the stress-strain relationship no longer accurately represents the material's behaviour. Continuing to use the stress-strain relation introduces a strong mesh dependency based on strain localization, such that the energy dissipated decreases as the mesh is refined. Figure 4.3 illustrates this effect for the example of a simple tensile rod with different element sizes. Damage localizes in a single element, depicted by a lighter color, all other elements remain undamaged. If a stress-strain relation is used to describe the softening of the element, the size of the element influences the process and ultimate failure occurs earlier in the global stress-strain curve for higher mesh refinement. This effect can be overcome, when a stress-displacement response is used instead of a stress-strain response.

The fracture energy proposal of Hillerborg et al. (1976) is used to reduce mesh dependency by creating a stress-displacement response after damage is initiated. Using brittle fracture concepts, Hillerborg et al. (1976) define the energy G_f required to open a unit area of crack as a material parameter. The introduction of a characteristic internal length L_i , which is a measure for the size of the localized area, the softening response after damage initiation is characterized by a stress-displacement response rather than a stress-strain response. The crack localization area is characterized by multiple microcracks that dissipate energy independently from each other until some of them coalesce into the macrocrack. It is important to note that the fracture energy or strain energy release rates G that are determined in experimental tests, e.g. double-cantilever beam or end-notch flexure test, are therefore valid only for a macrocrack, including several microcracks, but not for the microcracks themselves. The energy G_f required to open a unit area of crack, is

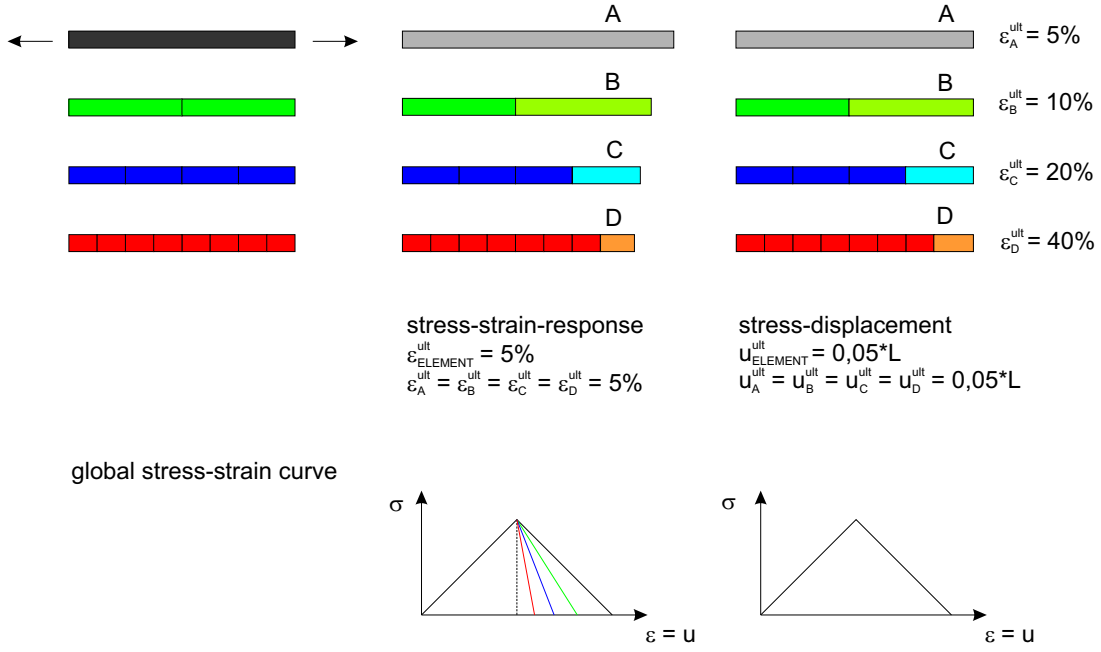


Figure 4.3: Mesh-dependency and regularization of softening

$$G_f = \int_{\bar{\epsilon}_{fail}^{pl}}^{\bar{\epsilon}_{ult}^{pl}} L_i \sigma_Y d\bar{\epsilon}^{pl} = \int_{\bar{u}_{fail}^{pl}}^{\bar{u}_{ult}^{pl}} \sigma_Y d\bar{u}^{pl} . \quad (4.8)$$

The implementation of this stress-displacement concept in a finite element model requires the definition of a characteristic element length L_e associated with an integration point. The fracture energy is then given as

$$G_f = \int_{\bar{\epsilon}_{fail}^{pl}}^{\bar{\epsilon}_{ult}^{pl}} L_e \sigma_Y d\bar{\epsilon}^{pl} = \int_{\bar{u}_{fail}^{pl}}^{\bar{u}_{ult}^{pl}} \sigma_Y d\bar{u}^{pl} . \quad (4.9)$$

This expression introduces the definition of the equivalent plastic displacement \bar{u}_p as the fracture work conjugate of the yield stress σ_y after the onset of damage:

$$\bar{u}^{pl} = L_e \bar{\epsilon}^{pl} . \quad (4.10)$$

The definition of the characteristic length L_e is based on the element geometry. For solid elements the cube root of the element volume is used. This definition of the characteristic length is chosen because the direction, in which fracture occurs, is not known in advance. Therefore, elements with large aspect ratios will have rather different behaviour depending on the direction in which the crack evolves. This leads to a mesh sensitivity of the simulation results, see section 4.1.5.1. To avoid this problem voxel-elements with an aspect ratio of unity should be used, see section 4.1.5.

The introduction of the characteristic element edge length L_e means, that occurring localized strains are "smeared" or distributed over the particular element width.

To determine \bar{u}_{ult}^{pl} not only the value of the dissipated fracture energy is needed, but also the curvature in the softening regime. As mentioned above the exact curvature is not known, but commonly assumed to be linear or exponential. For the linear case the equivalent plastic displacement at ultimate failure

$$\bar{u}_{ult}^{pl} = \frac{2G_f}{\sigma_Y} + \bar{u}_{fail}^{pl} \quad (4.11)$$

is needed for the determination of the damage variable

$$d_{lin} = \frac{\bar{u}^{pl} - \bar{u}_{fail}^{pl}}{\bar{u}_{ult}^{pl} - \bar{u}_{fail}^{pl}} . \quad (4.12)$$

In the case of exponential softening the damage variable can be determined directly

$$d_{exp} = 1 - e^{-\frac{\sigma_Y}{G_f} * (\bar{u}^{pl} - \bar{u}_{fail}^{pl})} . \quad (4.13)$$

The damage variable approaches ultimate failure asymptotically, therefore $d = 0.9999$ is taken to be ultimate failure. Both functions for d are shown in Figure 4.2. For regularization it is important that

$$\int_0^\infty 1 - d_{exp} = \int_0^1 1 - d_{lin} . \quad (4.14)$$

In both cases plastic displacements that occurred before failure \bar{u}_{fail}^{pl} are subtracted, because it is avoided that plasticity localizes in only one element, see section 3.3. Figure 4.4 shows how the fracture energy regularization formulation works, if plastic deformations occur in the model. Thus, assuming that plasticity before failure is mesh-independent, it must not influence the regularization mechanism to alleviate mesh-dependency of failure.

Figure 4.5 shows the influence of different curvatures in the softening of the epoxy resin on the stress-strain curves for a micromechanical unit cell, described in chapter 6 under tension and compression. Curves are given for

1. no damage at all, only plastic hardening,
2. ideally plastic behaviour after failure criterion is fulfilled,
3. linear softening and
4. exponential softening.

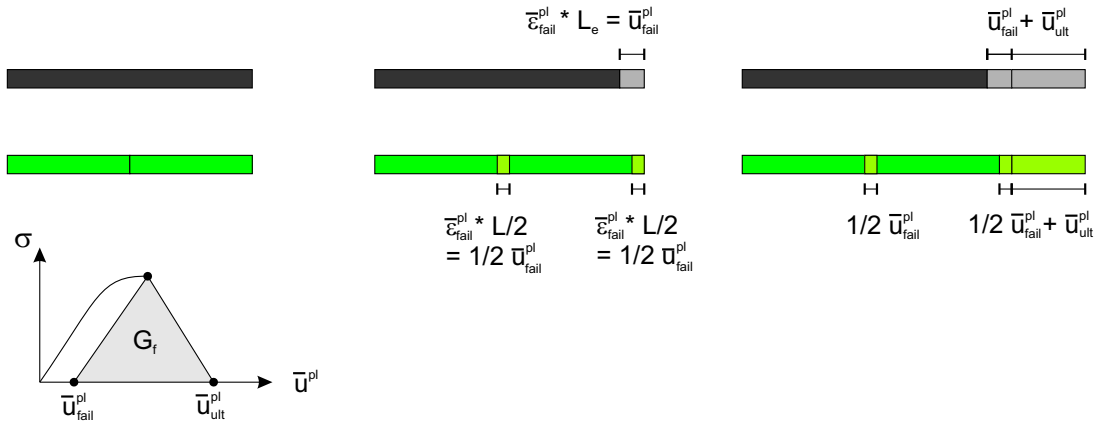


Figure 4.4: Determination of strain energy release rate/fracture energy G_f

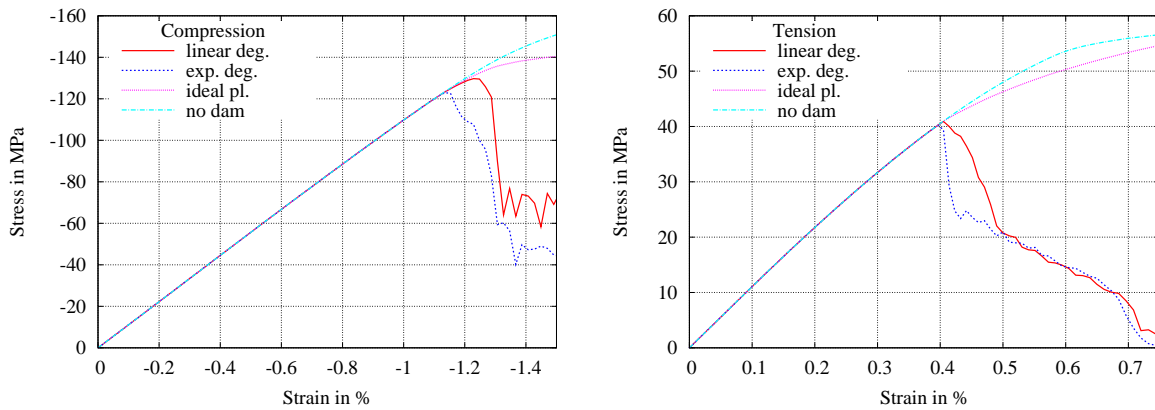


Figure 4.5: Stress-strain curves of micromechanical unit cell under tension and compression. Influence of softening on unit cell.

The first two curves are given as a comparison and to show the undamaged behaviour of the unit cell. As described above the damage is applied on ideally plastic behaviour. Generally, the exponential behaviour leads to an earlier failure of the unit cell, but this effect is more apparent under compression. The explanation for the earlier failure in general is the greater softening in the beginning of the exponential curve.

The reason for the greater effect of softening curvature under compression can be seen in Figures 4.6 and 4.7. There, the damage or, for the computations without damage, the equivalent plastic strain in the unit cell are shown. Under tension the "crack" localizes nearly in the same way, but under compression the localization zone is different depending on the softening curvature. Linear softening leads to a longer crack, at one point it is deviated from the path under exponential softening, obviously because the damage in some elements does not evolve fast enough. A longer crack leads to an higher energy dissipation overall and, thus, to a higher strength. However, the overall differences between exponential and linear softening are rather small, because the fracture energy consumed by the cracks are identical.

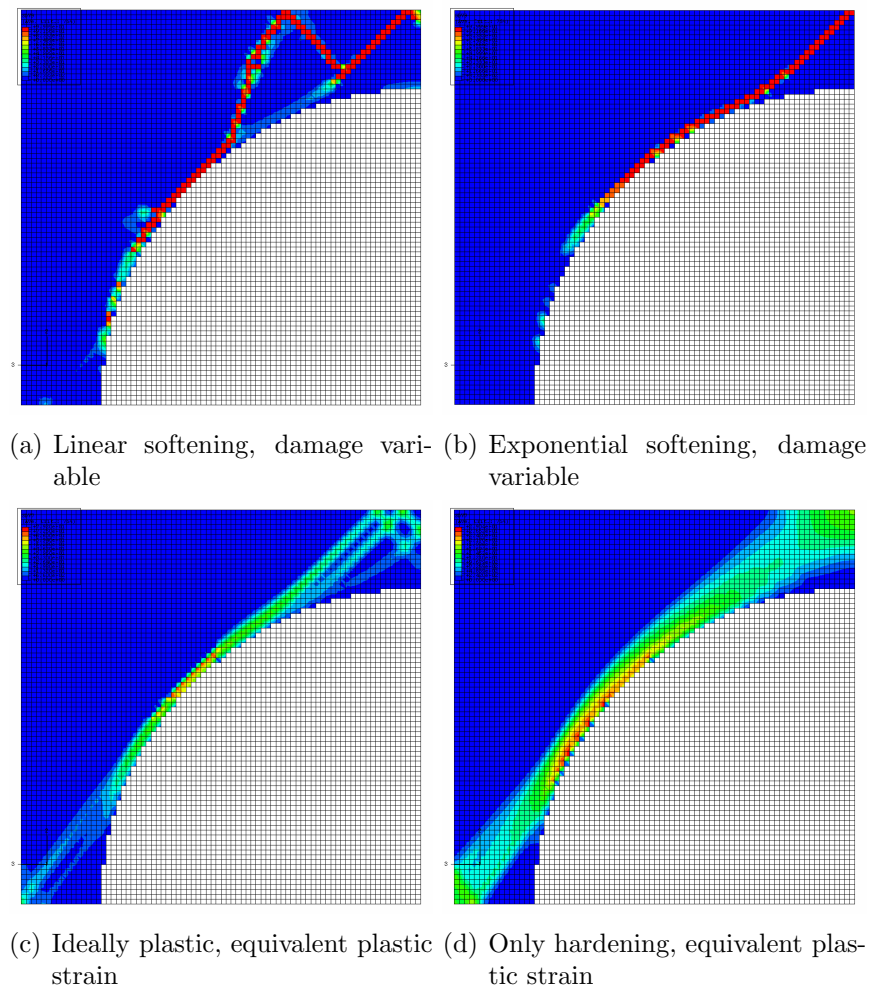


Figure 4.6: Influence of softening curvature on damage evolution in micromechanical unit cell under compression.

In Figures 4.6 and 4.7 it can also be seen why ideally plastic behaviour leads to mesh-dependent results. The localization zone, where plastic deformations occur, is just one element thick and remains one element thick for a refined mesh. Thus, the local strains are dependent on the element size and it is not possible to get reasonable result out of a maximum strain criterion. When further plastic hardening still takes place, the localized plastic zone is much wider and the mesh dependency is less pronounced. Under tension the hardening modulus is very small, therefore this effect can hardly be seen in Figure 4.7 and the differences in the stress-strain curves in Figure 4.5 under ideally plastic behaviour and under plastic hardening.

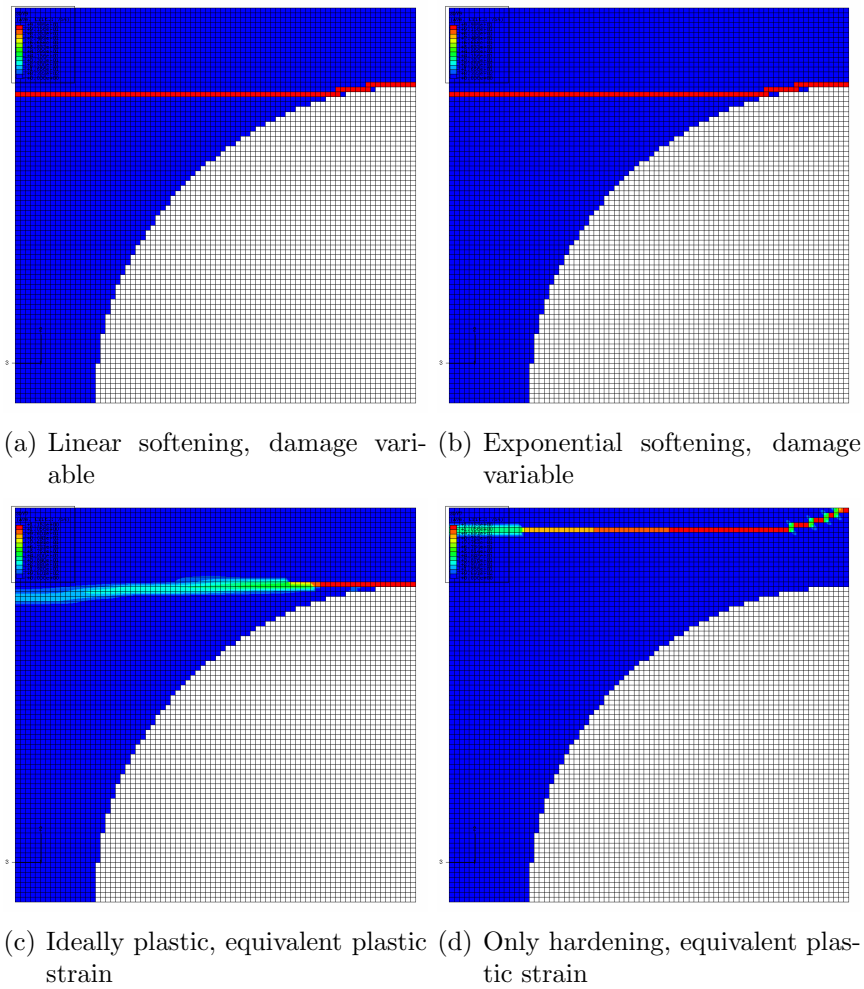


Figure 4.7: Influence of softening curvature on damage evolution in micromechanical unit cell under tension.

4.1.4 Tension Rod Regularization

In order to demonstrate the functionality of the presented fracture energy regularization a tension rod is computed with different mesh refinements. The dimensions of the rod are $2 \times 1 \times 1$ mm, it is discretized with $2 \times 1 \times 1$, $4 \times 2 \times 2$ and $8 \times 4 \times 4$ volume elements, respectively, it is loaded displacement-driven in 1-direction. Figure 4.8 gives the load-displacement curves of the tension rod dependent on the discretizations. Prerequisite for the regularization formulation to work is that damage occurs only in one element (row), which is fulfilled for all discretizations. It can be seen that the regularization formulation generally works very well. The curves do not match exactly, because of Poisson's effect, that has a considerable influence at higher mesh refinement, because it forces the elements to adopt shear deformations. However, this small inaccuracy is negligible.

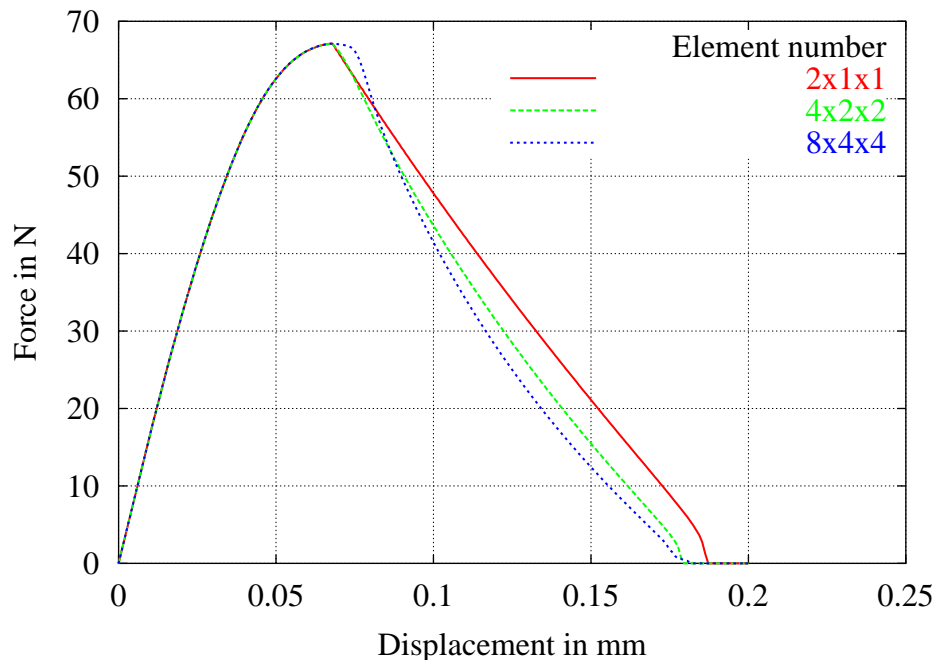


Figure 4.8: Load-displacement curve of tension rod for different mesh refinement

4.1.5 Voxel Discretization

Conventional modelling leads to a number of irregular elements, in particular for a mesomechanical unit cell of a textile composite, but also for the micromechanical unit cell. In combination with the strain energy based regularization irregular elements lead to a mesh-dependent solution, see Ernst, Hühne, and Rolfes (2006), because the regularization requires elements with an aspect ratio of unity. To avoid this drawback of irregular elements, the unit cells shown here are meshed with voxel elements, meaning "volume pixel". They have an aspect ratio of one, hence the geometry can only be approximated because the mesh is regular.

Another advantage of the approximate meshing is that it simplifies the discretization of complicated geometries in the mesomechanical unit cell and the application of periodic boundary conditions. For periodic boundary conditions it is an enormous simplification to have matching opposite faces of the RVE, because a node-by-node connection can be established, see section 5.2. Gunnion (2004) has shown that the voxel method is well suited to determine stiffness of textile composites.

Disadvantage of the voxel mesh are the singularities that occur at the boundary between two materials with different stiffness in the form of stress peaks. However, these stress peaks can be smoothed out by use of plastic material behaviour, although a distortion remains. Compared to a conventional mesh, a voxel mesh usually contains more elements, but in an explicit analysis the size of the smallest element is rather more important than the element number, because it determines the critical time step.

4.1.5.1 Influence of Irregular Elements

By the example of the square micromechanical unit cell, see chapter 6 the influence of irregular elements in a conventional mesh shall be demonstrated here. The interface between fibre and matrix is modelled perfectly in a conventional mesh, see Fig. 4.9. Two meshes are shown, in Figure 4.9(a) the original mesh generated by ABAQUS and in Figure 4.9(b) an altered mesh that has only elements with an aspect ratio close to one at the interface between fibre and matrix. The influence of the irregular elements that incur a mesh dependency is indicated by the different damage evolution in the meshes shown in Fig. 4.9. In Fig. 4.9(a) it can easily be seen that the irregular elements in the middle of the original mesh act as “crack-stoppers” and deviate the crack away from the interface. In the altered mesh the damage evolutes along the interface. The reason for this behaviour is that the characteristic element length L_E , see Sec. 4.1, is an isotropic value, determined for each element as the cubic root of its volume. It is taken for each direction and multiplied with the strains, see Eq. 4.10, hence irregular elements degrade faster in one direction than in others.

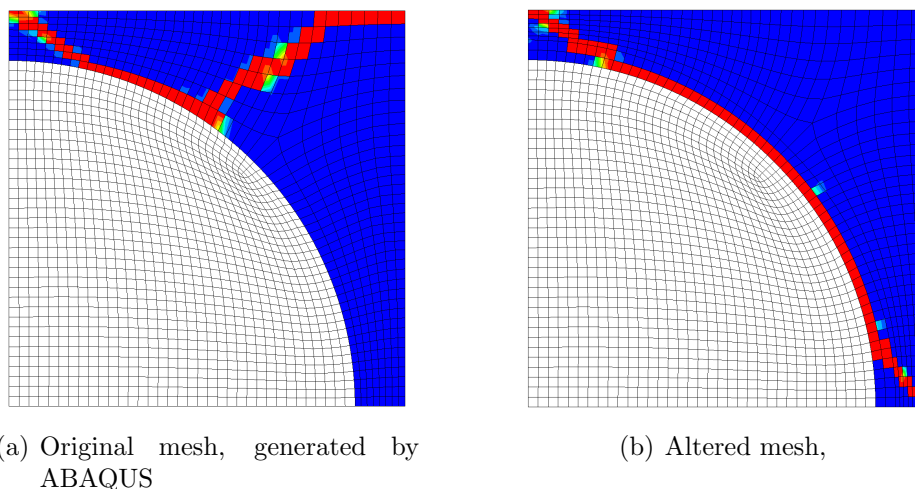


Figure 4.9: Damage evolution in conventional mesh dependent on mesh

Whilst for this rather simple geometry the mesh-dependency comes out clearly, it is quite cumbersome to prevent it by manually generating regular elements in sensitive areas. Furthermore, it is not clear which areas are sensitive and require regular meshing, neither before the simulation, nor after the simulation, because the mesh influences the result of the simulation drastically. For more complicated textile fibre geometries it is almost impossible to avoid irregular elements in sensitive areas. In a voxel mesh this kind of mesh dependency does not occur, therefore it is very useful for application together with the fracture energy approach. Figure 4.10 shows the damage evolution in the same load case as in Figure 4.9

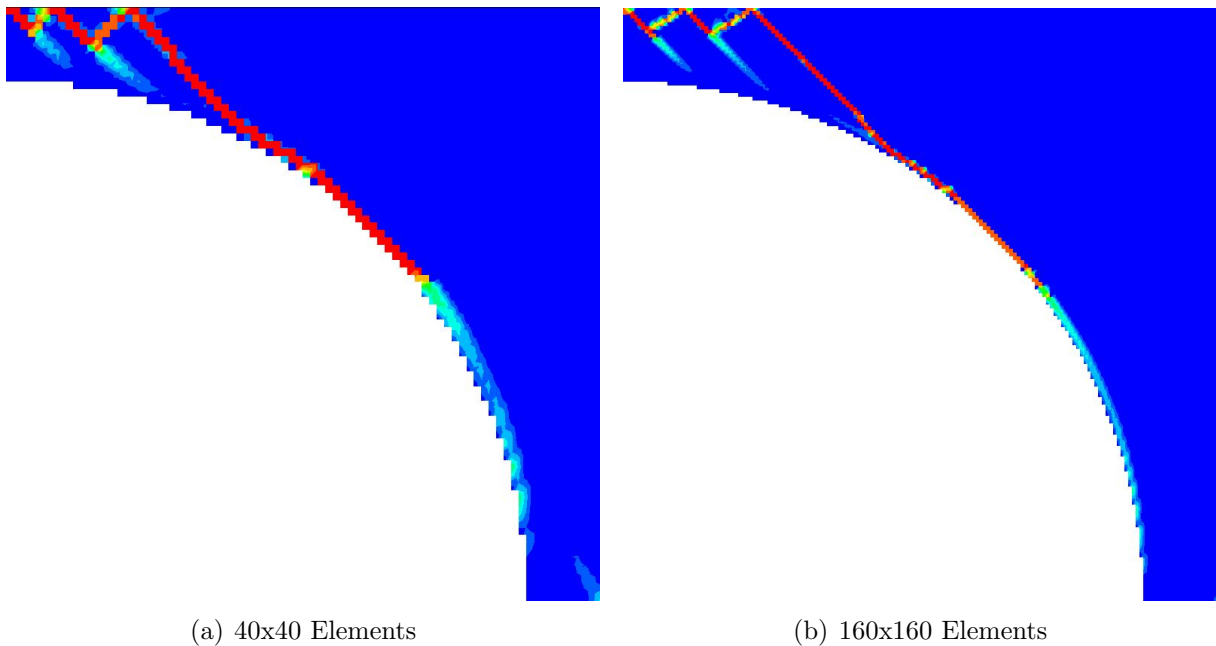
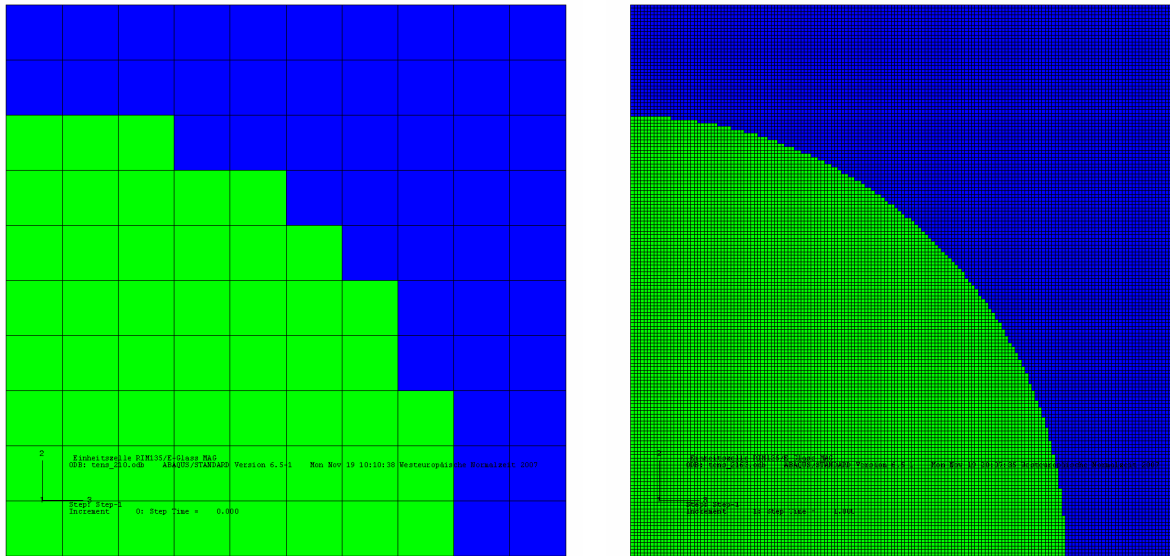


Figure 4.10: Damage evolution under compression

4.1.5.2 Convergence of Voxel-Approach

The convergence of voxel-meshed square unit cells has been tested under transverse tension. Discretization ranged from 10x10 elements up to 163x163 elements, which is shown in fig. 4.11.

The transverse stiffness predicted of the voxel-unit-cell is mainly influenced by two effects, the volume fraction realized in the model and the number of elements used. Especially in coarse meshes it is not always possible to generate the desired volume fraction, an uneven element number, for example, will never give a volume fraction of $v_f = 0.5$. Figure 4.12 shows the deviation of transverse stiffness of coarser meshes against the finest mesh used. The approximate meshing algorithm does not always allow for an exact realization of the targeted volume fraction, therefore only meshes with a volume fraction of exactly 50% have been selected and displayed.



(a) 10x10 Elements

(b) 163x163 Elements

Figure 4.11: Discretization of square unit cell

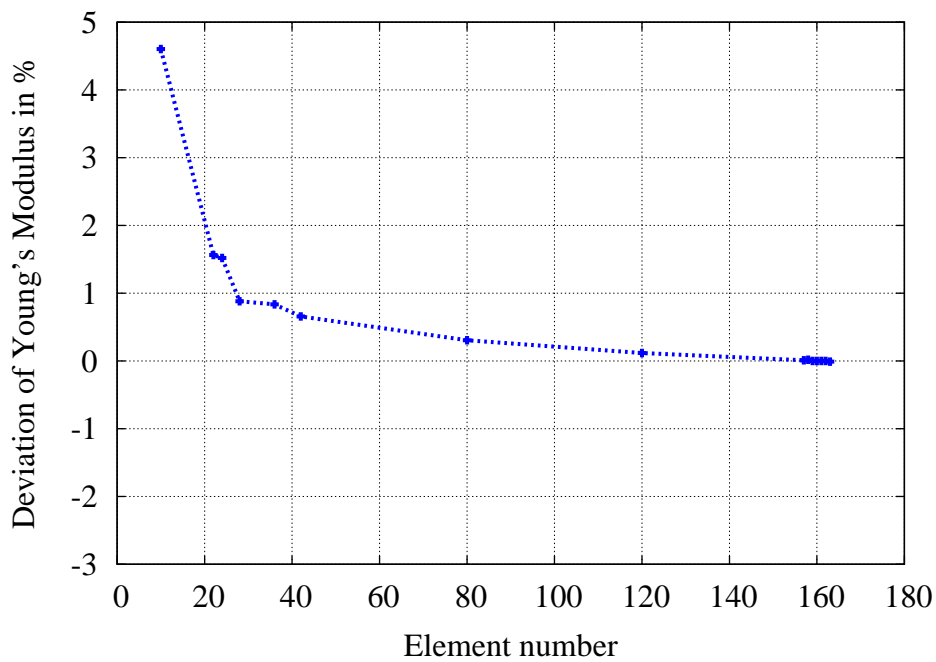


Figure 4.12: Influence of discretization and volume fraction on predicted stiffness

The stiffness computed with a 163x163 elements mesh has been used as a reference value for the predicted stiffnesses. Overall, the convergence is very good and the error is above 1% only for very coarse meshes.

4.2 Transversely Isotropic Failure Criteria and Softening Formulations for UD-Composites

To describe failure of a whole multidirectional UD-laminate in one lamina an anisotropic failure criterion is needed, in combination with an extensive experimental test program to determine all required parameters. In contrast, failure of a lamina can be described by a transversely isotropic failure criterion with much less effort. Therefore, failure of UD-laminates is predicted as failure of the layers they are composed of. One layer is usually discretized as one lamina with this method, but it is also possible to use more than one lamina for each layer.

As input parameters strengths of a lamina under tension and compression in fibre $R_{\parallel}^{t,c}$ and transverse $R_{\perp}^{t,c}$ direction as well as in-plane shear $R_{\parallel\perp}$ can be experimentally determined. According to Schürmann (2007) in fibre direction relatively reliable strengths can also be determined by analytical micromechanics. For in-plane shear and transverse strengths, including also transverse shear, micromechanical unit cell computations are presented in chapter 6. The prediction of failure under a combination of these uniaxial loadings is usually done in the failure criterion, because an experimental testing of biaxial load cases would be too cumbersome.

Modelling softening and failure of UD-composites, usually two damage initiation conditions for fibre failure and inter-fibre failure are introduced. The motivation for dividing the failure criterion in two conditions are the different consequences of these failures and thus, the different softening formulations invoked after failure initiation. If fibre-failure is detected, all material properties are degraded, because a crack in fibre direction does include matrix failure as well. Inter-fibre failure on the other hand does only affect the matrix properties, the fibres are considered to remain intact.

In this work, softening formulations for UD-composites are used at different scales, which makes an important difference. On the macroscale, in an UD-laminate, the softening formulation for a single lamina has to consider the "in-situ-effect" as well. Due to the redundancy of the laminate, local inter-fibre failure does not necessarily lead to complete failure of a lamina. In contrast, the lamina never fails completely, because softening stops when the characteristic damage state (CDS) is reached, see section 2.3.2. On the mesoscale a local entity of UD-composites is modelled in a unit cell and locally a complete failure is possible. Therefore, the softening formulation has to be chosen depending on the occurrence of the in-situ-effect.

4.2.1 Failure Criteria and Softening Formulations from Literature

A variety of failure criteria has been published in literature. Nahas (1986) gives a review on about 30 criteria in 1986, another selection was compared in the World-Wide-Failure-Exercise by (Hinton et al., 2004). The criterion of S. W. Tsai and Wu (1971) was published among the first and is probably the most often used criterion. It employs a single global, quadratic failure condition and thus is very efficient in computational cost. Due to the

single global formulation it does not provide information about the type of failure, which is, however, very important for the design engineer, on the one hand to judge upon the criticality of the failure, and on the other hand to improve the laminate. The substantial differentiation between fibre-failure and inter-fibre failure was first postulated by Puck and Schneider (1969). It was taken up by (Hashin, 1980) and enhanced by the use of invariants and a Mohr-coulomb fracture approach. The latter was considered to laborious at that time, therefore it was no longer pursued until it was taken up again by Puck (1996). Criteria that differentiate failure modes, e.g. Puck and Schürmann (2004), Cuntze and Freund (2004), have proven their reliability in the WWFE.

A further outcome of the WWFE was that pre-failure non-linear material behaviour and post-failure material softening are as well very important for a realistic failure description. Non-linear material models have been described in section 3.2.

Twelve post-failure-theories for IFF with completely different approaches have been reviewed by Nahas (1986). In Figure 4.13 four models are shown that basically differ in the stiffness reduction after IFF has occurred.

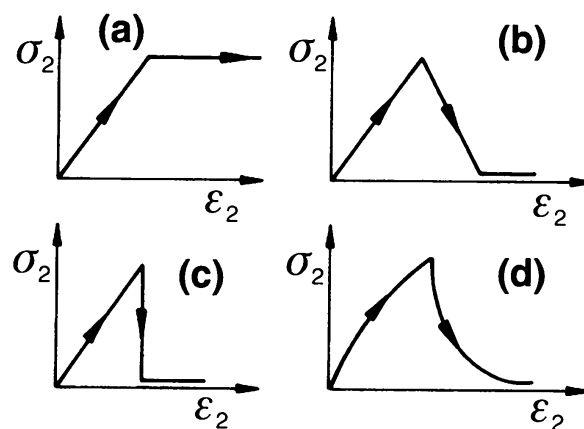


Figure 4.13: Post-failure softening approaches, taken from (Puck, 1996): (a) *Hahn*, Tsai-method, (b) *Petit*, Waddoups-model, (c) *Chiu*-model, (d) *Nahas*-model.

In the following, failure criteria of Hashin, Puck and Jeltsch-Fricker are described in more detail.

4.2.1.1 Hashin

The first main idea of Hashin (1980) was that the criterion should be invariant under any rotation around the fibres. Therefore, the following invariants proposed by Mulhern, Rogers, and Spencer (1967) were used:

$$I_1 = \sigma_{11} \quad (4.15a)$$

$$I_2 = \sigma_{22} + \sigma_{33} \quad (4.15b)$$

$$I_3 = \tau_{23}^2 - \sigma_{22}\sigma_{33} \quad (4.15c)$$

$$I_4 = \tau_{12}^2 + \tau_{13}^2 \quad (4.15d)$$

$$I_5 = 2\tau_{12}\tau_{23}\tau_{13} - \sigma_{22}\tau_{13}^2 - \sigma_{33}\tau_{12}^2 \quad (4.15e)$$

From these invariants Hashin (1980) states the most general transversely isotropic quadratic approximation:

$$A_1 I_1 + B_1 I_1^2 + A_2 I_2 + B_2 I_2^2 + C_{12} I_1 I_2 + A_3 I_3 + A_4 I_4 = 1 \quad (4.16)$$

The invariant I_5 in (4.15e), which is of cubic order in stresses does not appear in the failure criterion, to keep it quadratic in stresses. The four failure modes defined by Hashin are tensile and compressive fibre and matrix failure. Each mode is associated with a set of invariants that contribute to failure. This results in the following equations:

Fibre failure

$$\left(\frac{\sigma_{11}}{R_{\parallel}^t}\right)^2 + \frac{1}{R_{\perp\parallel}^2} (\tau_{12}^2 + \tau_{13}^2) = 1 \quad , \quad \sigma_{11} > 0 \quad (4.17)$$

$$-\frac{\sigma_{11}}{R_{\parallel}^c} = 1 \quad , \quad \sigma_{11} < 0 \quad (4.18)$$

Matrix failure

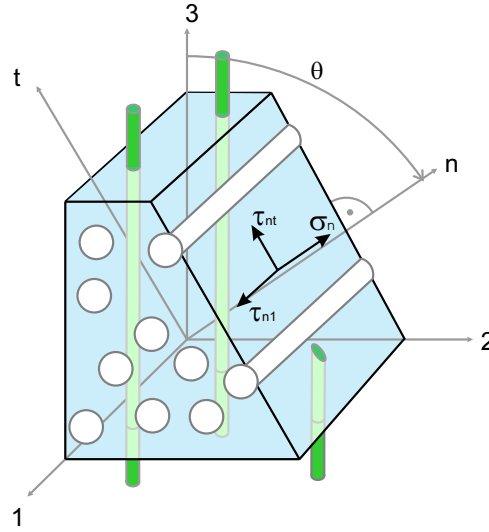
$$\frac{1}{R_{\perp}^{t2}} (\sigma_{22} + \sigma_{33})^2 + \frac{1}{R_{\perp\perp}^2} (\tau_{23}^2 - \sigma_{22}\sigma_{33}) + \frac{1}{R_{\perp\parallel}^2} (\tau_{12}^2 + \tau_{13}^2) = 1 \quad , \quad \sigma_{nn} > 0 \quad (4.19)$$

$$\begin{aligned} \frac{1}{R_{\perp}^c} \left[\left(\frac{R_{\perp}^c}{2R_{\perp\perp}}\right)^2 - 1 \right] (\sigma_{22} + \sigma_{33}) + \frac{1}{4R_{\perp\perp}^2} (\sigma_{22} + \sigma_{33})^2 \\ + \frac{1}{R_{\perp\perp}^2} (\tau_{23}^2 - \sigma_{22}\sigma_{33}) + \frac{1}{R_{\perp\parallel}^2} (\tau_{12}^2 + \tau_{13}^2) = 1 \quad , \quad \sigma_{nn} < 0 \end{aligned} \quad (4.20)$$

The orientation of the action plane and normal stress σ_{nn} is illustrated in Figure 4.14. In analogy to Mohr's failure theory the stresses σ_{nn} , τ_{1n} and τ_{nt} are responsible for matrix failure. The normal stress σ_{nn} is given by

$$\sigma_{nn} = \sigma_{22}\cos^2\theta + \sigma_{33}\sin^2\theta \quad (4.21)$$

and used to distinguish between tensile and compressive matrix failure. Hashin did not engage further in this theory, because he estimated its numerical costs would be too high. However, it was taken up later by Puck.

Figure 4.14: Definition of fracture plane angle θ

4.2.1.2 Puck's Parabolic Criterion and Softening Formulation

As a continuation of Hashin's work Puck (1996) developed an action-plane-based strength criterion that is widely spread today and has shown its performance in the WWFE, see Hinton et al. (2004). An important part in the success of this criterion is not only its physical basis, but also the softening formulation provided in the context of the criterion itself. The physical basis makes it possible to extract an interpretation of the significance of failure out of the result and the softening formulation enables prediction of progressive failure. Puck (1996) distinguishes two FF modes and three IFF modes, as described in section 2.3.2, that are identified by four failure conditions altogether.

Fibre failure conditions

For FF, the simple conditions

$$\frac{\sigma_1}{R_{\parallel}^t} = 1 \text{ for } \sigma_1 \geq 0 \quad , \quad (4.22)$$

$$-\frac{\sigma_1}{R_{\parallel}^c} = 1 \text{ for } \sigma_1 < 0 \quad , \quad (4.23)$$

are generally considered to be sufficient.

Inter-fibre failure conditions

In analogy to Hashin's failure criterion, Puck evaluates IFF on the action-plane defined in Figure 4.14. The transformation of the stresses from the ply coordinate system (x_1, x_2, x_3) to the (x_1, x_n, x_t) coordinate system of the action plane is accomplished by

$$\begin{aligned} \rightarrow \begin{bmatrix} \sigma_1 \\ \sigma_n \\ \sigma_t \\ \tau_{nt} \\ \tau_{t1} \\ \tau_{n1} \end{bmatrix} &= \begin{bmatrix} 1 & 0 & 0 & 0 & 0 & 0 \\ 0 & c^2 & s^2 & 2sc & 0 & 0 \\ 0 & s^2 & c^2 & -2sc & 0 & 0 \\ 0 & -sc & sc & (c^2 - s^2) & 0 & 0 \\ 0 & 0 & 0 & 0 & c & -s \\ 0 & 0 & 0 & 0 & s & c \end{bmatrix} \begin{bmatrix} \sigma_1 \\ \sigma_2 \\ \sigma_3 \\ \tau_{23} \\ \tau_{31} \\ \tau_{21} \end{bmatrix} \end{aligned} \quad (4.24)$$

where $c = \cos(\theta)$ and $s = \sin(\theta)$ have been substituted for a more compact notation. Puck (1996) assumes that the normal stress σ_n of the action plane divides IFF into two different modes. The stress exposure factor f_E , also known as effort, is therefore given dependent on σ_n

$$f_E(\theta) = \sqrt{\left(\frac{1}{R_{\perp}^A} - \frac{p_{\perp\Psi}^t}{R_{\perp\Psi}^A}\right)^2 \sigma_n^2 + \left(\frac{\tau_{nt}}{R_{\perp\perp}^A}\right)^2 + \left(\frac{\tau_{n1}}{R_{\perp\parallel}}\right)^2} + \frac{p_{\perp\Psi}^t}{R_{\perp\Psi}^A} \sigma_n \quad \text{for } \sigma_n \geq 0 \quad (4.25)$$

$$f_E(\theta) = \sqrt{\left(\frac{\tau_{nt}}{R_{\perp\perp}^A}\right)^2 + \left(\frac{\tau_{n1}}{R_{\perp\parallel}}\right)^2 + \left(\frac{p_{\perp\Psi}^c}{R_{\perp\Psi}^A} \sigma_n\right)^2} + \frac{p_{\perp\Psi}^c}{R_{\perp\Psi}^A} \sigma_n \quad \text{for } \sigma_n < 0 \quad (4.26)$$

with:

$$\frac{p_{\perp\Psi}^t}{R_{\perp\Psi}^A} = \frac{p_{\perp\perp}^t}{R_{\perp\perp}^A} \cos^2 \Psi + \frac{p_{\perp\parallel}^t}{R_{\perp\parallel}} \sin^2 \Psi \quad (4.27)$$

$$\frac{p_{\perp\Psi}^c}{R_{\perp\Psi}^A} = \frac{p_{\perp\perp}^c}{R_{\perp\perp}^A} \cos^2 \Psi + \frac{p_{\perp\parallel}^c}{R_{\perp\parallel}} \sin^2 \Psi \quad (4.28)$$

$$\Psi = \arctan \frac{\tau_{n1}}{\tau_{nt}}, \quad \cos^2 \Psi = 1 - \sin^2 \Psi = \frac{\tau_{nt}^2}{\tau_{nt}^2 + \tau_{n1}^2} \quad (4.29)$$

$$R_{\perp\perp}^A = \frac{R_{\perp}^c}{2(1 + p_{\perp\perp}^c)} \quad (4.30)$$

Since the stress exposure factor is dependent on the action-plane angle $\theta = \angle(x_2, x_n)$, it has to be varied from -90° to $+90^\circ$ in order to find the maximum value of f_E . The angle associated to maximum f_E is called θ_{fp} . When the maximum $f_E = 1$, it is assumed that a fracture plane is formed under the angle θ_{fp} .

The shear stress $\tau_{n\Psi}$ is introduced to allow for longitudinal sections with $\Psi = \text{const.}$, making a simpler formulation of the contour lines of the master fracture body possible, compared to using cross-sections with $\sigma_n = \text{const.}$ (Cuntze, 1997). The so-called master fracture body is a visualization of all stress states that yield $f_E = 1$, its sections are illustrated in fig. 4.15.

The slope parameters p determine the inclination of the master fracture body at the shear axis. Recommended values are given by VDI (2006), see table 4.2, because they are not considered to be determined for each lamina.

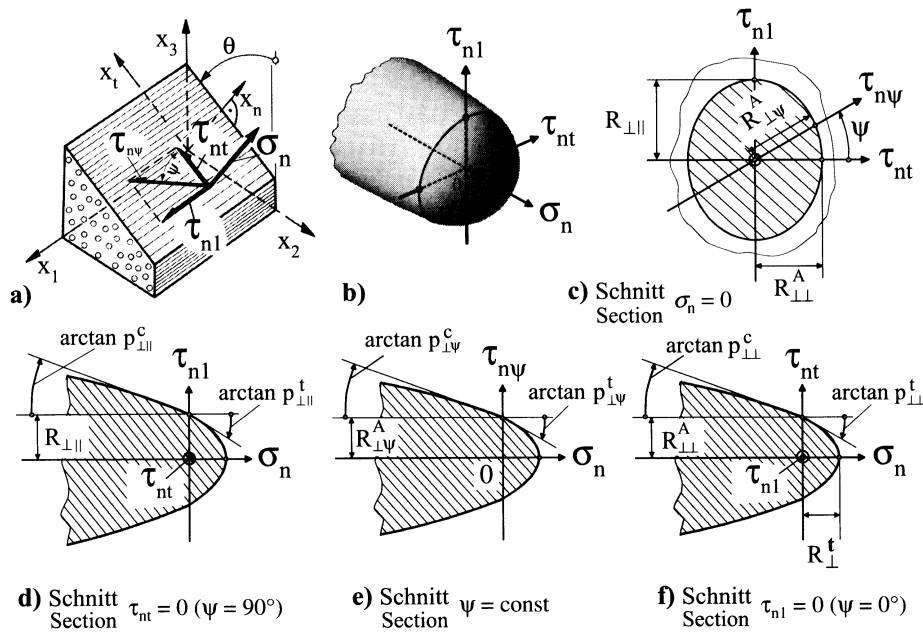


Figure 4.15: Master fracture body and its sections (VDI, 2006):

- a) Stresses acting on the fracture plane
- b) Master fracture body
- c) Cross-section ($\sigma_n = 0$)
- d) - f) Longitudinal sections ($\tau_{nt} = 0$ and $\tau_{n1} = 0$).

	$p_{\perp\parallel}^c$	$p_{\perp\parallel}^t$	$p_{\perp\perp}^t = p_{\perp\perp}^c$
GFRP	0, 25	0, 30	0, 20 bis 0, 25
CFRP	0, 30	0, 35	0, 25 bis 0, 30

Table 4.2: Slope parameters for criterion of Puck, as recommended by VDI (2006)

The fracture angle θ_{fp} can be identified analytically in case of a plane stress state ($\sigma_1, \sigma_2, \tau_{12}$) by

$$\theta_{fp} = \sqrt{\frac{R_{\perp\perp}^A}{-\sigma_2}}, \quad (4.31)$$

where the slope parameters $p_{\perp\parallel}^c$ and $p_{\perp\perp}^c$ are coupled by

$$p_{\perp\perp}^c = p_{\perp\parallel}^c \frac{R_{\perp\perp}^A}{R_{\perp\parallel}}. \quad (4.32)$$

This drastically decreases computational effort. Puck, Kopp, and Knops (2002) state that this is a valid assumption for 95% of all FRP components, because FRP are usually employed in thin-walled structures. However, regions of three-dimensional stress states, e.g. connections between FRP components, seem to be most critical in the author's view.

Allocation of fracture modes and fracture angles

Puck (1996) discriminates three different failure modes, as described in section 2.3.2, that are judged to be differently critical. The allocation of these modes is very simple in the case of plane stress. It is accomplished over the normal stress σ_n and the fracture angle θ_{fp} . Fracture mode A is indicated by $\sigma_n \geq 0$, whereas $\sigma_n < 0$ indicates either mode B or C. For discrimination between modes B and C the fracture angle θ_{fp} is used. Mode C fracture is indicated by $\theta_{fp} > 0$. It is considered to be critical, because it may lead to a wedge-shaped failure of the lamina that results in stability failure of the whole laminate.

Basically, in a three-dimensional stress state the shear stress $\tau_{\perp\perp}$ is added to the stresses of the action plane. A fourth mode A* is introduced by Puck for a combination of a tensile normal stress $\sigma_n \geq 0$, $\tau_{\perp\parallel}$ and $\tau_{\perp\perp}$, whilst mode A contains only $\sigma_n \geq 0$ and $\tau_{\perp\parallel}$ stresses.

As described in section 4.2.1.2, the fracture plane angle has to be determined by an iterative search.

Influence of fibre-parallel stresses on IFF

The stress exposure factor f_E , given in eqs. (4.25) and (4.26), does not account for fibre parallel stresses, although IFF is influenced by these stresses. Puck (1996) has chosen to reduce the strengths of the fracture plane to incorporate this interaction. The algorithm has changed since then, a simplified method was published in VDI (2006) and by Schürmann (2007) recently. A weakening factor η_w is introduced that increases the stress exposure factor

$$f_{E_w} = \frac{f_E}{\eta_w} \quad . \quad (4.33)$$

The weakening factor η_w is given dependent on two parameter s and m by

$$\eta_w = \frac{c \left(a \sqrt{c^2 (a^2 - s^2) + 1} + s \right)}{(ca)^2 + 1} \quad , \quad (4.34)$$

with

$$c = \frac{f_E}{f_E(FF)} \quad \text{and} \quad a = \frac{1 - s}{\sqrt{1 - m^2}} \quad . \quad (4.35)$$

Figure 4.16 illustrates the functionality of the weakening factor and the meaning of the parameters s and m . It shows the σ_1 - σ_2 failure envelope of a UD-lamina. The parameter m gives the maximum value of η_w , whereas the starting point of the interaction is given by the parameter s . For both parameters a value of 0.5 is recommended by VDI (2006), but these values were not validated yet.

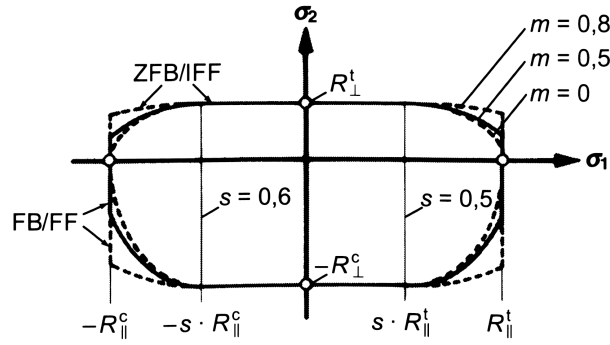


Figure 4.16: Progressive weakening of IFF resistances due to the influence of high fibre-parallel stresses σ_1 . (VDI, 2006)

Softening after Inter Fibre Failure

A laminate is a redundant structure, as discussed earlier in section 2.3.2, i.e. inter-fibre failure does not lead to a complete failure of a whole lamina. The lamina reaches a characteristic damage state asymptotically, but parts of it remain intact and carry minimal loads. In contrast, FF is always accounted for as a complete failure of the lamina.

Puck (1996) proposes a softening of the lamina dependent on the stress exposure factor of the undamaged lamina. The softening factor

$$\eta = \frac{1 - \eta_R}{1 + c(f_E - 1)^\xi} + \eta_R \quad (4.36)$$

is multiplied with selected elastic constants. The reduced elastic constants are then used to compute the actual stresses in the lamina. Young's E_\perp and shear modulus $G_{\perp\parallel}$ are reduced by the softening factors η_e and η_g in mode A failure, whereas only the shear modulus is reduced under failure modes B and C, because the crack is assumed to remain closed and able to transmit normal stresses over contact under compressive fracture plane stress σ_n . Knops (2003) has shown by experiment that the softening of Poisson's ratio $\nu_{\perp\parallel}$ in failure mode A, as described by (Puck, 1996) and (Puck & Schürmann, 2004) is not reasonable. The parameters of the softening function as recommended by Knops (2003) are given in table 4.3 for GFRP and CFRP. Figure 4.17 illustrates the softening factor dependent on the stress-exposure factor f_E and the asymptotical values of the characteristic damage state. The shear modulus is degraded less than Young's modulus, because the in-situ effect is stronger for this load.

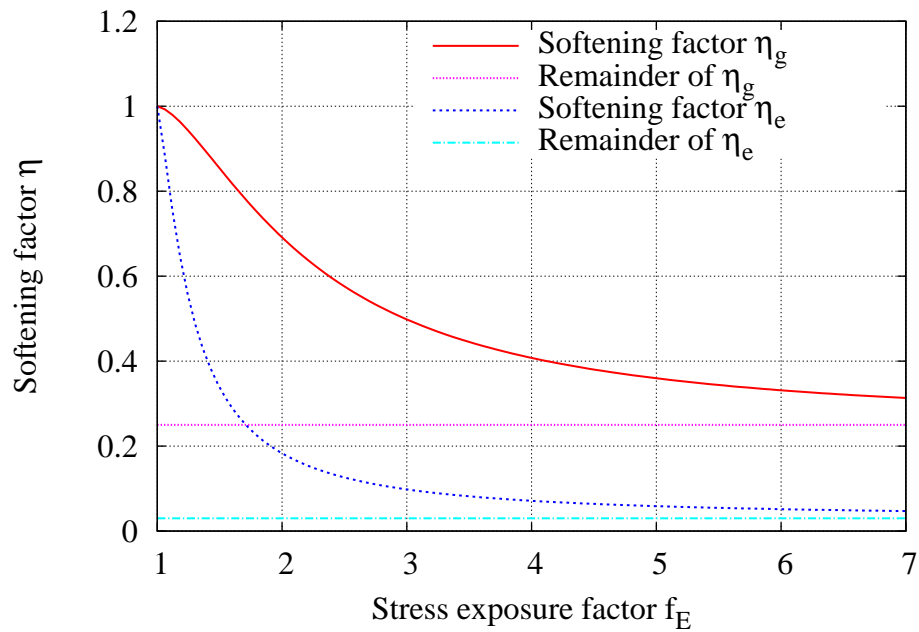
It has to be noted that the softening formulation of Puck is dependent on stresses and strains, respectively. As described in section 4.1.1 stress-strain relations for the description of softening lead to a mesh-dependency, that will be shown in the following section.

Tension Rod Softening

The functionality of Puck's softening formulation will be demonstrated on the example of a tension rod. Since the softening algorithm is used for IFF only, the material is loaded

		η_r	c	ξ
GFRP	E_{\perp}	0,03	5,34	1,31
	$G_{\perp\parallel}$	0,25	0,70	1,53
CFRP	E_{\perp}	0,03	5,34	1,31
	$G_{\perp\parallel}$	0,67	0,95	1,17

Table 4.3: Softening parameter for PUCK's criterion recommended by Knops (2003)

Figure 4.17: Puck's softening function $\eta = f(f_E)$ for the elasticity parameters $E_{\perp s}, G_{\perp\parallel s}$ depending on the effort $f_E \geq 1$. Values were taken from table 4.3 for GFRP

in transverse direction. The dimensions of the rod are $2 \times 1 \times 1$ mm, it is discretized with $2 \times 1 \times 1$, $4 \times 2 \times 2$ and $8 \times 4 \times 4$ volume elements, respectively, it is loaded displacement-driven in x-direction (2-direction of the material). Figure 4.18 gives the load-displacement curves of the tension rod dependent on the discretizations.

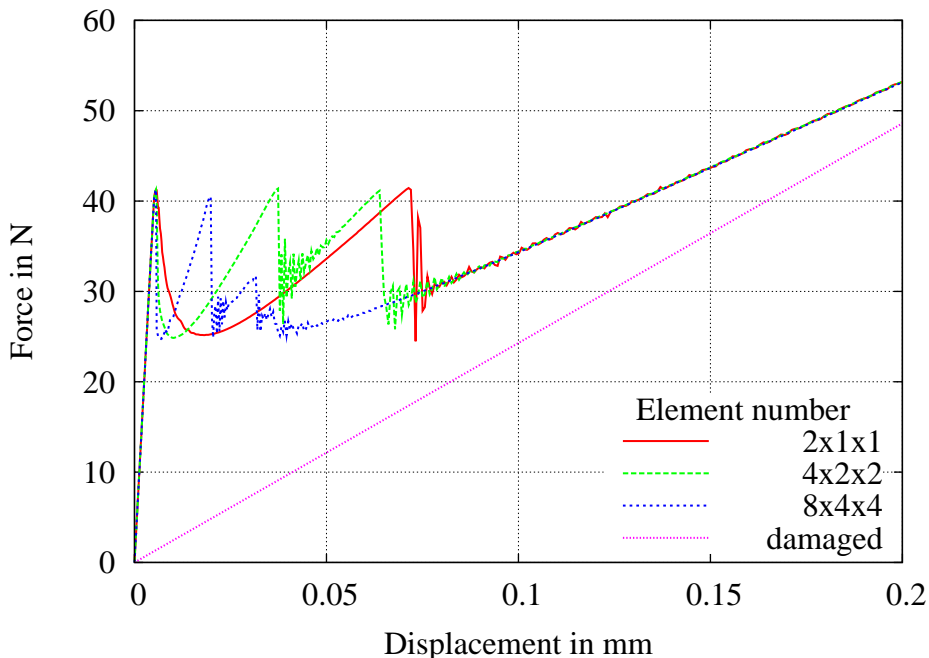


Figure 4.18: Load-displacement curves of tension rod

The post-failure behaviour of Puck's softening formulation is made for laminates of FRP, that never fail completely, but reach a characteristic damage state due to the in-situ effect and retain a certain percentage of the initial stiffness, see section 2.3.2. In FRP IFF does not localize from a macroscopic view, only on the mesoscale numerous cracks localize in the lamina. Therefore, a fracture energy regularization, that assumes the aggregation of failure in one macrocrack, is not reasonable, as described in section 4.1, In contrast, a regularization is not required, because all elements fail consecutively, as the load-displacement curve in Figure 4.18 shows. However, the energy consumed by damage, which is the area under the load-displacement curve, is mesh-dependent in this example. This can be considered only a minor weakness, because the final damage state is mesh-independent. For lamina that do not adopt the characteristic damage state this softening formulation should not be used, because it yields wrong results

4.2.1.3 Simple Parabolic Criterion (SPC)

The simple parabolic criterion (SPC) by Jeltsch-Fricker (1996) is a simplification and a numerical stabilization of Puck's IFF condition. The stress exposure factors f_E for inter-fibre failure read

$$f_E = \sqrt{(1 - p^t)^2 \left(\frac{\sigma_n}{R_{\perp}^t}\right)^2 + \left(\frac{\tau_{nt}}{R_{\perp\perp}^A}\right)^2 + \left(\frac{\tau_{n1}}{R_{\perp\parallel}}\right)^2} + p^t \frac{\sigma_n}{R_{\perp}^t} \quad \text{for } \sigma_n \geq 0 \quad (4.37)$$

$$f_E = \sqrt{(p^c)^2 \left(\frac{\sigma_n}{R_{\perp}^c}\right)^2 + \left(\frac{\tau_{nt}}{R_{\perp\perp}^A}\right)^2 + \left(\frac{\tau_{n1}}{R_{\perp\parallel}}\right)^2} + p^c \frac{\sigma_n}{R_{\perp}^c} \quad \text{for } \sigma_n < 0 \quad . \quad (4.38)$$

IFF is detected for $f_E = 1$. The slope parameters are coupled by the equation

$$\frac{p_{\perp\parallel}^{t,c}}{R_{\perp\parallel}} = \frac{p_{\perp\perp}^{t,c}}{R_{\perp\perp}^A} \quad , \quad (4.39)$$

which is a restriction compared to Puck's criterion that uses four uncoupled parameters. Boundaries for the parameters p^t, p^c are

$$0 < p^t < 1 \quad , \quad 0 < \frac{p^c}{R_{\perp}^c} \leq \frac{p^t}{R_{\perp}^t} \quad . \quad (4.40)$$

Recommended values are $p^t = 0.3, p^c = 0.25$.

A softening formulation was not provided by Jeltsch-Fricker (1996), but due to the similarity of the whole criterion to Puck's criterion it is reasonable to use Puck's softening approach. The recommended input parameters can be taken as well. However, it has been stated before that this softening model is not regularized and thus exhibits a mesh dependency.

4.2.2 New Invariant-based Quadratic Failure Criterion (IQC) and Softening Formulation

4.2.2.1 Fibre Failure Condition

It is assumed, that the strength in fibre direction is mainly governed by the strength of the fibres and that the fibres are only subject to stresses in fibre direction. Therefore the fibre failure condition is relatively simple:

$$\frac{\mathbf{a}\boldsymbol{\sigma}\mathbf{a}}{R_{\parallel}} = 1 \quad (4.41)$$

The fibre tensile strength R_{\parallel}^t and a compressive strength R_{\parallel}^c , representing the resistance of the UD-Composite under uniaxial tension and compression in fibre direction, are needed as input data. If one of these strengths is achieved, the material fails and there is no remaining load carrying capacity. The term $\mathbf{a}\boldsymbol{\sigma}\mathbf{a}$ is the projection of the stress tensor onto the preferred direction and R_{\parallel} is the resistance of the fibre bundle in fibre direction in tension ($R_{\parallel} = R_{\parallel}^t$) and in compression ($R_{\parallel} = R_{\parallel}^c$) respectively.

4.2.2.2 Inter-Fibre Failure Condition

Inter-fibre failure is formulated in the format of the yield locus in section 3.2, based on the invariants presented there. The failure surface is:

$$r = \beta_1 I_1 + \beta_2 I_2 + \beta_3 I_3 + \beta_{32} I_3^2 - 1 \quad (4.42)$$

The failure criterion is active, when $r = 0$. The parameters β_1 , β_3 and β_{32} are obtained in the same manner as the parameters α_1 , α_3 and α_{32} for the yield function eq.3.30. Therefore, the material strengths of uniaxial tension R_{\perp}^t and compression R_{\perp}^c perpendicular to the fibre and the material strength of transverse shear $R_{\perp\perp}$ and in-plane shear $R_{\parallel\perp}$ have to be inserted instead of the yield stresses in eq.3.30. If not available from experimental tests the required strengths R_{\perp}^t , R_{\perp}^c , $R_{\perp\perp}$ and $R_{\parallel\perp}$ can be obtained from simulations with the micromechanical unit cell, see section 6. If the inter-fibre failure condition is reached, the current stress state is saved as effective stress, i.e. hardening modulus is set to zero and ideally plastic behaviour is assumed. Stiffness degradation is then initiated and controlled by a scalar damage variable d , as already described in sec. 4.1.1 for the isotropic model. Here, the damage variable d does not affect the stresses in fibre direction σ_{11} .

Figure 4.19 shows yield and fracture surface in the $\sqrt{I_1}$ - I_3 -invariant-plane, where I_3 can be seen as hydrostatic pressure and $\sqrt{I_1}$ as deviatoric stresses. Please note that the horizontal axis describes biaxial stress states, because the stresses in fibre direction are not included in invariant I_3 . Initially the yield surface is smaller than the yield surface for all stress states, but in the hardening process it widens until it meets the failure condition in the given stress state. It is important to note that hardening can still progress, if the yield surface meets the failure surface somewhere else, but not in the current stress state. This

fact enables a differently pronounced plasticity for different stress states, e.g. tension and shear, as it is encountered in UD-composites.

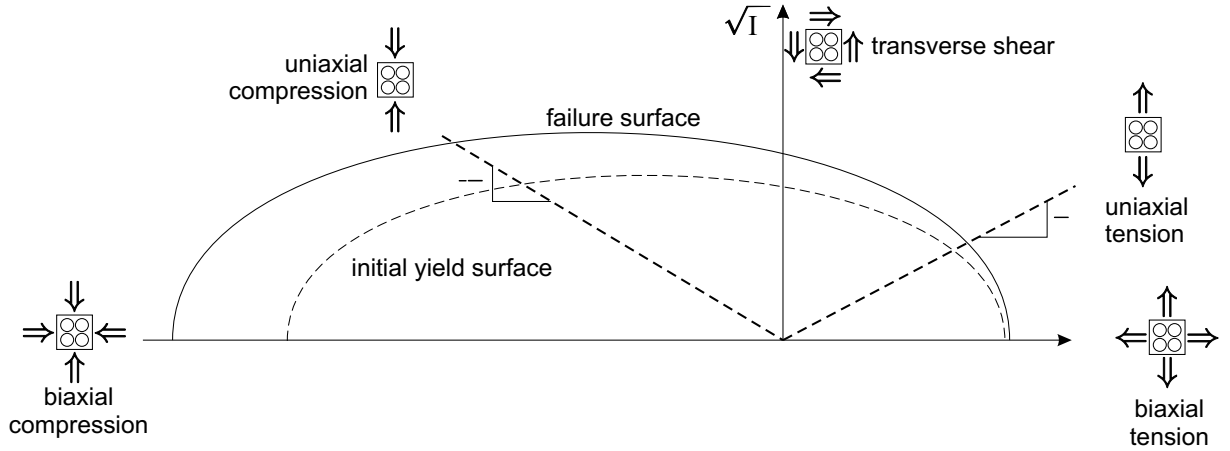


Figure 4.19: Yield and failure surface of the transversely isotropic material model in $\sqrt{I_1}$ - I_3 -invariant-plane

An example for the shape of the IQC-failure surface is given in Figure 4.20 in σ_2 - σ_3 - τ_{23} -space.

4.2.2.3 Softening Formulation

If the failure criterion is fulfilled, a softening formulation equal to the formulation for the epoxy resin, given in section 4.1.1 is applied. However, it has to be accounted for the transverse isotropy of the material. Thus, two different damage variables are used for FF and IFF. If the IQC detects IFF, the plasticity algorithm changes from plastic hardening to ideally plastic behaviour, and an isotropic damage variable is multiplied with the effective plastic stress to give the nominal stresses. The evolution of the damage variable is governed by the fracture energy regularization technique, i.e. dependent on strain energy release rate and equivalent plastic displacement since damage initiation. All elastic constants, apart from the stiffness in fibre direction are damaged in the same way. Therefore, only fibre stresses remain in the element. If FF is detected, the fibre direction stresses are degraded with a formulation analogous to Hillerborg's softening, but without the need of plasticity. This softening formulation is used only for regularization purposes, therefore the applied strain energy release rate does not have a physical basis, but is chosen such that it has a minimal effect. The damage variable d_f is calculated from the displacement at damage initiation

$$u_{fail}^{t,c} = L_e \frac{R_{\parallel}^{t,c}}{E_{\parallel}} \quad (4.43)$$

and the displacement at ultimate failure

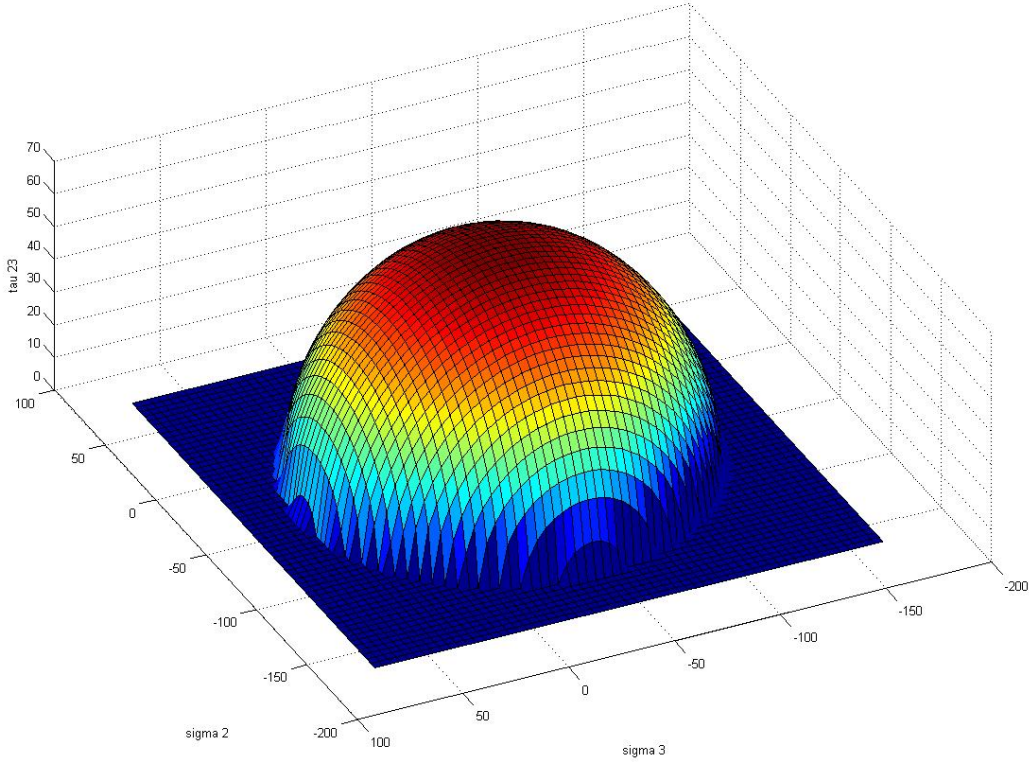


Figure 4.20: Failure surface of IQC in stress space

$$u_{ult}^{t,c} = 2 * \frac{G_{Ic}}{R_{||}^{t,c}} + u_{fail}^{t,c} \quad (4.44)$$

and the actual displacement u over

$$d_f = \frac{u - u_{fail}}{u_{ult} - u_{fail}}. \quad (4.45)$$

The nominal stresses are then calculated by multiplication of the fibre direction stresses with the damage variable d_f .

The softening formulation does not take the in-situ-effect of lamina embedded in laminates into account, because it is to be applied in mesomechanical unit cell simulations that model this effect discretely rather than in a smeared way.

4.2.3 Comparison of Failure Criteria

For UD-composites several benchmarks were published in the World-Wide Failure Exercise, that are used to show the capabilities of the presented failure criteria and softening formulations. Firstly, table 4.4 gives a comparison of the input parameters required by the failure criteria Puck, SPC and IQC. It can be seen, that the criterion of Puck requires the most parameters, especially a number of slope parameters, which are not easily determined experimentally. Mostly they can be associated to a physical effect, like e.g. internal friction, but they don't have a concrete physical meaning like e.g. strengths. Puck gives reference values for these slope parameters, because they are not supposed to be determined for each laminate. In table 4.4 the reference values are given to clarify which parameters are usually not determined for the actual material. Reference values are given for GFRP.

Table 4.4: Input parameters of failure criteria (for GFRP)

Parameter	Puck	SPC	IQC
Strengths	$R_{\perp}^{t,c}$ $R_{\parallel}^{t,c}$ $R_{\perp\parallel}$	$R_{\perp}^{t,c}$ $R_{\parallel}^{t,c}$ $R_{\perp\parallel}$	$R_{\perp}^{t,c}$ $R_{\parallel}^{t,c}$ $R_{\perp\parallel}$ $R_{\perp\perp}$
Slope Parameters	$p_{\perp\parallel}^t = 0.3$ $p_{\perp\parallel}^c = 0.25$ $p_{\perp\perp}^t = 0.2$ $p_{\perp\perp}^c = p_{\perp\perp}^t$	$p^t = 0.3$ $p^c = 0.25$	
Magnification factor	$m_{\sigma f} = 1.3$	-	-
Fibre-parallel Weakening	$s = m = 0.5$ $0, 5 \leq \eta_w \leq 1$	-	-
Softening	$\eta_{r,E_{\perp}} = 0.03$ $c_{E_{\perp}} = 5.34$ $\xi_{E_{\perp}} = 1.31$ $\eta_{r,G_{\perp\parallel}} = 0.25$ $c_{G_{\perp\parallel}} = 0.7$ $\xi_{G_{\perp\parallel}} = 1.53$	-	G_{Ic}

In contrast to Puck's criterion and the SPC, for the presented inter-fibre failure condition in eq. 4.42 a strength $R_{\perp\perp}$ is required, that is hardly determinable experimentally. Thus, either a micromechanical unit cell can be used for determination or an approximation given by Puck (1996)

$$R_{\perp\perp} = \frac{R_{\perp}^t}{\sqrt{2}}. \quad (4.46)$$

The different number of parameters for degradation is mainly caused by the fact that Puck's model incorporates the in-situ-effect and the IQC-model does not. To account for this effect multiple cracks have to be smeared over one element which increases the complexity drastically. Because of this smearing procedure, Puck's degradation is a phenomenological approach. In contrast, the degradation model of the IQC is physically motivated and regularized, but does not account for the in-situ-effect.

4.2.3.1 Laminate Models and Load Cases from the WWFE

In the WWFE five different laminate configurations and single UD-layers have been used. The laminates and their dimensions are shown in Figure 4.21.

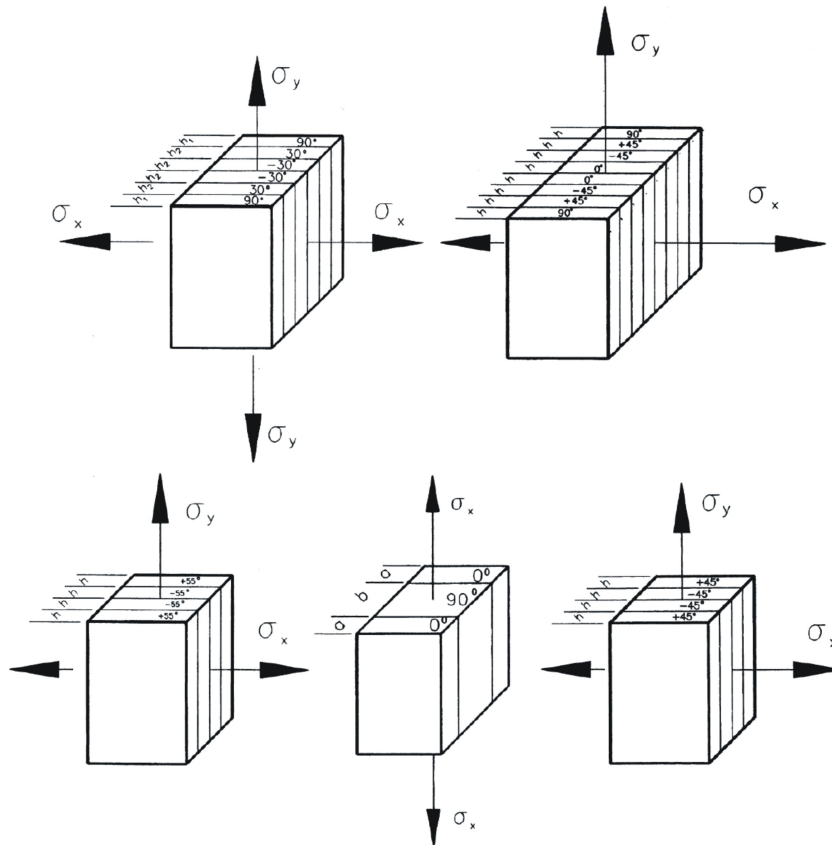


Figure 4.21: Implemented laminates from the WWFE (Hinton et al., 2004).

$(90^\circ/\pm 30^\circ)_s$, total thickness: 2.0 mm, $h_1 = 0.172$ mm and $h_2 = 0.414$ mm.

$(0^\circ/\pm 45^\circ/90^\circ)_s$, total thickness: 1.1 mm, $h = 0.1375$ mm

$(\pm 55^\circ)_s$, total thickness: 1.0 mm, $h = 0.25$ mm

$(0^\circ/90^\circ)_s$, total thickness: 1.04 mm, $b = 0.52$ mm, $a = 0.26$ mm

$(\pm 45^\circ)_s$, total thickness: 1.00 mm, $h = 0.25$ mm

Those laminates are made of four different materials:

GFRP-1 E-glass fibres and epoxy resin LY556/HT907/DY063,

GFRP-2 E-glass fibres and epoxy resin MY750/HY917/DY063,

CFRP-1 Carbon fibres AS4 and epoxy resin 3501-6,

CFRP-2 Carbon fibres T300 and epoxy resin BSL914C.

The material data are given in table 4.5. Table 4.6 shows which laminate was made of which material. Altogether 14 load cases are given with different requirements and result types. For some load cases the result is provided as a non-linear stress-strain curve, for others biaxial test data is provided that should be compared with a failure envelope.

The boundary conditions applied on the lamina and laminates are given in Figure 4.22(b). It is assumed that the load is applied on an infinite shell, thus no free-edge effects or inter-laminar shear stresses have to be considered. Each lamina is represented by one element and the elements are stacked in z-direction. The faces of the elements are restricted to remain parallel to their reference configuration, but they can deform freely, if no load is applied. Thus, in the given load case in Figure 4.22(b) under σ_x - and σ_y -tensile load the laminate contracts freely in thickness direction.

Table 4.5: Material properties of UD laminae used for the implementation (Hinton et al., 2004)

	CFRP-1	CFRP-2	GFRP-1	GFRP-2
Fibre type	AS4	T300	E-glass	E-glass
Matrix type	3501-6	BSL914C	LY556	MY750
Fibre volume fraction, v_f in %	60	60	62	60
Longitudinal modulus E_{\parallel} in GPa	126	138	53.48	45.6
Transverse modulus E_{\perp} in GPa	11	11	17.7	16.2
In-plane shear modulus $G_{\perp\parallel}$ in GPa	6.6	5.5	5.83	5.83
Major Poisson's ratio $\nu_{\perp\parallel}$	0.28	0.28	0.278	0.278
Through thickness Poisson's ratio $\nu_{\perp\perp}$	0.4	0.4	0.4	0.4
Longitudinal tensile strength R_{\parallel}^t in MPa	1950	1500	1140	1280
Longitudinal compr. strength R_{\parallel}^c in MPa	1480	900	570	800
Transverse tensile strength R_{\perp}^t in MPa	48	27	35	40
Transverse compr. strength R_{\perp}^c in MPa	200	200	114	145
In-plane shear strength $R_{\perp\parallel}$ in MPa	79	80	72	73
Fibre: Longitudinal modulus $E_{\parallel f}$ in GPa	225	230	80	74
Fibre: Major Poisson's ratio $\nu_{\perp\perp f}$	0.2	0.2	0.2	0.2
Fibre: Long. tensile failure strain $\epsilon_{\parallel f}^t$	1.488	1.086	2.687	2.905

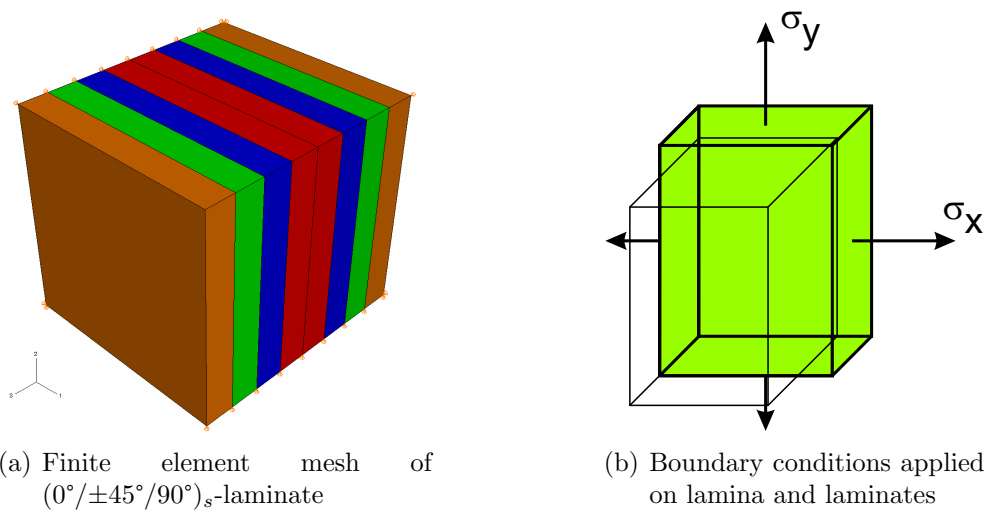


Figure 4.22: Finite element discretization of WWFE tests

Table 4.6: WWFE load cases: overview

Nr.	Laminate	Material	Load case	envelope/ curve	Linear/ nonlinear	Plot
1	0°	E-glass/LY556/HT907/DY063 (GFRP-1)	σ_2, τ_{12}	envelope	linear	σ_2, τ_{12}
2		T300/BSL914C (CFRP-1)	σ_1, τ_{12}	envelope	linear	σ_1, τ_{12}
3		E-glass/MY750/HY917/DY063 (GFRP-2)	σ_1, σ_2	envelope	linear	σ_1, σ_2
4	(90°/±30°) _s	E-glass/LY556/HT907/DY063 (GFRP-1)	σ_y, σ_x	envelope	linear	σ_y, σ_x
5			σ_x, τ_{xy}	envelope	linear	σ_x, τ_{xy}
6	(0°/±45°/90°) _s	AS4/3501-6 (CFRP-2)	σ_y, σ_x	envelope	linear	σ_y, σ_x
7			ϵ_y	curve	linear	$\epsilon_x, \epsilon_y, \sigma_y$
8			$\sigma_y/\sigma_x = 2/1$	curve	linear	$\epsilon_x, \epsilon_y, \sigma_y$
9	(±55°) _s	E-glass/MY750/HY917/DY063 (GFRP-2)	σ_y, σ_x	envelope	linear	σ_y, σ_x
10			ϵ_y	curve	non-linear	$\epsilon_x, \epsilon_y, \sigma_y$
11			$\sigma_y/\sigma_x = 2/1$	curve	non-linear	$\epsilon_x, \epsilon_y, \sigma_y$
12	(0°/90°) _s	E-glass/MY750/HY917/DY063 (GFRP-2)	ϵ_y	curve	linear	$\epsilon_x, \epsilon_y, \sigma_y$
13	(±45°) _s	E-glass/MY750/HY917/DY063 (GFRP-2)	$\sigma_y/\sigma_x = 1/1$	curve	linear	$\epsilon_x, \epsilon_y, \sigma_y$
14			$\sigma_y/\sigma_x = 1/-1$	curve	non-linear	$\epsilon_x, \epsilon_y, \sigma_x$

4.2.3.2 UD-Layer

Load Case 1: σ_2 - τ_{12} -envelope

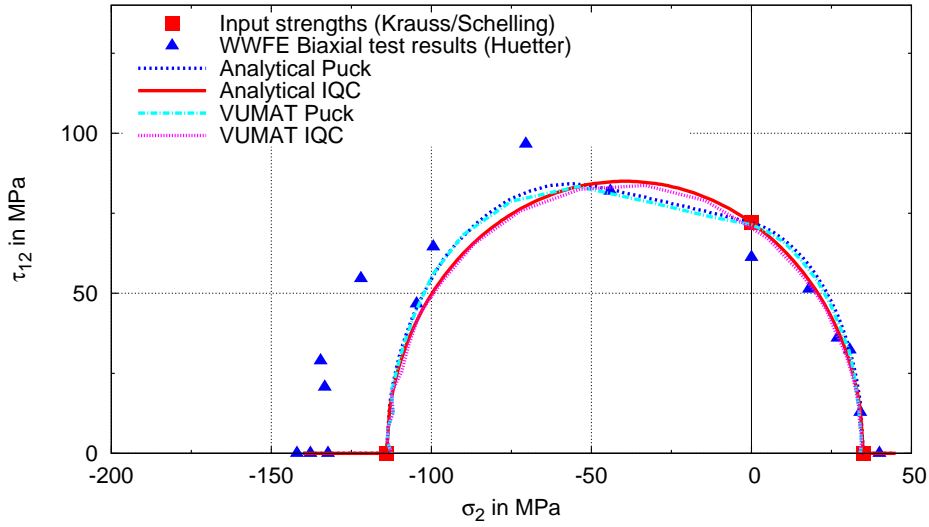
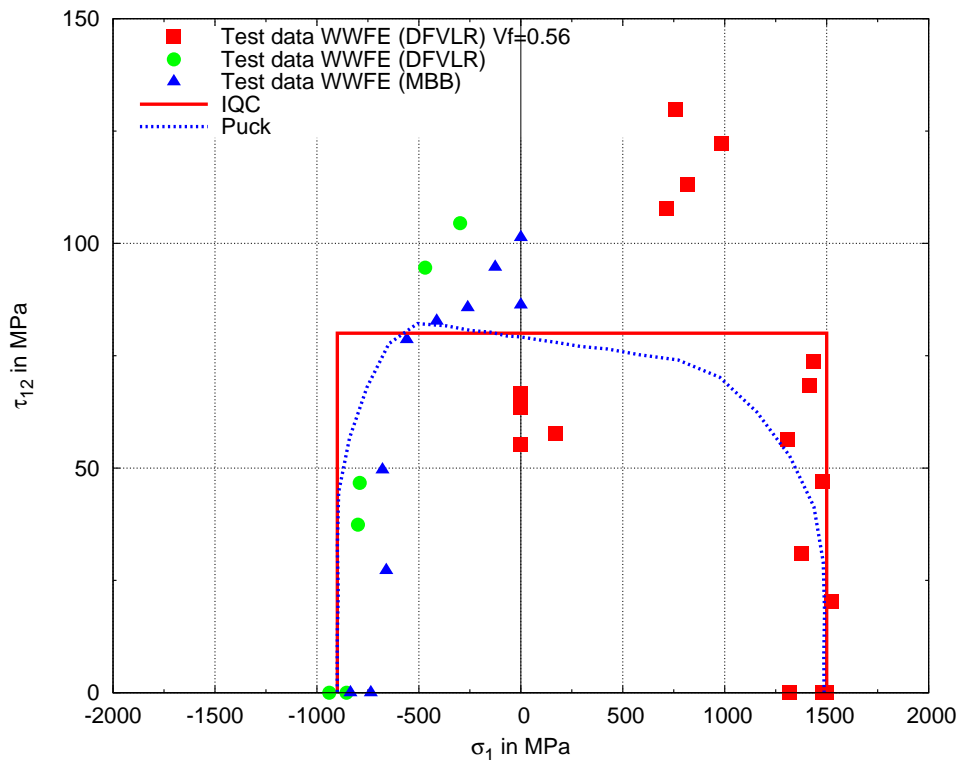


Figure 4.23: Load case 1: σ_2 - τ_{12} -failure envelope for GFRP-1 UD-Layer

Figure 4.23 shows failure envelopes of Puck and IQC for IFF in the σ_2 - τ_{12} -plane compared with test data. Firstly, it is apparent that the difference between the experimental results for input by Kraus/Schelling and for validation by Hütter is relatively large, especially under compression. Therefore, the simulation results are too conservative, but the shape is predicted well by both models. Overall, the differences between the criteria are very small, compared to the variance of the test data.

Load Case 2: σ_1 - τ_{12} -envelopeFigure 4.24: Load case 2: σ_1 - τ_{12} -failure envelope for CFRP-2 UD-Layer

Failure envelopes of Puck and IQC for FF and IFF in the σ_1 - τ_{12} -plane compared with test data are shown in Figure 4.24. Once again it is quite hard to interpret the test data, because of its wide variance. Especially under shear it is not clear why the test deliver such high values compared to the given in-plane shear strength of $R_{12} = 80\text{MPa}$. But it is also well known, that shear strengths are difficult to determine. Although the shapes of the two criteria are rather different it is not clear which predicts failure better. The IQC assumes that fibre-parallel stresses do not contribute to inter-fibre failure, in analogy to the formulation of the plastic yielding. Therefore, it resembles a maximum stress criterion in this load case, that works very well under tension. However, Puck's criterion predicts strength under compression better.

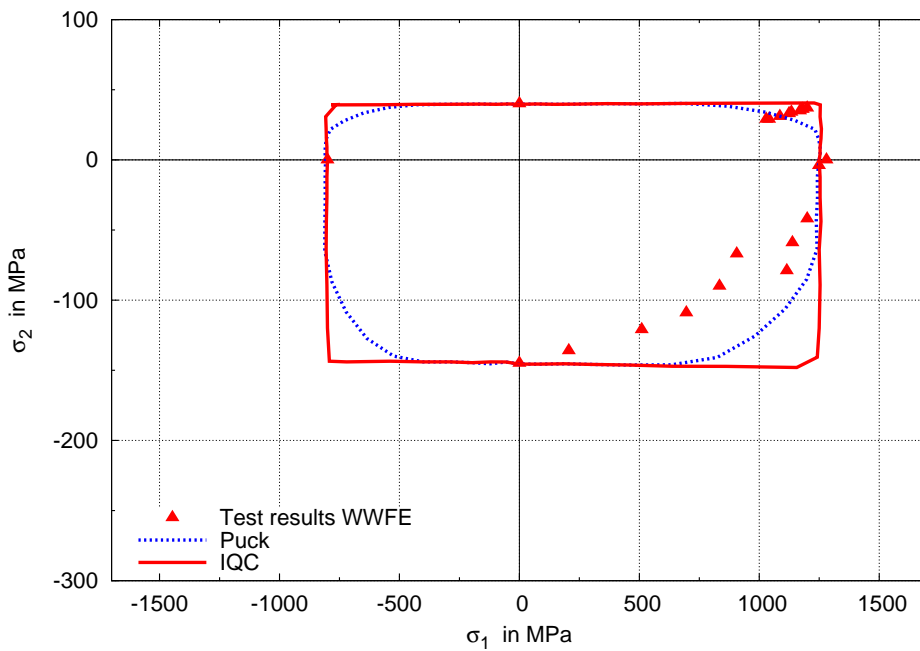
Load Case 3: σ_1 - σ_2 -envelope

Figure 4.25: Load case 3: σ_1 - σ_2 -failure envelope for GFRP-2 UD-Layer

Figure 4.25 shows failure envelopes of Puck and IQC for FF and IFF in the σ_1 - σ_2 -plane compared with test data. In this load case the criterion of Puck shows an advantage over the IQC, because it predicts the influence of fibre-parallel stresses better, see section 4.2.1.2. However, the strengths are still overestimated by Puck's criterion in mixed tension/compression load cases. It should be considered to consider the fibre-parallel stresses in the IFF-condition of the IQC, for instance over an additional invariant I_4 that incorporates these stresses as well.

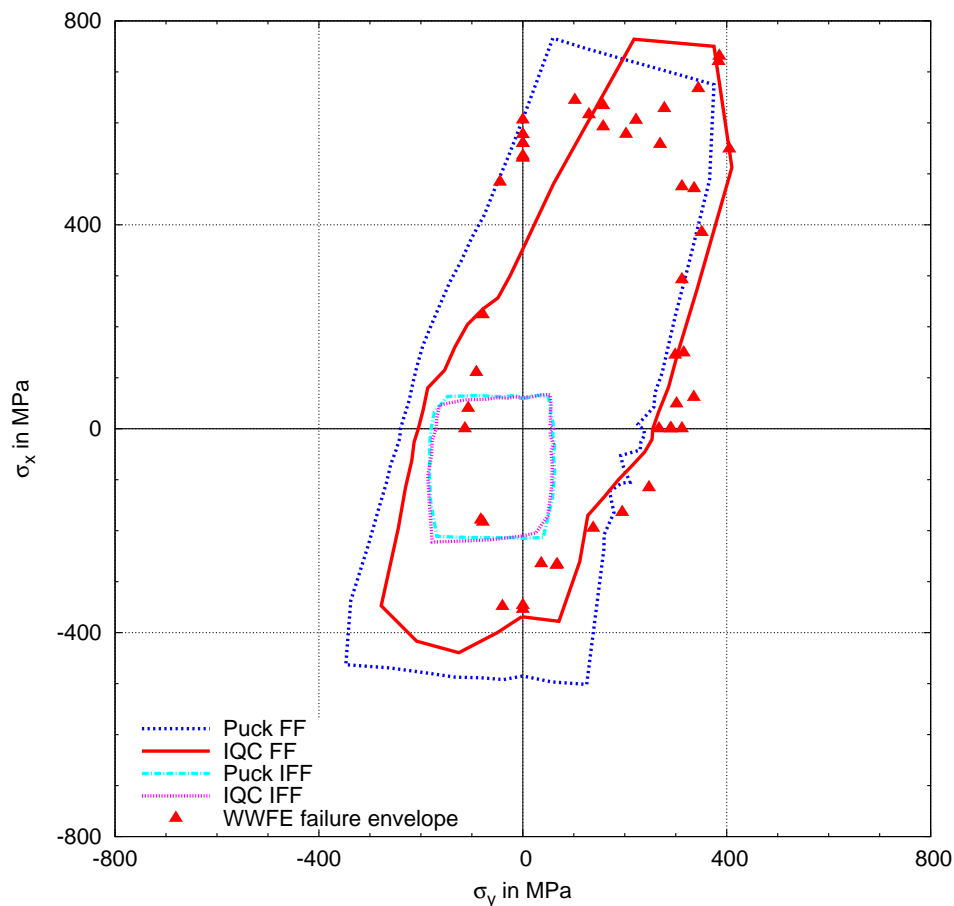
4.2.3.3 $(90^\circ/\pm 30^\circ)_s$ -LaminateLoad Case 4: σ_x - σ_y -envelope

Figure 4.26: Load case 4: σ_x - σ_y -failure envelope for GFRP-1 $(90^\circ/\pm 30^\circ)_s$ -Laminate

Failure envelopes of Puck and IQC for FF and IFF in the σ_x - σ_y -plane compared with test data are shown in Figure 4.26. The IFF curves depict the predicted first-ply failure, which was not determined in the tests. Both criteria show very little differences for IFF, but overestimate the compressive strengths of the laminate. Concerning the compressive failure it is stated in the WWFE by Hinton et al. (2004) that it was controlled whether buckling occurred during the tests. Buckling was neither considered in the simulation therefore it is probable that this overestimation can be attributed to buckling. In all other load cases the difference between the criteria is rather small and both can be judged equally good.

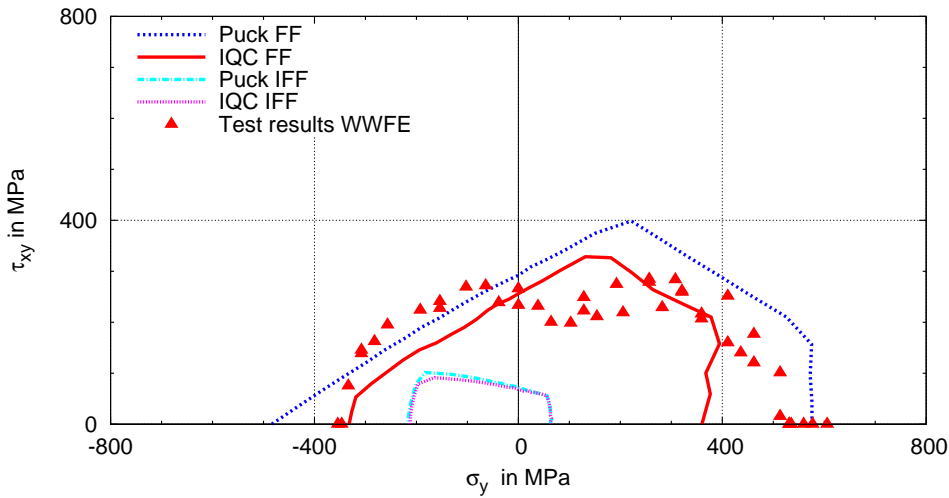
Load Case 5: σ_y - τ_{xy} -envelope

Figure 4.27: Load case 5: σ_y - τ_{xy} -failure envelope for GFRP-1 ($90^\circ/\pm 30^\circ$)_s-Laminate

Figure 4.27 shows failure envelopes of Puck and IQC for FF and IFF in the σ_y - τ_{xy} -plane compared with test data. The differences between the criteria in the detection of FPF, depicted here by IFF, are once again negligible, but unfortunately no test data exist for a validation. In final failure the IQC is more conservative than Puck's criterion, probably because the softening formulation does not take the in-situ effect into account, but degrades the stiffnesses relatively fast to zero. Especially for shear this has a great effect, because in Puck's degradation model about 20% of the initial shear stiffness remain. Overall, strengths are overestimated by Puck's criterion, but the IQC also overestimates strengths under shear. Hinton et al. (2004) state that an undocumented shear buckling might have taken place in the tests.

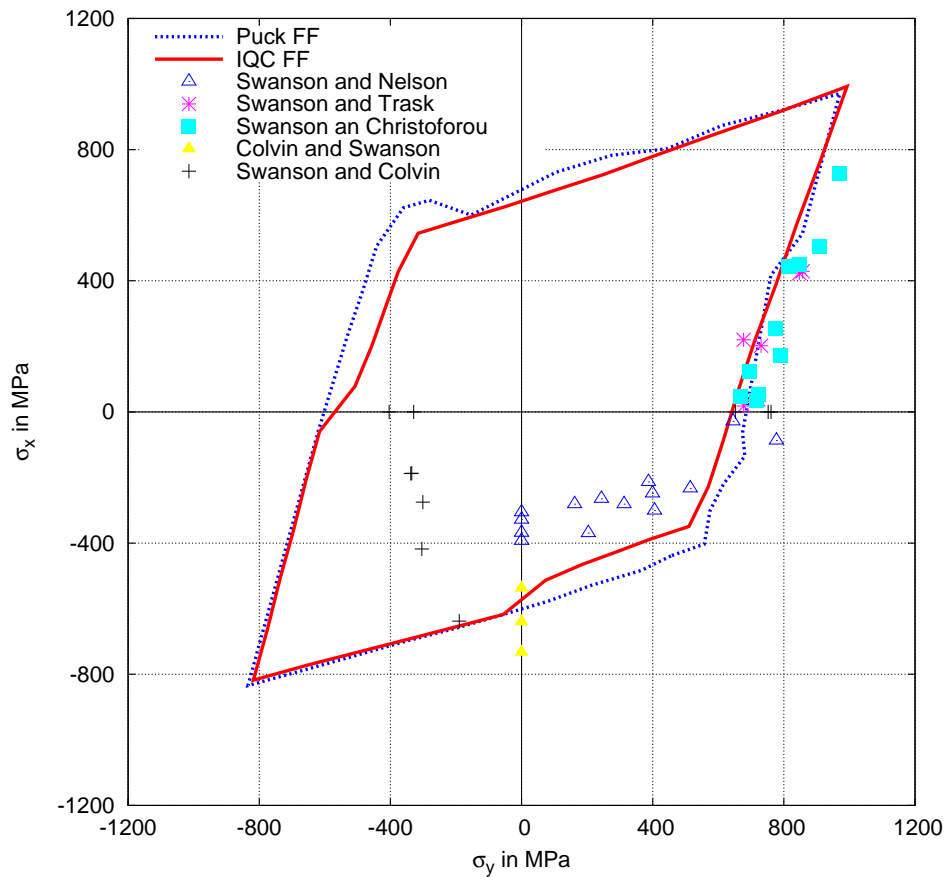
4.2.3.4 $(0^\circ/\pm 45^\circ/90^\circ)_s$ -LaminateLoad Case 6: σ_y - σ_x -envelope

Figure 4.28: Load case 6: σ_y - σ_x -failure envelope for CFRP-1 $(0^\circ/\pm 45^\circ/90^\circ)_s$ -Laminate

Failure envelopes of Puck and IQC for FF in the σ_y - σ_x -plane compared with test data are shown in Figure 4.28. In this load case the differences between Puck's criterion and the IQC are negligible. Once again, buckling in the tests might be an explanation of the overestimation of the compressive strengths of both models, see Hinton et al. (2004). Under mixed tension/compression the IQC reproduces the tendency of the test results slightly better.

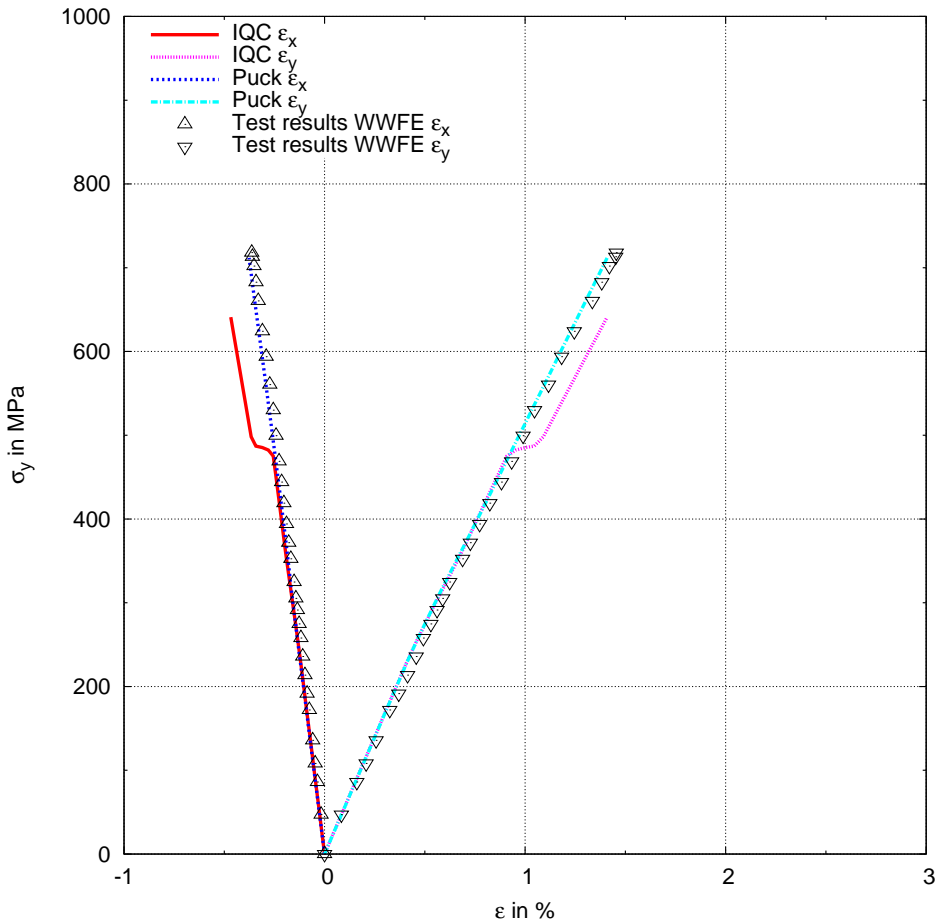
Load Case 7: ε_y 

Figure 4.29: Load case 7: σ_y - $\varepsilon_{x,y}$ -curve for CFRP-1 ($0^\circ/\pm 45^\circ/90^\circ$)_s-Laminate

Figure 4.29 shows stress-strain curves of Puck and IQC for a displacement-driven tensile load in ε_y direction compared with test data. At first glance, Puck's prediction is better than the prediction with the IQC, the difference to the test data is negligible. The IQC predicts the initial curve very well until an in-plane shear failure in the 45° -layers at 450-500 MPa that leads to a deviation. Interestingly Hinton et al. (2004) report a possible matrix failure at about 400 MPa which coincides perfectly with the prediction of the IQC. Due to the in-situ effect this matrix failure is not so apparent in the stress-strain curve, because the degradation spreads only slowly throughout the whole specimen. The softening formulation does not consider the in-situ effect and thus predicts a relatively sudden failure. Therefore, the simulation deviates from the test.

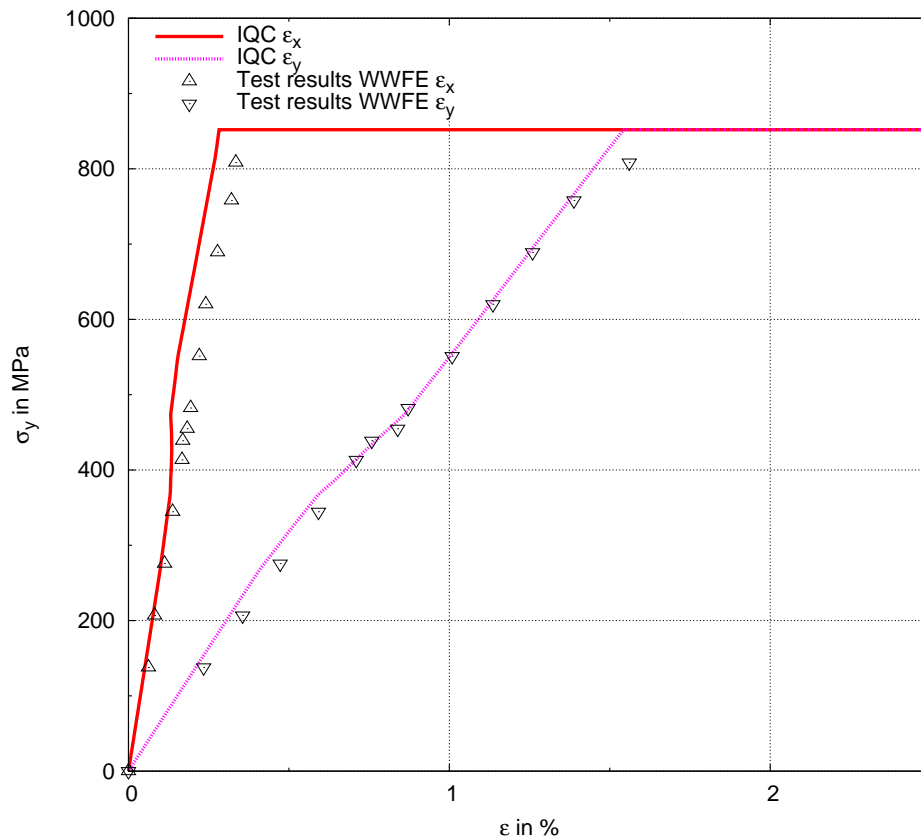
Load Case 8: $\sigma_y/\sigma_x = 2/1$ 

Figure 4.30: Load case 8: σ_y - $\epsilon_{x,y}$ -curve for CFRP-1 $(0^\circ/\pm 45^\circ/90^\circ)_s$ -Laminate

Stress-strain curves of Puck and IQC for a force-driven biaxial $\sigma_y/\sigma_x = 2/1$ load compared with test data are shown in Figure 4.30. The prediction of Puck's criterion is missing in this diagram, because of numerical problems. Test data and simulation fit very well together, especially the IFF at around 400 MPa is very well predicted by the simulation. However, the effect of IFF is slightly overestimated by the softening formulation of the IQC.

4.2.3.5 $(\pm 55^\circ)_s$ -Laminate

Load Case 9: σ_y - σ_x -envelope

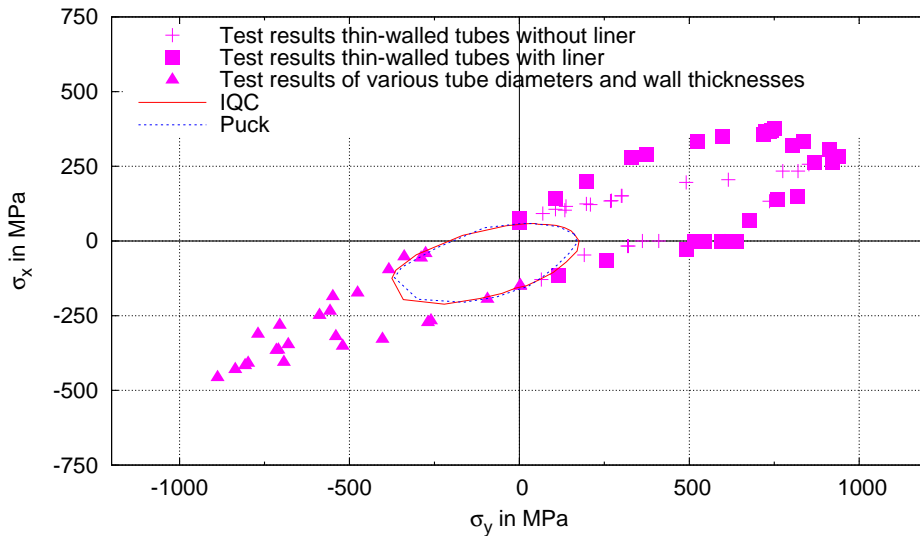
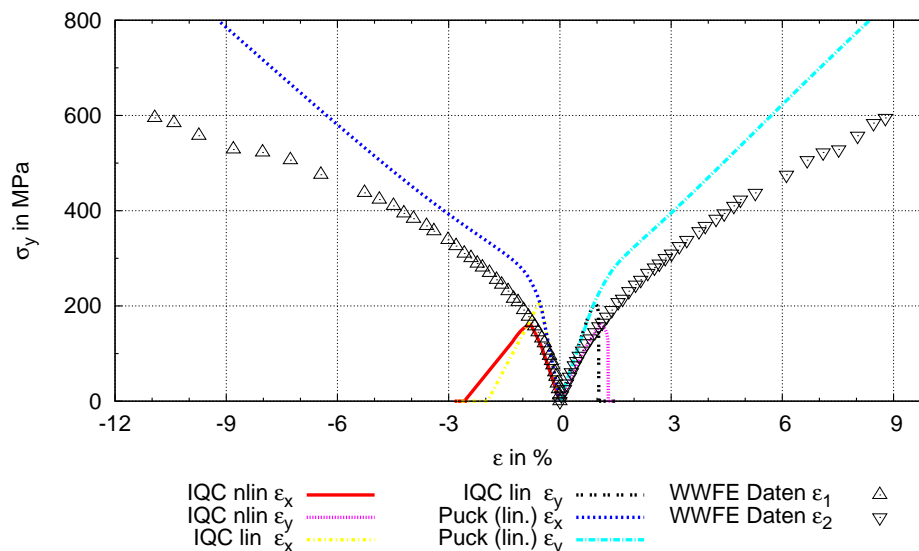


Figure 4.31: Load case 9: σ_y - σ_x -failure envelope for GFRP-2 $(\pm 55^\circ)_s$ -Laminate

Figure 4.31 shows failure envelopes of Puck and IQC for IFF in the σ_y - σ_x -plane compared with test data. This load case is not predicted very well by either of the failure criteria. The prediction of first-ply IFF is nearly identical and in good correspondence with the test results. However, the laminate lay-up leads to a simultaneous IFF of all layers and thus makes it complicated to judge upon the fatality of this failure. Puck and Schürmann (2004) introduce additional conditions, such as a maximum shear deformation of $\gamma=20\%$ to judge upon failure of the whole laminate. However, even with these additional conditions, a satisfying prediction could not be reproduced. Therefore, the prediction of final failure in this load case remains unresolved.

Load Case 10: ε_y Figure 4.32: Load case 10: σ_y - $\varepsilon_{x,y}$ -curves for GFRP-2 ($\pm 55^\circ$)_s-Laminate

Stress-strain curves of Puck and IQC for a displacement-driven tensile load in ε_y direction compared with test data are shown in Figure 4.32. In this load case the lamina are mainly loaded with shear stresses. Therefore, the application of a non-linear material behaviour, described in section 3.2, in the IQC yields much better results than with linear material. Once again the IQC degradation does not take into account the in-situ effect and thus estimates too conservative strengths. Although Puck's criterion predicts too high strengths the degradation model obviously catches the softening much better.

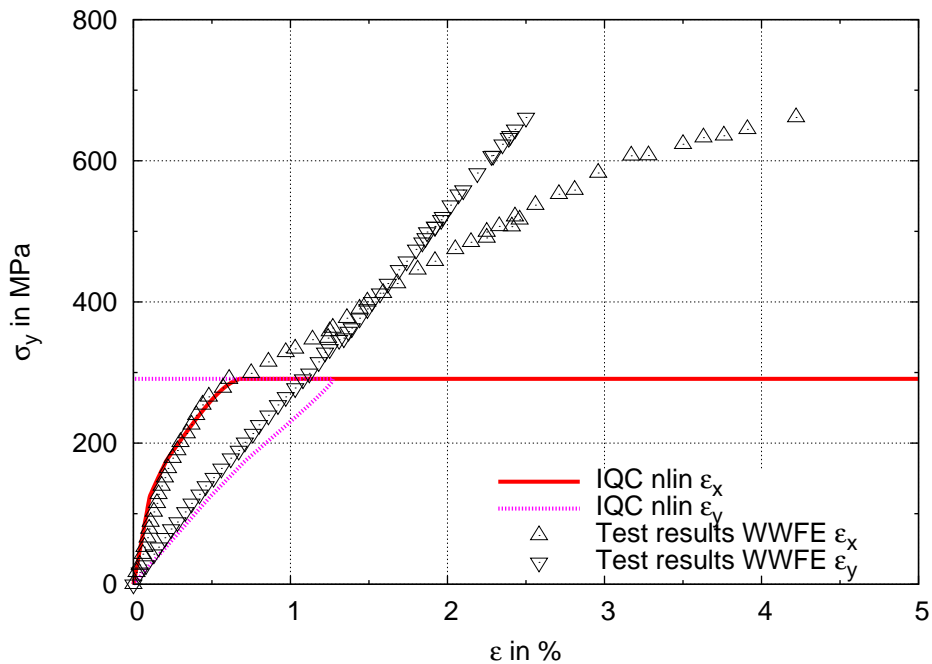
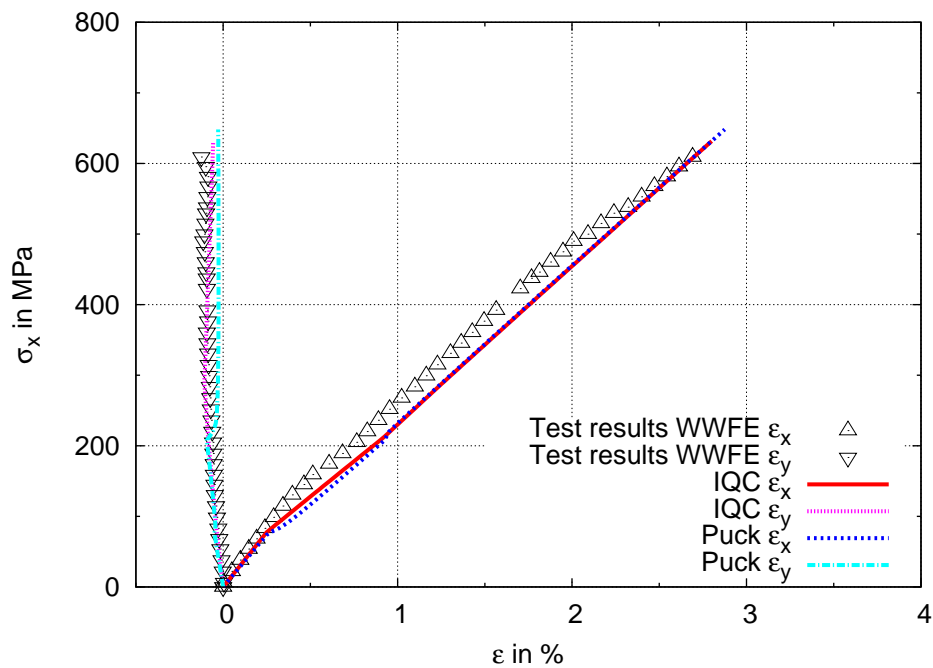
Load Case 11: $\sigma_y/\sigma_x = 2/1$ 

Figure 4.33: Load case 11: σ_y - $\varepsilon_{x,y}$ -curves for GFRP-2 ($\pm 55^\circ$)_s-Laminate

Figure 4.33 shows stress-strain curves of the IQC for a force-driven biaxial $\sigma_y/\sigma_x = 2/1$ load compared with test data. Predictions of Puck's criterion are not given here, because this load case requires non-linear material behaviour, which was not implemented. The stress-strain curves are predicted very well with the presented material model, also in the nonlinear regions. Failure is predicted early, however it is in good correspondence with the test results nonetheless, because a weeping of unlined tubes was reported at the same stress level, see Hinton et al. (2004). The weeping is caused by IFF, which is as well predicted by the IQC. Due to the applied softening formulation IFF leads to complete failure of the laminate, because the material is degraded up to zero stiffness.

4.2.3.6 $(0^\circ/90^\circ)_s$ -LaminateLoad Case 12: ε_y Figure 4.34: Load case 12: σ_y - $\varepsilon_{x,y}$ -curves for GFRP-2 $(0^\circ/90^\circ)_s$ -Laminate

Stress-strain curves of Puck and IQC for a displacement-driven tensile load in ε_y direction compared with test data are shown in Figure 4.34. This load case is predicted very well by both simulations.

4.2.3.7 $(\pm 45^\circ)_s$ -Laminate

Load Case 13: $\sigma_y/\sigma_x = 1/1$

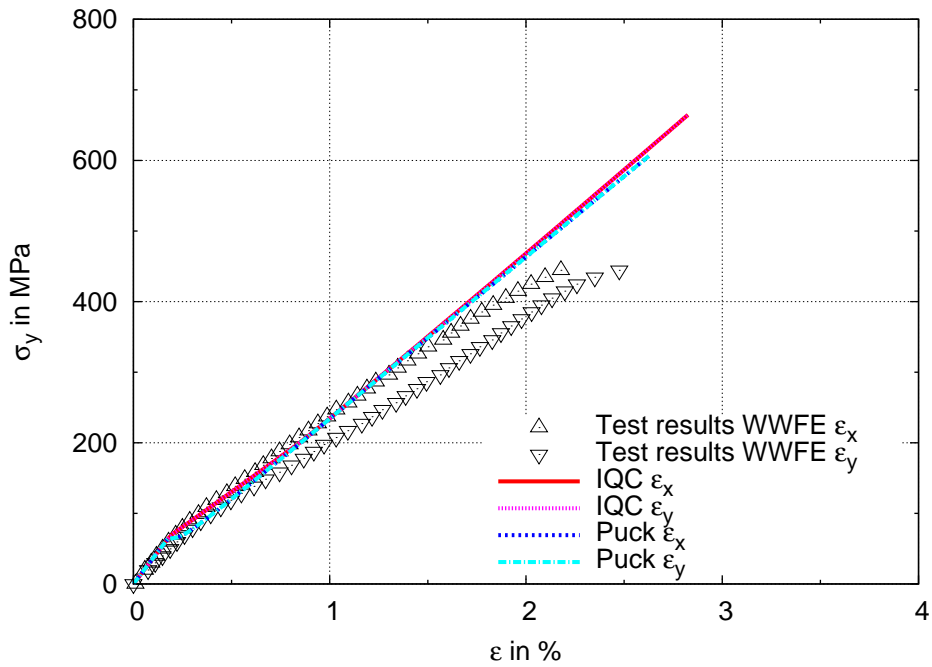


Figure 4.35: Load case 13: σ_y - $\varepsilon_{x,y}$ -curves for GFRP-2 $(\pm 45^\circ)_s$ -Laminate

Figure 4.35 shows stress-strain curves of Puck and IQC for a force-driven biaxial $\sigma_y/\sigma_x = 1/1$ load compared with test data. Both simulations overestimate the strength of the laminate in this load case. The nonlinearity of the test results is not described by the models. Nevertheless, the prediction of the first damage at around 70 MPa is predicted very well by both models.

Load Case 14: $\sigma_y/\sigma_x = 1/ -1$

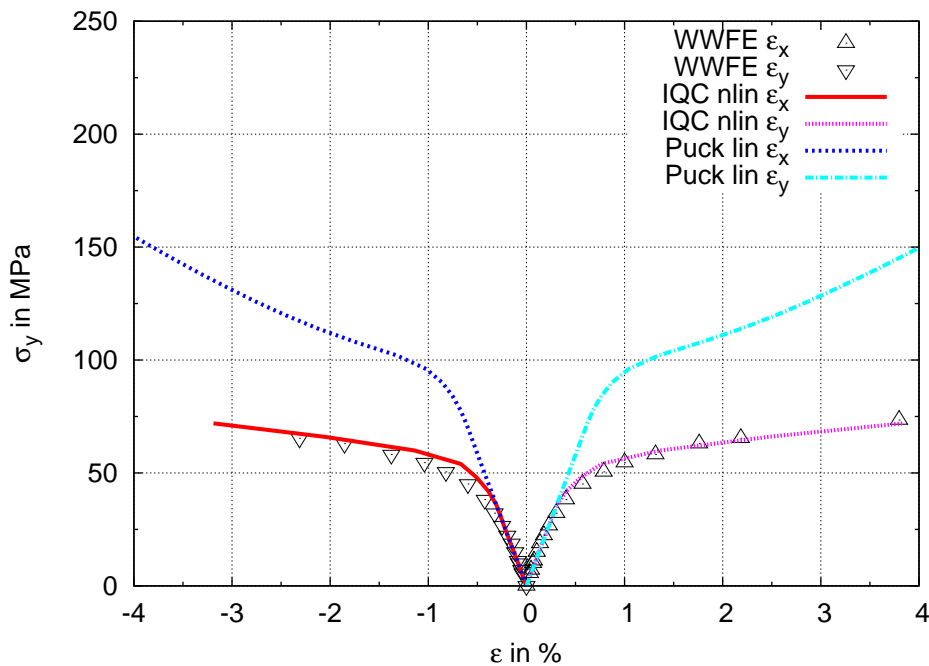


Figure 4.36: Load case 14: σ_y - $\varepsilon_{x,y}$ -curves for GFRP-2 ($\pm 45^\circ$)_s-Laminate

Stress-strain curves of Puck and IQC for a force-driven biaxial $\sigma_y/\sigma_x = 1/ -1$ load compared with test data are shown in Figure 4.36. The nonlinear behaviour prior to failure is characteristic for this load case. Therefore, the linear material used together with Puck's criterion model does not perform very well. Both failure criteria predict an IFF at $\sigma_y \cong 70$ MPa correctly, but the predictions for the deformations are very different. The softening formulation of Puck does not yield reasonable results for this load case, probably due to the fact that all laminas fail simultaneously, which means that the in-situ effect does not occur. This result shows that the incorporation of the in-situ effect in the softening formulation can be misleading and requires a thorough checking on each application.

In combination with the nonlinear material model presented in section 3.2, the nonlinearity of the stress-strain curve can be simulated very well with the IQC. A nonlinear material model was not implemented for Puck's criterion, therefore it cannot be judged which criterion works better with a nonlinear material model. However, it is evident that a nonlinear material model is needed for a realistic failure prediction.

4.2.3.8 Conclusion

Overall, the failure criteria are equally suited for failure prediction of FRP-laminates. Especially IFF is mostly detected at the same stress levels. In the load cases 4, 5 and 6 the strengths are partly overestimated in the compression or shear regime, but this can probably be explained by buckling in the tests.

The main differences between the numerical results can be attributed to the material and degradation models. As a matter of fact, the Puck degradation model works little bit better for laminates, because it accounts for the in-situ effect. If the strength of laminates should be evaluated with the presented degradation model, an adapted degradation model that considers the in-situ effect would be necessary. However, load case 14 shows that an incorporation of the in-situ effect can also overestimate strength, if failure in adjacent lamina takes place simultaneously. The presented softening approach with zero remaining stiffness predicts conservative results, but does not lead to such overestimations. For computations on the mesoscale the in-situ effect should be neglected anyway and the regularization of the softening behaviour is of most importance. Therefore, the presented degradation model is better suited for such simulations.

The load cases 7, 13 and 14 have also been computed with the SPC in combination with Puck's degradation model and were found to give identical results. Considering the fact that the SPC is the simpler approach, it seems to be the better choice, because the results are equal.

4.3 Failure Criterion for Textile Composites

One textile layer incorporates at least two different fibre directions, because it consists of an impregnated textile fabric. Mostly, these different fibre directions are also arranged in distinguishable layers inside the textile layer that are connected through a textile technique. Therefore, failure criteria for textile composites can be formulated in two different ways.

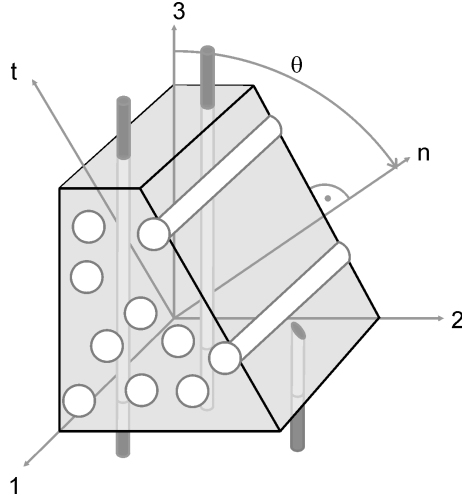
Firstly, the failure criterion can be formulated for the whole textile layer. The advantage of this method is, that the required strengths can be determined experimentally. However, numerous tests may have to be carried out, because a textile layer exhibits orthotropic, or even anisotropic behaviour. Furthermore, the determination of through-thickness strengths is problematic, because only specimens with the thickness of the textile layer can be produced, that are usually too thin for through-thickness testing, see section 2.4.2. The disadvantage of this method is, that the failure mechanisms cannot be described very well, because the experimental detection of inter-fibre failure is not possible, see section 7.3. The previous chapter, however, showed clearly that especially a good description of the failure mechanisms is required for a good estimation of the strengths in simulation.

Secondly, the failure criterion can be formulated for one layer inside a textile layer. Thus, a textile layer is modelled with multiple laminas, one for each fibre direction. This method allows for a very detailed description of the failure mechanisms in each lamina. Unfortunately, it is not possible to determine the properties of the laminas experimentally, because the textile layer cannot be disassembled for testing. This method is used nonetheless, with properties of the laminas derived from UD-layers. Although each lamina has orthotropic material behaviour, due to the through-thickness reinforcements, failure criteria for UD-composites are then used for failure prediction. For thin laminates in thin-walled structures, this simplification is probably not very restrictive. However, the positive influence of the through-thickness reinforcements is neglected by this method and a criterion for an orthotropic lamina is favorable.

4.3.1 Failure Criterion of Juhasz

Juhasz et al. (2001) have proposed a criterion for an orthotropic lamina in a textile layer. It is based on the SPC, see section 4.2.1.3, the only difference are the strengths of the action plane. Juhasz et al. (2001) generalize the concept of the action plane in so far that the action plane may be crossed by the through-thickness reinforcements, under the preposition that the through-thickness reinforcements are much weaker than the in-plane reinforcements. In fact, they consider the action plane only as the plane of damage initiation, but not necessarily as the plane of damage evolution.

Fibre failure is evaluated with the conditions of Puck, given in eq. 4.25 and eq. 4.26. The algorithm for the IFF condition is the same as in Puck's criterion and in the SPC. Through a variation of the action-plane angle θ , see Figure 4.37, the plane of maximum effort is determined. In contrast to the SPC the action-plane strengths are not constant

Figure 4.37: Definition of action-plane angle θ

in the criterion of Juhasz et al. (2001), but dependent on the action plane angle θ to account for the influence of the through-thickness reinforcements:

$$\begin{aligned}
 R_n^{(z,d)} &= \tilde{R}_2^{(z,d)} \sin^2 \theta + \tilde{R}_3^{(z,d)} \cos^2 \theta + \tilde{R}_{23}^{(z,d)} |\sin 2\theta| \\
 R_{nt}^{(z,d)} &= \left(\tilde{R}_2^{(z,d)} + \tilde{R}_3^{(z,d)} \right) |\sin 2\theta| + \tilde{R}_{23}^{(z,d)} \\
 R_{n1}^{(z,d)} &= \tilde{R}_{12}^{(z,d)} |\sin \theta| + \tilde{R}_{13}^{(z,d)} |\cos \theta|.
 \end{aligned} \tag{4.47}$$

After transformation of the lamina stresses on the action plane in analogy to eq. 4.24 the IFF action-plane criterion of Juhasz et al. (2001) reads

$$\sqrt{(1-p^z)^2 \left(\frac{\sigma_n}{R_n^z} \right)^2 + \left(\frac{\tau_{nt}}{R_{nt}^z} \right)^2 + \left(\frac{\tau_{n1}}{R_{n1}^z} \right)^2} + p^z \frac{\sigma_n}{R_n^z} = 1 \tag{4.48a}$$

for $\sigma_n \geq 0$ and

$$\sqrt{(p^d)^2 \left(\frac{\sigma_n}{R_n^d} \right)^2 + \left(\frac{\tau_{nt}}{R_{nt}^d} \right)^2 + \left(\frac{\tau_{n1}}{R_{n1}^d} \right)^2} + p^d \frac{\sigma_n}{R_n^d} = 1 \tag{4.48b}$$

for $\sigma_n < 0$ in analogy to the SPC. Table 4.7 summarizes the parameters required by the criterion of Juhasz et al. (2001).

It is important that Juhasz (2003) discriminates between strengths $R_i^{(t,c)}$ and strength parameters $\tilde{R}_i^{(t,c)}$ of the IFF criterion. The strength parameters $\tilde{R}_2, \tilde{R}_3, \tilde{R}_{12}, \tilde{R}_{13}$ and \tilde{R}_{23} as well as the slope parameters are determined with a fitting procedure from off-axis tests in the 1-2- and 1-3-plane from the strengths R_2, R_3, R_{12}, R_{13} and R_{23} . For a reduction of

Table 4.7: Strengths and strength parameters of Juhasz's criterium

Strengths R_σ, R_τ of orthotropic layer			Strength parameters $\tilde{R}_\sigma, \tilde{R}_\tau$ of Juhasz-criterium			Slope parameters p	
tension	compression	shear	tension	compression	shear	tension	compression
R_1^t	R_1^c	R_{12}	-	-	$\tilde{R}_{12}^{t,c}$	p^t	p^c
R_2^t	R_2^c	R_{13}	\tilde{R}_2^t	\tilde{R}_2^c	$\tilde{R}_{13}^{t,c}$		
R_3^t	R_3^c	R_{23}	\tilde{R}_3^t	\tilde{R}_3^c	$\tilde{R}_{23}^{t,c}$		

the experimental effort mesomechanical unit cells are presented in chapter 7, that allow for a numerical determination of these parameters.

The criterion of Juhasz et al. (2001) is made for a lamina inside a textile layer that has a weaker through-thickness than in-plane reinforcement. The boundaries of its applications are not yet determined, but a non-crimp fabric is certainly a textile composite that fits this definition. However, for a very weak through-thickness reinforcement it is probably also possible to use criteria for UD-composites without much loss of accuracy.

Juhasz (2003) does not propose a softening formulation for the simulation of progressive failure. Due to the common basis of this criterion and Puck's criterion it is possible to use Puck's softening model. The softening formulation has to be extended to orthotropic layers.

4.3.2 Off-Axis Tests for Criterion of Juhasz

The criterion of Juhasz requires a parameter-fitting procedure with off-axis tests, which include tests in through- thickness direction. Coupon specimens for such a test have to incorporate through-thickness reinforcements over the whole length of the specimen. Juhasz (2003) has therefore proposed coupon specimens that correspond to such a through-thickness reinforced lamina.

For in-plane off-axis tests 2 mm thick laminates solely of 0° -layers are used. Coupon specimens are cut out under different angles α , see left hand side of Figure 4.38. The through-thickness reinforcements are neglected in these tests.

For out-of-plane (1-3-plane) off-axis tests 2 mm thick $[0^\circ[0^\circ/90^\circ]_20^\circ]_S$ -laminates are used. The 90° orientation represents the through-thickness reinforcements. Coupon specimens are cut out under different angles α corresponding to the 0° -direction, see right hand side of Figure 4.38.

Figure 4.39 shows the experimentally determined strengths normalized with the tensile and compressive strengths, dependent on the off-axis angle α . Results for in-plane off-axis tests are given in Figure 4.39(a), for out-of-plane off-axis tests in Figure 4.39(b). A comparison of both curves shows the influence of the through-thickness reinforcement under an angle of $\alpha = 90^\circ$.

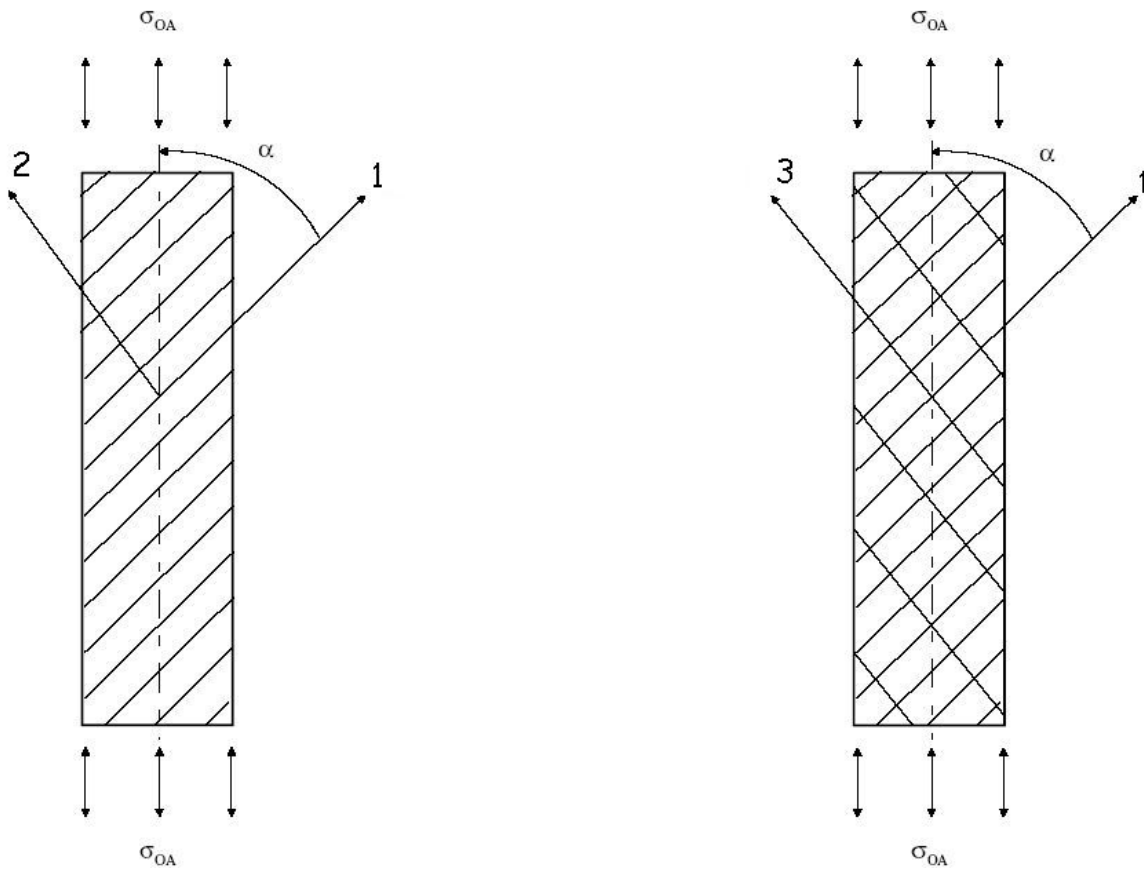


Figure 4.38: Off-axis-tests source: (Juhasz, 2003)

The subsequent parameter fitting procedure is given in Juhasz (2003) in detail.

4.3.3 Discussion of Juhasz-Criterion

Naturally, it is required to make assumptions in the formulation of a failure criterion. Some assumptions of Juhasz appear to be questionable and thus shall be discussed in this section. Juhasz assumes different shear strengths under tension and compression $R_{nt}^z \neq R_{nt}^d$ to make his FF and IFF conditions meet the same strength for an in-plane off-axis-load at $alpha = 2^\circ$. This assumption leads to discontinuities in the failure surface that are physically not reasonable. Furthermore, these discontinuities are problematic in numerical simulations, where the numerical precision can easily lead to changes of σ_n from positive to negative values and back between time steps. To the author it seems questionable, that the transition between FF and IFF has to take place at an angle $alpha = 2^\circ$ for tension and compression, because prove for such behaviour could not be found in literature. A different transition angle between FF and IFF under tension and compression seems physically more senseful than different shear strengths under tension and compression.

The criterion of Juhasz is made especially for weak through-thickness reinforcements, i.e. for an orthotropic layer with $R_2^{(z,d)} \approx R_3^{(z,d)}$. It is based on the SPC, see section 4.2.1.3, but

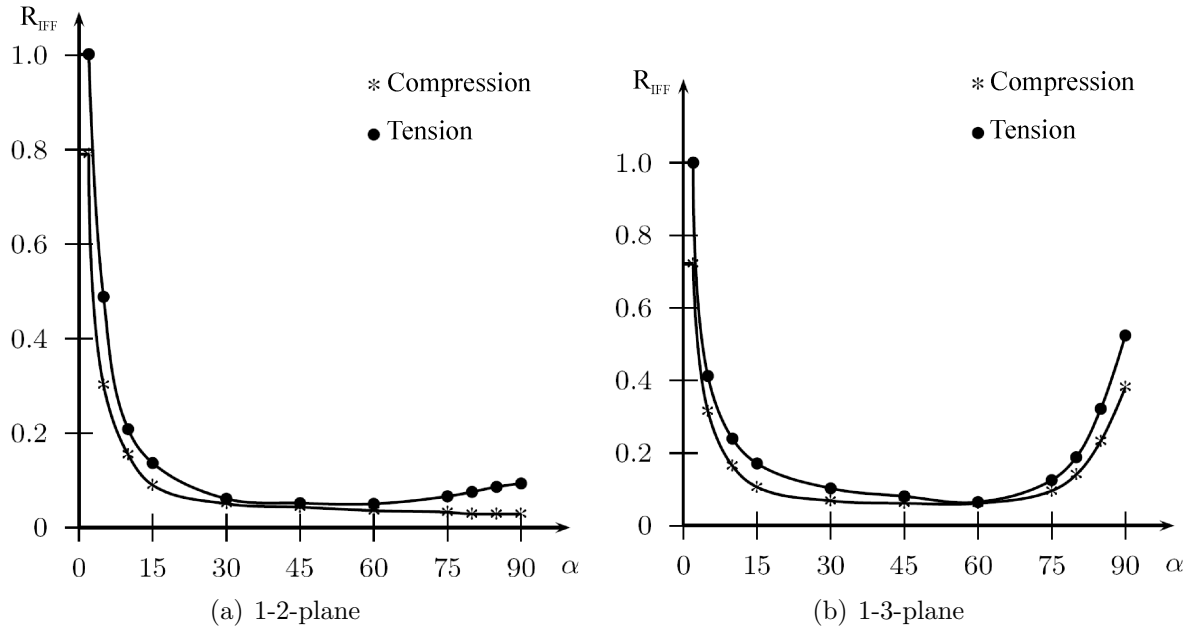


Figure 4.39: Normalized strength dependent on off-axis angle α (source: DLR/FA)

the SPC is not comprised in Juhasz' criterion for the special case of transversely isotropic material behaviour. If transversely isotropic strengths $R_2^{(z,d)} = R_3^{(z,d)} = R_{\perp}^{(z,d)}$, $R_{12} = R_{13} = R_{\parallel}$ are input in Eq. 4.47, the strengths of the action plane

$$\begin{aligned}
 R_n^{(z,d)} &= R_{\perp}^{(z,d)} \sin^2 \theta + R_{\perp}^{(z,d)} \cos^2 \theta + R_{\perp\perp}^{(z,d)} |\sin 2\theta| \\
 &= R_{\perp}^{(z,d)} + R_{\perp\perp}^{(z,d)} |\sin 2\theta| \neq R_{\perp}^{(z,d)} \\
 R_{nt}^{(z,d)} &= \left(R_{\perp}^{(z,d)} + R_{\perp}^{(z,d)} \right) |\sin 2\theta| + R_{\perp\perp} \neq R_{\perp\perp} \\
 R_{n1} &= R_{\parallel} |\sin \theta| + R_{\parallel} |\cos \theta| \neq R_{\parallel}
 \end{aligned} \tag{4.49}$$

are not the same as in the SPC. The eqns 4.49 are illustrated in Figure 4.40, that shows the dependence of the action-plane strength parameters on the action plane angle θ for the transversely isotropic case. In contrast to the SPC, in the criterion of Juhasz the action plane strengths are not constant, only their minima for $\theta = 0^\circ$ and $\theta = 90^\circ$ coincide with the physical value. Therefore, the criterion of Juhasz yields other results than the SPC for UD-composites and thus is probably not suited well for very weak through-thickness reinforcements.

Juhasz does not use test specimen with weak through-thickness reinforcements. The presented off-axis test specimen are rather usual laminates than through-thickness reinforced layers, in which 25 % of the fibres are oriented in "thickness"-direction. Such a strong through-thickness reinforcement can surely be found only locally in composite structures.

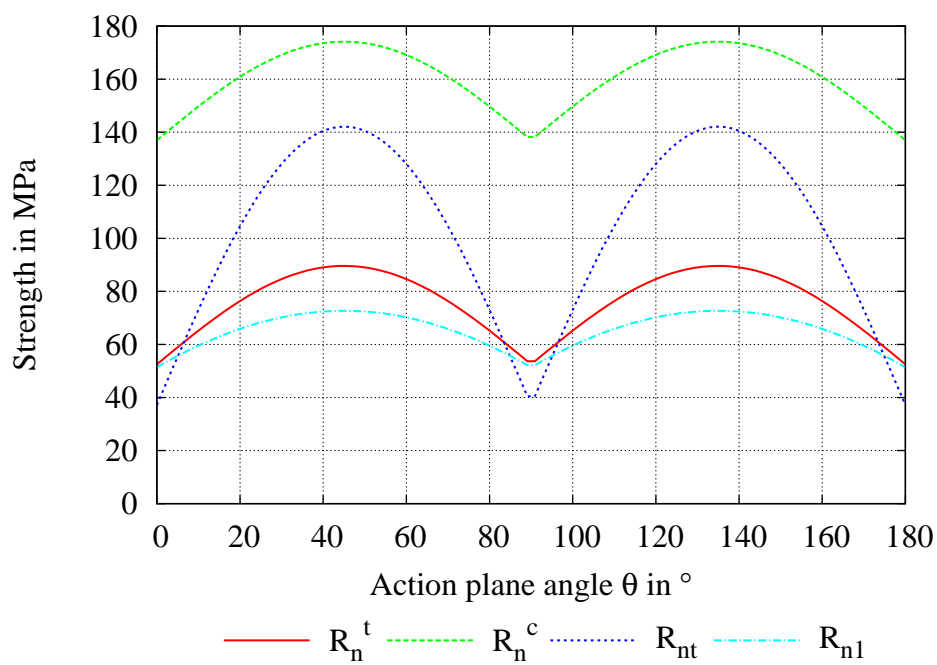


Figure 4.40: Action-plane strengths after Juhasz for transversely isotropic material

5 Multiscale Analysis

In this chapter firstly a short introduction into the theory of multiscale analyses and homogenization is given that includes a description of boundary conditions used for homogenization in the presented multiscale algorithm. Secondly, a multiscale algorithm for determination of stiffness and strength of textile composites is presented, see also Rolfes, Ernst, Vogler, and Hühne (2008).

5.1 Basic Concept of Multiscale Analysis

The main idea of conducting a multiscale simulation is to incorporate effects from lower levels into a computation of a structure at macroscale, because it is not possible to account for the heterogeneity of the material on this scale alone. Therefore, the multiscale analysis has a special importance for virtual testing, because it is able to account for various effects on different scales at a time.

5.1.1 Need for Different Length Scales

When dealing with atomic structures it becomes very clear that every matter is a structure and that there is no such thing as a continuum material. Of course, an engineer cannot simulate the atomic structures of bridges or aeroplanes. Therefore, the atomic structure is homogenized and regarded as a continuum. A phenomenological material model is then needed for this continuum, to describe the material behaviour. The parameters of the material model are determined by experimental tests and the atomic structure is of no concern. When on the other hand experimental tests shall be replaced or reduced, it is possible to derive the material properties of the continuum with a homogenization procedure from the atomic structure. This is called a bottom-up approach. At nanoscale a Representative Volume Element (RVE) is discretized that should be representative for the material on macroscale. Unfortunately, most materials have defects, or flaws, that are very important for the behaviour on macroscale, but that are too big to fit in the nanoscale RVE. Thus, another RVE has to discretize the structure of the flaws in between nanoscale and macroscale. Most macroscale materials have quite numerous intrinsic structures at different scales, that have to be taken into account in a complete bottom-up approach. Diamonds and metals are relatively perfect, but especially composites have many intrinsic structures. Therefore, a multi-scale simulation is needed to determine its macroscale material properties. A multiscale simulation does not necessarily start at nanoscale, if the material behaviour on a higher scale can be described reliably. Material behaviour

of glass-fibres and epoxy resin is well-known, see chapter 2 and sophisticated material models, failure criteria and softening formulations are presented in chapters 3 and 4. Therefore it is only natural to take the microscale, where fibre and matrix are discretized, as a starting point for a multiscale simulation of textile composites.

Fortunately for the engineer most structures behave predictably linear within certain limits. In the past mostly the limits of linearity were determined and structures were designed to remain within these limits. Growing knowledge about non-linearities of materials makes it possible to gain economic profits from building lighter structures that exhibit uncritical nonlinear behaviour.

5.1.2 Information-passing and Coupled Multiscale Analysis

There are mainly two types of multiscale analysis, coupled multiscale analysis on the one hand and information-passing multiscale analysis on the other. They have in common that results from a lower scale are homogenized and used as the material behaviour on the upper scale. Furthermore, both employ the same RVEs or unit cells.

In the coupled multiscale analysis the computation is carried out simultaneously on all scales. Each macroscale integration point in a FE-analysis has a lower scale RVE that is used to simulate the material behaviour in each increment. Main challenge of this method is to define boundary conditions top-down and bottom-up as well as to make the RVE on the lower scale as small as possible to save computational time. The advantage of this coupling is that no material model is needed on macroscale, the RVE only is used to describe the constitutive behaviour on macroscale. In an FE-simulation the macro-strains of the Gauss point are applied on the micro-model, and the resulting mean stresses are taken as the macro-stresses. Thus, no further assumptions or approximations commonly made in a material model restrain the results of this analysis. The development of an appropriate material can cost a significant amount of development time, and a great effort has to be made that the macroscale material model is able to incorporate all effects from the lower scale. Another advantage of the coupled multiscale analysis is that the mesh on microscale can easily be adapted to known local imperfections on the macroscale. If, for instance, a textile fabric is sheared in the draping process, its lay-up may differ significantly from the initial configuration. In a coupled multiscale analysis at each Gauss point another micromodel may be applied according to the mesomechanical geometry, see Haasemann, Kästner, and Ulbricht (2006). The main disadvantage of this method is of course its long runtime, because of the many RVEs that have to be simulated. Therefore, it is crucial that the FE-mesh of the RVE is as coarse as possible, which implies that the results are compromised, if no sophisticated techniques, like e.g. X-FEM, see Kästner, Haasemann, Brummund, and Ulbricht (2008), are applied. The high computational cost also forbids the use of monte-carlo simulations of the RVE. For example randomized micromechanical RVEs with a high number of fibres, as described in section 6.3, could not be simulated in each increment in a reasonable time. However, increasing computational power will make this disadvantage disappear in future.

In the information-passing multiscale analysis different scales are computed sequentially. Usually, the simulation starts on the lowest scale. The homogenized results are then passed

to the next scale, where they are used as input for a material model. Main challenge of this method is to define appropriate material models that are able to describe all relevant effects from the lower scale. The advantage of the information-passing multiscale analysis is its shorter runtime, especially if numerous computations, for example many load cases, must be carried out on macroscale. No matter how many simulations are carried out on macroscale, lower scale simulations have to be carried out only once. Therefore, it is no problem to use very refined RVEs on microscale and thus to produce better results on the lower scales. If, for instance, a statistical fibre distribution on microscale should be evaluated, this does not effect the computational time on macroscale. On the other hand, consideration of local imperfections on macroscale, e.g. fibre misalignments from draping as described above, is relatively labor-intensive, because many computations have to be carried out on the microscale. However, an efficient scripting technique may alleviate this disadvantage. Another possible drawback is that the material model applied on the macroscale may contain restrictive assumptions that can easily be overlooked.

5.2 Homogenization

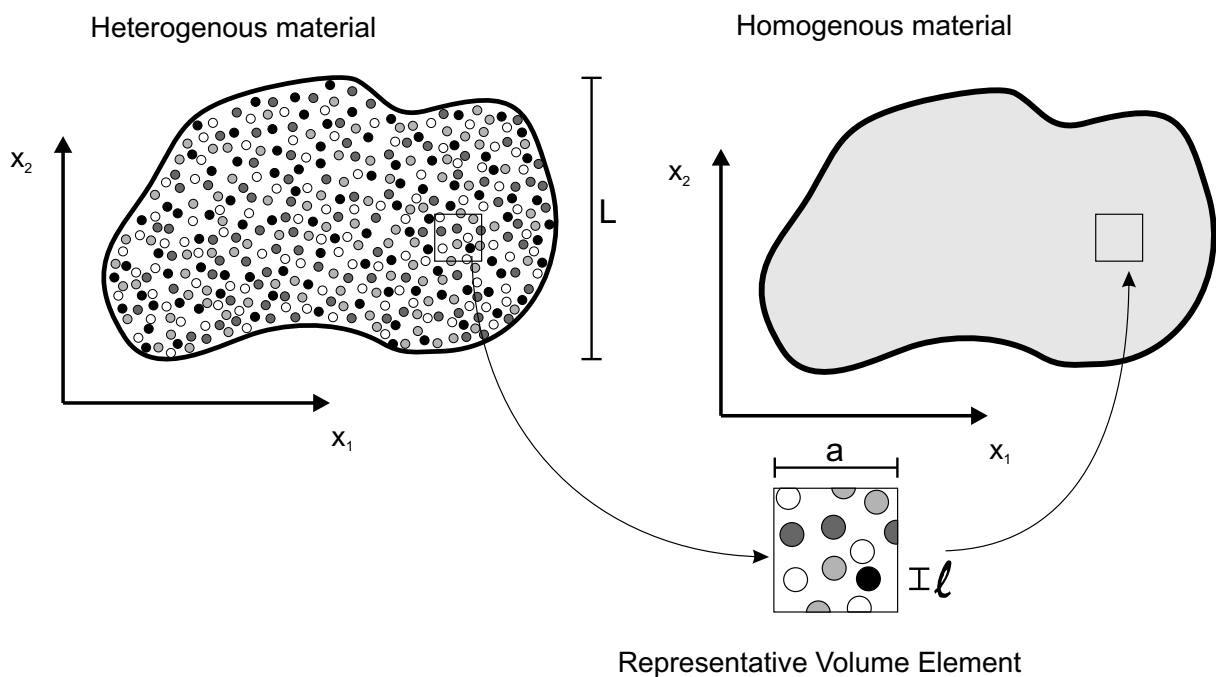


Figure 5.1: Homogenization of heterogeneous structure via Representative Volume Element (RVE)

Homogenization is used to simplify a heterogeneous material as a homogeneous one, see Figure 5.1. It bridges the two characteristic length scales of lower scale l and upper scale L . These length scales are also important for the geometry and dimension of the RVE that is used to describe the heterogeneity of the material on the lower scale. In a homogenization from micro- to mesoscale for the lower scale length l is the diameter of a

fibre on the microscale, for example, whereas the fibre bundle thickness on the mesoscale is the upper scale length L , see Figure 5.1. The same fibre bundle thickness is the lower scale length l in a homogenization from meso- to macroscale. Typical upper scales lengths L on the macroscale are layer thickness, stringer height or stringer spacing of a stiffened panel. Thus, the length L is dependent on the direction, i.e. in thickness direction it can be smaller than in in-plane direction.

5.2.1 Representative Volume Element and Unit Cell

The RVE is used to describe a representative part of the material. It should incorporate all relevant components, e.g. fibre and matrix on the microscale, in a statistically homogeneous distribution. The statistical homogeneity requires the dimension of the RVE, a , to meet the criterion

$$l \ll a \quad . \quad (5.1)$$

If this criterion is fulfilled, the properties of the RVE can be assumed to be representative for the properties of the material. Unfortunately, an inhomogeneity throughout the whole RVE violates the requirement of statistical homogeneity. Therefore, this criterion prohibits the determination of strength and softening, because either of these requires the localization of a crack, plastic zone, etc. through the whole RVE.

Usually, a uniform load distribution is assumed in the boundary conditions of the RVE, although an inhomogeneous stress or strain distribution is present on the upper scale. Therefore, the RVE is required to be much smaller than the length scale L of the upper scale,

$$a \ll L \quad (5.2)$$

to enable a piecewise linear approximation of the inhomogeneous upper scale stress or strain distribution. If it is not possible to account for this condition, because the RVE size a is too large, further load distributions have to be applied on the RVE. A linear strain distribution resulting from a moment is for instance used by Karkkainen and Sankar (2006).

A special case of the RVE is the unit cell (UC). It is used in case the material has a periodic substructure and it consists of only one single substructure. If such a periodicity occurs, the requirement of statistical homogeneity is of no concern, thus $l \approx a$. Therefore, a UC is much smaller than an RVE, e.g. it contains 1 fibre instead of 100. Inhomogeneities like cracks can spread through the whole UC, because they are assumed to appear periodically in the whole material. Figure 5.2 shows a crack in a square micromechanical unit cell, see section 6.2 with one quarter of a fibre and with four fibres. The cracks are identical and periodic, thus, the stress-strain curves are identical as well. Therefore, it is possible to determine strength and softening with a UC.

If a material substructure is not strictly periodic due to imperfections and localized cracks occur, a homogenization of unit cell strengths is not allowed, strictly spoken. However, it has to be remembered that IFF does not lead to a single crack in a composite, but to multiple cracks in the characteristic damage state due to the in-situ effect. Therefore, IFF strength is not a classical material failure with a single localization, but a smeared failure that appears throughout the whole layer. Thus, IFF localization does not occur in composites on macroscale, but only in RVEs on micro- and mesoscale, respectively. In this work, the application of a fracture energy regularization is used to enable strength computation with UCs. The strain energy release rate is a material property, that incorporates micro-effects that make homogenization of strengths theoretically impossible. It is the amount of energy dissipated through the coalescence of microcracks in an advancing crack. This crack band has a material specific width, or characteristic internal length L_i , see table 4.1, that is determined by the heterogeneity of the material, i.e. the size of its constituents and the microcracks. By using the characteristic internal length as size of the unit cell and the strain energy release rate for regularization of the softening, the localization can be smeared over the whole unit cell. Therefore, the unit cell is regarded as representative also for the strength prediction.

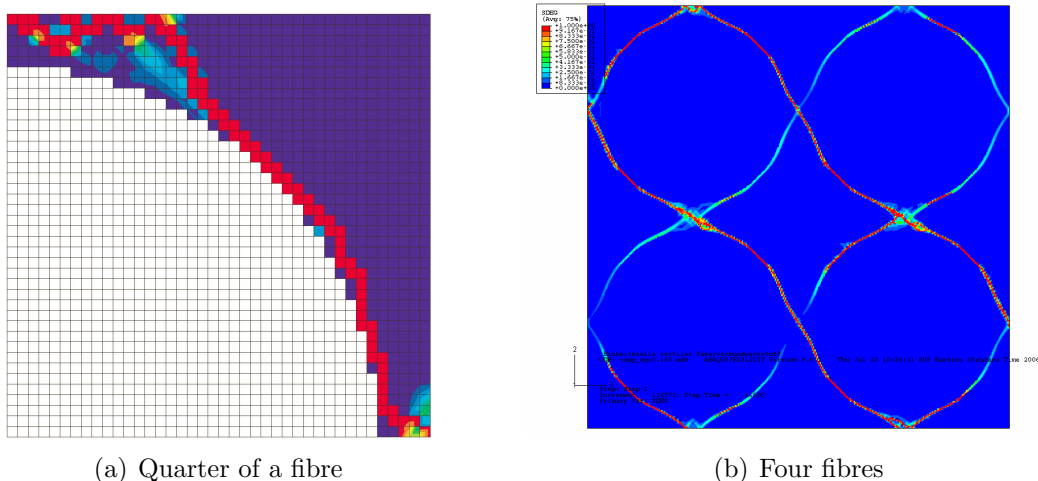


Figure 5.2: Crack under transverse compression in different unit cells

Nevertheless, in section 6.3.2 it is investigated if a randomized unit cell (RUC) can be used for determination of strengths. The randomized unit cell is an approximation for imperfect or inhomogeneous microstructures, it consists of randomly arranged fibres and matrix. In contrast to a completely stochastic RVE, its structure is periodic, i.e. the white fibre in Figure 5.3, lying on the boundary, can be found at the top and bottom of the RUC. This is not necessarily the case in an RVE, but it is also not forbidden. Most important, in combination with periodic boundary conditions, see below, the stress state in the RUC is much smoother, because there are no stiffness singularities between the boundaries. The effect of the periodicity vanishes with the number of fibres in the RUC. Therefore, an RUC with a high number of fibres can be seen as an approximation of an RVE.

In practice, the statistical homogeneity of an RVE is seldomly fulfilled, because the re-

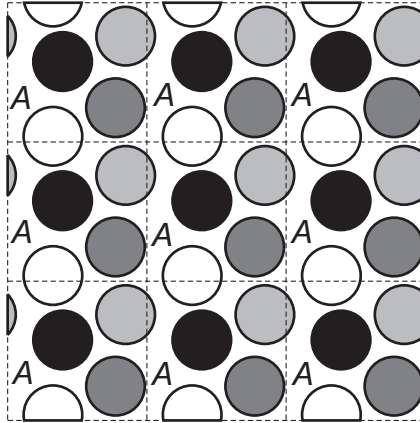


Figure 5.3: Randomized unit cell

quired large size of the RVE is numerically too expensive. Therefore, a number of smaller RVEs is computed and the mean behaviour of these is taken as the homogenized macro material behaviour. Thus, the RUC can be considered as equal to an RVE.

5.2.2 Boundary Conditions

The boundary conditions applied on the RVE/UC are as important as its geometry. In the homogenization procedure the discontinuous stress and strain fields on the boundary of the RVE/UC are averaged and taken as the macro-stresses and -strains, see Figure 5.4. As a prerequisite, the boundary conditions of the RVE have to fulfill the Hill condition (Hill (1963)):

$$\langle \sigma_{ij} \varepsilon_{ij} \rangle = \langle \sigma_{ij} \rangle \langle \varepsilon_{ij} \rangle . \quad (5.3)$$

It states that the energy stored in the heterogeneous microfields σ_{ij} and ε_{ij} must be the same as in the homogeneous macrofields $\langle \sigma_{ij} \rangle$ and $\langle \varepsilon_{ij} \rangle$.

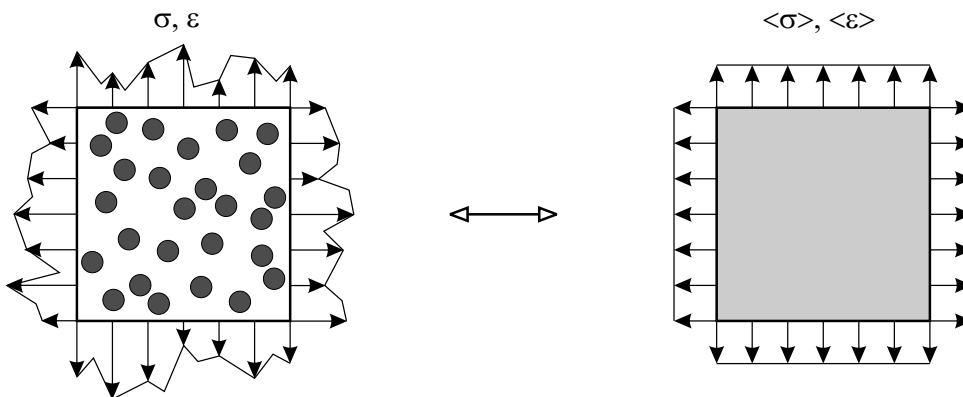


Figure 5.4: Averaging of stresses and strains of the RVE

Homogeneous strain or stress micro-fields are the simplest valid assumptions for the unknown micro-field. They are also called Voigt approximation, based on *average strain theorem*, and Reuss approximation, based on *average stress theorem*. The Voigt approximation provides an upper bound for the elastic parameters, whereas the Reuss approximation gives a lower bound. If the elastic phases of a heterogeneous material are considered as springs, the Voigt model represents parallel springs and the Reuss model represents series springs. Voigt and Reuss bounds are very important, but more exact approximations are required. Therefore, several methods were presented in the past. For example, Hashin and Shtrikman (1963) have formulated tighter bounds over a variational principle.

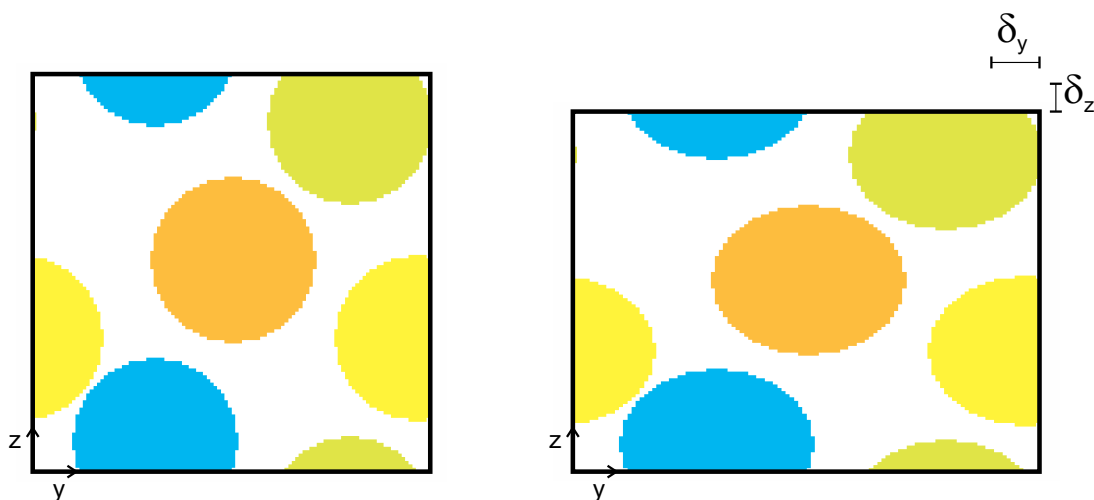


Figure 5.5: Displacement boundary conditions on randomized unit cell

In analogy to Voigt and Reuss bounds, displacement or force boundary conditions can be applied on the RVE. Figure 5.5 illustrates displacement boundary conditions on a RUC, where the displacement of each boundary is prescribed by a uniform value, e.g. δ_y and δ_z . Thus, only the stress field has to be averaged in the example. However, displacement boundary conditions add artificial stiffness to the RVE, therefore they represent an upper bound, whereas force displacement conditions represent a lower bound. Another approach are periodic boundary conditions (PBC) that can be seen as mixture of both. Periodic boundary conditions enforce periodic displacements and anti-periodic tractions on either side of the RVE/UC. Therefore, in an FE-mesh each node on the boundary of the RVE is associated with the corresponding node on the other side of the RVE/UC. These nodes share degrees of freedom (u,v,w) and therefore deformations and stresses are equal. How PBCs are applied on the unit cell is presented in detail in the following sections. Compared to DBC and FBC, PBCs give a considerably better prediction for the properties of the RVE, however, it is not known whether they over- or underestimate the properties. In case of a UC they give the exact solution, because of the periodic stress and strain fields in the UC. Therefore, they are applied on the UCs computed in chapters 6 and 7.

5.2.2.1 General Periodic Boundary Conditions

Super-degrees-of-freedom $u^{super}, v^{super}, w^{super}$ that are representative for the mean deformation of the whole RVE are introduced for application of periodic boundary conditions. They are coupled with the boundary as shown in Figure 5.6. Nine super-degrees-of-freedom are needed for a three-dimensional RVE, three degrees-of-freedom times three boundary pairs. In Figure 5.6 only two super-degrees-of-freedom are shown for reasons of simplicity. For an RVE with the dimensions a, b and c in x-,y- and z-direction the periodic boundary conditions can be written as

$$\begin{aligned} v(x, 0, z) + v_{1000}^{super} &= v(x, b, z) \\ w(x, y, 0) + w_{1000}^{super} &= w(x, y, c) \end{aligned} \quad (5.4)$$

If a displacement δ_y is applied on node 1000 the whole RVE is elongated by δ_y , but the shape of the boundary is not prescribed, i.e. the distance between the corresponding nodes, e.g. 1 and 11, is equal for all nodes, but the absolute displacements are free. The displacement of node 1000 in z-direction is correlated to Poisson’s effect under such load conditions.

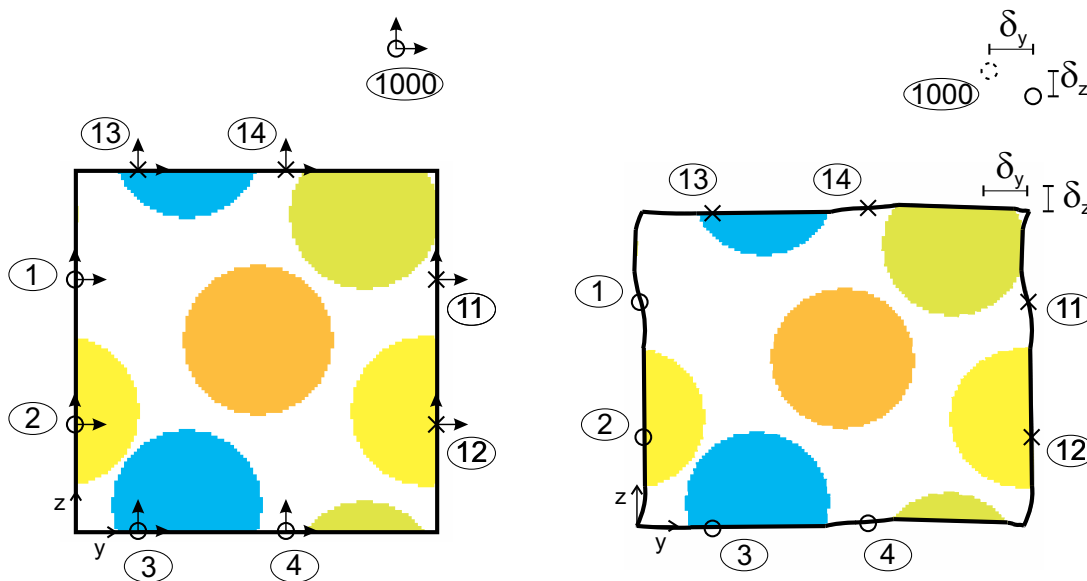


Figure 5.6: General Periodic boundary conditions

In ABAQUS these boundary conditions can be applied on matching nodes of opposite RVE boundaries using the *EQUATION Keyword. It has to be pointed out that the introduction of these boundary conditions on the whole RVE slows down a simulation with an explicit time integration scheme. Sometimes it is possible to avoid the application of such boundary conditions on the whole RVE, i.e. the deformations in the x-direction in Figure 5.6 could be assumed to be evenly distributed over the whole RVE without loss of generality.

In practice, an advantage of this method is that the mean deformations and stresses needed for the homogenization are already summarized as displacements δ_i and reaction forces F_i in the super-nodes by the FE-program. How the elastic parameters are determined from these values is described in section 5.2.3.

5.2.2.2 Periodic Boundary Conditions for Symmetric Unit Cell

The micromechanical unit cells with square and hexagonal fibre arrangement, presented in chapter 6, and the mesomechanical unit cell for a non-crimp fabric, presented in chapter 7 are symmetric structures. If a symmetric structure is subject to a symmetric load it will exhibit symmetric deformations. Therefore, simplified periodic boundary conditions can be applied, as described by Sun and Vaidya (1996). To determine all homogenized material parameters it is necessary to apply direct (or: normal) and shear load on the micro- and mesomechanical unit cells. The simplified periodic boundary conditions for these load cases are summarized in fig. 5.7 for an x-y-z coordinate system. Depending on the load case, x, y and z are to be replaced by the directions of the layer, 1, 2 and 3. Periodic boundary conditions require opposing unit cell boundaries to remain compatible to each other, i.e. to show periodic displacements and anti-periodic stresses. Usually, degrees of freedom of opposing nodes are connected over equations, but in the case of a symmetric unit cell the boundaries can be assumed to remain even due to the symmetry.

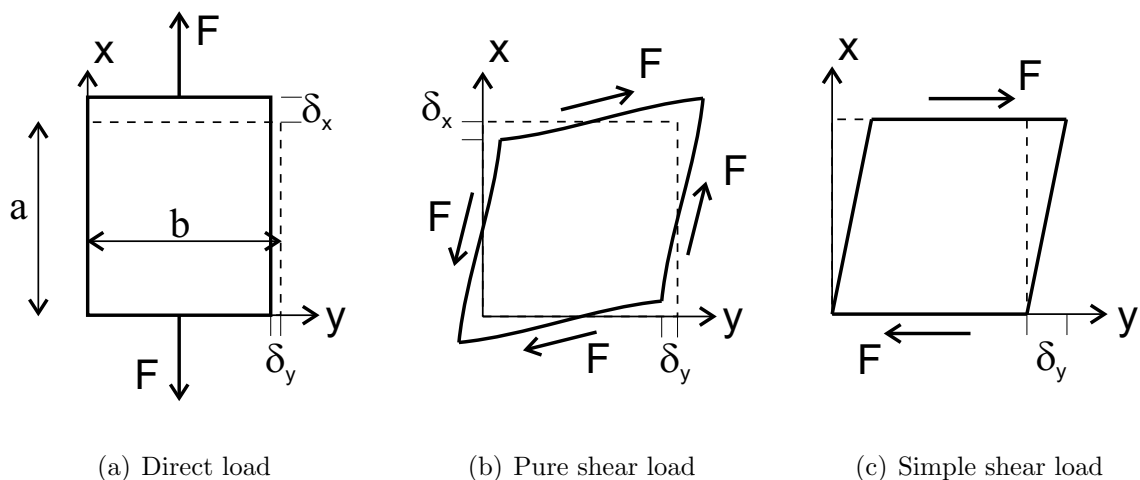


Figure 5.7: Symmetric Periodic boundary conditions

Direct Load In case of direct load, see Figure 5.7(a) it has to be ensured that the boundaries, which are axes of symmetry, remain even and a uniform displacement is applied. Under a displacement load δ_x for most boundaries a deformation can be given

$$\begin{aligned}
u(0, y, z) &= 0, & u(a, y, z) &= \delta_x \\
v(x, 0, z) &= 0 \\
w(x, y, 0) &= 0 \quad .
\end{aligned} \tag{5.5}$$

So far, the boundaries are not different to displacement boundary conditions, however, the other boundaries are allowed to deform, but to remain straight and orthogonal, which can be realized by a linear equation

$$\begin{aligned}
v(x, b, z) &= v(a, b, c) = \delta_y = \text{const.} \\
w(x, y, c) &= w(a, b, c) = \delta_z = \text{const.} \quad .
\end{aligned} \tag{5.6}$$

This is a hidden force condition, because it implies that the mean stress in y-direction is zero on all y-boundaries and thus ensures anti-periodic tractions. The degrees of freedom $v(x, b, z)$ and $w(x, y, c)$ are eliminated without the introduction of a further system of equations, which is very efficient concerning the computational time. Like the general periodic boundary conditions presented before a full three dimensional stress state is present under these boundary conditions.

Shear Load For a symmetric unit cell under x-y-shear opposing boundaries of the unit cell are enforced to remain parallel to each other:

$$\begin{aligned}
u(0, y, z) &= u(a, y, z) \\
v(x, 0, z) &= v(x, b, z) \\
w(x, y, 0) &= w(x, y, c) = 0 \quad .
\end{aligned} \tag{5.7}$$

Two different shear modes can be applied: simple shear and pure shear. In simple shear, see Figure 5.7(c), displacements are applied only in one direction:

$$u(0, y, z) = u(a, y, z) = 0 \tag{5.8}$$

$$v(0, y, z) = 0 \tag{5.9}$$

$$v(a, y, z) = \delta_y \quad .$$

Through the reaction forces in x-direction at the opposing boundaries a moment is introduced in the unit cell that causes an uneven σ_x -stress distribution on the $(0, y, z)$ and (a, y, z) -boundary. If the unit cell is only one element thick, the stresses are still equal

on the opposing boundaries. However, if the unit cell is thicker these are displacement boundary conditions. The moment is not avoided by the application of pure shear:

$$\begin{aligned} u(x, 0, z) &= -u(x, b, z) = -\delta_x \\ v(0, y, z) &= -v(a, y, z) = -\delta_y \quad , \end{aligned} \quad (5.10)$$

but an opposing moment is built up by the reaction forces in y-direction, see Figure 5.7(b). However, this is only possible in the plane of isotropy, because otherwise the moments would not have the same value.

5.2.3 Determination of Homogenized Material Properties

The forces F shown in fig. 5.7 are the integrals over the stresses of the boundary that are equal to the sum of the nodal reaction forces and yield the homogenized stresses when divided by the corresponding boundary area. Deformations δ_i convert into homogenized unit cell strains and Poisson's ratios. The homogenized Young's Modulus is given as

$$E_x = \frac{\sigma_x}{\varepsilon_x} = \frac{F_x}{\frac{\delta_x}{a}} = \frac{aF_x}{bc\delta_x} \quad (5.11)$$

based on engineering stresses and strain whereas the use of true stresses and strains yields

$$E_x = \frac{\sigma_x}{\varepsilon_x} = \frac{F_x}{\ln\left(\frac{a+\delta_x}{a}\right)} \cdot \frac{(b-\delta_y)(c-\delta_z)}{bc} \quad (5.12)$$

The homogenized Poisson's ratio reads

$$\nu_{xy} = -\frac{\varepsilon_y}{\varepsilon_x} = -\frac{\frac{\delta_y}{b}}{\frac{\delta_x}{a}} = -\frac{a\delta_y}{b\delta_x} \quad (5.13)$$

based on engineering stresses and strain whereas the use of true stresses and strains yields

$$\nu_{xy} = -\frac{\varepsilon_y}{\varepsilon_x} = -\frac{\ln\left(\frac{b+\delta_y}{b}\right)}{\ln\left(\frac{a+\delta_x}{a}\right)} \quad (5.14)$$

True stresses and strains are used here, however, the differences have proven to be negligible in the considered examples.

The shear modulus is given for simple shear as

$$G_{xy} = \frac{\tau_{xy}}{\gamma_{xy}} = \frac{\frac{F_y}{bc}}{\frac{\delta_y}{a}} = \frac{aF_y}{bc\delta_y} \quad (5.15)$$

and for pure shear as

$$G_{xy} = \frac{\tau_{xy}}{\gamma_{xy}} = \frac{\frac{F_y}{bc}}{\frac{2\delta_y}{a} + \frac{2\delta_x}{b}} = \frac{\frac{F_y}{bc}}{\frac{4\delta_y}{a}} = \frac{aF_y}{4bc\delta_y} \quad (5.16)$$

Here, engineering strains and stresses are used for the conversion

5.3 Multiscale Algorithm for Stiffness and Strength of Textile Composites

Aim of the work is to determine stiffness and strength of textile composites via virtual tests, see section 1.3. These mechanical properties are dependent on material inhomogeneities, e.g. the textile architecture, that have much lower length scales. Therefore, a multiscale algorithm is used to model the effect of the inhomogeneities on macroscale material behaviour. It enables a replacement or at least an reduction of experimental tests and makes it possible to provide stress-strain curves for the preliminary design. An information-passing approach is used, thus different scales are simulated subsequently, and material parameters are passed from lower to upper scale. On mesoscale a unit cell is used to describe the textile architecture of the fibre bundles to provide material parameters for the macroscale. The material parameters of the fibre bundles discretized in the mesomechanical unit cell are computed with a micromechanical unit cell that describes the behaviour of the UD-material of the fibre bundles.

An overview of the workflow is given in Figure 5.8. If only material parameters for fibre and matrix are given, first of all a micromechanical unit cell is generated. It constitutes of fibre and matrix and gives homogenized stress-strain curves of the UD-material. On mesoscale, the textile architecture is modelled in the mesomechanical unit cell. Therefore, the stress-strain curves from microscale are used as material input for the fibre bundles. The homogenized stress-strain curves of the mesomechanical unit cell can then be used on macroscale for strength computation of the textile laminate, e.g. in a three-point bending test.

Four major challenges arise from the whole task:

1. Proper **material model** and **softening formulation** for the description of epoxy resin and UD-material

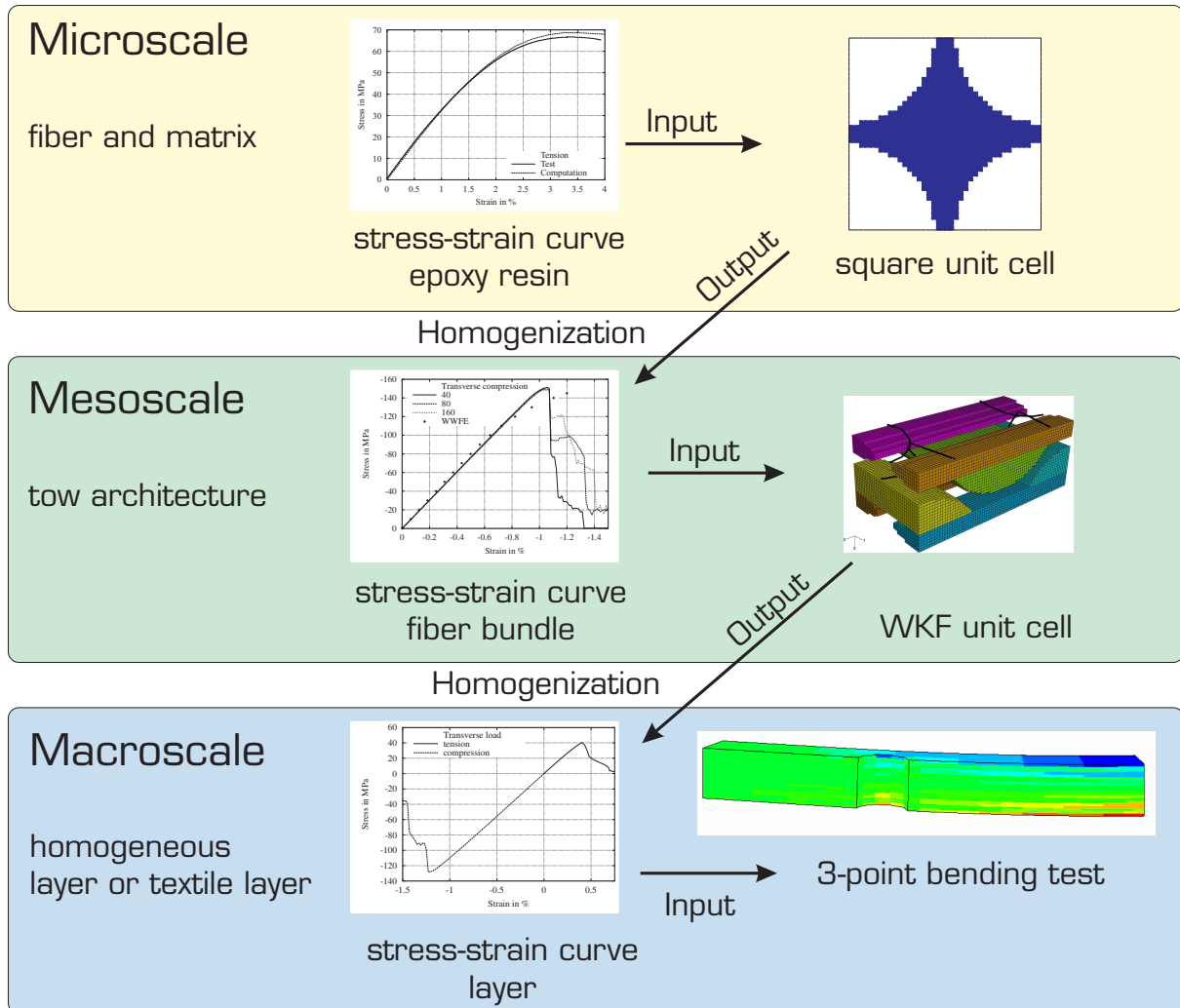


Figure 5.8: Multiscale algorithm

2. Identification of **material parameters**
3. To **model the textile architecture** accurately
4. Application of valid **boundary conditions** on the unit cells

Two very accurate material models for the description of the non-linear, pressure-dependent material models have been presented in chapter 3. The identification of material parameters for these models is very easy, because hardening curves are used as input for the nonlinearity. Furthermore, sophisticated failure criteria and damage formulations have been developed for epoxy resin and UD-composites, see chapter 4. A speciality of the presented algorithm is that the resulting stress-strain-curves of the lower scale computations are required as input parameters of the upper scale material models. Therefore, the transition between the scales is very smooth. Periodic boundary conditions for the unit cells are introduced in the previous section 5.2. In the following sections the modeling of the textile architecture will be presented.

5.3.1 Micromechanical Unit Cell

The micromechanical unit cell constitutes of fibre and matrix. It is needed to determine the nonlinear material behaviour and strength of UD-composite material, especially the tows in the mesomechanical unit cell. Material parameters for epoxy resin and fibres are required for this computation. Fibres are considered to behave linearly elastic up to fracture. The nonlinear plastic behaviour of epoxy resin is input as a stress-strain curve. A strain energy release rate of the epoxy has to be given for the description of softening behaviour. Different unit cell geometries, including random fibre arrangement and the virtual tests carried out with these unit cells are given in the following chapter 6.

5.3.2 Mesomechanical Unit Cell

On the mesoscale the textile fibre architecture is considered. The unit cell can incorporate one layer of a non-crimp fabric or MLG or it can comprise several fabrics. Both approaches have particular advantages and drawbacks, as described in chapter 7, where mesoscale virtual tests are presented.

The unit cell mainly constitutes of the tows that are modelled as transversely isotropic UD-composite material presented in section 3.2. Epoxy resin pockets between the tows are modelled with the isotropic material given in section 3.1. Both constituents show nonlinear behaviour and stress-strain curves for the plastic regime have to be given. The material parameters required for the tow material can either be taken from unidirectional test specimens, where given, or from micromechanical unit cell computations. A strain energy release rate is required for the softening formulation.

The mesomechanical unit cell gives stress-strain curves of the textile composite that can be used for the extraction of elastic and inelastic material parameters for an orthotropic material on the macroscale, see Figure 5.8.

5.3.3 Macroscale Computations

Macroscale simulations are presented in chapter 8 as a validation of the material parameters determined with the mesomechanical unit cell.

On the macroscale different modelling strategies can be used: layer and textile layer homogenization. Layer homogenization is common for UD-composites where it is combined with Classical Laminate Theory. For textile composites it is potentially more useful to apply homogenization of whole textile layers, where all layers of one textile layer are combined in one anisotropic lamina, because the layers are connected by through-thickness reinforcements.

6 Micromechanical Unit Cell Examples

In this chapter, methods for stiffness and strength determination of UD-composites are presented. All methods have in common that they predict the material properties of UD-composites from the material properties of fibre and matrix, as well as the fibre volume fraction v_f . Section 6.1 gives an overview on analytical rules of mixture from literature that are widely employed for stiffness prediction. In the following section, the use of unit cells with an assumed perfectly periodic fibre arrangement for the determination of stiffnesses and strengths of UD-composites is presented. To investigate the influence of the assumed perfectly periodic fibre arrangement, randomized unit cells are analyzed in Section 6.3.

6.1 Analytical Rules of Mixture for Stiffness and Strength of UD-composites

Analytical rules of mixture for stiffness of UD-composites are state of the art. Especially for Young's Modulus in fibre direction a very good estimate is

$$E_{\parallel} = E_F * \varphi + E_M * (1 - \varphi) \quad . \quad (6.1)$$

Here, E_F is Young's Modulus of the fibre in longitudinal direction, E_M is Young's Modulus of the matrix and φ is the fibre volume fraction. It has to be noted that this is the most influential of the elasticity constants, because the fibres are mainly responsible for load carrying in composites. Furthermore, it has to be stressed, that this constant is subject to reasonable variance in experimental tests. Between tensile and compressive Young's Modulus a difference of 10% is not unusual.

If strength of the epoxy resin is neglected in fibre direction, the strength of the UD-composite in fibre direction $R_{\parallel}^{t,c}$ can be calculated analytically from the strength of the fibre $R_{fibre}^{t,c}$ and fibre volume fraction v_f

$$R_{\parallel}^{t,c} = R_{fibre}^{t,c} * v_f \quad . \quad (6.2)$$

For other elasticity constants various approximations exist that yield quite different results. Therefore, they are presented in the following sections.

6.1.1 Transverse Young's Modulus E_{\perp}

Most of the rules of mixture for the transverse Young's Modulus E_{\perp} are based on micro-mechanical models. One of the easiest is the parallel springs model that is based on the *average strain theorem*:

$$E_{\perp} = \frac{E_M^H E_F}{E_F(1 - \varphi) + E_M^H \varphi} \quad (6.3)$$

with

$$E_M^H = \frac{E_M}{1 - \nu_M^2} \quad . \quad (6.4)$$

It gives an upper bound. Amongst others formulas were presented by Chamis (1987)

$$E_{\perp} = \frac{E_M}{1 - \sqrt{\varphi} \left(1 - \frac{E_M}{E_{F\perp}}\right)} \quad , \quad (6.5)$$

and Geier (1982)

$$E_{\perp} = \frac{1}{S_s - (0.2 + 0.4\varphi)(S_s - S_q)} \quad (6.6)$$

with

$$S_s = \frac{\varphi}{E_{F\perp}} + \frac{1 - \varphi}{E_M}, S_q = \frac{1}{\varphi E_{F\perp} + (1 - \varphi)E_M} \quad . \quad (6.7)$$

Results of these formula for the materials investigated in the following chapters are given in Figure 6.26.

6.1.2 In-Plane Shear Modulus $G_{\parallel\perp}$

Rules of mixture also exist for the in-plane shear modulus $G_{\parallel\perp}$. The Parallel Springs model:

$$G_{\parallel\perp} = \frac{G_F G_M}{G_F(1 - \varphi) + G_M \varphi} \quad (6.8)$$

again can be seen as an upper bound. Other equations were presented by Chamis (1987):

$$G_{\parallel\perp} = \frac{G_M}{1 - \sqrt{\varphi} \left(1 - \frac{G_M}{G_{F\perp}}\right)} \quad . \quad (6.9)$$

and Geier (1982)

$$G_{\parallel\perp} = \frac{1}{G_s - (0.4 + 0.4\varphi)(G_s - G_q)} \quad , \quad (6.10)$$

with

$$G_s = \frac{\varphi}{G_{F\parallel\perp}} + \frac{2(1-\varphi)(1+\nu_M)}{E_M}, G_q = \frac{1}{\varphi E_{F\perp} + \frac{(1-\varphi)E_M}{2(1+\nu_M)}}. \quad (6.11)$$

Figure 6.27 shows the results of these formulas for the example of an E-Glass/RIM135-UD-composite.

6.2 Periodic Unit Cells

The rules of mixture give very good estimates for the fibre direction, but the predictions for the other directions are rather imprecise and ambiguous. Furthermore they lack to predict inelastic properties such as strength and plastic hardening. Thus, a micromechanical unit cell can be used to determine these parameters, if experimental data are not available. This is often the case for textile composites, because the tests required cannot be done with the whole preform, but only with a part of it, the fibre bundles. Thus the specimens would have to be produced especially for these tests.

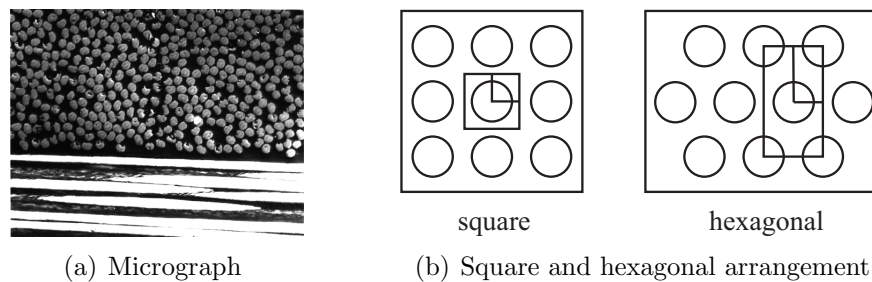


Figure 6.1: Micromechanical unit cell

A micrograph of unidirectional composite material is shown in Figure 6.1(a). It might be possible to model fibre and matrix arrangement in a finite element mesh to find out the behaviour of this UD-layer. However, it has to be noted that the fibre arrangement seen in this figure is not constant in the whole layer, it looks completely different at another cross section. Therefore, it becomes clear that an exact modelling the fibre arrangement is not reasonable and that assumptions have to be done. Neglecting the random fibre distribution over the cross section, perfectly periodic fibre arrangements, square or hexagonal are usually assumed, as shown in Figure 6.1(b). A unit cell can be used for simulation of such a periodic arrangement, so only one fibre has to be discretized in the square arrangement or five in hexagonal arrangement, indicated by boxes. For symmetric load cases, these unit cells can even be reduced further to a quarter of the original unit cell, because of their symmetric geometry. A square unit cell containing a quarter of a fibre is shown in Figure 6.2.

To determine stiffness, hardening and strength parameters in directions apart from fibre direction, four virtual tests, summarized in fig. 6.3, have to be computed: tension, shear and compression in transverse direction and in-plane shear. The transverse shear test

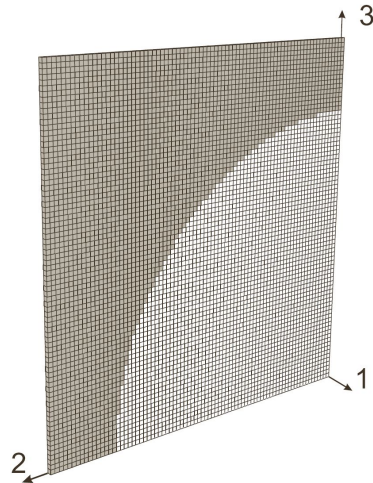


Figure 6.2: Discretization of one quarter of micromechanical unit cell

is only necessary because of the pressure-dependency of the epoxy resin. Otherwise, the transverse shear modulus $G_{\perp\perp}$ could be determined from Young's Modulus E_{\perp} and Poisson's Ratio $\nu_{\perp\perp}$, which are both determined under transverse normal load, over

$$G_{\perp\perp} = \frac{E_{\perp}}{2(1 + \nu_{\perp\perp})} \quad (6.12)$$

This relation is valid because of the isotropic behaviour in the 2-3-plane.

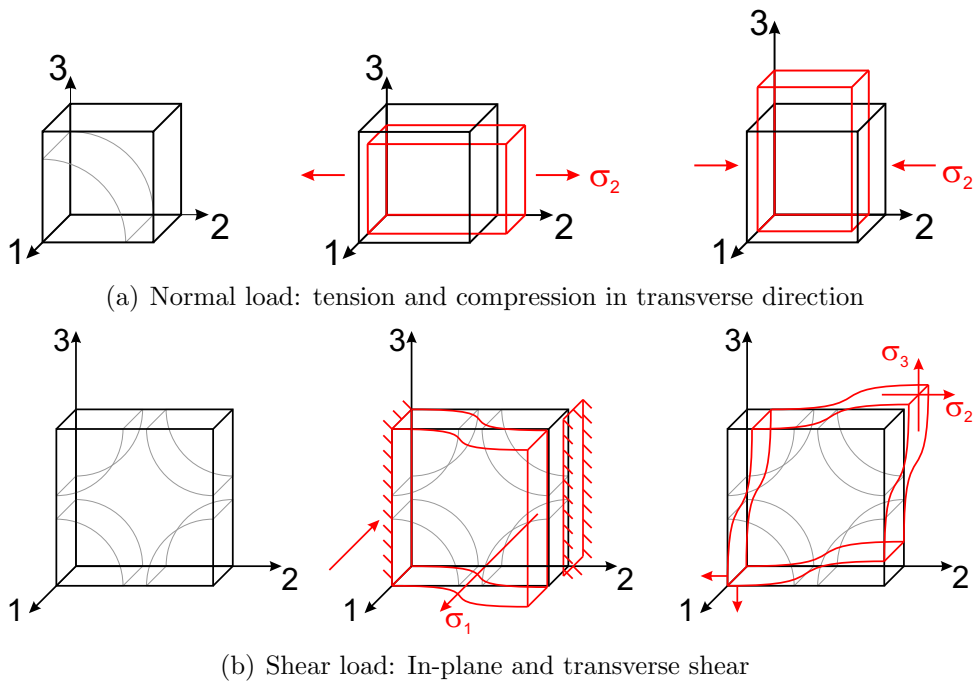


Figure 6.3: Virtual tests for homogenization

All virtual tests are simulated with periodic boundary conditions for symmetric unit cells given in section 5.2.2.2. In-plane shear is applied as simple shear, whereas for transverse shear pure shear boundary conditions are used. The elastic material constants are then determined by the formulas given in section 5.2.3, the maximum stress in the stress-strain curve is taken to be the strength of the material.

Convergence The convergence of the presented material in combination with the voxel mesh is very good as seen in fig. 6.4. It shows stress-strain curves from computations on the micromechanical unit cell under transverse compression and in-plane shear with different mesh refinements (40x40, 80x80 and 160x160 elements).

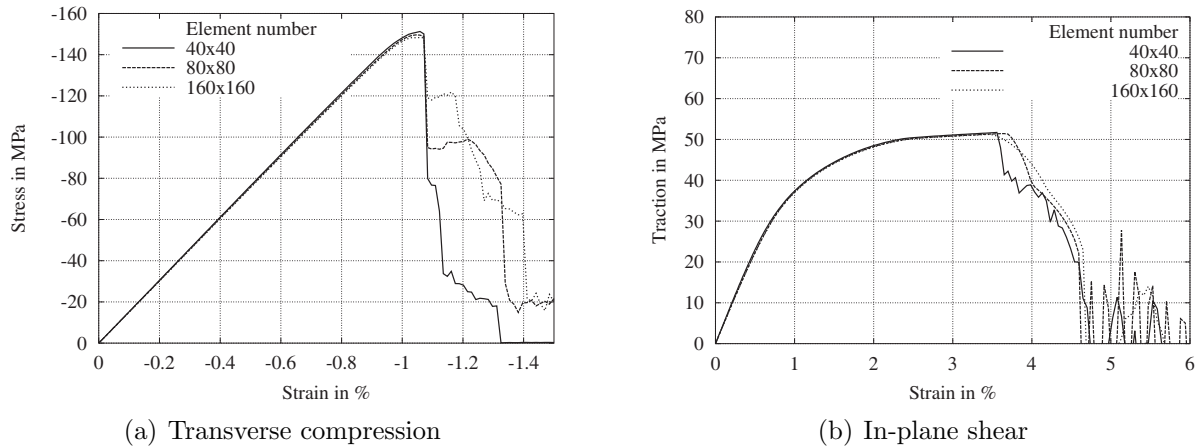


Figure 6.4: Stress-strain curves of micromechanical unit cell computations with different element number

Size of unit cell If strengths of UD-composites are determined with a unit cell, it has to be considered how and at which scale the strengths of the materials in the unit cell have been determined. The strain energy release rate, or fracture energy, used in this work for the softening formulation is a size-dependent value as well. It is a macroscale material property that describes the development and coalescence of multiple microcracks into a single macroscale crack. Therefore, microscale inhomogeneities, i.e. random fibre arrangement, residual thermal stresses, interface/interphase between fibre and matrix, are contained in this property and influence it. Random fibre arrangement plays an important role, because it causes local stress peaks that initiate and promote crack growth.

The strain energy release rate $G_f = 0.165 \frac{\text{N}}{\text{mm}}$ of a UD-layer, given in the WWFE, is used here, to cover all microscale inhomogeneities of the UD-layer. Therefore, microcracks, residual thermal stresses, interface as well as interphase strength are contained indirectly in the simulation without being modelled explicitly. The use of this strain energy release rate, however, requires the unit cell dimension to comply with the characteristic internal length given in table 4.1, i.e. the size of the localization zone in the experiment. If the unit cell is smaller than the internal length, respectively the localization zone, the results are

physically not valid. In the softening process the elastic strain energy stored in the unit cell is dissipated by a crack through a single element row. The elastic energy, however, is dependent on the dimension of the unit cell, i.e. in a larger unit cell the crack evolves faster than in a smaller one. Therefore, it becomes clear that the outer dimensions of the unit cell have an important influence on the softening behaviour of the unit cell. An outer dimension of 1 mm x 1 mm is chosen for the unit cell as a conservative assumption. The geometry of the unit cell must be seen as an expression for the mean stress inhomogeneities induced by the different stiffness of the components fibre and matrix, it does not stand for a single fibre at the microscale. The crack is a representation of multiple microcracks induced by microscale inhomogeneities and coalescing in a single macrocrack. Therefore, only one crack of one element thickness is allowed in the unit cell, because otherwise too much strain energy would be released in the softening process.

6.2.1 Comparison with Test Results from WWFE

For a validation of the micromechanical unit cells, experimental results of the WWFE on UD-composites made of glass fibres and epoxy resin MY750/HY917/DY063 with a fibre volume fraction of $v_f = 0.6$ are used. Both are isotropic materials, whose elastic material parameters and strengths are well known, see table 6.1. However, hardening curves under tension and shear are required for the material model presented in section 3.1 that is used here. Such hardening curves are not given in the WWFE, therefore the hardening of epoxy resin RIM 135, shown in Figure 2.1 are used instead. In table 6.1 it can be seen that this epoxy resin is very similar to MY750/HY917/DY063.

A summary of the material parameters determined with the four virtual tests described above is given in table 6.2. Results are given for experimental tests from the WWFE and for virtual tests with square and hexagonal unit cell.

The square unit cell does not show transversely isotropic material behaviour, although stiffness and strength are equal in 2- and 3-direction. It becomes obvious that the behaviour is orthotropic by comparison of transverse shear modulus $G_{\perp\perp}$ determined from the virtual transverse shear test and from eq. 6.12, both shown in table 6.2. These values should match if transversely isotropic behaviour exists, but they do not. In contrast, the

Table 6.1: Material properties of fibre and matrix

Parameter	Unit	E-Glass	RIM 135	MY750/HY917/DY063
Young's modulus	GPa	74	3.35	3.35
Strength	MPa	2150/1450 ¹	69/120/55 ²	80/120 ¹
Failure strain	%	2.950/1.959 ¹	3.4/4.2/22 ²	5./ ⁻¹
Shear modulus	GPa	30.8	1.24	1.24
Poisson's ratio		0.2	0.35	0.35

¹ tension/compression

² tension/compression/shear

Table 6.2: Mechanical properties of E-Glass/MY750/HY917/DY063-epoxy lamina

Properties	Unit	WWFE	Hexagonal unit cell	Square unit cell
Longitudinal modulus ¹ E_{\parallel}	GPa	45.6	45.7	45.7
Longitudinal tensile strength R_{\parallel}^t	MPa	1280.	1308.	1308.
Longitudinal tensile failure strain $\varepsilon_{\parallel}^t$	%	2.807	2.905	2.905
Longitudinal compressive strength R_{\parallel}^c	MPa	800.	870.	870.
Longitudinal compressive failure strain $\varepsilon_{\parallel}^c$	%	1.75	1.96	1.96
Transverse modulus ¹ E_{\perp}	GPa	16.2	11.89	15.06
Transverse compressive strength R_{\perp}^c	MPa	145	118.5	149.5
Transverse compressive failure strain ε_{\perp}^c	%	1.2	1.07	1.05
Transverse tensile strength R_{\perp}^t	MPa	45	41.7	38.3
Transverse tensile failure strain ε_{\perp}^t	%	0.25	0.39	0.3
In-plane Shear Modulus ¹ $G_{\parallel\perp}$	GPa	5.83	4.27	4.66
In-plane Poisson's ratio $\nu_{\parallel\perp}$		0.278	0.25	0.25
In-plane Shear Strength $R_{\parallel\perp}$	MPa	73	56.0	51.7
In-plane Shear failure strain $\nu_{\parallel\perp u}$	%	4	2.98	3.42
Transverse Shear Modulus ¹ $G_{\perp\perp}$	GPa	–	4.11	3.3
dito, $G_{\perp\perp} = \frac{E_{\perp}}{2(1+\nu_{\perp\perp})}$	GPa	5.79	4.25	5.97
Transverse Poisson's ratio $\nu_{\perp\perp}$		0.4	0.4	0.262
Transverse Shear Strength $R_{\perp\perp}$	MPa	–	44.47	51.04
Transverse Shear failure strain $\nu_{\perp\perp u}$	%	–	1.49	3.17

¹ Initial modulus

hexagonal unit cell shows (at least approximately) transversely isotropic material behaviour. However, compared with the test results from the WWFE, the overall performance of the square unit cell is better.

To validate the presented model stress-strain curves from experimental tests on unidirectional lamina published in the World-Wide Failure Exercise by Hinton et al. (2004) are compared with stress-strain curves from the square micromechanical unit cell. In the WWFE test results are given for transverse compression and in-plane shear of unidirectional lamina comprised of E-Glass fibres and epoxy resin MY750/HY917/DY063 with a volume fraction $v_f = 60\%$. The stress-strain curves are shown in Figure 6.5.

First of all, the virtual tests reproduce the main characteristics of the experimental results very good. The material and softening model are obviously able to describe the material characteristics well. Under compression, the results are in good agreement with the experimental curves, although the nonlinearity is not modelled too well. Parameter fitting by lowering the strength to 100 MPa and increasing the strain energy release rate to $G_f = 0.330 \frac{\text{N}}{\text{mm}}$ yields a better correspondence between test and simulation, see Figure 6.5. It can be seen, that the strain energy release rate is a very influential value, see

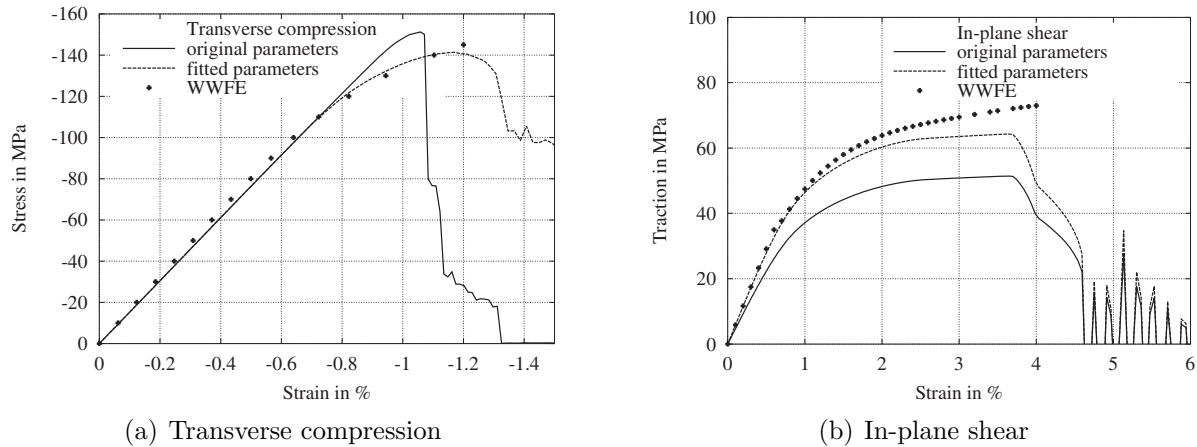


Figure 6.5: Stress-strain curves of micromechanical unit cell computations compared with test results from WWFE

also Rolfes, Ernst, Hartung, and Teßmer (2006)

Under shear, the test results are much stiffer, about 25%, than the unit cell computations. A probable weakness of the unit cell is the periodic fibre arrangement, because it can be shown that a random fibre arrangement has an considerable influence on the shear behaviour, see section 6.4. However, Hinton states in the WWFE that the experimental determination of shear and compression properties is particularly difficult and material data given might be inaccurate. The hardening curve provided by these micromechanical unit cell computations is used in load case 14 in section 4.2.3 for validation of the IQ-criterion and performs extraordinarily well. This allows the assumption that the computed material behaviour might be more realistic than the experimental results. The experimental results can be obtained in the computation by increasing shear modulus and hardening curve by about 25%, as shown in Figure 6.5.

Fig. 6.6 shows the evolution of the crack path through the 40x40 elements unit cell. Under in-plane shear a damage is initiated on the interface between fibre and matrix and then localizes in a straight crack band through the unit cell. Under compression the crack is not initiated on the interface but in the upper left corner where the highest strains are in the matrix, but the crack then evolves along the interface, where big shear deformations occur.

The in-plane shear strength calculated here is a little lower than the shear strength of the epoxy 51.74 MPa < 55.0 MPa. This result is reasonable because the crack runs straight through the epoxy matrix, see fig. 6.6 and therefore the unit cell strength cannot exceed the epoxy strength. Actually, it is a little smaller due to the inhomogeneous stress distribution in the unit cell.

In principle, the strength of the unit cell is mainly dependent on the strength of the epoxy matrix, which is the weaker of the two constituents. Therefore, an apparently implausible result of the computation is that the strength under compression is higher than the one given for the epoxy resin in tab. 6.1, the strength under uniaxial compression. However,

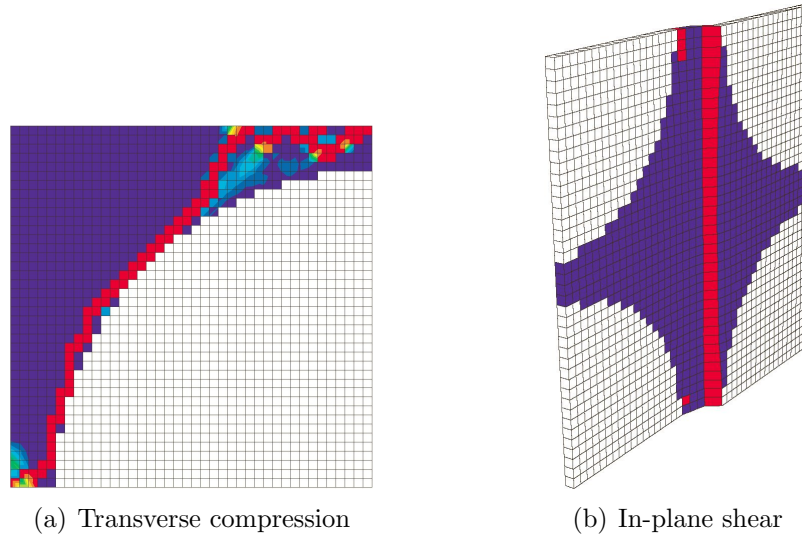


Figure 6.6: Damage evolution in micromechanical unit cell

in the micromechanical unit cell a three-dimensional stress state occurs. It is caused by different Young's modulus and Poisson's ratio of fibre and matrix and the fact that the unit cell is built of volume elements and not under plain stress conditions. In sec. 3.1 it can be seen, that the stress triaxiality has a considerable influence on the strength. Multiaxial stresses under compression increase the strength, under tension the strength decreases. The stress triaxiality $\frac{p}{\sigma_{vM}}$ in a square unit cell under transverse compression is shown in Figure 6.7. For interpretation, table 6.3 shows the values of triaxiality the stress states are associated with.

The area above the fibre, where failure is initiated, is loaded in a biaxial compression stress state. Therefore, the material is able to carry higher loads than the given uniaxial compressive strength. This is the reason why under compression the strength of the unit cell is higher than that of epoxy under uniaxial compression and why under tension the strength of the unit cell is very small. However, the stress triaxiality alone does not allow for an estimation, where failure will be initiated, this can only be judged with the knowledge of the absolute stress values. Figure 6.8 shows the distribution of the hydrostatic

Table 6.3: Values of stress triaxiality

Stress state	$\frac{p}{\sigma_{vM}}$
Triaxial compression	$-\infty$
Biaxial compression	$-\frac{2}{3}$
Uniaxial compression	$-\frac{1}{3}$
Transverse shear	0
Uniaxial tension	$\frac{1}{3}$
Biaxial tension	$\frac{2}{3}$
Triaxial tension	∞

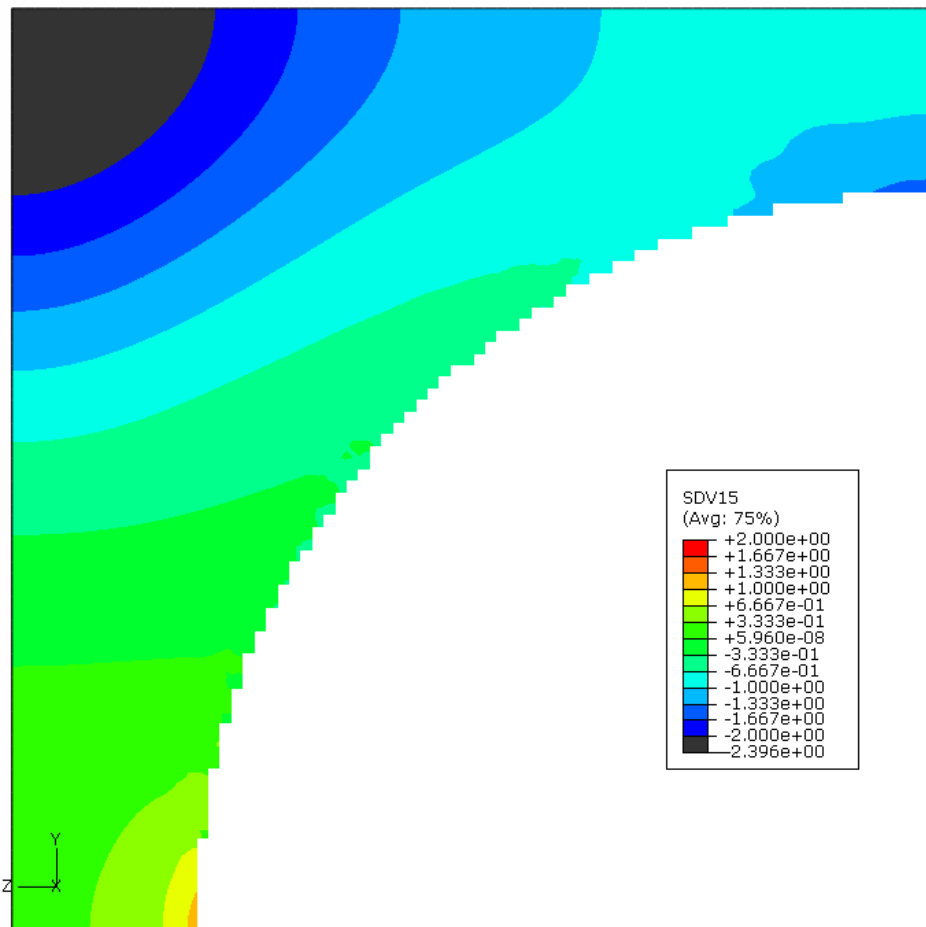


Figure 6.7: Stress triaxiality $\frac{p}{\sigma_{vM}}$ in micromechanical unit cell under transverse compression

pressure and von-Mises stress in a square unit cell under transverse compression. It can be seen that as well hydrostatic pressure as von-Mises stress are very high in the region above the fibre.

6.2.2 Different Stiffness of Arrangements

Obviously the square arrangement is stiffer than the hexagonal arrangement, see also Ernst et al. (2006). This can be easily understood when looking at the unit cells in Fig. 6.9. Both unit cells have the same fibre volume fraction of $V_f = 60\%$. For transverse compression fibre and matrix can be seen as series springs. The fibre is stiffer than the matrix by an order of magnitude, therefore the matrix is mainly responsible for the transverse stiffness. In the square arrangement the radius of the fibre is greater, i.e. the proportion of the matrix d_m in load-direction is smaller. Hence the square-packed unit cell is stiffer than the hexagonal-packed unit cell. The strain distributions in Fig. 6.9 show the relevance of this fibre to matrix proportion.

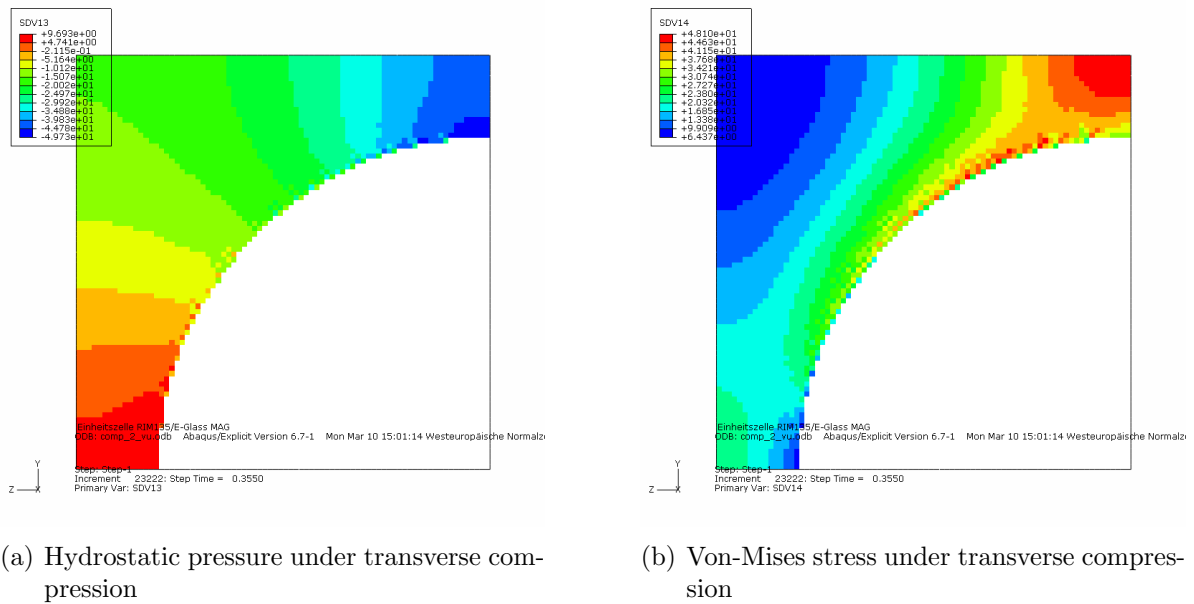


Figure 6.8: Stress Invariants in micromechanical unit cell

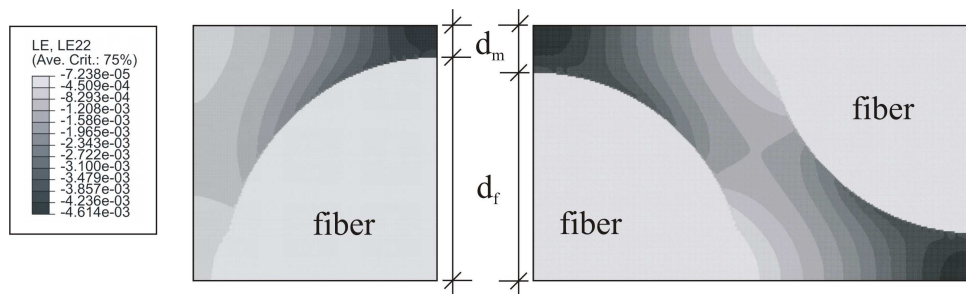


Figure 6.9: Strain distribution in square and hexagonal arrangement of unit cell

If the aspect ratio of the unit cell is varied keeping the volume fraction constant, the stiffness of the unit cell changes according to Fig. 6.10. It is shown that the stiffness of the unit cell is mainly dependent on the ratio of the epoxy to the height of the cell $r_e = \frac{d_m}{d} = \frac{d_m}{d_m + d_f}$. For unit cells with a small ratio r_e there are almost no differences between hexagonal and square arrangement. With growing ratio r_e the results differ only slightly. Thus it must be concluded that the square arrangement can be seen as an upper bound, whereas the hexagonal unit cell represents a lower bound for a UD-lamina.

6.3 Unit Cells with Random Fibre Arrangement

The assumption of a periodic fibre arrangement is very common in micromechanical approaches for determination of stiffness and strength of UD-composites, but the consequences are seldom investigated. Therefore, randomized unit cells will be studied in this section. They incorporate from 4 up to 49 fibres that are distributed randomly over the

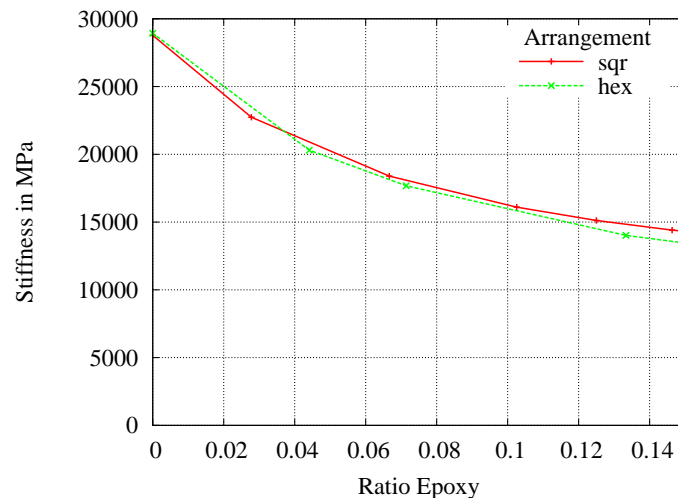


Figure 6.10: Stiffness of square and hexagonal unit cells after variation of aspect ratio

unit cell. In Figure 6.11 three different examples for such unit cells are given. It has to be noted that the unit cell is still periodic, see section 5.2. Each fibre that is cut by a boundary is complemented on the other side of the unit cell.

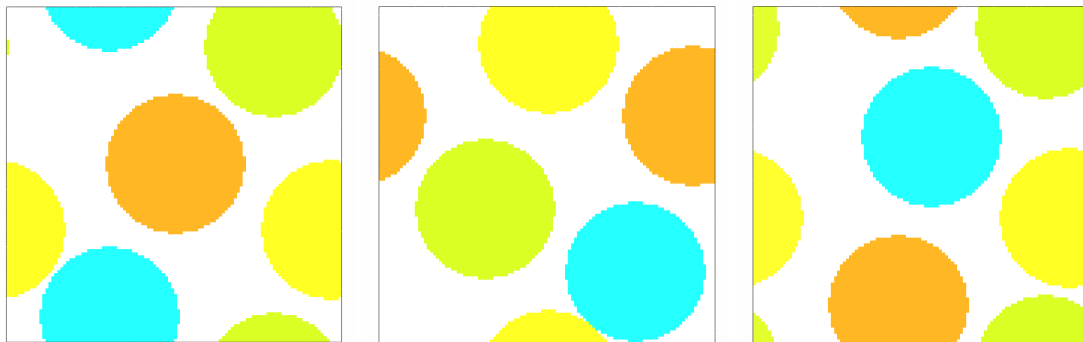


Figure 6.11: Different distributions of 4 fibres

Periodic boundary conditions, described in section 5.2.2.1, and displacement boundary conditions are applied on the randomized unit cells. Figure 6.12 shows the periodicity of deformations and stresses in the unit cell under periodic boundary conditions. This periodicity has of course an influence on the results, but its effect vanishes the more fibres are incorporated in the randomized unit cell. The displacement boundaries are applied for comparison. They introduce additional stiffness in the unit cell and therefore serve as an upper bound, see section 5.2. This effect of additional stiffness also vanishes the more fibres are incorporated in the randomized unit cell.

6.3.1 Linear-elastic Stiffness Prediction

As a first step, the elastic properties are determined with a linear-elastic material model. Altogether four virtual tests are carried out on each randomized unit cell: tension in 2-

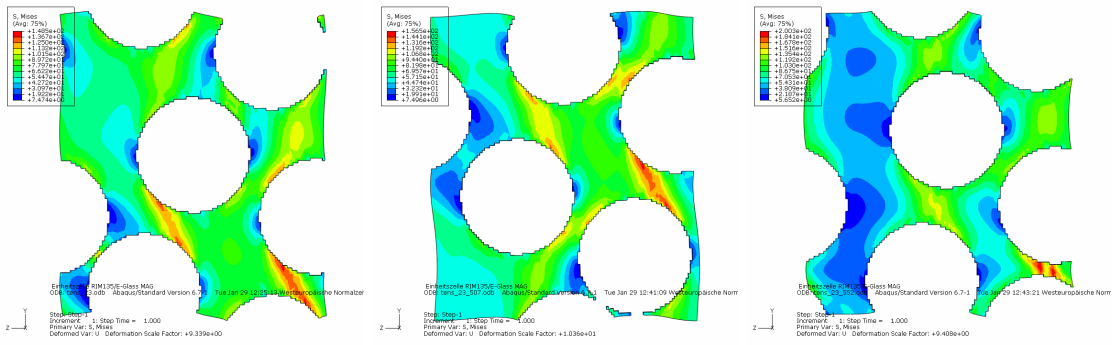


Figure 6.12: Deformations and von-Mises stresses of randomized unit cells under tension

and 3-direction, simple in-plane shear and pure transverse shear. A double convergence is needed in this procedure. Firstly, a convergence for a given number of fibres in the randomized unit cell, i.e. a statistical mean is calculated for a number of randomized unit cells. If this mean does not change significantly, when further results are included, the first convergence is reached. This convergence is calculated for each number of fibres in the randomized unit cell. Figures 6.13, 6.14, 6.15 and 6.16 show the convergence of the mean elastic parameters over a number of tests with periodic boundary conditions for different fibre numbers. Higher fibre numbers lead to a faster convergence and a smaller standard deviation.

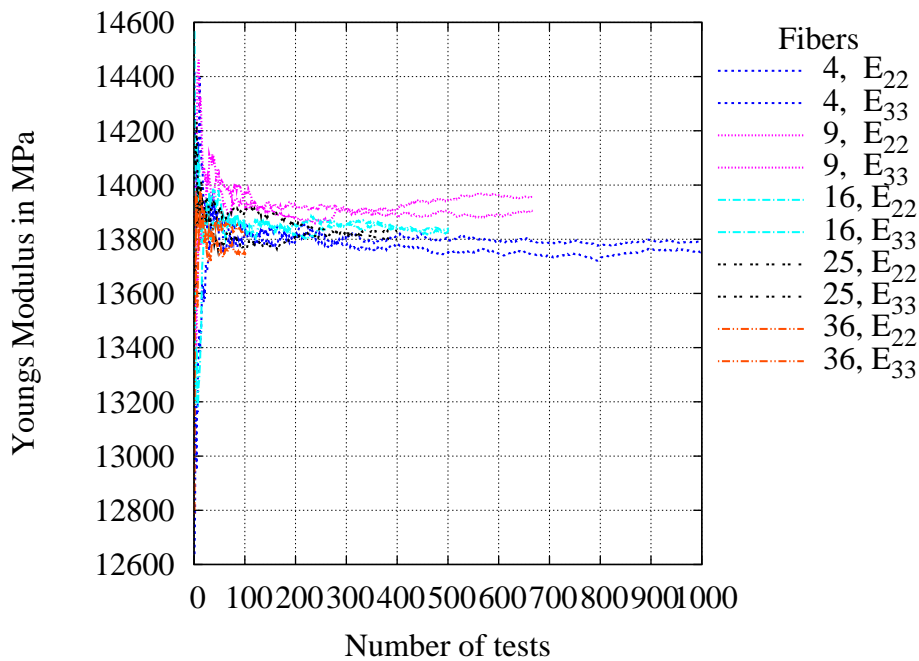


Figure 6.13: Evolution of mean Young’s Modulus E_{22} and E_{33} over number of tests and increased fibre number

In Figure 6.14 two values for the transverse shear modulus are given for each fibre number. The first value (thick line) is “simulated” from the virtual test, the second, indicated by a

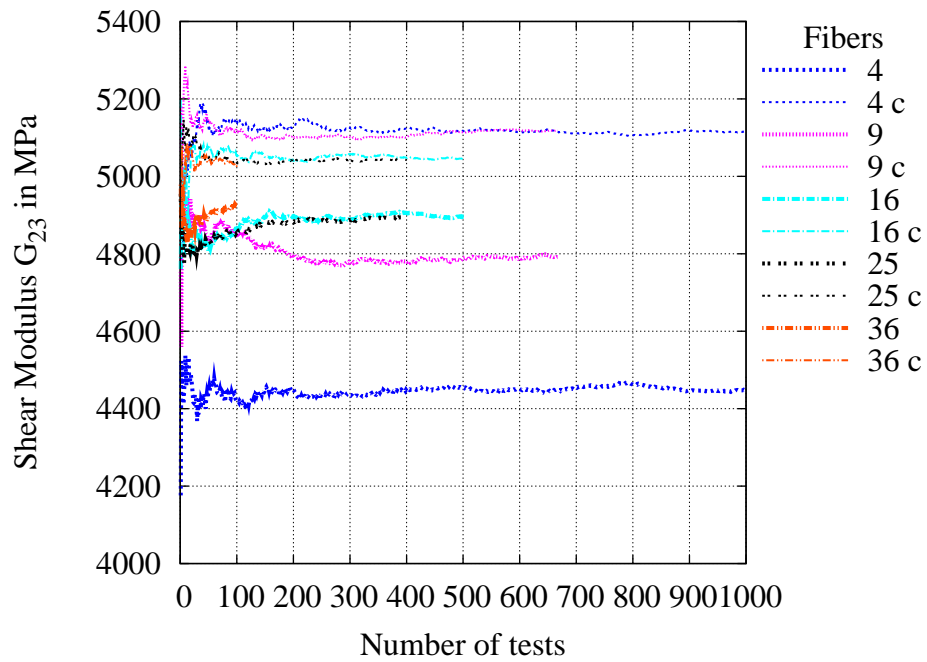


Figure 6.14: Evolution of mean Shear Modulus G_{23} over number of tests and increased fibre number; Values of virtual shear test are compared with calculated values Young's modulus and Poisson's ratio, denoted by "c"

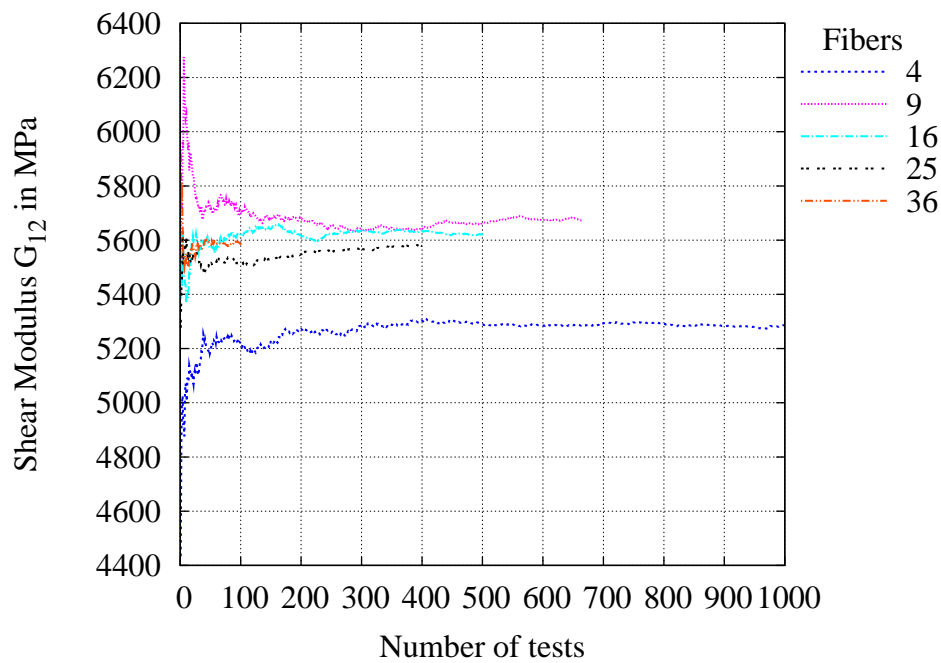


Figure 6.15: Evolution of mean Shear Modulus G_{12} over number of tests and increased fibre number

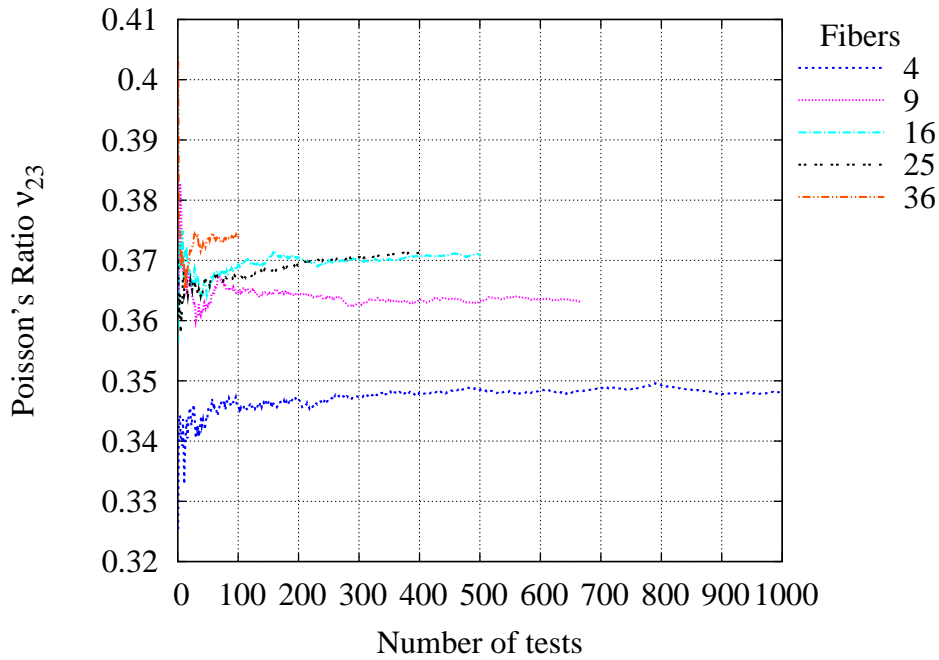


Figure 6.16: Evolution of mean Poisson's ratio ν_{23} over number of tests and increased fibre number

“c”, is “calculated” from E_{22} and ν_{23} using eq. 6.12. For transversely isotropic behaviour these values must be equal, which they are nearly for a high number of fibres. The difference is greater for a small number of fibres, but converges against a small value of about 2 %. Apparently, for a good description of shear behaviour a higher fibre number is needed, because mainly the shear modulus from the virtual shear test changes. The small remaining difference is probably caused by a modelling imprecision of the voxel mesh. If two fibres touch each other in the voxel mesh, they are acting as a solid coalescence, that influences shear deformations obviously more than normal deformations. For a smaller fibre volume fraction of $v_f = 50 \%$ the likeliness of such coalescences is reduced and there is no difference between computed and calculated shear modulus for high fibre numbers, i.e. the randomized unit cell behaves transversely isotropic. However, the error is negligible, therefore no measures were taken to alleviate this modelling imprecision.

Shear modulus G_{12} , Figure 6.19 and Poisson's ratio ν_{23} , Figure 6.20, are also influenced considerably by an increasing number of fibres.

Figure 6.13 shows the Young's Moduli E_{22} and E_{33} , that can be considered to be equal. It has to be noted that the influence of the number of fibres on the mean value is negligible. Obviously the prediction is already very good with a small number of fibres. Besides, there is no monotonic convergence trend for an increasing fibre number, because the periodic boundary conditions do not represent an upper or lower bound. In Figure 6.17 the predicted Young's Moduli E_{22} and E_{33} are plotted against each other for each randomized unit cell. Two interesting aspects can be seen. Firstly, for a low fibre number, plotted in Figure 6.17(a) two barriers seem to exist, for low stiffness in each direction, that yield a

characteristic triangular shape of the scatterplot. The higher the stiffness in one direction the higher the stiffness also in the other direction. Randomized unit cells with a very low stiffness in one direction also exhibit a very low stiffness in the other direction. In these cells the fibres are dispersed very evenly, but their stiffness always remains above the stiffness of the hexagonal unit cell $E_{\perp\perp} = 11886\text{MPa}$. Secondly, the variance of the stiffness decreases and the scatterplot adopts a circular shape for increasing fibre numbers in Figure 6.17(b).

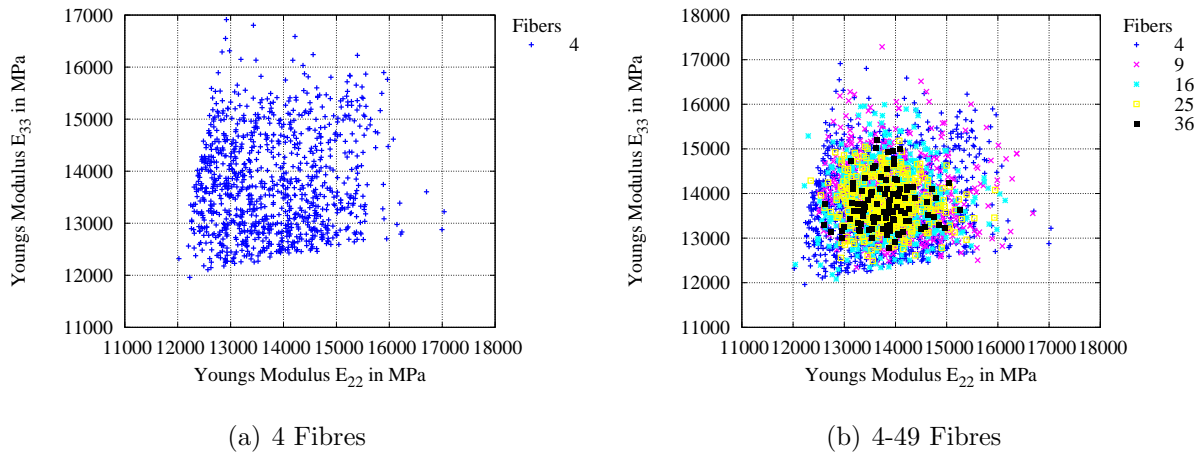
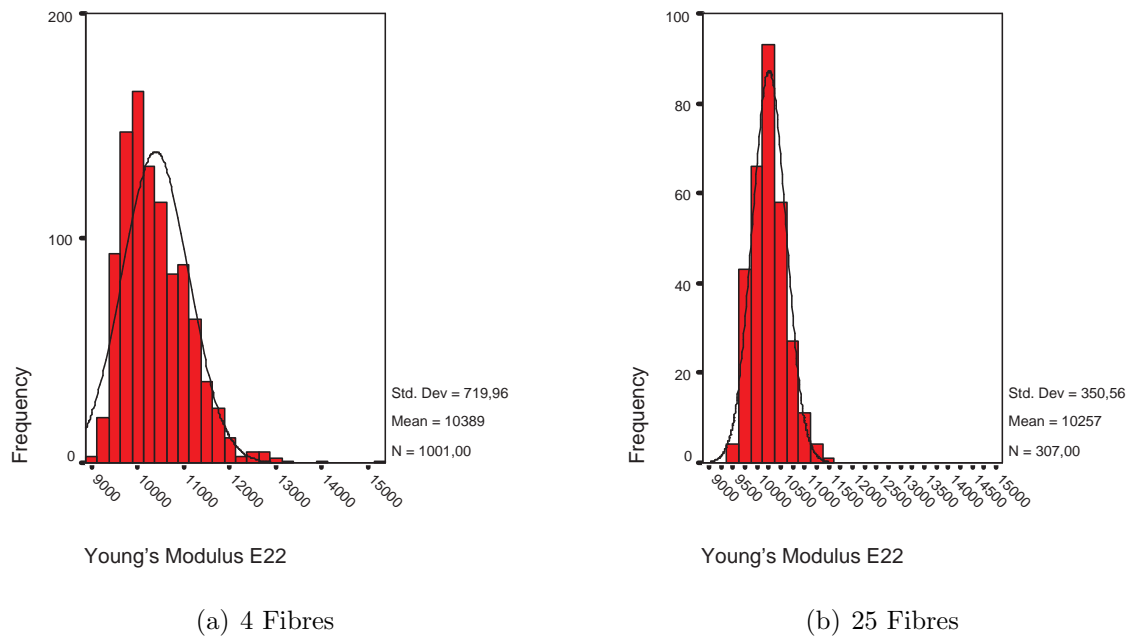
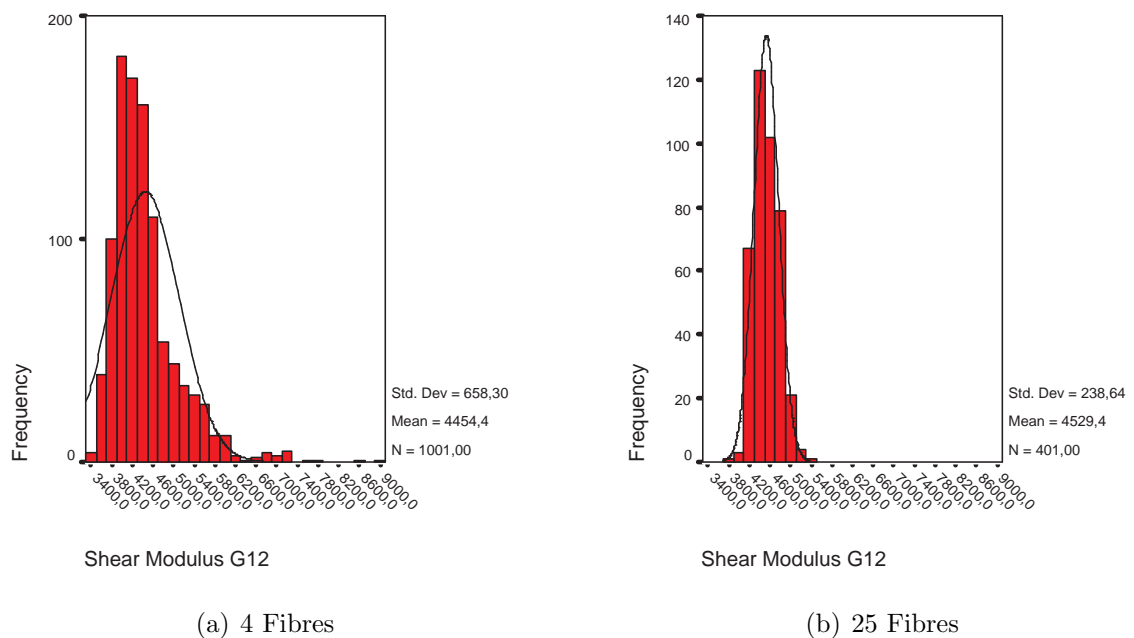


Figure 6.17: Young's Modulus E_{22} over E_{33}

The distribution of the elastic material constants is shown in Figures 6.18, 6.19 and 6.20 for 4 and 25 fibres. A normal distribution curve calculated from mean and standard deviation is plotted in each histogram as a black line. For an increased number of fibres the standard deviation and the width of the curve decrease. The histograms show an unbalanced distribution of the parameters for a low fibre number, but for a high number of fibres the distribution conforms to the normal distribution indicated by the black line. It is interesting that the mean value of the Young's modulus remains unchanged although the distribution is changing noticeably.

Figure 6.21 shows the convergence of the mean values for an increasing fibre number in the randomized unit cells that is the second convergence of this procedure. Young's Moduli E_{22} and E_{33} , shear moduli G_{12} and G_{23} and Poisson's Ratio ν_{23} are given under periodic boundary conditions. Furthermore, values are also given for displacement boundary conditions, indicated by "v" (for VOIGT), that can be seen as the upper bound (at least for Young's Modulus). Young's Moduli determined by hexagonal and square unit cell are shown for comparison as well as the calculated shear modulus indicated by "c", description see above. A number of 16 fibres obviously gives a converged result, although standard deviations decrease further for increased fibre numbers.

Figure 6.18: Histograms of Young's Modulus E_{22} for different fibre numberFigure 6.19: Histograms of shear modulus G_{12} for different fibre number

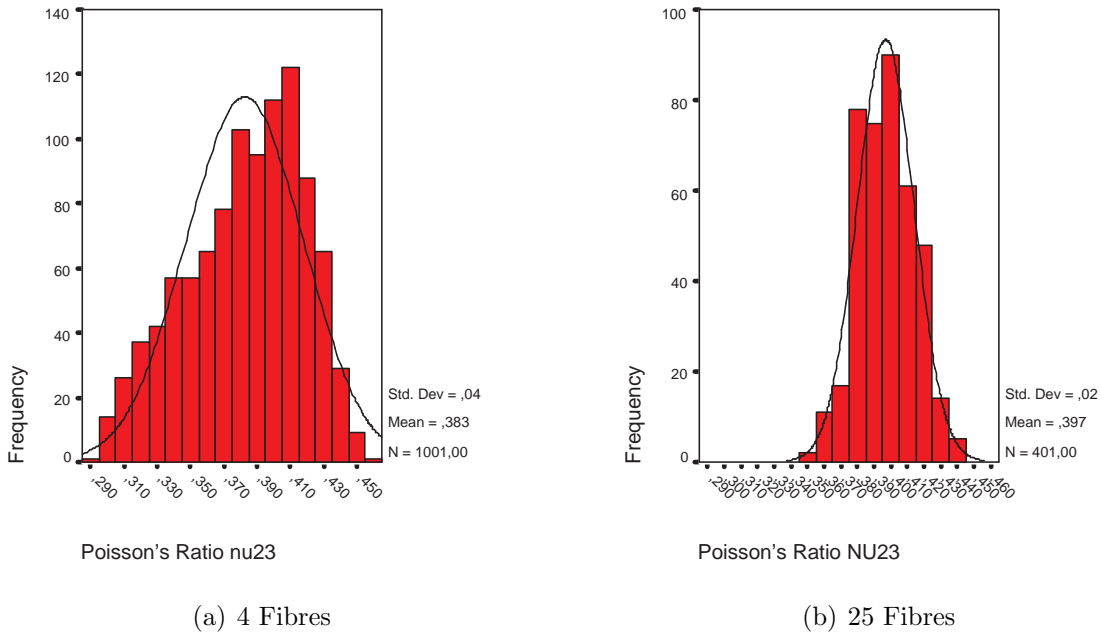


Figure 6.20: Histograms of Poisson's ratio ν_{23} for different fibre number

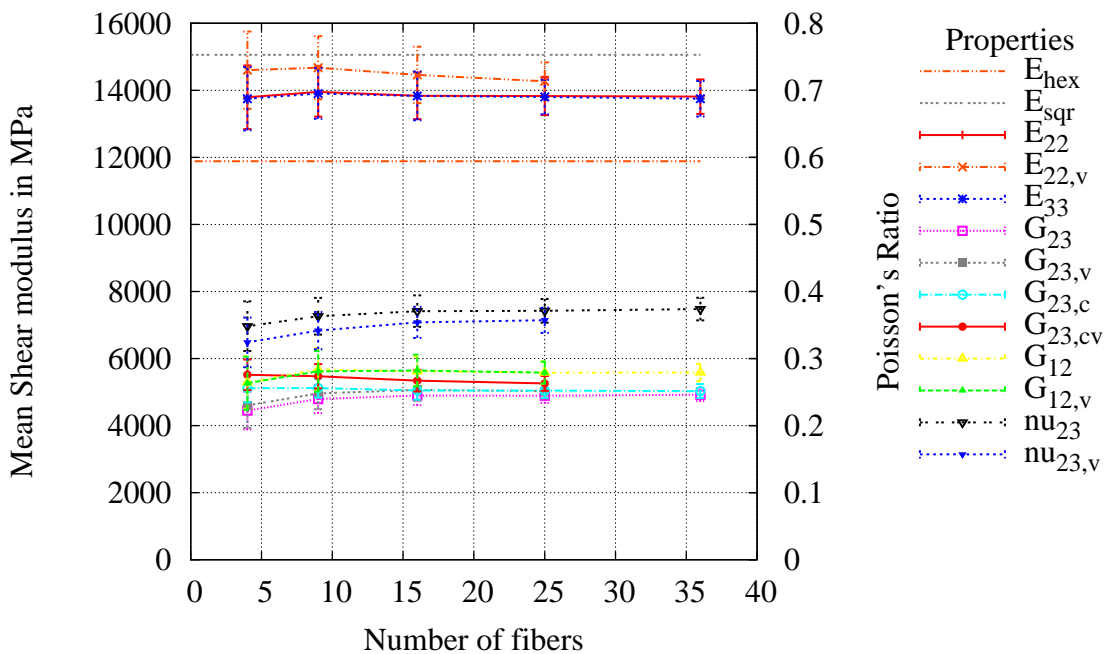


Figure 6.21: Mean elastic parameters for different fibre number

6.3.2 Inelastic Computations

A number of randomized unit cells has been loaded under transverse compression with the nonlinear material model for epoxy resin presented in section 3.1 and the failure criterion given in section 4.1.1. Explicit time integration has been used to be able to compute softening. Therefore, it was not possible to use the periodic boundary conditions given in section 5.2.2.1, because they require solving an equation system that slows the computation down drastically. Displacement boundary conditions have been used instead.

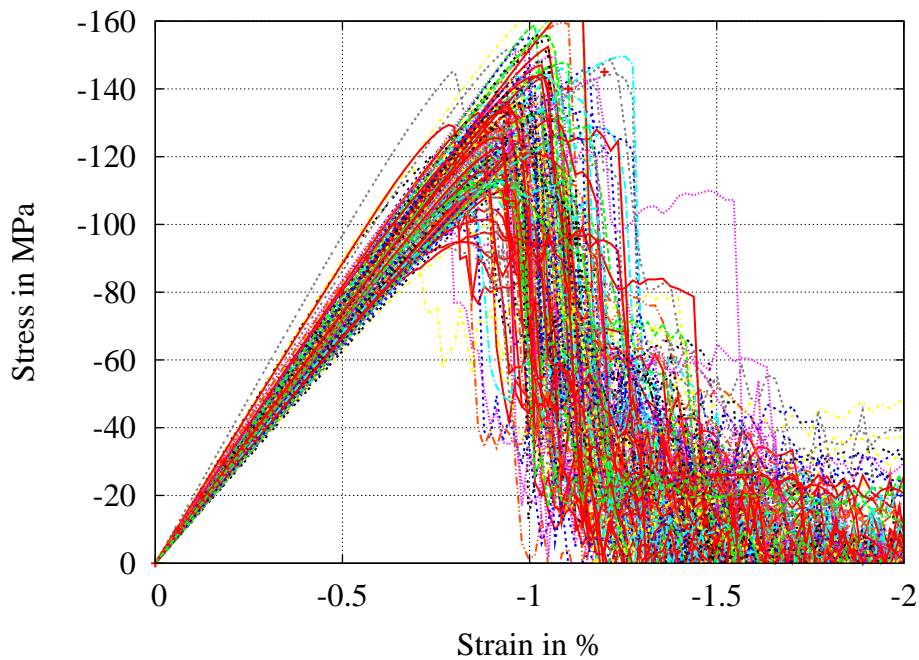


Figure 6.22: Stress-strain curves of randomized unit cells with 4 fibres

The resulting stress-strain curves of 172 randomized unit cells with four fibres are shown in Figure 6.22. A mean of these curves is given in Figure 6.23 with the blue line.

Basically, the random fibre distribution has a detrimental influence on the predicted strengths, because brittle failure occurs. It leads to weakest link behaviour, i.e. the weakest spot is responsible for the strength of the randomized unit cell. Therefore, an increased number of fibres comes along with a higher probability of a weaker spot and thus a decreased strength of the unit cell. This effect is illustrated very well by Figure 6.23, where a stress-strain curve from randomized unit cells with 16 fibres is given as well. The randomized unit cell with 16 fibres fails reasonably earlier than the 4-fibre unit cell. The effect of the weakest spot is considerably high in the presented 4- and 16-fibre randomized unit cells due to the comparatively low fibre number, compared to a UD-layer. Therefore, a convergence of the strength with an increased fibre number is expected by the author, because the influence of the weakest spot vanishes with higher fibre numbers. However, higher fibre numbers have not been simulated due to the high numerical effort. Figure 6.24 shows the points of failure for all randomized unit cells that have been averaged for the

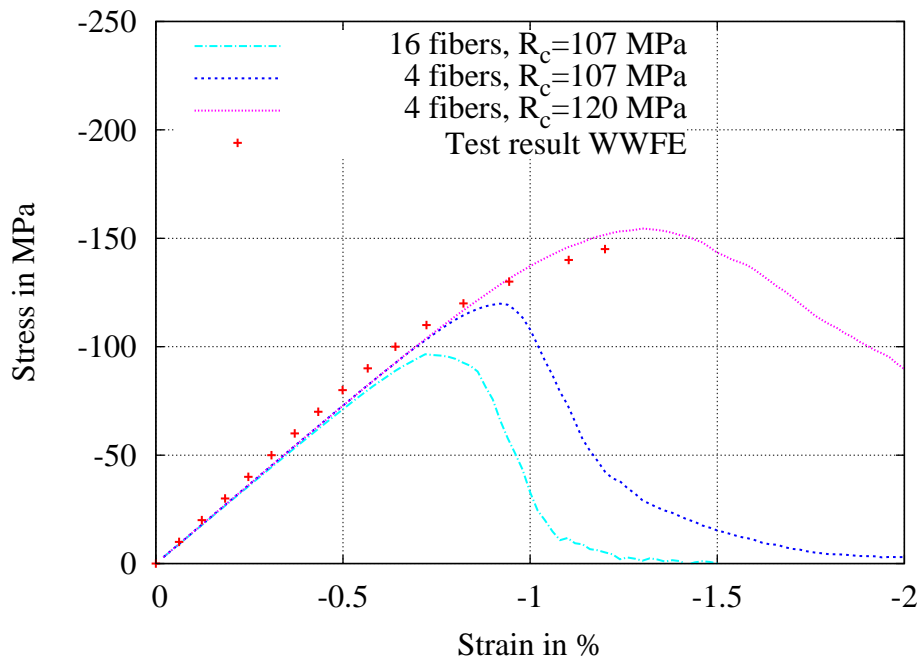


Figure 6.23: Averaged stress-strain curves of randomized unit cells under compression, sensitivity analysis

stress-strain curves in Figure 6.23 It can be seen that the randomized unit cells of equal fibre number exhibit a very broad range of strength and that the ranges of the strength of 4- and 16- fibre RUCs overlap considerably. This overlap stresses the fact that a higher fibre number leads to a lower strength only in a statistical sense, but that discrete examples do not exhibit this behaviour.

The weakest link behaviour can be overcome by enabling higher plastic deformations in the epoxy, that allow for a redistribution of the stresses. In the presented material model this can be achieved by an increased compressive strength R_{\perp}^c . An increased compressive strength of about 10 % leads to a 33 % increase in unit cell strength, shown in Figure 6.23. Thus, the RUC strength is very sensitive against the strength of the epoxy resin.

The strength distribution shown in Figure 6.25 conforms to the normal distribution independently on the number of fibres in the randomized unit cell even though the number of samples is comparatively low due to the numerical effort.

Discussion First of all, it has to be noted that the computation of strengths with an RVE/RUC is usually not permitted by the homogenization theory. The requirement of statistical homogeneity of the RVE/RUC is violated by the localized crack running through the whole RVE/RUC. However, the randomized unit cells can be seen as a parameter study of possible fibre arrangements at the microscale. Therefore, material behaviour of epoxy resin at the microscale is needed, that is different from the material behaviour observed in macroscale experimental tests, described in section 2.1. Microcracks and other inhomogeneities existing in the material are contained in this macroscale behaviour. Considering

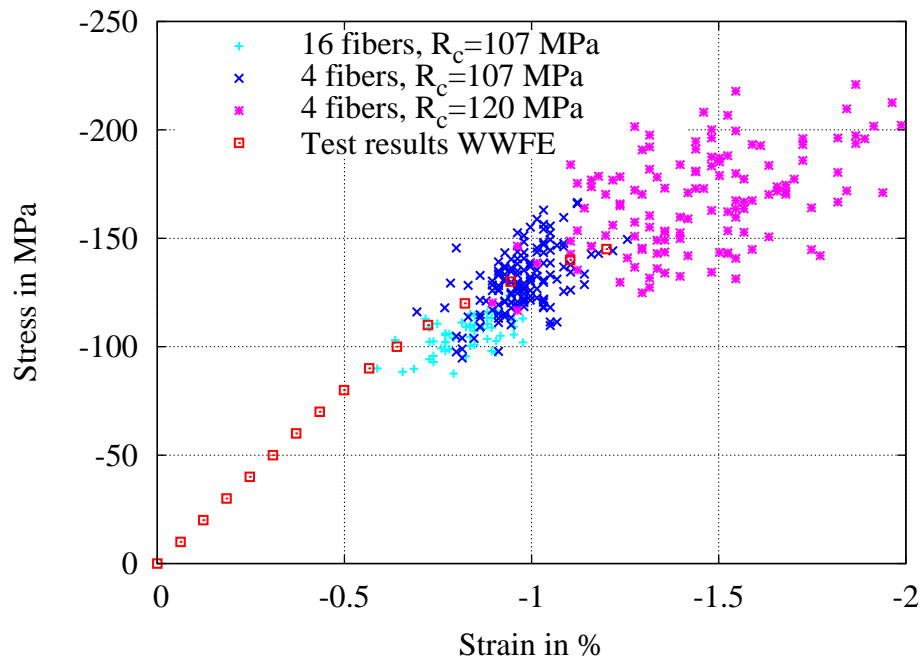
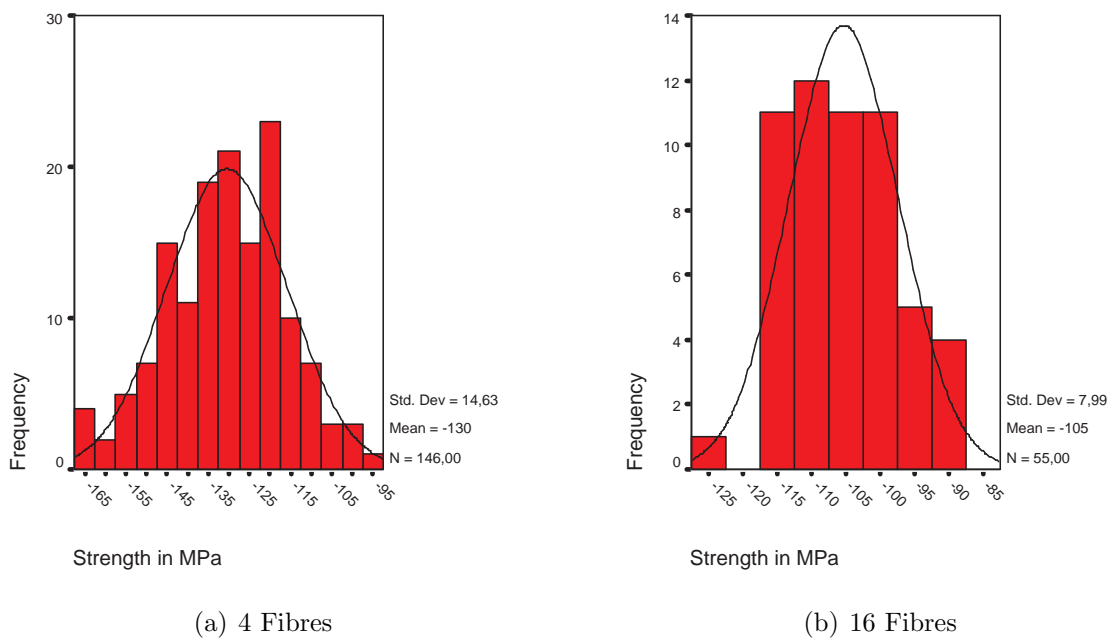


Figure 6.24: Failure of randomized cells

Figure 6.25: Histograms of Strength R_c for different fibre number

the homogenized microcracks in the macroscopic behaviour it can be concluded that the epoxy resin has a much more ductile behaviour on the microscale. It has been shown in Figure 6.23 that the ductility of the material and the strength have a over-proportional

influence on the strength of the RUC.

Furthermore, the strain energy release rate used here in the softening formulation is a macromechanical material property that is determined in an experimental test. Therefore, it incorporates the effect of the weakest spot, which is modelled with the random fibre arrangement as well, i.e. it is simulated twice. Thus, it would be necessary to determine material behaviour of epoxy at the microscale and to find out more about microcracks and other material inhomogeneities to build a more representative microscale structure.

6.4 Summary

Figure 6.26 gives a summary on the predicted transverse modulus $E_{\perp} = E_{22} = E_{33}$ for different volume fractions. Results are given for the rules-of mixture given in section 6.1, randomized unit cells with periodic boundary conditions “RUC PBC”, as well as with displacement boundary conditions “RUC DBC”, for periodic unit cells with square “UC sqr” and hexagonal fibre arrangement “UC hex” and for experimental results from the WWFE. The numerical predictions tend to be higher than the analytical ones and thus perform better, because the test results are higher than all predictions. This is an interesting result, because the randomized unit cell subjected to displacement boundary conditions should give an upper bound.

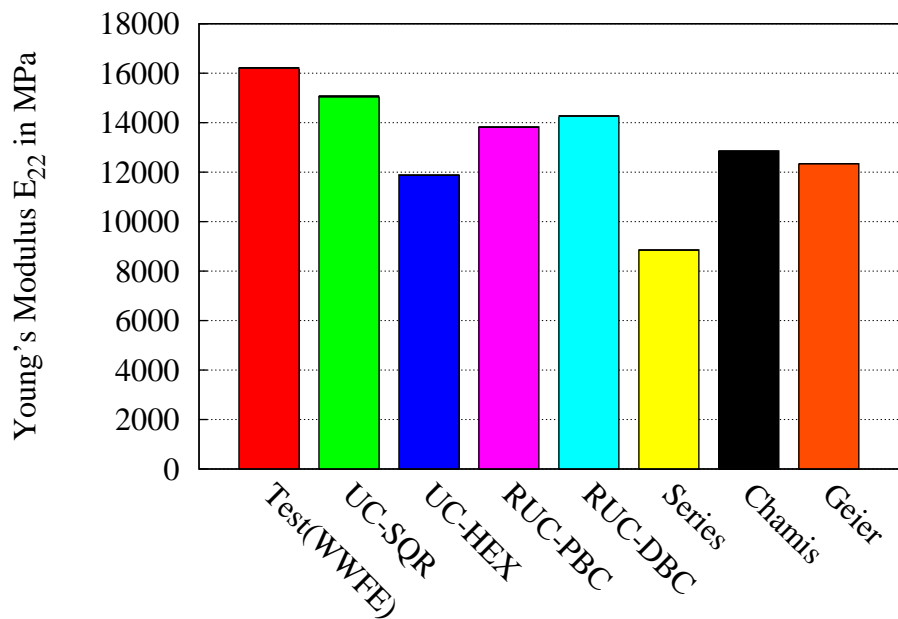


Figure 6.26: Transverse Young’s modulus E_{\perp} from test result, unit cell computations (25 fibres) and analytical rules of mixture

The transverse Young’s Moduli of the randomized unit cells lie between periodic square and hexagonal arrangement also for other fibre volume fractions than $v_f = 60\%$. Figure 6.27 shows the estimated in-plane shear moduli $G_{\parallel\perp} = G_{12}$ from rules-of mixture and numerical approaches. Interestingly, the randomized unit cells predict higher values than the periodic unit cells, that agree better with the experimental results. Once again, this result stresses the prominent influence of the random fibre arrangement seems on the shear behaviour.

Compared to the experimental results, the square unit cell yields a better overall prediction, although it does not exhibit transversely isotropic behaviour. However, the prediction of the transverse shear modulus should be neglected and the calculated transverse shear modulus should be used instead.

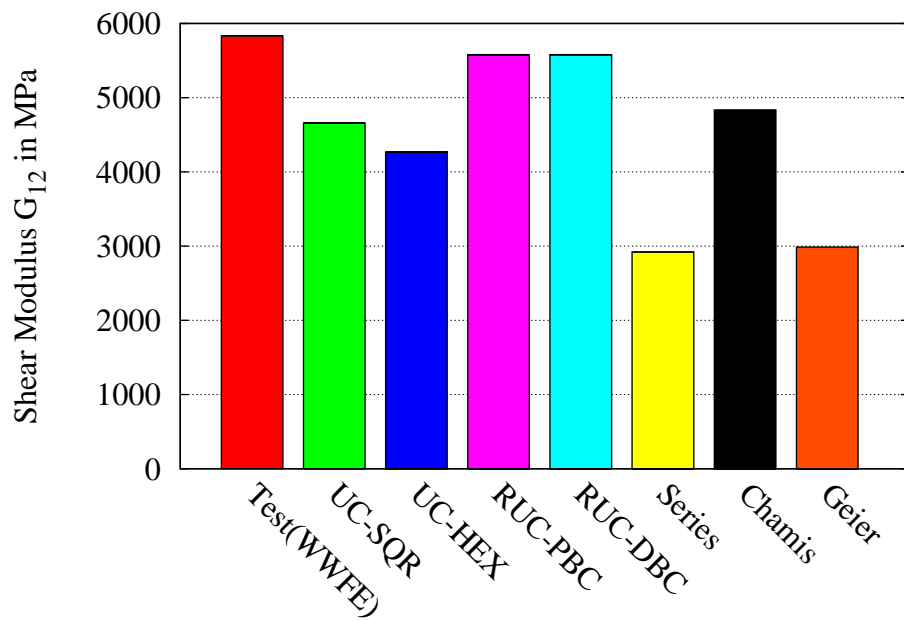


Figure 6.27: In-plane shear modulus $G_{\parallel\perp}$ from test result, unit cell computations (25 fibres) and analytical rules of mixture

The inelastic simulations on the randomized unit cells show that strength prediction with representative unit cells is problematic, especially because the results are very sensitive. However, the results of the periodic unit cell are promising, in spite of the substantial assumption of periodic fibre arrangement.

7 Mesomechanical Unit Cell Examples

The mesomechanical unit cell is used to model the fibre architecture and to determine material properties of textile composites on macroscale. The number of layers homogenized in one lamina depends on the type of preform. In the following examples for a mesomechanical unit cell of a non-crimp fabric, see fig. 7.2 and a weft-knitted fabric, see fig. 7.10 are given. Both examples consist of glass fibres and epoxy resin Rim 135.

In general, cracks in a composite firstly evolute in the layers and secondly between layers. Thus, regarding progressive failure of the structure it is advantageous to model each layer in one separate lamina on the macroscale, because damage can be easily attributed and identified for each layer separately. For textile composites this means to neglect some effects of the fibre architecture, that connects the layers, on the material behaviour. In case of the non-crimp fabric each layer is modelled separately, because through-thickness reinforcement density and influence are considerably low. Thus, the advantage of modelling each layer in separate lamina prevails a neglect of some reinforcement influence. However, in case of the weft-knitted fabric the material inhomogeneity is more pronounced, thus it is only possible to identify single fibre bundles rather than separate layers. Therefore one lamina on the macroscale has to represent two fabrics at once. On macroscale both examples are treated as orthotropic textile layers, so nine elastic material constants and nine strengths have to be determined.

Due to periodicity of stitching and knitting patterns a unit cell is used. The fibre bundles are modelled as transversely isotropic UD-material described in sec. 3.2, epoxy resin with isotropic material described in sec. 3.1.

Voxel meshing, see section 4.1.5, is used for discretization of the unit cell. It is required for the softening formulation to work properly. Furthermore, the definition of clear boundaries between fibre bundle and epoxy is problematic, because the fibre bundle itself contains epoxy and thus it is not clear where the fibre bundle ends and the epoxy resin pocket begins.

7.1 Material Parameters of Fibre Bundles

The material parameters for the fibre bundles are determined with a square micromechanical unit cell. The homogenized stress-strain curves of the four required virtual tests are given in Figure 7.1. Material parameters for epoxy resin RIM 135 are given in tab. 6.1, the plastic hardening curves are shown in fig. 3.5 and the strain energy release rate $G_f = 0.165 \frac{\text{N}}{\text{mm}}$ is taken from the similar material of the WWFE.

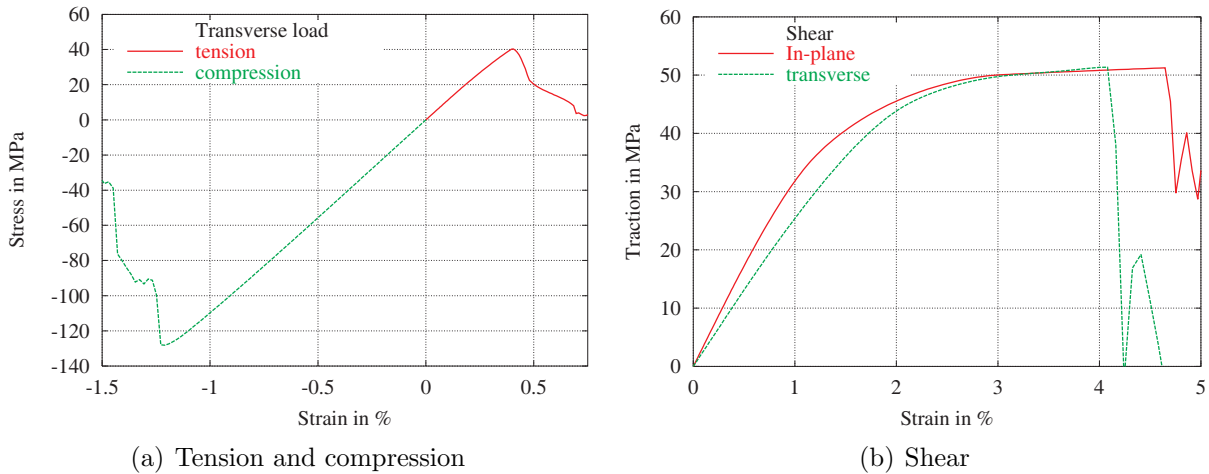


Figure 7.1: Stress-strain curves of square micromechanical unit cell computations for use in mesomechanical unit cells $v_f = 0.5$

Figure 7.1 illustrates the pressure dependent behaviour of UD-composites: a pronounced plastic hardening is found only under shear. The material parameters in longitudinal direction are determined with rules-of-mixture, see section 6.1, the remaining are determined from these curves, see table 7.1.

7.2 Non-Crimp Fabrics

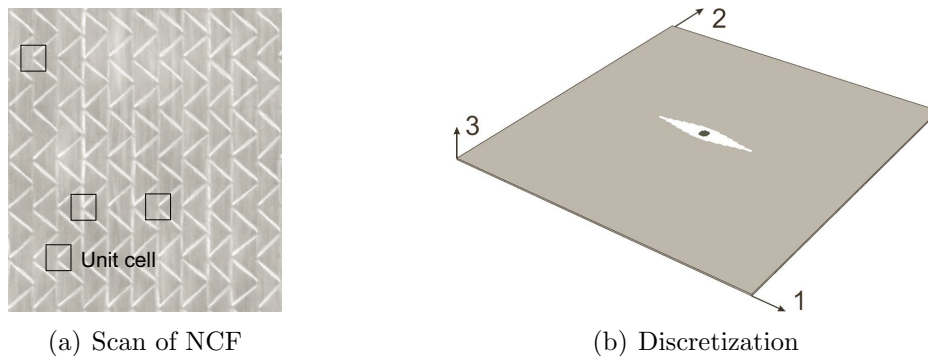


Figure 7.2: mesomechanical non-crimp fabric unit cell

Figure 7.2(a) shows a scan of a dry, unimpregnated non-crimp fabric. The lay-up of this fabric consists of four layers with the stacking sequence $[0^\circ/-45^\circ/90^\circ/45^\circ]$, the upper 0° -layer can be seen. However, the layers have different thicknesses, the thickness fractions are (48.7 % 0° , 23.0 % -45° , 4.8 % 90° , 23.0 % 45°). They are held together by a PES-yarn that has a mass fraction of 0.5 %. The periodic (trikot) stitch pattern has a spacing of the stitches of 5 mm in 0° - and 90° -direction. Of all textile fabrics the structure of the non-crimp fabric resembles UD-laminates most. Fibre layers can easily be identified

Table 7.1: Mechanical properties of E-Glass/RIM 135 fibre bundles

Properties	Unit	square unit cell
Longitudinal modulus ¹ E_{\parallel}	GPa	38.7
Longitudinal tensile strength R_{\parallel}^t	MPa	1075.
Longitudinal tensile failure strain $\varepsilon_{\parallel}^t$	%	2.905
Longitudinal compressive strength R_{\parallel}^c	MPa	725.
Longitudinal compressive failure strain $\varepsilon_{\parallel}^c$	%	1.96
Transverse modulus ¹ E_{\perp}	GPa	11.07
Transverse compressive strength R_{\perp}^c	MPa	128.5
Transverse compressive failure strain ε_{\perp}^c	%	1.21
Transverse tensile strength R_{\perp}^t	MPa	40.3
Transverse tensile failure strain ε_{\perp}^t	%	0.4
In-plane Shear Modulus ¹ $G_{\parallel\perp}$	GPa	3.51
In-plane Poisson's ratio $\nu_{\parallel\perp}$		0.264
In-plane Shear Strength $R_{\parallel\perp}$	MPa	51.2
In-plane Shear failure strain $\varepsilon_{\parallel\perp u}$	%	4.64
Transverse Shear Modulus ¹ $G_{\perp\perp}$	GPa	2.63
dito, $G_{\perp\perp} = \frac{E_{\perp}}{2(1+\nu_{\perp\perp})}$	GPa	4.19
Transverse Poisson's ratio $\nu_{\perp\perp}$		0.32
Transverse Shear Strength $R_{\perp\perp}$	MPa	51.4
Transverse Shear failure strain $\varepsilon_{\perp\perp u}$	%	4.08

¹ Initial modulus

and the disturbance through stitch yarns is comparatively low. Therefore, it is logical to model each layer of the non-crimp fabric separately to identify the material parameters. In Figure 7.2(a) several unit cells for this purpose are marked on the dry fabric. A comparison of the marked areas reveals that the periodicity of the pattern has several imperfections. During impregnation the shape of these imperfections will probably be changed and it would be an interesting prospect to identify different imperfections and their influence on the material parameters. In this work the imperfections will be neglected and a perfectly periodic unit cell is assumed. This is only a small simplification, because the non-crimp fabric is a periodic structure through the stitch pattern.

Lomov et al. (2002) describe the internal structure of non-crimp fabrics in great detail. They give measures for the epoxy resin pockets around the through-thickness stitches based on the stitching parameters and for channels for the in-plane part of the yarns on the face and back of the non-crimp fabric. In this work, however, the in-plane part of the yarn and its channels are neglected, because the yarn has a very small diameter and provides 0.5% of the mat weight. Furthermore, the PES-yarn has not such a good mechanical performance as the glass fibres. Lomov et al. (2002) distinguish between inner and outer layers of a non-crimp fabric, but these differences are as well neglected here. For the 45°-layers another unit cell geometry would be favorable, but through the wide spacing of the stitches and the high 0°-layer fibre proportion this difference can be neglected. It has to be noted, that despite all simplifications the strengths determined with this unit cell remain on the safe side in the macroscopic examples in chapter 8.

Figure 7.2(b) illustrates the discretization of the unit cell, it consists of 200x200x1 elements, and the layer coordinate system, where 1 is the fibre direction. The fibre bundle structure in thickness direction is neglected, hence only one element is used in this direction. Fig. 7.3 shows the different components, fibre bundle, epoxy resin pocket and stitching yarn, of the unit cell and their dimensions. From the mat weight of the PES-yarn a radius $r_N = 0.054$ mm was calculated. After Lomov et al. (2002) an inner layer resin pocket thus is $L_H = 2.64$ mm long and $b_H = 0.352$ mm wide.

It is clear that fibre undulations and local variations in the fibre volume fraction occur around the epoxy resin pocket. The variable fibre volume fraction is neglected here. To account for the variable fibre orientation around the epoxy resin pocket, a variation of the material orientation in the elements is applied. An harmonic function is assumed to describe the angle of misalignment

$$\varphi = \frac{2\pi}{l} \left[\frac{b_H}{2} - \frac{\frac{b_H}{5} - (y - (1 - \frac{b_H}{2} \cos \frac{2\pi}{l} x))}{1 - \frac{b_H}{5} (1 - \cos \frac{2\pi}{l} x)} \right] \sin \frac{2\pi}{l} x \quad (7.1)$$

dependent on the coordinates x, y of the center point of the element, and the length l of unit cell and width b_H of the resin pocket. A distribution of the fibre misalignment angles can be seen in Figure 7.4(a), where a unit cell with a reduced number of elements is shown for reasons of clarity. To simplify preprocessing, the angles of misalignment are not given exactly in each element, but grouped in seven groups. Figure 7.4 shows which elements share a mean equal fibre orientation.

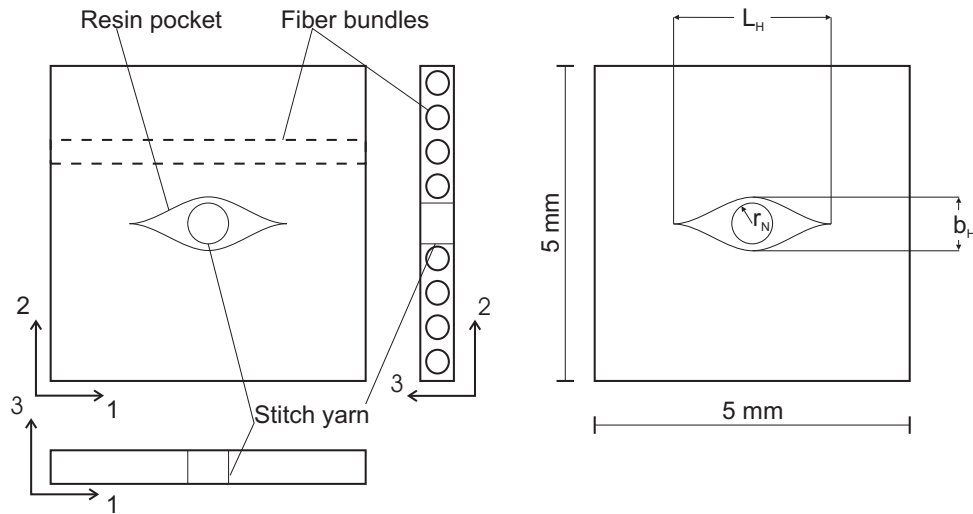
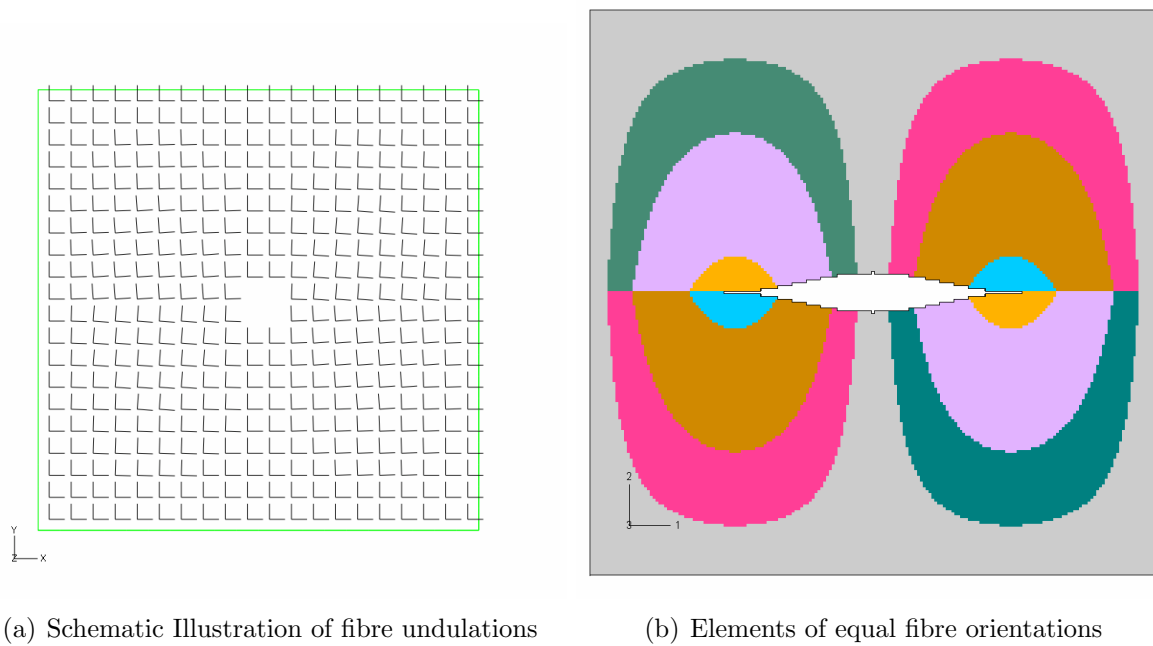


Figure 7.3: Geometry of mesomechanical unit cell for non-crimp fabric



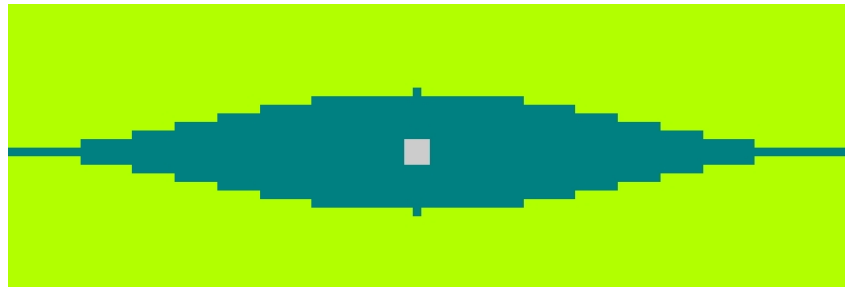
(a) Schematic Illustration of fibre undulations

(b) Elements of equal fibre orientations

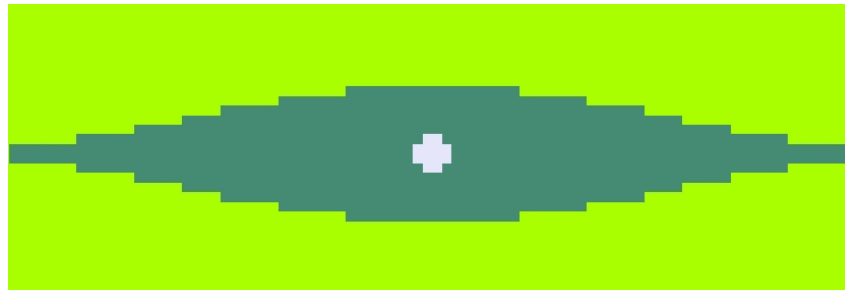
Figure 7.4: Fibre orientation in mesomechanical NCF unit cell

It has to be noted that the voxel meshing technique requires a thorough checking of the mesh. Due to the serrated interface between different constituents it is possible that single elements act as a notch and thus develop a big influence on strength of the unit cell.

The material behaviour of the fibre bundles in the mesomechanical unit cell has been simulated with the material model described in sec. 3.2. Required mechanical properties have been determined with the micromechanical unit cell, as described in the previous section. The IQC and the softening formulation presented in section 4.2 are used for



(a) Unfavorable configuration



(b) Favorable configuration

Figure 7.5: Different discretization of epoxy resin pocket with voxel mesh

strength prediction. To use one consistent set of material parameters, the results of the square unit cell, listed in table 7.1, are taken as input here, because it overall yielded better estimations, see section 6.4. For numerical regularization of FF a strain energy release rate of $G_f = 0.3 \frac{\text{N}}{\text{mm}}$ has been used.

The simulated unit cell exhibits orthotropic behaviour, thus nine virtual tests are needed to determine the material parameters. An overview is given in Figure 7.6. Tension and compression are applied in each normal direction, with symmetric periodic boundary conditions, described in section 5.2.2.2. Shear loads are applied in 1-2-, 1-3- and 2-3-direction. In-plane shear (1-2-direction) is modelled with general periodic boundary conditions, described in section 5.2.2.1, but top and bottom surface of the unit cell are constrained in thickness direction, to save computational cost. For both other shear load cases the general periodic boundary conditions require too much computational cost, therefore symmetric periodic boundary conditions for pure shear are used.

Stress-strain curves for normal loads and shear are shown in fig. 7.7.

Under normal loads the material behaves nearly linear elastic until failure, whereas under shear plastic deformations occur. Experimental tests with a new test method developed by Hartung, Aschenbrenner, and Teßmer (2007) yield a through-thickness strength (in 3-direction) of 42 MPa to 52 MPa, which is in very good correspondence with the results of the virtual tests presented in fig. 7.7(a). It is possible to compare these results, because from the fracture surface of the specimens can be seen that intralaminar failure occurred. Other results cannot be compared, because very special specimens would have to be prepared consisting of only one layer with through thickness reinforcement. A validation of the estimated material parameters is therefore carried out on the macroscale, see section 8.

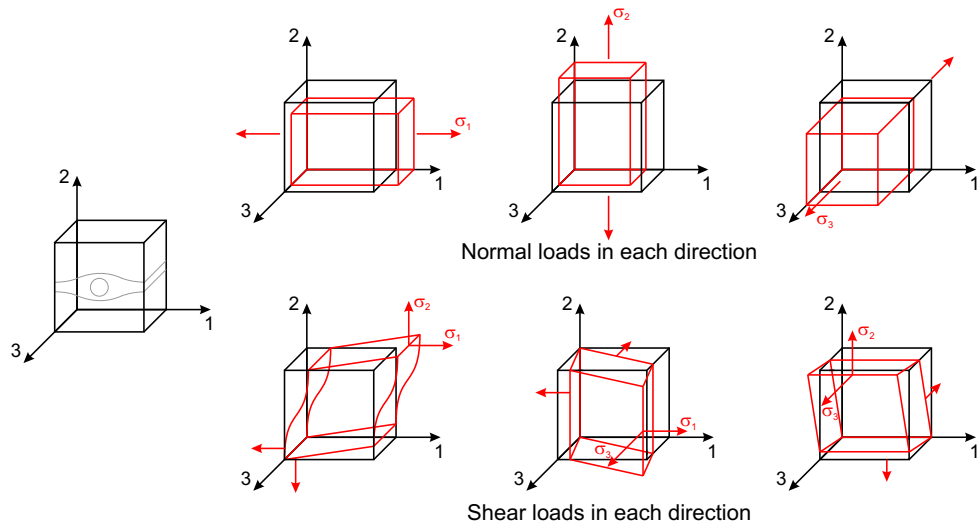


Figure 7.6: Load cases of mesomechanical unit cell for non-crimp fabric

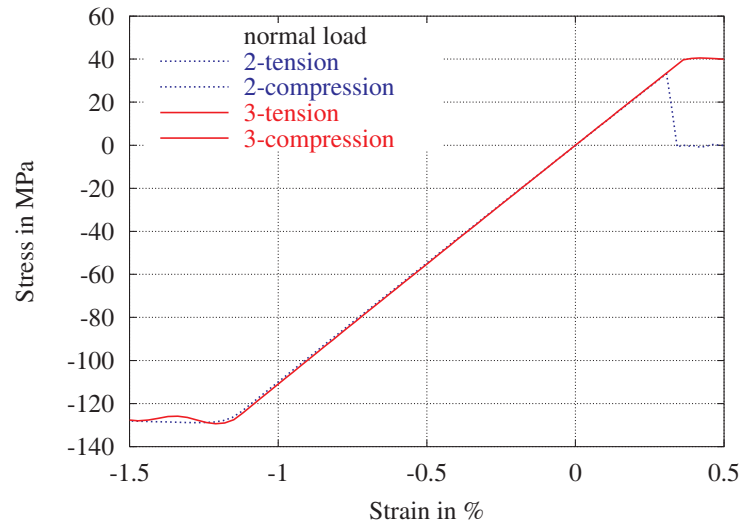
Due to the localization of the plastic deformations in a shear band, seen in fig. 7.8(b) for in-plane shear (marked with 12) the overall behaviour of the unit cell does not exhibit such pronounced plastic deformations as the epoxy resin or fibre bundle material alone. Fig. 7.8(a) also shows a crack under transverse tension that starts at the epoxy resin pocket and evolves into through the fibre bundles. The epoxy resin pocket does not exhibit damage, because the tensile strength of epoxy resin is higher than the transverse tensile strength of the fibre bundles. Under shear, fig. 7.8(b), both epoxy resin pocket and fibre bundles show plastic deformations, but the crack starts in the fibre bundle because the resin pocket is by far more ductile. Figure 7.8 shows very clearly that the cracks are oriented in the material orientation and evolve parallel to the fibres.

The resulting stiffnesses and strengths are summarized in table 7.2.

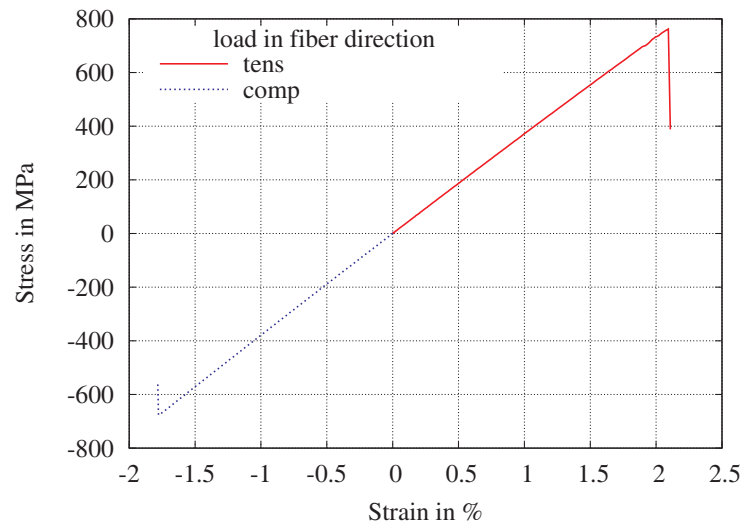
Table 7.2: Mechanical properties of non-crimp fabric layer made of E-Glass/RIM 135

Properties	Unit	Value
Longitudinal modulus ¹ E_1	GPa	37.5
Longitudinal tensile strength R_1^t	MPa	762.1
Longitudinal compressive strength R_1^c	MPa	676.3
Transverse modulus ¹ E_2	GPa	10.8
Transverse compressive strength R_2^c	MPa	128.8
Transverse tensile strength R_2^t	MPa	40.4
Through-thickness modulus ¹ E_3	GPa	11.07
Through-thickness compressive strength R_3^c	MPa	128.5
Through-thickness tensile strength R_3^t	MPa	40.1
In-plane Shear Modulus ¹ G_{12}	GPa	3.49
In-plane Poisson's ratio ν_{12}		0.25
In-plane Shear Strength R_{12}	MPa	49.21
Out-of-plane Shear Modulus ¹ G_{13}	GPa	4.33
Out-of-plane Poisson's ratio ν_{13}		0.25
Out-of-plane Shear Strength R_{13}	MPa	48.42
Transverse Shear Modulus ¹ G_{23}	GPa	2.52
Transverse Poisson's ratio ν_{23}		0.4
Transverse Shear Strength R_{23}	MPa	38.13

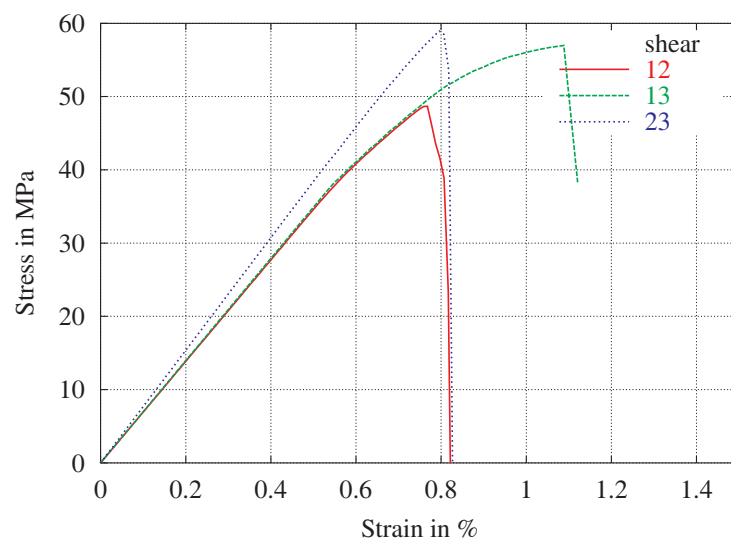
¹ Initial modulus



(a) Transverse normal loads in 2- and 3- direction

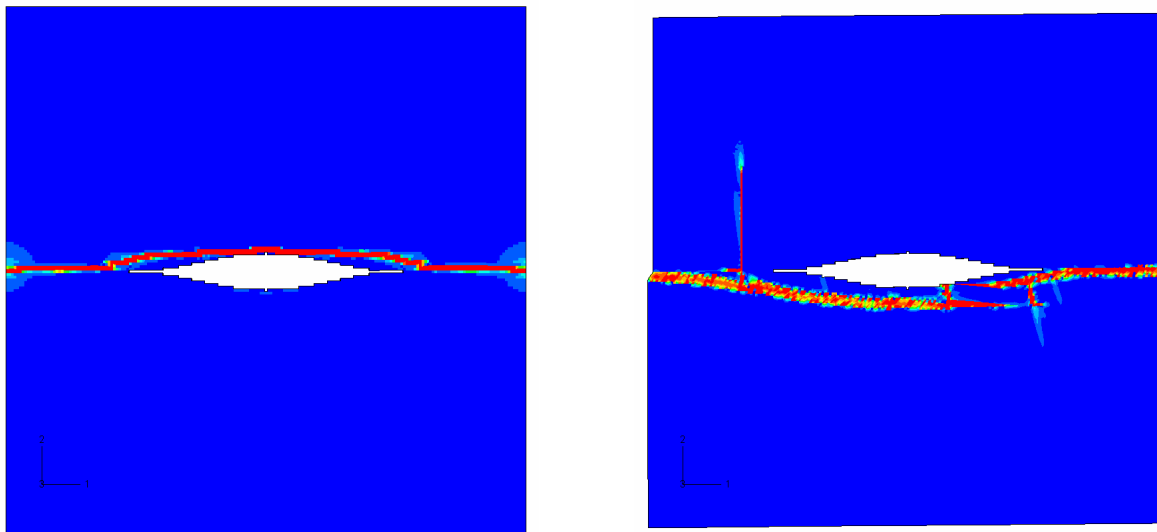


(b) Fibre direction normal loads



(c) Shear in 12-, 13- and 23-direction

Figure 7.7: Stress-strain curves of mesomechanical NCF unit cell computations



(a) In-plane transverse tension

(b) In-plane shear

Figure 7.8: Damage evolution in mesomechanical NCF unit cell

7.3 Biaxial Weft-Knit Fabrics

In this section a unit cell of a biaxial weft-knitted fabric (BWKF) is described as an example for a more complicated unit cell. The biaxial weft-knit fabric mainly consists of tows in warp- and fill-direction, respectively. The layers are connected with a weft-knitted glass-fibre yarn. Two of these textile layers are combined such that a $[90^\circ/0^\circ//0^\circ/90^\circ]$ lay-up is resulting. The fabric consists of glass fibres and is infiltrated with epoxy resin RIM 135.

Compared to the non-crimp fabric described above, in the biaxial weft-knit fabric a thicker yarn is used, although still the yarn diameter is smaller than the fibre bundle diameter. Furthermore, the loops of the yarn are denser and the yarn is stronger, because it consists of glass fibres instead of PE. The material structure of the biaxial weft-knit fabric is much more heterogeneous, the individual fibre bundles are clearly identifiable in a ct-scan, see Figure 2.9. In the draping process, the 0° -layers of the fabric thus penetrate each other and "interlock", as can be seen in Figure 7.10, where the smallest unit cell of the weft-knitted fabric is illustrated. The unit cell consists of fibre bundles in warp- and fill-direction, the knitting yarn and the epoxy resin. The fibre bundles and epoxy resin are discretized with volume elements, whereas the knitting yarn, is modelled with embedded truss elements, because of its lower diameter. On the right hand side of fig. 7.10 the epoxy resin is removed to make the knitting yarn visible.

The dimensions of the unit cell are taken from Ulbricht and Haasemann (2007). Material parameters for epoxy resin are given in table 6.1. For the fibre bundles the material parameters are taken from table 6.2 for a fibre volume fraction of $v_f = 0.5$. It is not so important that the resulting fibre volume fraction of the unit cell is not very realistic, because this example shall only demonstrate the general implications of modelling multiple layers in one unit cell.

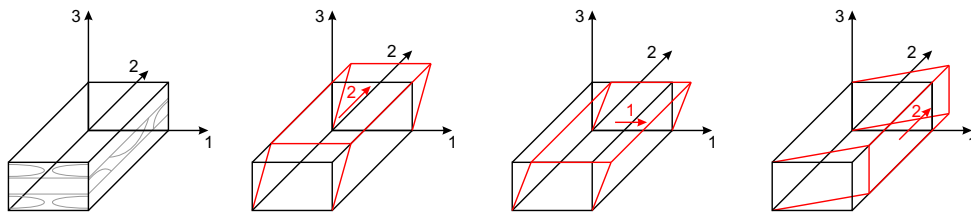


Figure 7.9: Shear load cases of mesomechanical unit cell for weft-knitted fabric

Figure 7.9 summarizes the shear load cases applied on the unit cell. In all cases simple shear has been used to keep the computational effort as low as possible. Normal loads have been applied in analogy to the NCF unit cell.

Figure 7.11 shows the computed stress-strain curves of the weft-knitted fabric unit cell. In comparison with the stress-strain curves of the NCF in Figure 7.7 the BWKF behaves less linear, because of its multiple layers. Under tension first damage occurs at around 50 MPa in 2-direction and at 140 MPa in 1-direction, but the load can be increased further.

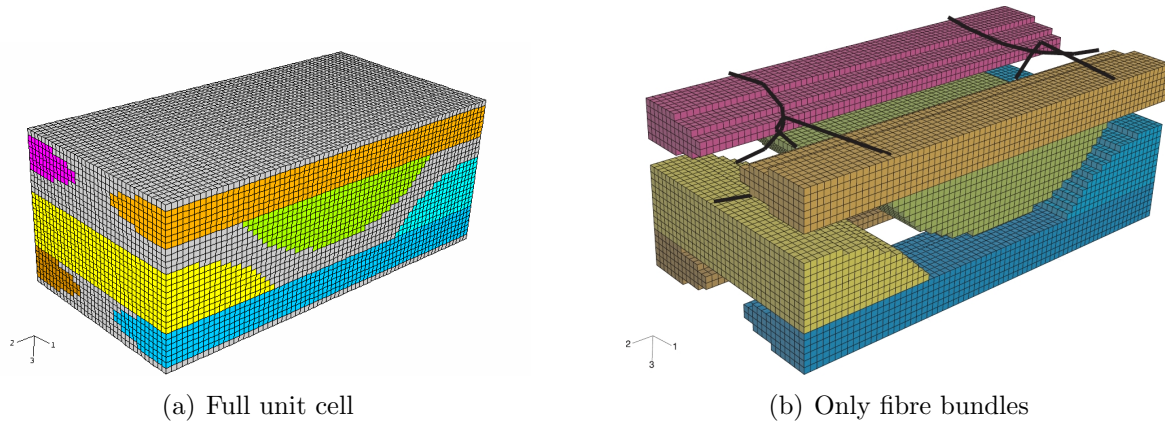
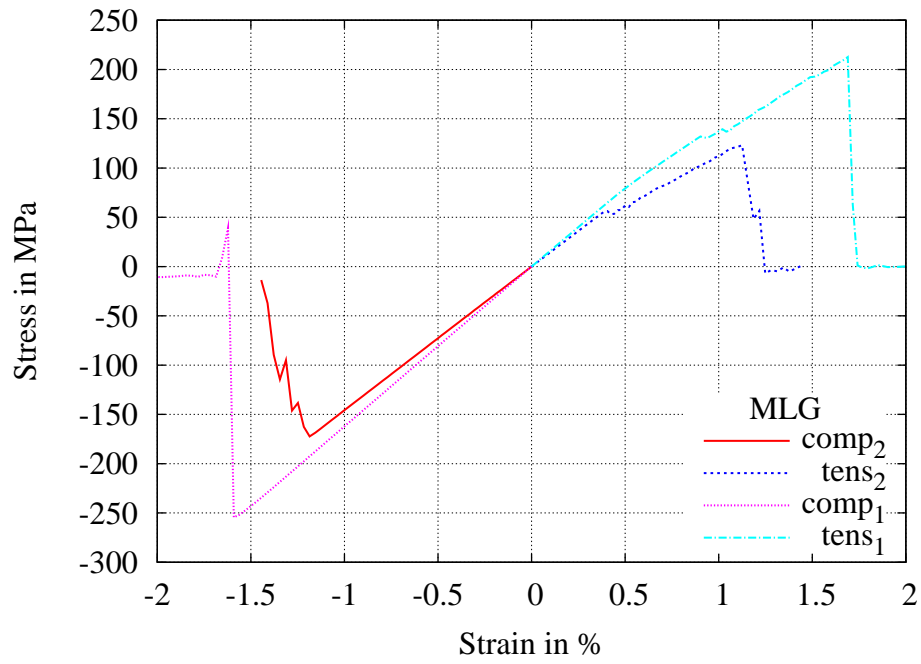


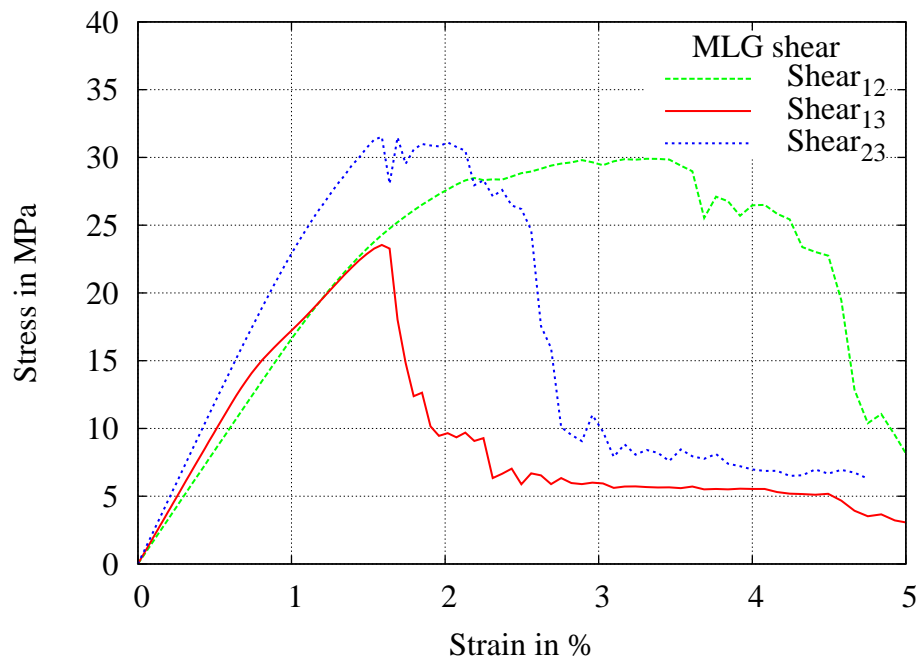
Figure 7.10: Geometry of mesomechanical unit cell for two weft-knitted fabrics

These stress-strain curves can be used to define a homogenized orthotropic continuum as a description of the weft-knitted fabric. This orthotropic continuum would be representative for normal loads only, because of the assumption of a uniform stress distribution over the RVE, see section 5.2. However, if a laminate consists of the two fabrics discretized in the unit cell the macro-stresses are no longer homogeneous over the height of unit cell under bending. Such a laminate shows pronounced differences in the bending stiffness dependent on the direction. Therefore, the use of a standard orthotropic CAUCHY continuum is problematic, because the different bending stiffnesses of warp- and fill-direction are not considered.

Haasemann and Ulbricht (2006) thus present a COSSERAT continuum capable of accounting for these different bending effects. It requires a number of additional virtual tests on the mesomechanical unit cell for homogenization to include bending and torsional deformation modes. Another possibility to include the direction-dependent bending and torsional behaviour is a stiffness matrix equivalent to the ABD-Matrix that is used in classical laminate theory. The description of inelastic material behaviour, however, becomes even more complicated in such approaches, because the all deformation modes are probably influenced differently by localized inelastic effects. It is not an easy task to find a formulation capable of describing these coupling effects and to identify the required material parameters. Therefore, a layer-wise simulation seems favorable, even if it neglects the coupling effects between the layers. In such a simulation the presented unit cell would be divided in three layers, where tows of equal direction would be grouped in. It would be an interesting prospect to quantify the errors of a layer-wise approach compared to a textile layer-wise approach. Furthermore, the differences in computational effort of both approaches are interesting as well.



(a) Normal load



(b) Normal load

Figure 7.11: Stress-strain curves of weft-knitted fabrics unit cell

8 Macroscopic Examples

In this chapter macroscopic simulations are carried out to validate the multiscale algorithm presented in this work. Therefore, experimental results from tests conducted by DLR Braunschweig are compared with the computation. Firstly, a tensile test in 0° -direction of a coupon specimen is used for validation of the determined in-plane stiffness and strengths. Secondly, a 3-point bending test of a thick laminate gives information on how the model performs in the computation of three-dimensional stress states.

An orthotropic, linear elastic material is used in combination with the failure criterion of Juhasz, because nonlinear material models were not available. In contrast to the unit cell simulations at micro- and mesoscale, plasticity plays a minor role in the simulations at the macroscale, because the composite behaviour is dominated by the fibres, that behave nearly linear elastic elastic. However, nonlinear material behaviour plays a role under certain circumstances, e.g. in biaxial laminates under shear, but it can be neglected in the presented examples without major consequences. The post-failure behaviour of the material is crucial for a progressive damage analysis. The criterion of Juhasz is based on Puck's UD-composite criterion, therefore, it is possible to use the softening formulation of Puck, see section 4.2.1.2 for the description of lamina softening. If tensile IFF occurs ($\sigma_n > 0$), E_{22} and E_{33} are degraded simultaneously, an orthotropic damage is not included. Material parameters were determined by the mesomechanical unit cell for a non-crimp fabric presented in section 7.2.

8.1 Coupon Test

At DLR Braunschweig a coupon specimen made of two layers of non-crimp fabric was tested under tension. The non-crimp-fabrics are arranged such that the 0° -layers are at top and bottom. Therefore, the stacking sequence is $[0^\circ/-45^\circ/90^\circ/45^\circ// -45^\circ/90^\circ/45^\circ/0^\circ]$. It has to be noted that this is not a symmetric stacking sequence and the coupon exhibits coupling effects between bending and extension. In the experiments the load was applied displacement-driven and DMS were applied for measuring strains. The simulation was carried out on a cutout of an infinite plate, see Figure 8.1, equivalent to the laminate tests presented in section 4.2.3. Volume elements are used for the discretization of the laminate, one for each layer. The boundary conditions are such that the in-plane deformations are equal in all layers and that the elements remain rectangular. In through-thickness direction no boundary conditions are applied, i.e. the elements can deform freely, but through couplings the elements are forced to remain rectangular as well. Therefore, several imperfections have been neglected.

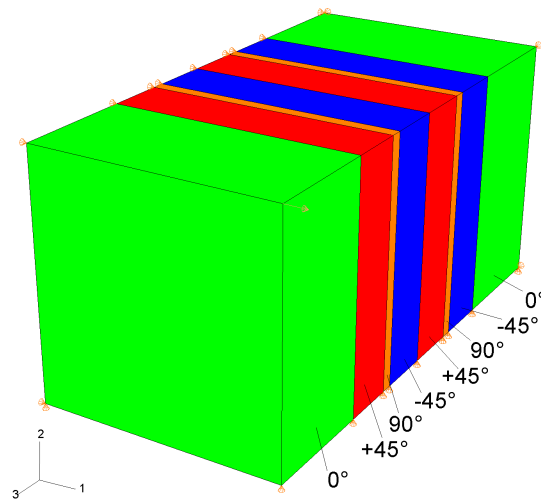


Figure 8.1: Discretization of coupon test

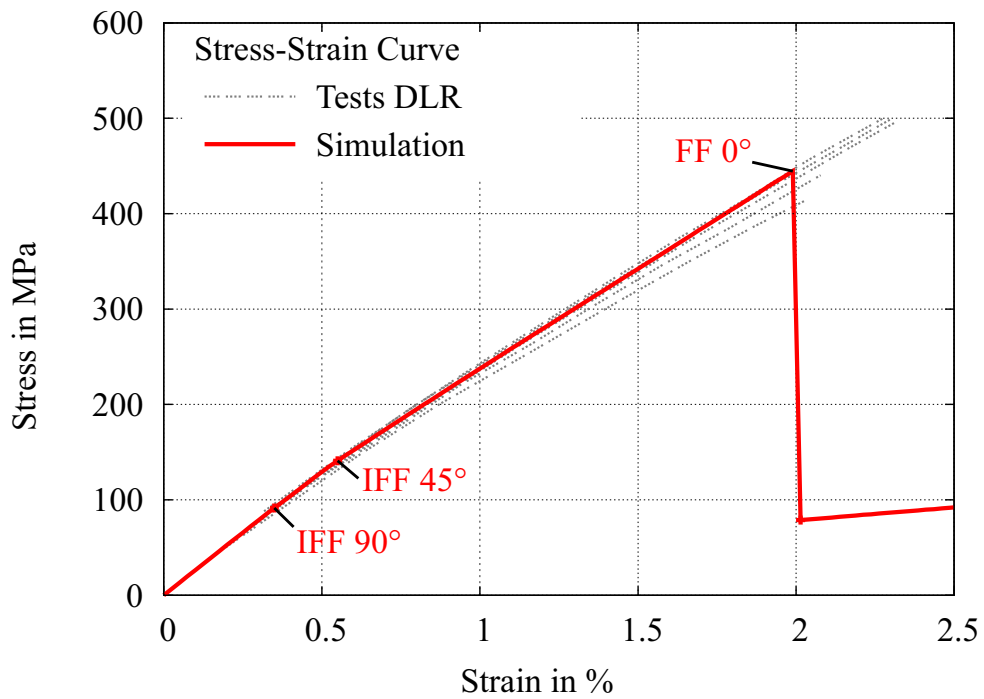


Figure 8.2: Tensile test in 0° direction: stress-strain curve experimental results vs Simulation

In Figure 8.2 the stress-strain curves from test and ABAQUS-simulation are compared. The numerically predicted elastic material parameters are in excellent correspondence with the test results. This can also be seen in Figure 8.3, where the material degradation of the longitudinal secant Young's Modulus is given over the applied strain. Furthermore,

the degradation of the coupon due to inter-fibre failure is modelled very well. Therefore, it can be concluded that the inter-fibre strengths, predicted by the mesomechanical unit cell, and the softening formulation are very good. In fibre direction, the numerically predicted $\sigma_x = 445$ MPa correspond very well with the mean coupon strength of $\sigma_x = 466$ MPa.

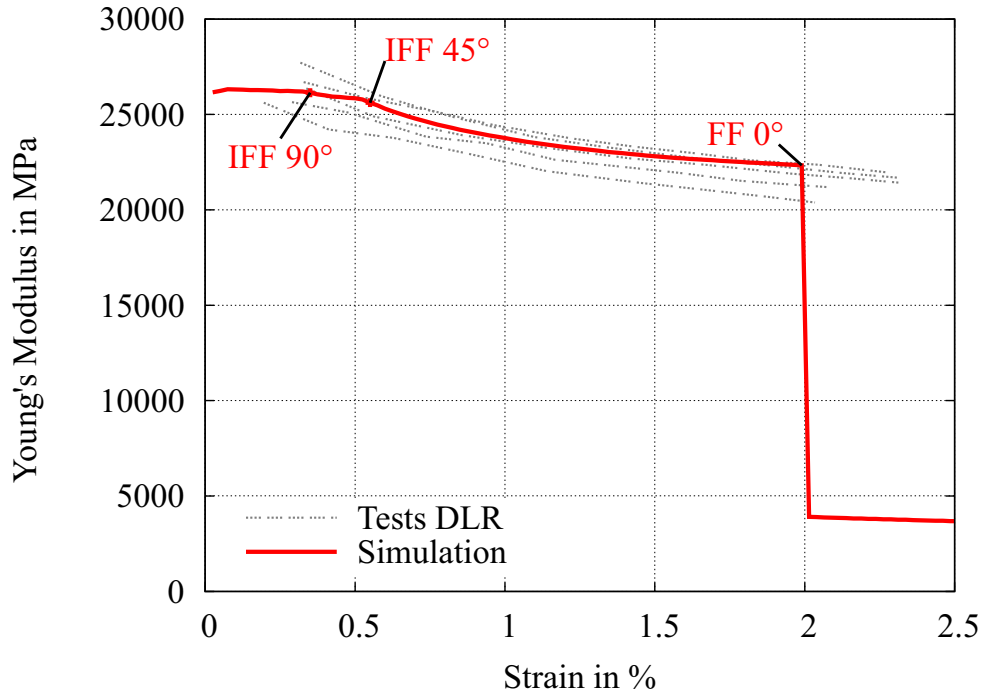


Figure 8.3: Young's Modulus from tensile test in 0° direction

8.2 3-Point-Bending Test

To account for a three-dimensional stress state, a thick specimen with two holes was tested under 3-point bending, see Figure 8.4. The specimen consists of 10 non-crimp fabrics and is 10 mm thick as well as 25 mm wide. The stacking sequence is $[0^\circ/-45^\circ/90^\circ/45^\circ// -45^\circ/90^\circ/45^\circ/0^\circ]_5$. The load was applied displacement-driven up to a maximum deflection of 20 mm. A quarter of the model is discretized only with symmetric boundary conditions in order to save computational time. The finite element mesh consisting of 158800 elements (ca. $105 \times 15 \times 100$) and the applied boundary conditions are shown in Figure 8.5. For numerical stabilization a fracture energy regularization as described in section 4.2.2.3, has been applied after FF. The strain energy release rate is chosen as small as possible such that oscillations of the load-displacement curve due to FF are reduced as far as possible, but the results are not influenced by the regularization. A parameter identification yielded a value of $G_f = 3.0 \frac{\text{N}}{\text{mm}}$ as a practical solution.

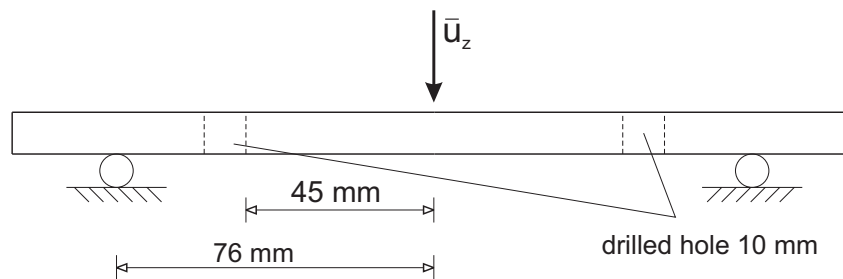


Figure 8.4: 3-point-bending test

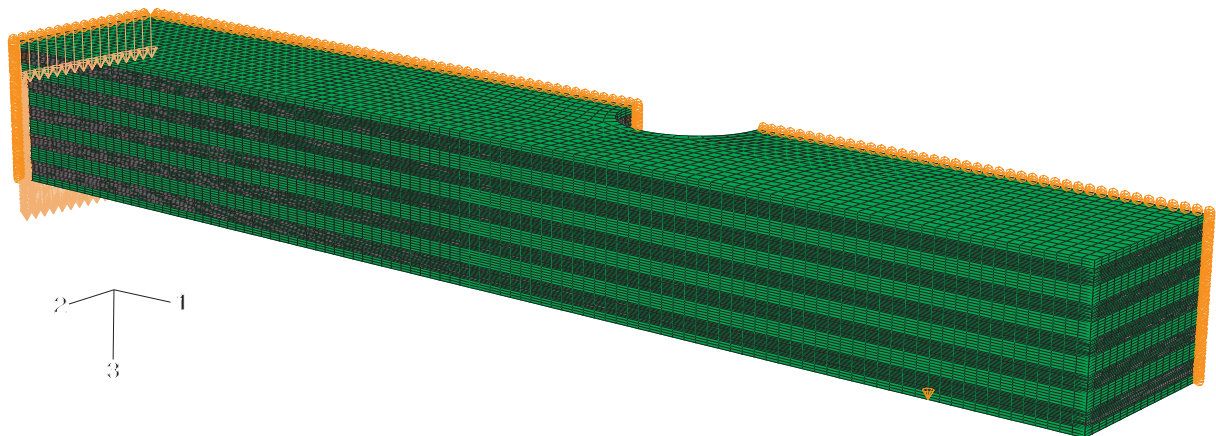


Figure 8.5: Finite-element mesh 3-point-bending test

Figure 8.6 shows, that the predicted elastic parameters match the experimental results outstandingly well. The simulated load-displacement curve fits the experimental results very good, although the results are conservative again. However, the material degradation of the simulation given in Figure 8.7 corresponds extraordinarily well with the test data. The strengths in transverse direction and the degradation could hardly get any better.

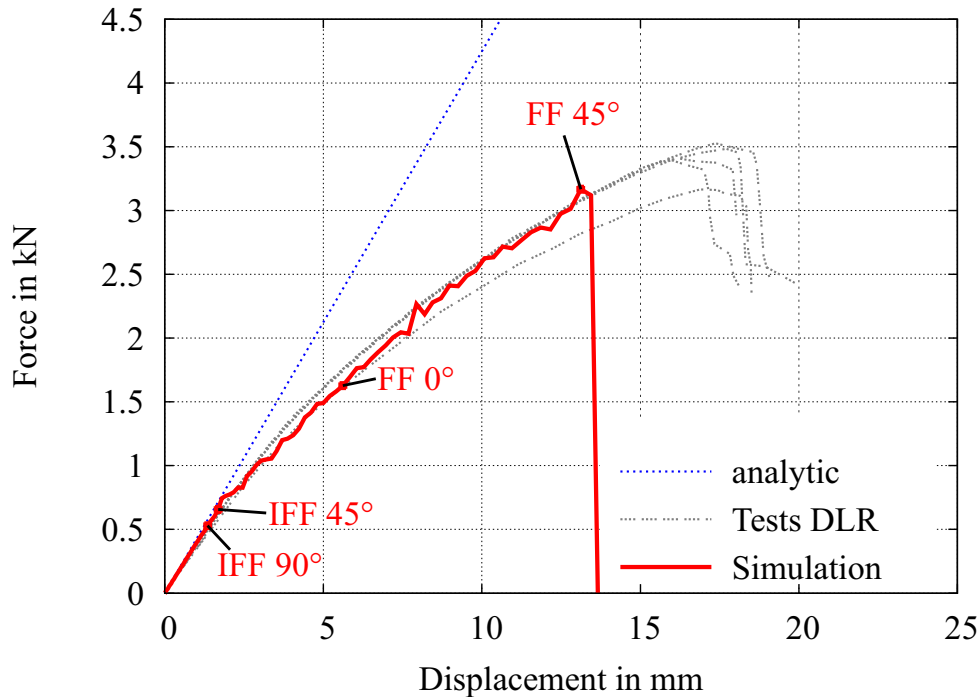


Figure 8.6: 3-point-bending test: load-displacement curve experimental results vs Simulation

The reason for final failure in the experiment is not documented, but delamination and subsequent buckling of a small number of layers are very common failure mechanisms in thick laminates. In the simulation, buckling occurs in the compression zone of the specimen after FF of the 45-layers and leads to final failure. Buckling is made possible by the degradation of material properties to 1 % of the initial value due to fibre failure, which equals an delamination. This degradation is based on assumptions and could not be validated. Therefore, more detailed test results, e.g. acoustic emission, would be very helpful to be able to interpret the nonlinear specimen behaviour. Eventually, other test setups might clarify the ongoing damage better than this very thick laminate.

The analytic solution given in Figure 8.6 is determined from the ABD-Matrix of an equivalent laminate of UD-layers. The Young's Modulus in specimen direction is given over

$$E_1 = \frac{1}{a_{11}d} \quad , \quad (8.1)$$

where a_{11} is the first entry of the inverse ABD-matrix, computed with classical laminate theory, and d is the thickness of the laminate. With this Young's modulus given, the approximate deflection of the specimen under a concentrated force can easily be determined, if the drilled holes are neglected.

Figure 8.8 shows the von-Mises stresses in the specimen.

Figure 8.9 shows the inter-fibre damage in the bottom 90°-layer of the 3-point bending specimen. The first crack originates in the middle of the specimen, which is at the left

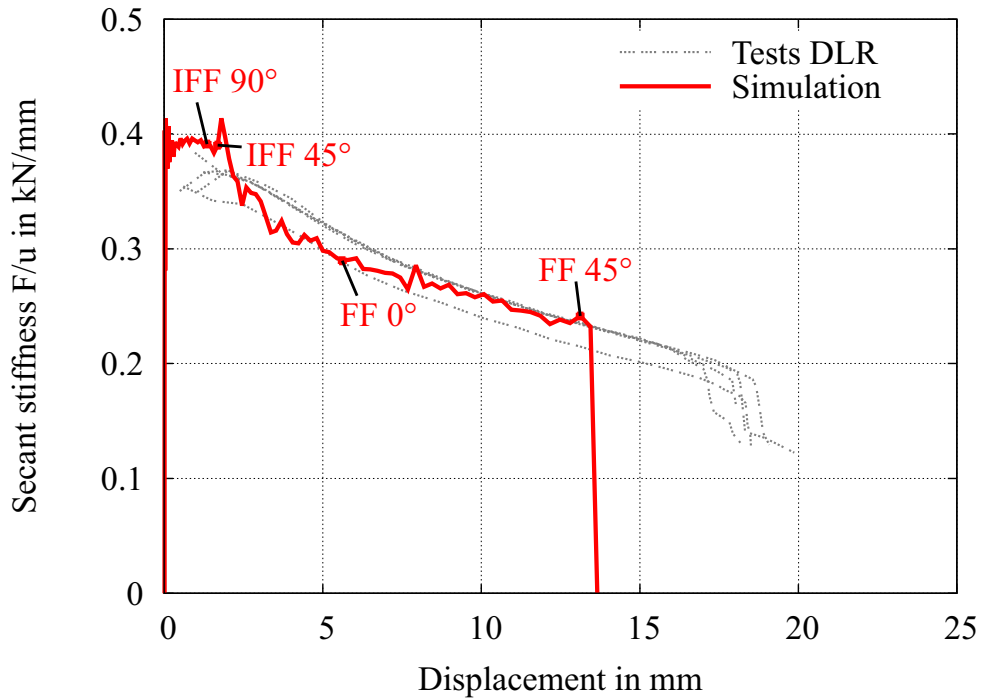


Figure 8.7: 3-point-bending test: Stiffness-displacement curve

boundary in Figure 8.9, where only a quarter of the specimen is shown. Secondly, a crack is originated at the drilled hole. In the following cracks evolve in the shown typical pattern that is in fact the characteristic damage state. This damage pattern evolves in thickness direction as well.

Figure 8.10 shows the FF damage variable at failure of the specimen. It can be seen that multiple layers fail in the tension zone, which leads to a complete failure of the specimen. The maximum load carried by the specimen is 3.0 MPa, which is a very good result compared to the mean result of the experiments, 3.4 MPa, with a deviation of only 12 %. In the previous section it has been shown that the strengths determined with the mesomechanical unit cell are in excellent correspondence with the experimental results, therefore it must be concluded that softening after FF is underestimated in the simulation. It has been reported by Maimi, Camanho, Mayugo, and Davila (2006) that it is important to model FF softening to yield good results. Actually, an increased strain energy release rate yields higher maximum loads, however, these values are hypothetical. Therefore, a slightly conservative result based on validated strengths is preferred over an excellent result without validation.

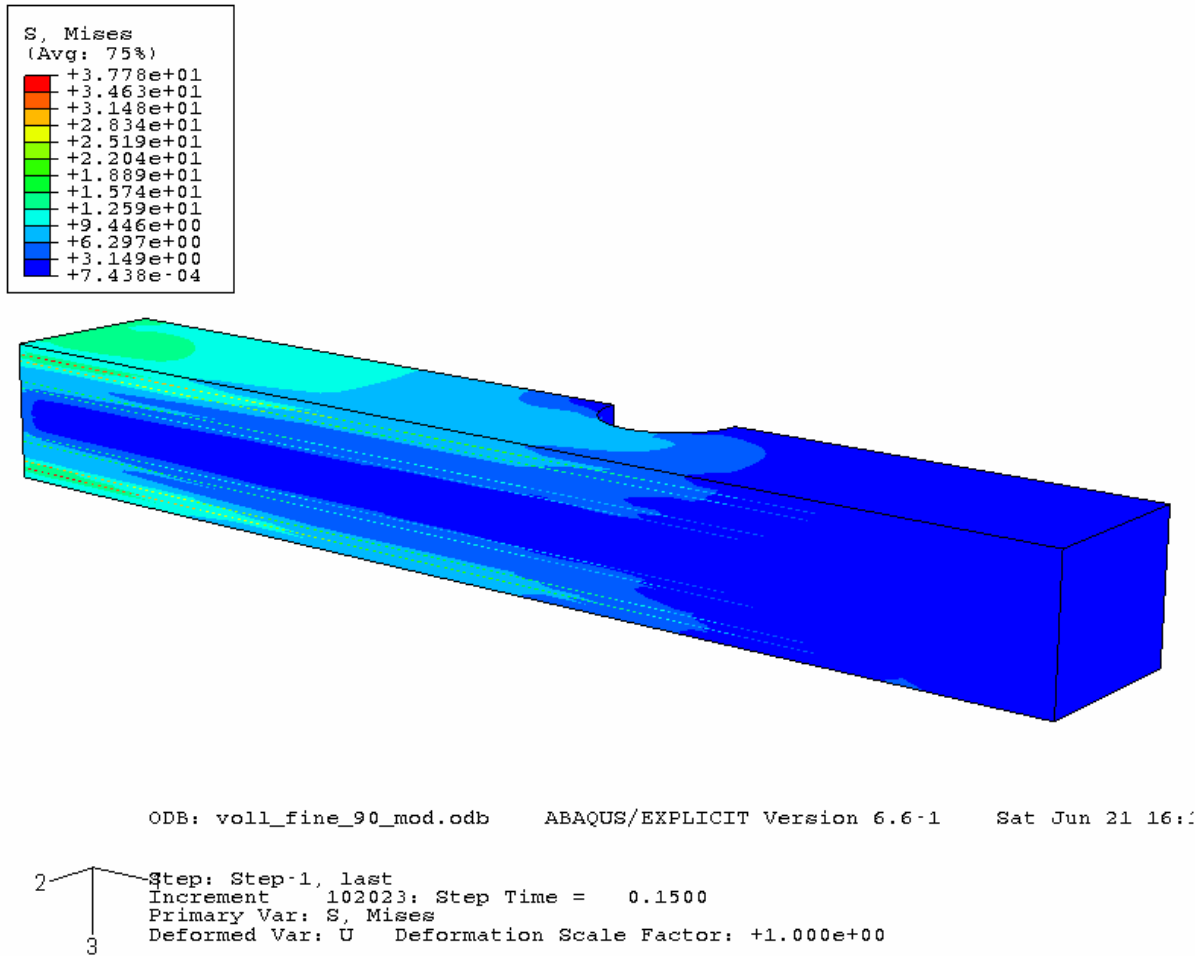


Figure 8.8: 3-point-bending test: finite-element mesh, fibre direction stress

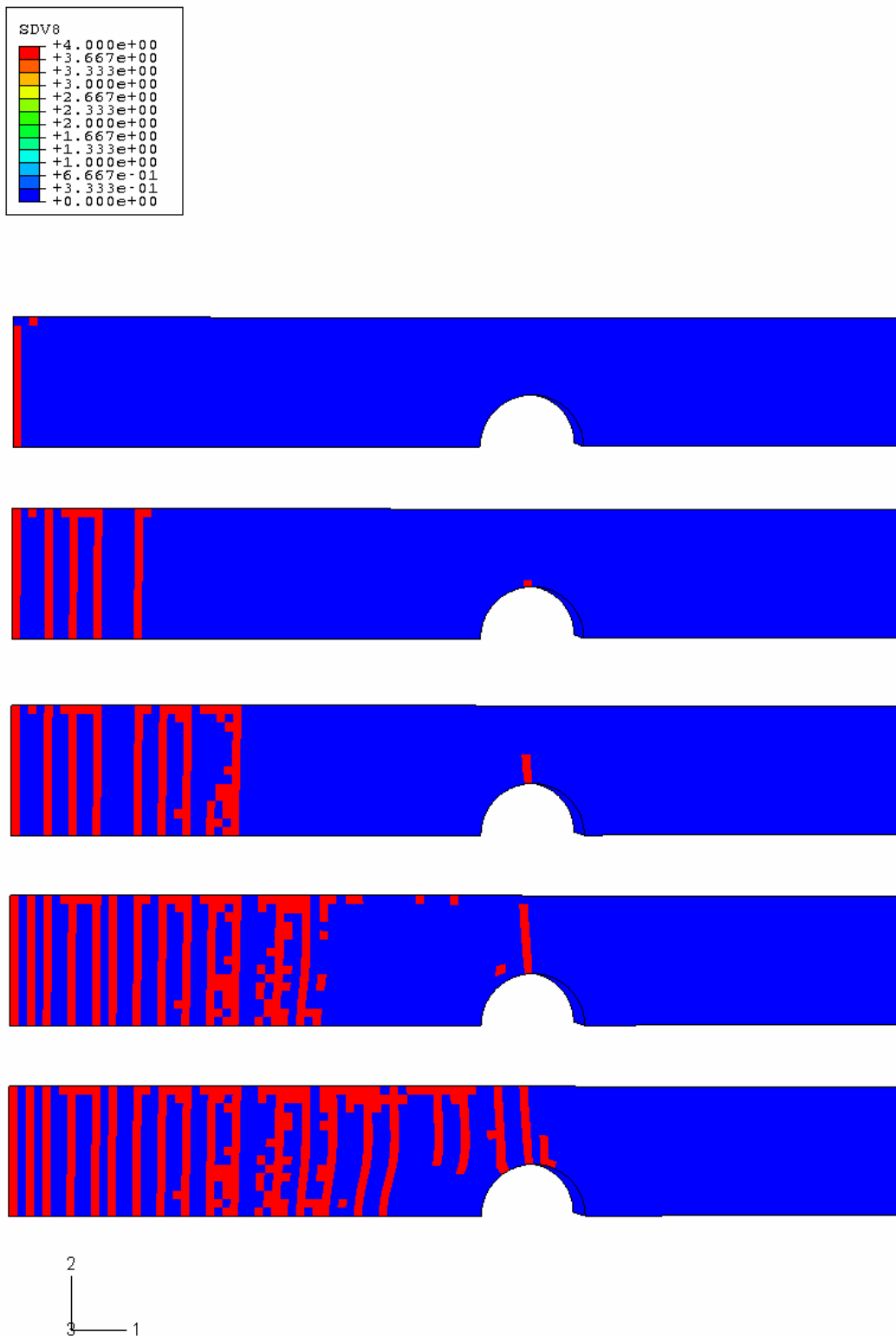


Figure 8.9: 3-point-bending test: damage in bottom 90°-layer, characteristic damage state

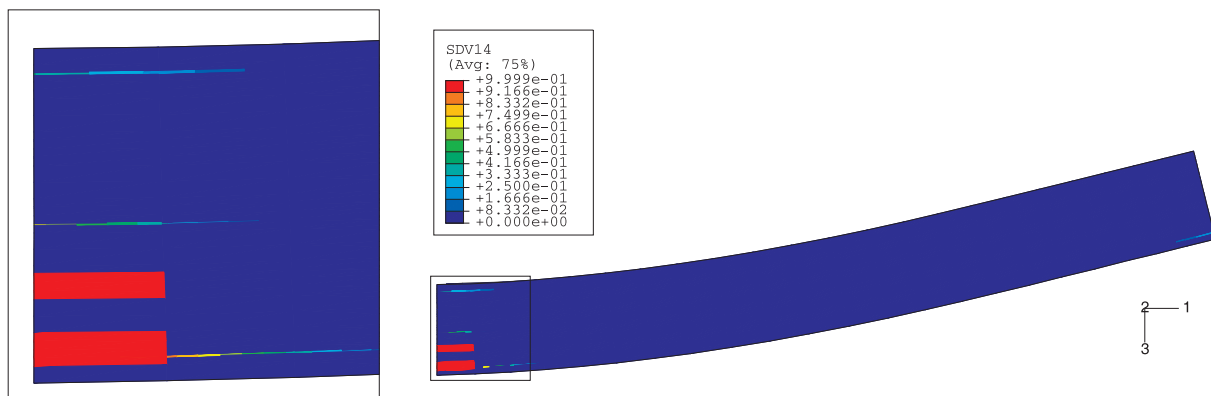


Figure 8.10: 3-point-bending test: finite-element mesh, FF damage variable at failure

8.3 Summary

In the coupon test it was shown that stiffness and strengths have been predicted very well in the mesomechanical unit cell. This is an outstanding result, considering that only fibre and epoxy resin material behaviour were used as input. The predicted parameters allow for an excellent simulation of first-ply failure without any difficulty. Furthermore, the progressive damage up to the first FF is modelled extraordinarily well in combination with the failure criterion of Juhasz and the degradation model of Puck. In the 3-point bending test the progressive damage is modelled very well even after FF occurs in the model. The final failure of the model is not reached, probably because of an underestimated remaining strength after FF.

However, the presented softening formulation is capable of delivering reliable predictions of IFF, progressive damage after IFF, and FF, only softening prediction after FF has to be improved. Considering the current design philosophies in industry, that do not allow for any damage in most instances, the presented multiscale analysis is thus capable of providing all required material parameters and even enables substantial improvements in the description of progressive damage.

9 Summary and Conclusion

9.1 Summary

A major advantage of FRP compared to other materials is the possibility to design the material for its special purpose. Textile composites offer an additional degree of adaptability through the textile fiber architecture compared to UD-composites. It is essential for the design process to predict the material properties, because experimental testing is costly and time consuming. A literature review shows that numerous multiscale algorithms have been proposed in the literature for the prediction of material properties of textile composites, but the nonlinear material behavior of the constituents has been disregarded so far. However, the material nonlinearity is crucial for a realistic description of composite strength. Therefore, a multiscale algorithm is developed in this work that focuses on the use of appropriate material and softening models. For this purpose, material models, failure criteria and softening formulations are presented that account for the pressure-dependent nonlinear behavior of epoxy resin and UD-composites.

The multiscale algorithm includes unit cells on micro- and mesoscale. Virtual tests are conducted with these unit cells for determination of UD-composite and textile composite stiffness and strength. UD-composite behavior is important in this context, because the mesomechanical unit cell mainly consists of fiber bundles, that can be seen as UD-composites. It should be noted therefore, that this multiscale algorithm is able to determine nonlinear UD-composite behavior and strength along the way as well.

The virtual tests are compared with experimental results, where data are available. Finally, two macroscale examples are simulated to prove the performance of the algorithm, material models, failure criteria and softening formulations.

9.1.1 Material Model

Epoxy resin and UD-composites exhibit pressure-dependent nonlinear material behavior, i.e. different behavior under tension, shear and compression. For example, under shear great plastic deformations occur, whereas under tension both materials behave nearly brittle. Therefore, invariant-based material formulations are presented that allow for a consideration of the pressure-dependency. Quadratic yield criteria and tabulated hardening curves allow for pressure-dependent hardening.

A major advantage of the hardening model is that the input parameters, hardening curves under tension and shear, are physically meaningful. This is very important for handling of the material model, because it makes checking the input deck easy.

9.1.2 Failure Criteria and Softening Formulations

Failure of epoxy resin, UD-composites and textile composites is also pressure-dependent.

For epoxy resin, an invariant based failure criterion is presented that has a quadratic shape under tension and a linear under compression, to account for different failure mechanisms. The material softening is regularized with a fracture energy approach presented by Hillerborg et al. (1976), to assure a mesh independent solution.

For UD-composites, the invariant-based quadratic criterion (IQC) is presented. It bases on the same invariants as the material model for UD-composites and has a quadratic shape. A softening formulation with the fracture energy regularization of Hillerborg is used for the prediction of progressive damage. The IQC is validated on 14 test cases published in the World-Wide Failure Exercise of Hinton et al. (2004). It shows a very good performance equal to Puck's criterion, but has the advantage that it needs less input parameters. Furthermore, only physically meaningful input parameters are used.

Failure of textile composites is predicted with the failure criterion of Juhasz, in combination with the softening formulation of Puck.

9.1.3 Micromechanical Unit Cells

The micromechanical unit cell is used to estimate material parameters of UD-composites, especially the hardening curves required as input for the nonlinear transversely material model. Square, hexagonal and randomized fiber arrangement, but also analytical rules of mixture, are compared and validated with experimental results from the WWFE. All predictions yielded lower stiffness and strength (where possible) than the experiments. The randomized fiber arrangement provides the best estimates for the elastic parameters, that are in very good agreement with the experimental results, but the determination of strength is problematic. A square fiber arrangement, in contrast, does not possess transversely isotropic material behavior, but yields a better overall estimation than the hexagonal fiber arrangement.

9.1.4 Mesomechanical Unit Cells

The material parameters of a textile lamina are determined with the mesomechanical unit cell. Therefore, two modeling strategies are investigated, layer-based and textile-layer homogenization. The difference between both strategies is the number of fiber orientations that are included in the unit cell. An example for layer-based homogenization is the presented unit cell of a non-crimp fabric that includes only a single layer of fibers sharing the same orientation. Therefore, the inter-layer interactions are not captured very well with this approach, but the analysis of failure can be carried out in great detail. In the textile-layer homogenization one or more textile layers are discretized in one unit cell. As an example two weft-knitted fabrics are discretized. The textile architecture and the interactions between the layers are incorporated completely, but the behavior of the unit

cell is likely to be anisotropic instead of orthotropic. Thus, more virtual tests are required for an appropriate description of the material behavior and failure can be observed only in a smeared fashion.

Due to the potential of more detailed failure analysis the layer-based homogenization is favorable, but because the inter-layer interactions are compromised in this method, it does not always give the best results.

9.1.5 Macroscale Computations

The material parameters determined with the mesomechanical non-crimp fabric unit cell are validated through the simulation of two experimental tests. In a coupon test the predicted stiffnesses and strengths agree very well with the experimental results. Especially the degradation of the coupon is captured excellently by the simulation.

In order to investigate the performance of the parameters in a three-dimensional stress state with progressive damage a simulation of a 3-point bending test is compared to experimental results. The predicted elastic parameters show excellent correspondence with the experimental results, but the failure occurs early in the simulation after the first plies have failed in FF mode. However, in this example it is clear that a better softening formulation after FF is required, because the strengths are validated by the coupon test. In contrast, the progressive damage after IFF is modelled outstandingly well, considering the complex stress state and failure process in the specimen. Overall, the predicted material parameters are in excellent agreement with the experimental results and the simulation of progressive damage works very well.

9.2 Outlook

The macroscale simulations show that a nonlinear material model and an appropriate softening model are needed for the orthotropic textile composite material. A validation of the mesomechanical unit cell is difficult, because it can be validated over macroscale simulations only that incorporate a number of other influences on the results. Therefore, it would be an interesting prospect to produce test specimen in analogy to the mesomechanical unit cell, to validate it directly, i.e. a UD-layer with through-thickness stitches. Another possibility of such mesoscale test specimens would be the inclusion of measured imperfections in the unit cell and a comparison with test results. At least a sensitivity analysis of the mesomechanical unit cell against imperfections should be performed in order to investigate the possible effects of defects. Furthermore, detailed tests of damage mechanisms in textile composites would help to improve the description of progressive damage in textile composites. Therefore, smaller specimens with less layers than the presented 3-point-bending test should prove valuable. Further, tests with the Arcan test rig developed by Hartung et al. (2007) could deliver useful experimental results.

An interaction of fiber-parallel stresses and inter-fiber failure would be a valuable improvement of the invariant-based quadratic criterion (IQC). Furthermore, an incorporation of

the in-situ effect in the softening formulation should improve the predictive capabilities IQC for UD-laminates as well. Delamination, another important failure mode for UD-composites, has to be included in the IQC and the softening formulation for a complete description of composite failure. Therefore, a more sophisticated damage description, including damage before failure would be a useful enhancement.

References

- Bibo, G. A., Hogg, P. J., Backhouse, R., & Mills, A. (1998). Carbon-fibre non-crimp fabric laminates for cost-effective damage-tolerant structures. *Composites Science and Technology*, 58, 129–143.
- Blackketter, D. M., Upadhyaya, D., & King, T. R. (1993). Micromechanics prediction of the transverse tensile strength of carbon fiber/epoxy composites: The influence of the matrix and interface. *POLYMER COMPOSITES, OCTOBER 1993, Vol. 14, No. 5*, 14(5), 437 – 446.
- Blackketter, D. M., Walrath, D. E., & Hansen, A. C. (1993). Modeling damage in a plain weave fabric-reinforced composite material. *Journal of Composites Technology and Research*, 15(2), 136 – 142.
- Boehler, J. (Ed.). (1987). *Applications of tensor functions in solid mechanics*. Springer.
- Bowden, P. B., & Jukes, J. A. (1972). The plastic flow of isotropic polymers. *Journal of Materials Science*, 7, 52-63.
- Chamis, C. C. (1987, July). Simplified composite micromechanics for predicting microstresses. *Journal of Reinforced Plastics and Composites*, 6, 268-289.
- Cox, B., Carter, W., & Fleck, N. (1994). A binary model of textile composites- i. formulation. *Acta metall. mater.*, 42(10), 3463 – 3479.
- Cox, B. N., & Flanagan, G. (1997). *Handbook of analytical methods for textile composites* (NASA Contractor Report No. 4750). NASA Langley Research Center.
- Crookston, J. J. (2005). *Prediction of elastic behaviour and initial failure of textile composites*. Doctoral dissertation, The University of Nottingham, Nottingham.
- Cuntze, R. (Ed.). (1997). *Neue Bruchkriterien und Festigkeitsnachweise für unidirektionalen Faserkunststoffverbund unter mehrachsiger Beanspruchung – Modellbildung und Experimente* -. Düsseldorf: VDI-Verlag.
- Cuntze, R. (2007). Prediction of static 3d and in-plane fracture failure of ud laminae composed of fibre-reinforced plastics. *NAFEMS Nordic Seminar on Material's Modeling*. (oral presentation)
- Cuntze, R., & Freund, A. (2004). The predictive capability of failure mode concept-based strength criteria for multidirectional laminates. In M. Hinton, A. Kaddour, & P. Soden (Eds.), *Failure criteria in fibre reinforced polymer composites: The World-Wide Failure Exercise* (pp. 429–489). Oxford: Elsevier Science.
- Dransfield, K., Baillie, C., & Mai, Y. W. (1994). Improving the delamination resistance of cfrp by stitching—a review. *Composites Science and Technology(UK)*, 50, 305–317.
- Edgren, F., & Asp, L. E. (2005, February). Approximate analytical constitutive model for non-crimp fabric composites. *Composites Part A: Applied Science and Manufacturing*, 36, 173–181.

- Edgren, F., Mattson, D., Asp, L. E., & Varna, J. (2004). Formation of damage and its effects on non-crimp fabric reinforced composites loaded in tension. *Composites Science and Technology*, *64*, 675–692.
- EN-2561. (1995). *Carbon fibre reinforced plastics - unidirectional laminates, tensile test parallel to the fibre direction* [EN-Standard].
- EN-2850. (1995). *Aerospace series - carbon fibre thermosetting resin unidirectional laminates - compression test parallel to fibre direction* [EN-Standard].
- Ernst, G., Hühne, C., & Rolfes, R. (2006). Micromechanical voxel unit cell for strength analysis of fiber reinforced plastics. *Proceedings of the CDCM06*, <http://www.ndt.net/article/cdcm2006/papers/ernst.pdf>, 1–9.
- Fiedler, B., Hojo, M., Ochiai, S., Schulte, K., & Ando, M. (2001). Failure behavior of an epoxy matrix under different kinds of static loading. *Composites Science and Technology*, *61*, 1615–1624.
- Geier, B. (1982). *Introduction to the mechanics of composite laminates* (Tech. Rep. No. IB 131-82/12). Braunschweig, Germany: Institut für Strukturmechanik, DFVLR.
- Gilat, A., Goldberg, R. K., & Roberts, G. D. (2005). *Strain rate sensitivity of epoxy resin in tensile and shear loading* (Tech. Rep. No. NASA/TM-2005-213595). Cleveland, Ohio: Glenn Research Center.
- Godbehere, A. P., Mills, A. R., & Irving, P. (1994). Non-crimped fabrics vs. prepreg cfrp composites-a comparison of mechanical performance. In *6th international conference on fibre reinforced composites(frc'94)* (p. 6).
- Gunnion, A. J. (2004). *Analytical assessment of fibre misalignment in advanced composite materials*. Doctoral dissertation, RMIT University, Melbourne.
- Gusev, A. A., Hine, P. J., & Ward, I. M. (2000, March). Fiber packing and elastic properties of a transversely random unidirectional glass/epoxy composite. *Composites Science and Technology*, *60*, 535–541.
- Haasemann, G., Kästner, M., & Ulbricht, V. (2006). Multi-scale modelling and simulation of textile reinforced materials. *CMC-TECH SCIENCE PRESS-*, *3*, 131–145.
- Haasemann, G., & Ulbricht, V. (2006). On the simulation of textile reinforced composites and structures. *Proceedings in Applied Mathematics and Mechanics*, *6*(1), 479 – 480.
- Hamstad, M. (1986, March). A review: Acoustic emission, a tool for composite-materials studies. *Experimental Mechanics*, *26*, 7-13.
- Hartung, D., Aschenbrenner, L., & Teßmer, J. (2007). Analysis of the through-thickness material and failure behaviour of textile composites. In P. P. Camanho, C. G. Dávila, S. T. Pinho, & J. Remmers (Eds.), *Eccomas thematic conference on mechanical response of composites*. Porto.
- Hashin, Z. (1980). Failure Criteria for Unidirectional Fiber Composites. *Journal of Applied Mechanics*, *47*, 329–334.
- Hashin, Z., & Shtrikman, S. (1963). A variational approach to the theory of the elastic behavior of multiphase materials,. *Journal of the Mechanics and Physics of Solids*, *11*, 127–140.
- Haufe, A., Bois, P. A. D., Kolling, S., & Feucht, M. (2005). A semi-analytical model for polymers subjected to high strain rates. In *5th european ls-dyna users' conference* (pp. 2b–58). Birmingham: ARUP UK.

- Herrmann, A. S., Pabsch, A., & Kleineberg, M. (2001). Sli-rtm fairings for fairchild dornier do 328 jet. In *22nd sampe europe international conference*. Paris.
- Hill, R. (1963, September). Elastic properties of reinforced solids: Some theoretical principles. *Journal of Mechanics Physics of Solids*, *11*, 357–372.
- Hillerborg, A., Modeer, M., & Petersson, P. E. (1976). Analysis of crack formation and crack growth in concrete by means of fracture mechanics and finite elements. *Cement and Concrete Research*, *6*, 773–782.
- Hinton, M. J., Kaddour, A. S., & Soden, P. D. (2004). *Failure Criteria in Fibre Reinforced Polymer Composites: The World-Wide Failure Exercise*. Oxford: Elsevier Science.
- Hoffman, O. (1967). The brittle strength of orthotropic materials. *Journal of Composite Materials*, *1*, 200–206.
- Hufenbach, W. (Ed.). (2007). *Textile Verbundbauweisen und Fertigungstechnologien für Leichtbaustrukturen des Maschinen- und Fahrzeugbaus*. SDV - Die Medien AG. (ISBN-13: 978-3-00-022109-5)
- Hughes, T. (2003). Efficient and simple algorithms for the integration of general classes of inelastic constitutive equations including damage and rate effects. In T. Hughes & T. Belytschko (Eds.), *Nonlinear finite element analysis course notes*.
- Ishikawa, T., & Chou, T.-W. (1982). Stiffness and strength behaviour of woven fabric composites. *JOURNAL OF MATERIALS SCIENCE*, *17*, 3211–3320.
- Jain, L. K., Dransfield, K. A., & Mai, Y.-W. (1998). On the effects of stitching in cfrps-ii. mode ii delamination toughness. *Composites Science and Technology*, *58*, 829–837.
- Jeltsch-Fricker, R. (1996). Bruchbedingungen vom Mohrschen Typ für transversal-isotrope Werkstoffe am Beispiel der Faser-Kunststoff-Verbunde. *ZAMM*, *76*(9), 505–520.
- Juhasz, T. J. (2003). *Ein neues physikalisch basiertes Versagenkriterium für schwach 3D-verstärkte Faserverbundlaminate*. Doctoral dissertation, Technische Universität Braunschweig.
- Juhasz, T. J., Rolfes, R., & Rohwer, K. (2001). A new strength model for application of a physically based failure criterion to orthogonal 3D fiber reinforced plastics. *Composite Science and Technology*, *61*, 1821–1832.
- Kaddour, A. S., & Hinton, M. J. (2005). The launch of wwfe-ii: Benchmarking of 3d strength and damage theories for polymer fibre composites. In *Proceedings iccm-15. cd edition*. Durban.
- Karkkainen, R. L., & Sankar, B. V. (2006). A direct micromechanics method for analysis of failure initiation of plain weave textile composites. *Composites Science and Technology*, *66*, 137–150.
- Karkkainen, R. L., Sankar, B. V., & Tzeng, J. T. (2007, August). A direct micromechanical approach toward the development of quadratic stress gradient failure criteria for textile composites. *Journal of Composite Materials*, *41*, 1917-1937.
- Kästner, M., Haasemann, G., Brummund, J., & Ulbricht, V. (2008). Computation of effective stiffness properties for textile-reinforced composites using x-fem. In P. P. Camanho, C. G. Dávila, S. T. Pinho, & J. Remmers (Eds.), *Mechanical response of composites* (Vol. 10, p. in print). Springer. (ISBN: 978-1-4020-8583-3)
- Kim, H. J., & Swan, C. C. (2003). Voxel-based meshing and unit-cell analysis of textile composites. *International Journal for Numerical Methods in Engineering*, *56*, 977–1006.

- Kleineberg, M., Herbeck, L., & Schäpinger, C. (2002). Advanced liquid resin infusion—a new perspective for space structures. In *European conference on spacecraft structures, materials and mechanical testing*. Toulouse, France.
- Knops, M. (2003). *Sukzessives Bruchgeschehen in Faserverbundlaminate*. Doctoral dissertation, Fakultät für Maschinenwesen der Rheinisch-Westfälischen Technischen Hochschule Aachen.
- Kumar, R. S., & Talreja, R. (2003). A continuum damage model for linear viscoelastic composite materials. *Mechanics of Materials*, *35*, 463–480.
- Ladeveze, P., & LeDantec, E. (1992). Damage modelling of the elementary ply for laminated composites. *Composites Science and Technology*, *43*, 257–267.
- Ladeveze, P., & Lubineau, G. (2002, March). An enhanced mesomodel for laminates based on micromechanics. *Composites Science and Technology*, *62*, 533–541.
- Lemaitre, J., & Chaboche, J.-L. (1988). *Mécanique des matériaux solides*. Dunod.
- Lemaitre, J., & Desmorat, R. (2005). *Engineering damage mechanics: Ductile, creep, fatigue and brittle failures*. Springer.
- Lomov, S. V., Belov, E. B., Bischoff, T., Ghosh, S. B., Chi, T. T., & Verpoest, I. (2002, September). Carbon composites based on multi-axial multiply stitched preforms. part 1. geometry of the preform. *Composites Part A: Applied Science and Manufacturing*, *33*, 1171–1183.
- Lomov, S. V., Ivanov, D. S., Verpoest, I., Zako, M., Kurashiki, T., Nakai, H., et al. (2007). Meso-fe modelling of textile composites: Road map, data flow, and algorithms. *Composites Science and Technology*, *67*, 1870–1891.
- Maimi, P., Camanho, P. P., Mayugo, J. A., & Davila, C. G. (2006). *A thermodynamically consistent damage model for advanced composites* (Tech. Rep. No. TM-2006-214282). NASA Langley Research Center.
- Mattsson, H. D., & Varna, J. (2007, April). Average strain in fiber bundles and its effect on ncf composite stiffness. *Journal of Engineering Materials and Technology*, *129*, 211–219.
- Mouritz, A. P., Leong, K. H., & Herszberg, I. (1997). A review of the effect of stitching on the in-plane mechanical properties of fibre-reinforced polymer composites. *Composites Part A: Applied Science and Manufacturing*, *28*, 979–991.
- Mulhern, J. F., Rogers, T. G., & Spencer, A. J. M. (1967, November). A continuum model for fibre-reinforced plastic materials. *Proceedings of the Royal Society of London. Series A, Mathematical and Physical Sciences*, *301*, 473–492.
- Nahas, M. N. (1986). Survey of Failure and Post-Failure Theories of Laminated Fiber-Reinforced Composites. *Composites Technology & Research*, *8*(4), 138–153.
- Paepegem, W. V., Baere, I. D., & Degrieck, J. (2006, August). Modelling the nonlinear shear stress-strain response of glass fibre-reinforced composites. part i: Experimental results. *Composites Science and Technology*, *66*, 1455–1464.
- Puck, A. (1996). *Festigkeitsanalyse von Faser-Matrix-Laminaten, Modelle für die Praxis*. München: Hanser.
- Puck, A., Kopp, J., & Knops, M. (2002). Guidelines for the determination of the parameters in Puck’s action plane strength criterion. *Composites Science and Technology*, *62*, 371–378.
- Puck, A., & Schneider, W. (1969). On failure mechanisms and failure criteria of filament-wound glass-fibre/resin composites. *Plastics and Polymers*, *37*, 33–44.

- Puck, A., & Schürmann, H. (2004). Failure analysis of FRP laminates by means of physically based phenomenological models. In M. J. Hinton, A. S. Kaddour, & P. D. Soden (Eds.), *Failure Criteria in Fibre Reinforced Polymer Composites: The World-Wide Failure Exercise* (pp. 264–297). Oxford: Elsevier Science.
- Rogers, T. (1987). Yield criteria, flow rules and hardening in anisotropic plasticity. In J. Boehler (Ed.), *Yielding, damage and failure of anisotropic solids* (Vol. 5, pp. 53–79). EGF Publication.
- Rolfes, R., Ernst, G., Hartung, D., & Teßmer, J. (2006). Strength of Textile Composites - A Voxel Based Continuum Damage Mechanics Approach. In C. A. M. Soares, J. A. C. Martins, H. C. Rodrigues, & J. A. C. Ambrosio (Eds.), *Computational mechanics -solids, structures and coupled problems* (pp. 497–520). Springer.
- Rolfes, R., Ernst, G., Vogler, M., & Hühne, C. (2008). Material and failure models for textile composites. In P. P. Camanho, C. G. Dávila, S. T. Pinho, & J. Remmers (Eds.), *Mechanical response of composites* (Vol. 10, p. in print). Springer. (ISBN: 978-1-4020-8583-3)
- Schröder, J. (1995). *Theoretische und algorithmische konzepte zur phänomenologischen beschreibung anisotropen materialverhaltens*. Doctoral dissertation, Universität Hannover.
- Schuecker, C., & Pettermann, H. E. (2007). Fiber reinforced laminates: Progressive damage modeling based on failure mechanisms. *Archives of Computational Methods in Engineering*, 1–22.
- Schürmann, H. (2007). *Konstruieren mit Faser-Kunststoff-Verbunden* (5 ed.). Berlin: Springer.
- Sickinger, C., & Herrmann, A. (2001). Structural stitching as a method to design high-performance composites in future. In *Proceedings techtextil symposium*. Frankfurt am Main: Messe Frankfurt.
- Simo, J., & Hughes, T. (1998). *Computational inelasticity*. New York: Springer.
- Smith, L. V., & Swanson, S. R. (1996). Strength design with 2-d triaxial braid textile composites. *Composites Science and Technology*, 56, 359-365.
- Spencer, A. (1987). Kinematic constraints, constitutive equations and failure rules for anisotropic materials. In J. Boehler (Ed.), *Applications of tensor functions in solid mechanics* (pp. 187–201). Springer.
- Sun, C. T., & Vaidya, R. S. (1996). Prediction of composite properties from a representative volume element. *Composites Science und Technology*, 56, 171–179.
- Takano, N., Uetsuji, Y., Kashiwagi, Y., & Zako, M. (1999). Hierarchical modelling of textile composite materials and structures by the homogenization method. *Modelling Simul. Mater. Sci. Eng.*, 7, 207–231.
- Tan, P., Tong, L., & Steven, G. P. (2000, March). Behavior of 3d orthogonal woven cfrp composites. part ii. fea and analytical modeling approaches. *Composites Part A: Applied Science and Manufacturing*, 31, 273-281.
- Thom, H. (1999). Finite element modeling of plain weave composites. *Journal of Composite Materials*, 33(16), 1491–1510.
- Truong, T. C., Vettori, M., Lomov, S., & Verpoest, I. (2005, September). Carbon composites based on multi-axial multi-ply stitched preforms. part 4. mechanical properties of composites and damage observation. *Composites Part A: Applied Science and Manufacturing*, 36, 1207–1221.

- Tsai, G.-C., & Chen, J.-W. (2005, June). Effect of stitching on mode I strain energy release rate. *Composite Structures*, *69*, 1–9.
- Tsai, S. W., & Wu, E. M. (1971). A general theory of strength for anisotropic materials. *Journal of Composite Materials*, *5*, 58–80.
- Ulbricht, V., & Haasemann, G. (2007). Werkstoffverhalten und -modelle. In W. Hufenbach (Ed.), *Textile Verbundbauweisen und Fertigungstechnologien für Leichtbaustrukturen des Maschinen- und Fahrzeugbaus*. Dresden: SDV - Die Medien AG. (ISBN-13: 978-3-00-022109-5)
- VDI. (2006). *Entwicklung von Bauteilen aus Faser-Kunststoff-Verbund, Berechnungen* [VDI-Richtlinien, VDI 2014, Blatt 3]. Düsseldorf: VDI-Verlag.
- Vogler, M., Ernst, G., Hühne, C., & Rolfes, R. (2007). A transversely isotropic plasticity model with damage for fiber-reinforced plastics and textile composites. In *Nafems seminar: Simulating composite: Materials and structures* (pp. 1–14). Bad Kissingen. (ISBN 978-1-874376-28-6)
- Wang, Y. (2002, March). Mechanical properties of stitched multiaxial fabric reinforced composites from manual layup process. *Applied Composite Materials*, *9*, 81–97.
- Woo, K., & Whitcomb, J. (1994). Global/local finite element analysis for textile composites. *Journal of Composite Materials*, *28*(14), 1305–1321.
- Woo, K., & Whitcomb, J. D. (1996, June). Three-dimensional failure analysis of plain weave textile composites using a global/local finite element method. *Journal of Composite Materials*, *30*, 984–1003.

Lebenslauf

Persönliches

Name	Gerald Ernst
Geburtstag	27.09.76
Geburtsort	Göttingen
Staatsangehörigkeit	deutsch
Familienstand	ledig

Schulbildung

1983 – 1987	Hainbundschole Göttingen (Grundschule)
1987 – 1989	Orientierungsstufe Göttingen-Nord
1989 – 1996	Felix-Klein-Gymnasium Göttingen Abschluß: Abitur (Note: 2,1)

Hochschulbildung

Okt. 1996 – Jan. 2002	Studium Bauingenieurwesen an der Universität Hannover mit Vertiefungsrichtung Konstruktiver Ingenieurbau
Okt. 2001 – Dez. 2001	Diplomarbeit zum Thema "Dynamische Untersuchungen von eingleisigen Eisenbahnbrücken zur Beurteilung der Resonanzgefahr mit dem Finite-Elemente-Programm SOFiSTiK" (Note: sehr gut)
Jan. 2002	Diplom (Gesamtnote: sehr gut)

Zivildienst

Apr. 2002 – Jan. 2003	Vogelwart beim Verein Jordsand am Rantumbecken Sylt
-----------------------	---

Wissenschaftliche Tätigkeiten

März 2003 – Jan. 2005	Wissenschaftlicher Mitarbeiter am Institut für Statik
Jan. 2005 – Juni 2008	Wissenschaftlicher Mitarbeiter am Institut für Statik und Dynamik
Mai 2006 – Aug. 2006	DAAD-Stipendium für Auslandsaufenthalt am Cooperative Research Center for Advanced Composite Structures in Melbourne, Australien

Mitteilungen des Instituts für Statik und Dynamik der Leibniz Universität Hannover

- 1 R. Rolfes/
C. Hühne Eröffnungskolloquium (Tagungsband) 2005
- 2 H. Rothert/
M. Kaliske/
L. Nasdala Entwicklung von Materialmodellen zur Alterung von Elastomerwerkstoffen unter besonderer Berücksichtigung des Sauerstoffeinflusses (DFG-Abschlußbericht) 2005
- 3 L. Nasdala Simulation von Materialinelastizitäten bei Nano-, Mikro- und Makrostrukturen - Stabilitätsprobleme, Schädigungs- und Alterungsprozesse bei Kohlenstoffnanoröhren und Elastomerwerkstoffen (Habilitationsschrift) 2005
- 4 C. Hühne Robuster Entwurf beulgefährdeter, unversteifter Kreiszyinderschalen aus Faserverbundwerkstoff (Dissertationsschrift) 2006
- 5 L. Nasdala/
K.-U. Schröder Finite Element Applications in Structural Analysis (Skript zur Hörsaalübung) 2006
- 6 Klausuraufgabensammlung, 4. Auflage 2007
- 7 R. Rolfes/
W.-J. Gerasch/
D. Rotert Vorlesung Tragwerksdynamik 2007
- 8 K.-H. Elmer/
K. Betke/
Th. Neumann Standardverfahren zur Ermittlung und Bewertung der Belastung der Meeresumwelt durch die Schallimmission von Offshore-Windenergieanlagen(Abschlußbericht zum BMU-Forschungsvorhaben) 2007
- 9 K.-U. Schröder Zur nichtlinearen Berechnung von Stahlbeton- und Verbundbauteilen (Dissertationsschrift) 2007
- 10 G. Ernst Multiscale Analysis of Textile Composites - Stiffness and Strength - (Dissertationsschrift) 2009